



HAL
open science

Modélisation des écoulements fluide multiphasiques avec une approche SPH

Abdelkader Krimi

► **To cite this version:**

Abdelkader Krimi. Modélisation des écoulements fluide multiphasiques avec une approche SPH. Mécanique [physics.med-ph]. Ecole nationale supérieure d'arts et métiers - ENSAM, 2018. Français. NNT : 2018ENAM0004 . tel-02068040

HAL Id: tel-02068040

<https://pastel.hal.science/tel-02068040>

Submitted on 14 Mar 2019

HAL is a multi-disciplinary open access archive for the deposit and dissemination of scientific research documents, whether they are published or not. The documents may come from teaching and research institutions in France or abroad, or from public or private research centers.

L'archive ouverte pluridisciplinaire **HAL**, est destinée au dépôt et à la diffusion de documents scientifiques de niveau recherche, publiés ou non, émanant des établissements d'enseignement et de recherche français ou étrangers, des laboratoires publics ou privés.

École doctorale n° 432 : Sciences des Métiers de l'ingénieur

Doctorat ParisTech

T H È S E

pour obtenir le grade de docteur délivré par

L'École Nationale Supérieure d'Arts et Métiers

Spécialité « Mécanique »

présentée et soutenue publiquement par

Abdelkader KRIMI

24 Janvier 2018

**Modélisation des écoulements fluide multiphasiques avec une
approche SPH**

**« Modeling of multiphase fluid flows with Smoothed Particle
Hydrodynamics approach »**

Directeur de thèse : **Sofiane KHELLADI**

Co-encadrement de la thèse : **Michael DELIGANT et Mehdi REZOUG**

Jury

M. Stéphane Aubert , Professeur des universités, École Centrale de Lyon, France	Président
M. Sébastien Martin , Professeur des universités, Université Paris Descartes, France	Rapporteur
M. Xesús Nogueira , HDR, Université de la Corogne, Civil Engineering School, Espagne	Rapporteur
M. Yan Delaure , Assistant Professor, Dublin City University, Irlande	Rapporteur
M. David Le Touzé , Professeur des universités, École Centrale de Nantes, France	Examineur
M. Sofiane Khelladi , Professeur des universités, Arts et Métiers ParisTech, France	Examineur
M. Michael Deligant , Maître de conférence, Arts et Métiers ParisTech, France	Examineur
M. Mehdi Rezoug , Enseignant-Chercheur, École spéciale des travaux publics (ESTP-Paris), France	Examineur

**T
H
È
S
E**

Acknowledgements

This research was supported totally by the Institut de Recherche en Constructibilité (IRC) of ESTP-Paris. It was in partnership with Dynfluid laboratory of ENSAM-Paris. I want to acknowledge the valuable help and confidence that have been given to me during all my Phd thesis period by the director of research at IRC Mr. Eric Croquesel, the director of Dynfluid laboratory Mr. Farid Bakir, the former director of research at IRC Mr. Jean-Lou Lebrun and of course by the director of ESTP school Mme. Florence Darmon.

First and foremost I would like to thank Prof. Sofiane Khelladi for being a prime example of good supervisor, advisor, scientist, and engineer. He has been always supportive, attentive, kind, and patient to me and I am greatly indebted to him for giving me the opportunity to work with him and his lab. His guidance helped me in all the time of research, and writing of scientific papers and this Phd thesis. And of course, I would like to thank also my co-supervisors Dr. Michael Deligant and Dr. Mehdi Rezoug for the continuous support of my Ph.D study and related research, for their patience and motivation.

Besides my advisors, I would like to thank the rest of my thesis committee : Prof. Stéphane Aubert, Prof. Xesús Nogueira, Prof. Sébastien Martin, Prof. Yan Delaure and Prof. David Le Touzé, for their insightful comments and encouragement, but also for the questions which incited me to widen my research from various perspectives.

My sincere thanks also goes to all IRC and DynFluid laboratories researchers and Ph.D students who provided me an opportunity to join their team, and who gave access to the laboratory and research facilities. Without their precious support it would not be possible to conduct this research.

Special thanks are dedicated to all my professors who taught me at University of BLIDA-Algeria and ENS de Cachan-France,. Without them, I could not explore the multidisciplinary fields : Mathematics, Computer science, Physics and build a passion for them.

Last but not the least, I would like to thank my family : my parents Zerrouk and Zohra "rahimahum Allah" that gave me everything they could give in their life to become what I am now, and also to my brothers and sisters (Hicham, Mahmoud, Lydia, Hassen, Hocine, Lyla,

Mohamed and Ammane Allah) for supporting me spiritually throughout my life especially in difficult times.

Finally, I would like to express my greatest gratitude to all my friends whose stand by me and provide me every possible support, , especially, Mohamed, Sofiane, Bahir, Djamel, Omar, Rabah, Sidahemed, Rechache, Walid, Brahim, Abderahmanne.

Résumé

La méthode Smoothed Particle Hydrodynamics (SPH) est une méthode lagrangienne, sans maillage développée initialement pour des simulations de phénomènes astrophysiques. Depuis, elle a connu de nombreuses applications, notamment pour la simulation des écoulements des fluides. Contrairement aux méthodes utilisant un maillage, la méthode SPH peut gérer de manière naturelle et sans traitement spécifique les simulations des écoulements à surface libre et multiphasiques avec interface subissant de grandes déformations. Dans cette thèse, une modélisation SPH des écoulements des fluides multiphasiques a été réalisée en tenant compte de différentes complexités (écoulements à surface libre et multiphasiques interfaciaux) et de natures d'écoulement (simulation des fluides, des sols et les deux en interactions). Un modèle SPH faiblement compressible (WCSPH) a été proposé pour simuler les écoulements des fluides multiphasiques avec interface comprenant plus de deux phases de fluide. Ce modèle inclut le développement d'une nouvelle formulation de force de tension de surface en utilisant un opérateur SPH consistant de premier ordre. Une modification de condition généralisée aux parois solides a été apportée pour qu'elle soit appliquée sur les écoulements des fluides multiphasiques avec des rapports de densité et de viscosité élevés. Une nouvelle loi de comportement dépendant de la pression nommée RBMC - α_μ (Regularized Bingham Mohr Coulomb où α_μ est un paramètre libre) a également été développée. Cette loi peut simuler les fluides (Newtonien, Binghamien), les sols (cohésif, frictionnel) et les deux en interactions. La loi précédente étant sensible à la pression, une extension du terme diffusif δ -SPH a été faite pour le cas des écoulements des fluides multiphasiques afin de réduire les oscillations de pression à haute fréquence qui sont dues à l'utilisation d'une équation d'état. La validation et l'application des modèles développés dans cette thèse sont montrées à travers plusieurs cas tests de difficulté croissante.

Abstract

Smoothed Particle Hydrodynamics (SPH) is a Lagrangian gridless method developed initially to simulate astrophysical phenomena, and since it has been known for a large number of applications, especially for fluid flow simulations. Contrary to the grid-based method, the SPH method can handle free surface and interfacial fluid flow simulation including large deformations naturally and without the need for any specific treatment. In this thesis a SPH modeling of multiphase fluid flows has been achieved with consideration of different complexities (free surface and interfacial fluid flows) and natures (simulation of fluids, soil and both in interactions). A consistent weakly compressible SPH model (WCSPH) has been proposed to simulate interfacial multiphase fluid flows with more than two fluid phases. This model includes a new expression of the surface tension force using a first order consistency SPH operator. A modification to the well known generalized wall boundary condition have been brought in order to be applied to multiphase fluid flow with large density and viscosity ratios. A new pressure-based constitutive law named RBMC- α_μ (Regularized Bingham Mohr Coulomb with α_μ is free parameter) has been developed in this thesis. This model can simulate fluids (Newtonian, Binghamton), soils (cohesive, frictional) and both in interactions. Because the previous model is pressure sensitive, an extension of δ -SPH diffusive term has been proposed for multiphase fluid flows to overcome the high frequency pressure oscillations due to the determination of pressure from an equation of state. The validation and application of the developed models have been shown in this thesis through several test-cases of increasing difficulty.

Contents

List of Figures	13
List of Tables	25
1 Introduction	27
1.1 Motivation and Objectives	29
1.2 Thesis outline	30
1.3 Contributions	31
1.4 Publications	31
1.4.1 Journals	31
1.4.2 Conferences	32
2 State of the art	33
2.1 Numerical simulation	34
2.2 Grid based numerical methods	35
2.3 Meshfree numerical methods	37
2.4 Smoothed Particle Hydrodynamics (SPH) method	38
2.5 Basics of SPH method	39
2.5.1 Kernel approximation	39
2.5.2 Choice of the smoothing kernel function	40
2.5.3 Kernel approximation of a function derivatives	43
2.5.4 Accuracy of kernel approximation	43
2.5.5 Particle approximation	45
2.6 Performance optimization and open source codes of SPH method	47
2.7 Applications	48
2.7.1 Fluid applications	48
2.7.2 Structure applications	50
2.7.3 Fluid structure interactions	53

3	SPH : Numerical development and governing equations discretization	63
3.1	Governing equations	64
3.2	Determination of pressure	68
3.2.1	Weakly Compressible Smoothed Particle Hydrodynamics	69
3.2.2	Incompressible Smoothed Particle Hydrodynamics	70
3.2.3	Explicit Incompressible Smoothed Particle Hydrodynamics	72
3.3	Discretization of governing equations	72
3.4	Surface tension for multiphase fluids	77
3.5	Rigid body-fluid interaction	78
3.6	Fluid-structure coupling strategies	79
3.7	Improvement in SPH method	80
3.7.1	Improvement in kernel approximation	80
3.7.2	Improvement by recovering the SPH particle approximation of the governing equations	85
3.8	Search neighboring particles	90
3.9	Boundary conditions	91
3.9.1	Wall boundary conditions	91
3.9.2	Inflow and OutFlow boundary conditions	94
3.9.3	Periodic boundary conditions	95
3.9.4	Free surface condition	95
3.10	Time integration algorithm	96
3.11	Stability conditions	97
4	SPH : Modeling of interfacial multiphase fluid flows	99
4.1	Multiphase model	102
4.1.1	Governing equations	102
4.1.2	Discrete form of governing equations	104
4.1.3	Wall boundary conditions	108
4.1.4	Time integration	110
4.1.5	Damping strategy for multiphase fluid flow	112
4.2	Conclusion	113
5	SPH : Modeling of water-soil interactions using a multiphase approach	115
5.1	Governing equations and physical model	119
5.1.1	Determination of the yield stress	123
5.2	Discrete form of governing equations	126
5.2.1	Modeling of the water suspended sediment	131

5.2.2	Wall boundary conditions	132
5.2.3	Time integration	133
5.3	Conclusion	135
6	Validation and application of SPH multiphase model	137
6.1	Vertical fluid column: Hydrostatic pressure condition	138
6.2	Rayleigh–Taylor instability	143
6.3	Interaction of two rising bubbles through a fluid column	146
6.4	Conclusion	147
7	Validation and application of SPH interfacial multiphase model	151
7.1	Square droplet deformation	152
7.2	Spreading lens between two stratified layers	156
7.3	Capillary-viscous wave	161
7.4	Single bubble rising through a vertical column of water	163
7.5	Gas bubble rising through two stratified fluid layers	166
7.6	Conclusion	170
8	Validation and application of SPH water-soil interactions model	173
8.1	Two phases hydrostatic stratified column	174
8.2	Bingham fluid dam-break	177
8.3	Spreading of granular pile on horizontal plan	178
8.4	Landslide-generated wave	183
8.5	Dam-break flow over an erodible bed	187
8.6	Multi-physics numerical benchmark : subaerial landslide, flooding and scour- ing erosion	189
8.7	Conclusion	194
9	Conclusion	201
9.1	Summary of Thesis Achievements	203
9.2	Applications	203
9.3	Future Work	204
	Bibliography	207
	Appendix A Parallelization technique on CPU of our SPH code	233

Appendix B	Demonstration of the equivalence between CSS and CSF formulations	237
Appendix C	The internal forces associated to the surface stress tensor are tangent to the interface ?	239
Appendix D	Pseudo-code of SPH interfacial multiphase model.	241

List of Figures

1.1	Shenzhen, Guangdong, Southeast China before (December 18, 2015) and after (December 21, 2015) the landslide (taken from [113]).	29
1.2	Lituya Bay tsunami: Gilbert Inlet illustration showing landslide dimensions, impact site and tsunami runup to 524 m on spur ridge directly opposite to landslide impact. Direction of view is north and the front of Lituya Glacier is set to 1958 post-slide position.(taken from [110])	30
2.1	Relation between the numerical simulations, theories and experiments.	34
2.2	Procedure of numerical simulation.	35
2.3	Representation of Lagrangian, Eulerian and combined approaches of falling drop water. They are classed from the left to the right of the figure, respectively. This figure is reproduced from [59].	37
2.4	Mesh free particle representation of the falling drop water.	38
2.5	Geometrical details of basics principles of SPH method. Ω is global domain that represent the continuum. W is the kernel function, $\Omega(kh)$ is the support compact of W centered at r_i . r_j are the neighboring particles of r_i within the support domain $\Omega(kh)$. Δx_0 is the initial inter-particles distance.	40
2.6	Snapshots of the evolution of the dam-break flow against a vertical wall (Marrone et al [216]).	49
2.7	Dam-break flow against a vertical wall. Comparison between the pressure loads measured experimentally by Buchner [44] and predicted by the numerical model at probes P_1 (top panel) and P_2 (bottom panel). Results are shown for three different space resolutions. (Marrone et al [216]).	50
2.8	Lid-driven cavity for Reynolds $R_e = 1000$: comparison of the results obtained after convergence with ISPH-USAW (left) and with FV (right). (Leroy et al [192])	51

2.9	Lid-driven cavity for $R_e = 100$. Comparison of the velocity profiles in $x^+ = 1/2$ and $z^+ = 1/2$ between ISPH-USAW, Incompressible SPH with the multiple boundary tangent (ISPH-MBT) [357], FV and the result of Ghia et al [116]. (Leroy et al [192])	51
2.10	The positions of the SPH particles at the dimensionless time 5 using 150×300 particles. The blue particles assign the light fluid.(Monaghan and Rafiee [238])	52
2.11	The time evolution of the highest point of the low-density fluid. The Layzer theory is shown by the continuous blue line. The small open circles the results for 50×100 particles. Red line hows the results for 75×150 particles and green the results for the simulation with 150×300 particles.(Monaghan and Rafiee [238])	52
2.12	WCSPH simulation of inviscid flow around a circular cylinder for $R_e = 2400$. Comparison of the predicted vorticity field between SPH (left) and Finite difference Navier-Stokes Solver (right) [74]. (Marrone et al [218])	53
2.13	Bubbly flow in a simplified closed oil-water separator. Density fields are shown at different times.(Grenier et al [129])	53
2.14	The SPH snapshots of the oblique coalescence at some characteristic time instants (top); the experimental snapshots in Brereton and and Korotney [42] (middle); the velocity field around the bubbles (bottom). (Zhang et al [358])	54
2.15	Different instants $t = \{2.2, 3.2, 10\}[s]$ of the simulation of a large wave interacting with an off-shore oil rig platform using 10^9 Particles. (Dominguez et al [90])	54
2.16	Simulation sequences of the elastic plate oscillation. (Gray and Monaghan [124])	55
2.17	Simulation sequences of the collision between two elastic rings . (Gray and Monaghan [124])	56
2.18	Convergence study of the oscillating plate test case using three particle resolutions with $n = \{10, 20, 30\}$ particles towards the direction of the plate thickness . (Gray and Monaghan [124])	56
2.19	The sediment dam break comparison between: (a) the experimental data of Bui et al [46], (b) Fourtakas and Rogers [108] results obtained via the visco-plastic model (c) comparison of the experimental profile and yielded surface of the sediment Bui et al.[46] and the Fourtakas and Rogers [108] model at the equilibrium state ($t=0.64s$) . (Fourtakas and Rogers [108]) . . .	57

2.20	Equilibrium state of collapse of a cylindrical sand column. The particles are colored with accumulative equivalent plastic strain. (a) side view; (b) isometric view. (Chen and Qiu [57])	57
2.21	Failure in uniaxial compression of gypsum sample with an angled flaw. The top figure shows the initial state of sample, while the bottom figures show the SPH crack simulation with considering several flaw angles.(Douillet-Grellier et al [92])	58
2.22	Comparison between frames from the experiment and images of SPH particle positions [6] every 0.04s from $t = 0[s]$ (a) until $t = 0.4[s]$ (k). (Antoci et al [6])	59
2.23	Horizontal and vertical displacements of the free end of the plate. (Antoci et al [6])	59
2.24	Comparison between Particle Finite Element Method (PFEM) [157] results and SPH [277] simulations for dam break on a hypoelastic baffle. (Rafiee and Thiagarajan [277])	60
2.25	Submarine landslide simulation: the left image represents the initial particles position of the land and the water (at $t = 0[s]$), while the right image is at $t = 0.8[s]$. (Capone et al [52])	60
2.26	Elevation of the water free surface at time $t = 0.8[s]$: comparison between SPH [52] results and experimental data by Rzadkiewicz et al [290] . (Capone et al [52])	61
2.27	Simulation of the impact of a violent water wave over Sines container terminal at times $t = \{0, 14, 18, 60\}[s]$. (Canelas et al [50])	61
3.1	Classification of fluids.(Roproduced from Johnson [165])	67
3.2	Flow curves of shear stress as a function of shear rate for time-dependent fluids.(Roproduced from Johnson [165])	67
3.3	Flow curves of shear stress as a function of shear rate for time-independent fluids.(Roproduced from Johnson [165])	67
3.4	Transition region of surface tension.	77
3.5	Stability regimes for cubic spline kernel function.	89
3.6	The principle of linked list algorithm.	92
3.7	Wall boundary conditions techniques: (a) repulsive force technique. (b) Ghost Particles technique. (c) Dummy particles Fixed Ghost Particles techniques. (d) Coupled dynamic boundary technique.	93
3.8	Inflow and Outflow open boundary conditions.	94
3.9	Open periodic boundary condition with clipped kernel support method.	95
3.10	Open periodic boundary condition with buffer zones method.	96

- 4.1 Geometrical description of the principal parameter of surface tension formulation in the case of two immiscible fluids 1 and 2: interface, transition region, normal vector n . The thickness of the transition region is equivalent to the diameter of the kernel function ($6h$ for the quintic kernel function). 107
- 4.2 Geometrical description of different parameters used in the generalized wall Boundary condition. Figure based on that presented in [4] 109
- 5.1 Proposed Regularized Bingham Plastic Model (RBPM) with $\alpha_\mu = \{10, 20, 100, 1000\}$ and original Bingham Plastic Model (BPM) (solid line). 123
- 5.2 Mohr-Coulomb yield criterion. The Mohr circle is based on the principal stresses σ_1 and σ_2 . The onset of yielding is occurring when the Mohr circle is tangent to the failure envelope. 124
- 5.3 The illustration of the hypothesis taken to calculate the diffusive term for multiphase fluid flow ($\mathcal{D}_i^{\delta-MSPH}$). 128
- 5.4 Geometrical description of different parameters used in the generalized wall Boundary condition. Figure based on that presented in [4] 133
- 6.1 Geometrical details of the initial configuration of vertical fluid column: The figure on the left describes the setup of the problem for the hydrostatic pressure condition. On the right, we show the initial state for the Rayleigh–Taylor instability test. 138
- 6.2 Time-evolution of pressure at the point (0.5, 0.5) (upper curves) and (0.5, 1.5) (lower curves) with (Dotted line with small circle) and without (dotted line with small square) the damping technique. The solid lines represent the stabilized pressure, and the dashed line presents the background pressure. 140
- 6.3 Hydrostatic pressure variation $\Delta p = p - p_{min}$ for the three different density ratios $\frac{\rho_2}{\rho_1}$. Below, we plot a zoom of the selected zones (a) (b) (c) (d). 141
- 6.4 The fluid column particles colored with normalized hydrostatic pressure for the density ratio $\frac{\rho_2}{\rho_1} = 4$ with the three particle resolutions 24×49 (left), 49×99 (center), 99×199 (right). It is also shown the pressure isolines in the range 3.5 to 8 [Pa]. 142
- 6.5 Time-evolution of pressure at the point (0.5, 0.5) (upper curves) and (0.5, 1.5) (lower curves) after the damping period for the for the density and viscosity ratios of $\frac{\rho_2}{\rho_1} = 100$ and $\frac{\mu_2}{\mu_1} = 10$. The solid lines represent the stabilized pressure, and the dashed line presents the background pressure. 142

- 6.6 Hydrostatic pressure variation $\Delta p = p - p_{min}$ for the density and viscosity ratios of $\frac{\rho_2}{\rho_1} = 100$ and $\frac{\mu_2}{\mu_1} = 10$. On the right we plot a zoom of the selected zone. 143
- 6.7 The fluid column particles for the density and viscosity ratios of $\frac{\rho_2}{\rho_1} = 100$ and $\frac{\mu_2}{\mu_1} = 10$. The left figure represents the fluid particles colored with phase color (gray color for fluid 2, black color for fluid 1). The figure of the center show the velocity magnitude of every fluid particle. The right figure represents the fluid and wall particles colored with hydrostatic pressure filed. 143
- 6.8 Rayleigh–Taylor instability at three different times $t = 1$ [s] (left column), $t = 3$ [s] (center column), $t = 5$ [s] (right column) after the damping period, and three different resolutions: 49×99 particles (top), 99×199 particles (middle) and 150×300 particles (bottom). 145
- 6.9 Comparison between the fluid interfaces of the present work and the references. The left figure compares the fluid interface of present SPH model with that of SPH model developed by Monaghan et al [238].The right figure compares the fluid interface of the present SPH method with that of Level-Set method [128]. 146
- 6.10 Time-evolution for the highest point (Y_{max}) of the lighter fluid. Dotted line with small open triangles shows the results for the simulation with 99×199 particles, the small open square for 49×99 particles and the small open circles for 150×300 particles. Layzer’s theory curve is represented by the continuous solid line. 147
- 6.11 Interaction of two rising bubbles through a fluid column: Geometrical setup. 148
- 6.12 Interaction of two rising bubbles through a fluid column First and second images columns represent the pressure and magnitude velocity, respectively. The third column presents the magnitude velocity with particle direction vector of isolated bubble. The simulations are presented in order at the times $t = \{0, 0.25, 0.5\}$ [s]. 149
- 6.13 Two rising bubbles through a fluid column. First and second images columns represent the pressure and magnitude velocity, respectively. The third column presents the magnitude velocity with particle direction vector of isolated bubble. The simulations are presented in order at the times $t = \{0.75, 1\}$ [s]. 150

7.1	The evolution of square droplet under the surface tension effort : The left figure describes the geometrical details. The middle figure shows the initial fluid particles at ($t = 0$ [s]) for the particle resolution $\frac{l_s}{40}$. The right figure describes droplet in equilibrium state after its evolution for the particle resolution $\frac{l_s}{40}$	153
7.2	Time evolution of droplet kinetic energy for particle resolutions $\frac{l_s}{40}$, $\frac{l_s}{80}$ and $\frac{l_s}{160}$	153
7.3	Surface tension forces orientation (on the left) and magnitude of the velocity (on the right) of droplet at equilibrium state for the particle resolution $\frac{l_s}{40}$	154
7.4	Square droplet test case. The left figure plots the normalized pressure ($\frac{p-p_2}{p_1-p_2}$) at the final stabilized state. The figure on the right plots a cut of the pressure field at $Y = 0$ obtained by the numerical method and the theoretical solution for different particle resolutions $\frac{l_s}{160}$, $\frac{l_s}{80}$ and $\frac{l_s}{40}$	155
7.5	Square droplet test case using low viscosity ($\mu_1 = \mu_2 = 0.001$ [Pa.s]) for the particle resolution of $\frac{l_s}{80}$. Particles colored with fluid phases (left). Magnitude velocity field (right).	155
7.6	A cut of the pressure field at $Y = 0$ obtained by the theoretical solution and the numerical method and numerical method with viscosity $\mu_1 = \mu_2 = 0.2$ [Pa.s] (dotted line with small circles) and $\mu_1 = \mu_2 = 0.001$ [Pa.s] (dotted line with small triangles) for the particle resolution of $\frac{l_s}{80}$	156
7.7	A cut of the pressure field at $Y = 0$ obtained by the theoretical solution and the numerical method and numerical method with viscosity $\mu_1 = \mu_2 = 0.2$ [Pa.s] and three density ratios $\frac{\rho_2}{\rho_1} = \{1, 10, 1000\}$ for the particle resolution of $\frac{l_s}{80}$	156
7.8	Schematical representation of contact angles at a triple junction point.	157
7.9	Spreading lens between two stratified layers: Time-evolution of kinetic energy for three different particle resolutions.	158
7.10	Spreading lens between two stratified layers: pressure field (left), particle distribution of three-phases stratification arrangement (middle) and magnitude velocity field (right).	159
7.11	Spreading lens between two stratified layers: pressure jump profile along $Y = 0$ (left) and $X = 0$ (right) lines.	159
7.12	Total spreading evolution of the fluid lens for the configurations : a) $\{\sigma^{1-2}, \sigma^{1-3}, \sigma^{2-3}\} = \{3, 1, 1\}$ [N/m] and b) $\{\sigma^{1-2}, \sigma^{1-3}, \sigma^{2-3}\} = \{1, 1, 3\}$ [N/m].	160
7.13	Droplet oscillation : droplet particle positions at $t = \{0.0, 0.08, 0.16, 0.26\}$ [s].	162
7.14	Convergence test of droplet oscillation: Center of mass position of the upper right-quarter section of the droplet.	162

- 7.15 Single bubble rising through a vertical column of water. Geometrical details of the initial setup. On the left it is schematically described the low-density ratio configuration (Case 1)[155] ($R = 0.25 [m]$) and on the right it is described the setup for the high-density ratio configuration (Case 2) [317]($R = 0.025 [m]$). 163
- 7.16 Single bubble rising through a vertical column of water. Case 1: Time evolution of the position of the gravity center (left) and vertical velocity (right) of the rising bubble for different number of particles. The solid line represents the results obtained by VOF method [156]. 164
- 7.17 Single bubble rising through a vertical column of water. Case 1: Comparison between the bubble interfaces at time $t = 3 [s]$: 66×133 SPH (Small triangles), 133×267 SPH (Small circles). Dashed line represent the interface obtained with the VOF method [155]. 165
- 7.18 Single bubble rising through a vertical column of water. Case 1: Pressure (top) and velocity (bottom) fields at times $t = 1 [s]$ and $t = 3 [s]$ for two different particle resolutions, 66×133 (left) and 133×267 (right). 166
- 7.19 Single bubble rising through a vertical column of water. Case 1: Direction of the velocity vector of the particles inside the bubble at $t = 1$ colored with magnitude velocity. On the left, results for 66×133 particles, and on the right we plot the results for the 133×267 particles case. 167
- 7.20 Single bubble rising through a vertical column of water. Case 2: Relative pressure ($\widetilde{\Delta p} = p - p_{min}$) and magnitude of the velocity of the column of water at the dimensionless time $t \sqrt{\|g\|/R} = 3.6$ 167
- 7.21 Single bubble rising through a vertical column of water. Case 2: Evolution of the bubble at nine different instants. The Bubble is colored with velocity magnitude field. 168
- 7.22 Single bubble rising through a vertical column of water. Case 2: Evolution of the bubble at nine different instants. Results obtained with the present SPH method (blue circles) and with a Level-Set approach [318] (black diamonds). 169
- 7.23 Gas bubble rising through two stratified fluid layers. Geometrical details of the problem setup. 170
- 7.24 Gas bubble rising through two stratified fluid layers. Starting from the left, first and second columns show the relative hydrostatic pressure field $\widetilde{\Delta p} = p - p_{min}$ for different normalized times $t^+ = t \sqrt{\|g\|/R}$. Third and fourth columns present the magnitude of the velocity field. The last two columns show the fluid phases distribution. 171

- 7.25 Gas bubble rising through two stratified fluid layers. On the top, we show the experimental sequence taken from [37]. On the bottom we plot the results obtained using the proposed SPH method. The dimensionless interval between two images is taken equal to $\Delta t \sqrt{\|g\|/R} = 4.3$ 172
- 8.1 Geometrical details of two phases hydrostatic stratified column configuration. $P_1 = (0.3, 0.5)$, $P_{int} = (0.3, 0.2)$, $P_2 = (0.3, 0.1)$ are the pressure measurement points located at the center of the layer of the fluid 1, the interface between the two fluids and the center of the fluid layer 2, respectively. . . . 175
- 8.2 Time evolution of pressure at the points P_1 , P_{int} and P_2 plotted against the analytical hydrostatic values represented in solid lines. The left figure represents the pressure results using the multiphase diffusive term $\mathcal{D}^{\delta-MSPH}$ of present work. The right figure represents the pressure results using the classical diffusive term $\mathcal{D}^{\delta-SPH}$ independently in each fluid phase. 176
- 8.3 Fluid phases distribution and hydrostatic pressure representation at $t = 7[s]$. The gray color is chosen for the phase 1 and the black for the phase 2). The colored part shows the hydrostatic pressure field. Figure (a) shows the results using the multiphase diffusive term $\mathcal{D}^{\delta-MSPH}$ presented in this work, whereas figure (b) shows the results using the classical diffusive term $\mathcal{D}^{\delta-SPH}$. Notice the smooth distribution obtained with the proposed methodology. 176
- 8.4 Computed pressure values at all particles for all fluid phases at time $t = 7[s]$ plotted against the analytical hydrostatic pressure (solid black line). On the left it is shown the pressure computed using the multiphase diffusive term $\mathcal{D}^{\delta-MSPH}$ presented in this work. On the right, the results using the classical diffusive term $\mathcal{D}^{\delta-SPH}$ 177
- 8.5 Bingham fluid dam-break configuration. 178
- 8.6 Time-evolution of dimensionless Bingham dam-break front position ($X_F/H = (x_F - L)/H$). We compare the results obtained using the proposed method with a plastic viscosity ($\mu = 0.07$) and coefficients $\alpha_{mu} = 100$ (dotted line) $\alpha_{mu} = 1000$ (dashed line), with INNSPH(Incompressible Non-Newtonian SPH) [352] (solid line) and with the experimental results of Komatina and Jovanovic [175] (small triangles). 179
- 8.7 Bingham dam-break flow at times $t = 0.1, 0.3, 0.6, 1, 2[s]$. The particles are colored with pressure values. The Y-axis is scaled by a factor of 5 for the sake of clarity. 179

8.8	Comparison between the free surface profiles of the present SPH method with a plastic viscosity ($\mu = 0.07$) and $\alpha_\mu = 1000$ (solid line), the INNSPH method [352] (dashed line) and CVFEM [352] (dotted line) at times $t = \{0.6, 2\}[s]$	180
8.9	Spreading of granular pile on horizontal plan: Schematics of the experimental configuration [183].	180
8.10	Spreading of granular pile on horizontal plan: Time-evolution of the dimensionless front position of the glass beads pile. We plot the results of the proposed numerical method using $\alpha_\mu = 100$ (dotted line), $\alpha_\mu = 1000$ (dash-dot line), $\alpha_\mu = 2000$ (dashed line) and $\alpha_\mu = 3000$ (solid line), and the experimental data of Lajeunesse et al [183] (small triangles).	181
8.11	Spreading of granular pile on horizontal plan: Sequences of the position of the granular material (glass beads) using the proposed SPH model with $\alpha_\mu = 3000$ (a) and experimental results of Lajeunesse et al [183] (b). . . .	182
8.12	Submarine land-slide-generated water wave: Geometrical details and setup of the problem.	184
8.13	Submarine land-slide-generated water wave: Particle distribution at times $t = 0.4[s]$ and $t = 0.8[s]$	184
8.14	Submarine land-slide-generated water wave: Comparison between the free surfaces at $t = 0.4[s]$ and $t = 0.8[s]$ obtained with the proposed SPH model, the SPH model of Capone et al. [52] and the experimental results of Rzakiewicz et al [290, 289].	184
8.15	Sub-aerial land-slide-generated water wave: Schematic view of the experimental setup and geometrical details.	186
8.16	Sub-aerial land-slide-generated water wave: Elevation of the free surface at each wave gauges G_1, G_2, G_3 and G_4 . The black solid line denotes the numerical results, while the dashed lines present the experimental results [342].	187
8.17	Sub-aerial land-slide-generated water wave: Comparison between the numerical (left) and experimental (right) results at the times $t = \{0.21, 0.43, 0.52\}[s]$	188
8.18	Dam-break flow over an erodible bed: Geometrical details and setup of the problem.	189

- 8.19 Dam-break flow over an erodible bed: Flow sequences at times $t = \{0.25, 0.5, 0.75\}[s]$. The experimental results are on the left side (grey-scale image), the magnitude of the velocity field is plotted on the right side and a plot with the position of the different phases are centered below the previous plots for each time. The material phases are colored in blue for water particles, in orange for the rigid bed particles and in green for the suspended particles of the bed. 190
- 8.20 Dam-break flow over an erodible bed: Flow sequences at times $t = \{1, 1.25, 1.5\}[s]$. The experimental results are on the left side (grey-scale image), the magnitude of the velocity field is plotted on the right side and a plot with the position of the different phases are centered below the previous plots for each time. The material phases are colored in blue for water particles, in orange for the rigid bed particles and in green for the suspended particles of the bed. 191
- 8.21 Dam-break flow over an erodible bed: Water free surface and sediment surface positions results using the proposed numerical model and compared with the experiments of [312] 192
- 8.22 Multi-physics numerical benchmark: Schematic view and geometrical details. 193
- 8.23 Multi-physics numerical benchmark: simulation sequence. The different material phases are represented with different colors: Water is dark blue, the granular material *GM1* is cyan, the granular material *GM2* is brown and yellow is the suspended layer. 195
- 8.24 Multi-physics numerical benchmark: simulation sequence. The different material phases are represented with different colors: Water is dark blue, the granular material *GM1* is cyan, the granular material *GM2* is brown and yellow is the suspended layer. 196
- 8.25 Multi-physics numerical benchmark: Simulation sequences. The particles of soil material (*GM1*) and (*GM2*) are colored with the effective viscosity values. Water particles are colored with the magnitude of the velocity and the flow direction is represented by black arrows. 197
- 8.26 Multi-physics numerical benchmark: Simulation sequences. The particles of soil material (*GM1*) and (*GM2*) are colored with the effective viscosity values. Water particles are colored with the magnitude of the velocity and the flow direction is represented by black arrows. 198
- 8.27 Multi-physics numerical benchmark: Evaluation of the impulsive wave height for the left reservoir at $x = 0.9[m]$ (G1 gauge) and height above the dyke (G2 gauge) at $x = 1.65[m]$ 199

8.28	Multi-physics numerical benchmark: Evaluation of maximum scouring depth on the granular material bed due to the over-topping flow.	199
A.1	Parallelization technique of SPH code on CPU using MPI library.	234
A.2	The time-evolution flows of particles loads on four processors for 20,000 particles.	235
A.3	The time evolution of load percentage on four processors for 20,000 particles.	236
A.4	Speed-Up of parallel SPH code	236
C.1	Application of stress surface tensor Π on an arbitrary vector f . Where n and t are the normal and tangential vectors on the interface, respectively.	240

List of Tables

2.1	Comparison of Lagrangian and Eulerian approaches (advantages and drawbacks).	36
3.1	Comparison between WCSPH and ISPH schemes.	72
6.1	Setup for the interaction of two rising bubbles through a fluid column test case. With Reynolds number $R_e = \frac{\rho_1 v_c L_c}{\mu_1}$ and Eötvös number $E_o = \frac{\rho_1 v_c^2 L_c}{\sigma}$	147
7.1	Setup for Case 1 and Case 2 tests.	166
8.1	Properties of the sand material of the dam-break induced sheet-flow	188

Chapter 1

Introduction

Le présent travail porte sur la modélisation et la simulation des écoulements de fluides multiphasiques de différentes complexités et natures. Les complexités comprennent la simulation des écoulements des fluides multiphasiques confinés, à surface libre, à grande déformation, avec présence d'interface et/ou avec des rapports de densité et de viscosité élevés, tandis que pour les natures, différentes lois de comportement (Newtonien et / ou non Newtonien) sont utilisées pour définir le comportement des fluides. En utilisant le code développé dans le cadre de cette thèse, une gamme d'applications peut être simulée afin de servir les domaines de recherche et de l'ingénierie. Parmi ces applications, nous pouvons citer par exemple:

- *En ingénierie offshore, notamment pour les dispositifs de séparation pétrole-eau, la compréhension de la dynamique des bulles de pétrole (fluide multiphasique avec présence d'interface) à travers la simulation numérique a une grande importance pour l'exploitation et le traitement des ressources pétrolières [109, 129, 358].*
- *La simulation des écoulements granulaires (un fluide non Newtonien qui s'écoule sous un critère spécifique) peut être réalisé en utilisant le code développé. La compréhension des écoulements granulaires peut avoir des directes applications dans l'industrie telles que la simulation de poudres et de granules, ainsi que pour les problèmes géophysiques, tels que la simulation de glissements de terrain [113], l'avalanche de roches [354] et de la neige [285]. La simulation de ces risques naturels peut aider à comprendre comment nous devrions procéder dans l'avenir pour atténuer les pertes humaines et matérielles. La catastrophe de Shenzhen est un bon exemple d'un aléa naturel causé par un glissement de terrain. Cette catastrophe naturelle a eu lieu à Shenzhen, Guangdong, dans le sud-est de la Chine, le 20 décembre 2015, 77 personnes ont été tués et 33 bâtiments ont été enterrés ou endommagés [113]. La figure 1.1 décrit les séquences avant et après cet aléa.*

- *Les problèmes d'interaction eau-sol (écoulement de fluide multiphase sous différentes natures) sont plus compliqués par rapport aux exemples précédents, car ils incluent deux natures physiques différentes (fluide et structure). La compréhension du phénomène d'interaction eau-sol joue un rôle important dans l'évaluation et l'atténuation de nombreux problèmes environnementaux et géotechniques, tels que l'érosion du sol, l'érosion autour des structures offshore, les vagues de tsunamis générées par les glissements de terrain, etc. L'exemple du tsunami Lituya Bay (Gilbert Inlet-Alaska en 1958) causé par un glissement de terrain subaérien est l'un des tsunamis les plus importants dans les temps modernes, et la modélisation de l'interaction entre l'eau et le sol peut être très utile pour comprendre son mécanisme. La figure 1.2 présente le scénario du tsunami de Lituya Bay et montre les différentes dimensions de Gilbert Inlet et de l'espace terrestre détruit.*

1.1 Motivation and Objectives

The present work deals with the modeling and the simulation of multiphase fluid flows under various complexities and natures. Complexities include the simulation of confined, free surface, large deformation and/or interfacial multiphase fluid flows with high density and viscosity ratios, whereas for the natures, different constitutive laws (Newtonian and/or Non-Newtonian) are used to define the fluid or the fluid-like mass behavior. Using the developed code in the framework of this thesis, a range of applications can be simulated in order to serve range of research and engineering fields. Among these applications we can cite for instance:

- In offshore engineering, especially for oil-water separation devices, the understanding of oil bubbles dynamics (interfacial multiphase fluid) through the numerical simulation has a great importance for exploitation and processing of oil resources [109, 129, 358].
- The simulation of granular flows (a non-Newtonian fluid that yields under a specific criterion) can be done using the developed code. The understanding of the granular flows can have an obvious applications in industry such as for the simulation of powders and granules, and in geophysical problems, such as for the simulation of landslides [113], rock avalanche [354] and snow avalanche [285]. The simulation of these natural hazards can help to understand how we should proceed in the future to mitigate losses in human life and material. The Shenzhen-landslide is a good example of a natural disaster caused by a landslide. This natural disaster occurred in Shenzhen, Guangdong, Southeast China in December 20, 2015, where 77 people were killed and 33 buildings were buried or damaged [113]. Figure 1.1 illustrates the sequences before and after this disaster.



Figure 1.1 – Shenzhen, Guangdong, Southeast China before (December 18, 2015) and after (December 21, 2015) the landslide (taken from [113]).

- The Water-Soil interaction problems (multiphase fluid flows under different natures) which are more complicated than previous examples since it includes two different

physics natures (Fluid and structure). The understanding of water-soil interaction phenomenon plays an important role in the assessment and mitigation of many environmental and geotechnical problems, such as soil erosion, scouring around offshore structures, landslide-generated tsunamis waves ... and so on. The example of Lituya Bay tsunami (Gilbert Inlet-Alaska in 1958) caused by subaerial landslide is the one of the largest known tsunami in modern times [110], and modeling of water-soil interactions can be a very useful way to understand its mechanism. Figure 1.2 presents the Lituya Bay tsunami scenario and shows the different dimensions of Gilbert Inlet and destroyed land space.

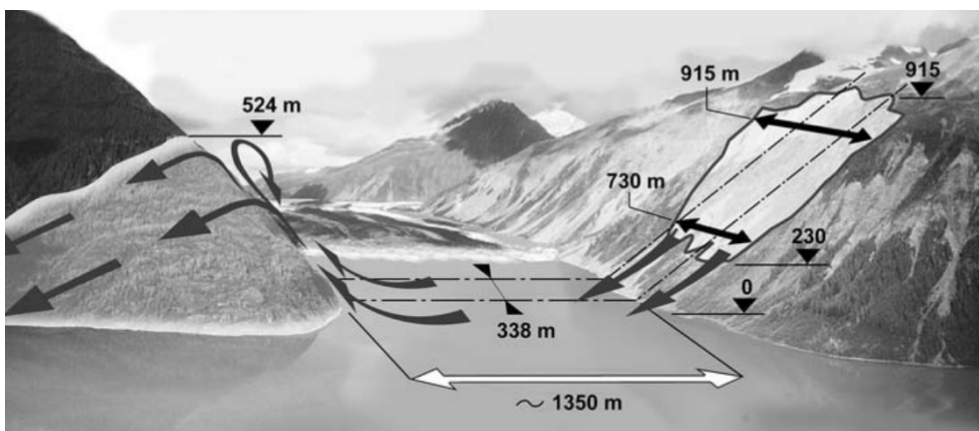


Figure 1.2 – Lituya Bay tsunami: Gilbert Inlet illustration showing landslide dimensions, impact site and tsunami runup to 524 m on spur ridge directly opposite to landslide impact. Direction of view is north and the front of Lituya Glacier is set to 1958 post-slide position.(taken from [110])

1.2 Thesis outline

The following PhD thesis is structured as follows. In Chapter 2, a state of the art on the smoothed particle hydrodynamics method (SPH) is given, underlining in particular an overview of mesh-based and meshless numerical methods and the principal basics and applications of SPH method. Chapter 3 discusses the fluid governing equations and different methods of SPH discretization. The Chapter 4 is devoted to modeling multiphase interfacial fluid flows including our original contribution regarding the surface tension formulation and conditions initialization via the damping technique. In chapter 5, the modeling of water-soil interactions using a SPH multiphase approach is presented. The validation and application of the developed SPH multiphase model, SPH interfacial multiphase model and SPH water-soil interactions model are shown through Chapter 6 , Chapter 7 and Chapter 8, respectively.

1.3 Contributions

The contributions of the present thesis can be summarized in the following points:

- Past and recent advances in SPH method improvement algorithms are presented;
- Different SPH discretization techniques of governing equations are discussed;
- A consistent SPH model was proposed to deal with interfacial multiphase fluid flow simulations;
- Robust non-conservative surface tension formulation that respects its tangential character to deal with two and more interfacial fluid phases is developed;
- A modification of the generalized wall boundary conditions proposed in [4] is presented to allow its use for the simulation of wall-bounded multiphase fluid flows
- Validation of the proposed SPH model via the application on several challenging test cases of multiphase fluid flows;
- Experimental verification of applicability and accuracy of the proposed SPH interfacial multiphase model is done;
- A weakly compressible multiphase smoothed particle hydrodynamics model was developed to deal with Water-Soil interaction problems.
- A Regularized Bingham Plastic/Mohr-Coulomb (RBPMC- α_μ) constitutive law was developed to model soil, water and both in interaction;
- Development of a new multiphase diffusive term $\mathcal{D}^{\delta-MSPH}$ to reduce the pressure oscillations in the context of Weakly compressible SPH;
- Validation of the SPH multiphase water-soil interactions model through several benchmarks .

1.4 Publications

1.4.1 Journals

- Abdelkader Krimi , Mehdi Rezoug , Sofiane Khelladi , Xesús Nogueira ,Michael Deligant , Luis Ramírez, “Smoothed Particle Hydrodynamics : A consistent model for interfacial multiphase fluid flow simulations”, Submitted to the Journal of Computational physics., 2016.
- Abdelkader Krimi , Sofiane Khelladi, Xesús Nogueira, Michael Deligant, Riadh Ata, Mehdi Rezoug, “Multiphase Smoothed Particle Hydrodynamics approach for modeling Soil-Water interactions”, Submitted to the Advances in Water Resources, 2017.

- Luis Ramírez, Xesús Nogueira, Sofiane Khelladi , Abdelkader Krimi, Ignasi Colominas, “A very accurate Arbitrary Lagrangian-Eulerian meshless method for Computational Aeroacoustics”, Submitted to Computer Methods in Applied Mechanics and Engineering , 2017.
- Abdelkader Krimi , Sofiane Khelladi, Xesús Nogueira, “An overview on Smoothed Particle Hydrodynamics method and applications on fluids, structures and both in interactions problems”, to be submitted to the Annual Review of Fluid Mechanics, 2017.

1.4.2 Conferences

- Abdelkader Krimi, Mehdi Rezoug, Sofiane Khelladi, Michaël Deligant, "Fast and accurate algorithm for modeling complex free surface flows", The 11th International Conference for Mesoscopic Methods in Engineering and Science. July 14-18, 2014. New York.
- Abdelkader Krimi, Mehdi Rezoug, Sofiane Khelladi, Michaël Deligant, "A Lagrangian parallel technique on CPU for smoothed particle hydrodynamics method", SimRace, Conference on numerical methods and High Performance Computing for industrial fluid flows. December 8-10, 2015. Paris.
- Abdelkader Krimi , Sofiane Khelladi, Riadh Ata, Xesús Nogueira, Michael Deligant, Mehdi Rezoug, "A Multiphase SPH Approach to Model Soil-Water interactions", 14th U.S. National Congress on Computational Mechanics July 17-20, 2017, Montreal, Quebec, Canada.

Chapter 2

State of the art

Dans ce chapitre, un état de l'art est fait sur les différentes méthodes numériques utilisant un maillage ou sans maillage pour mettre en évidence la méthode SPH. Les principes de base des formulations de la méthode SPH sont aussi abordés. Nous avons présenté quelques codes de calcul parallèle Open Source exploitant la méthode SPH. Des différents exemples d'applications sur des problématiques liées au fluide, structure et les deux en interaction sont extraits de la littérature pour montrer le grand intérêt que la méthode SPH a connu dans le domaine de recherche et de l'ingénierie.

In this chapter, a state of the art is achieved on the different grid-based and gridless numerical methods in order to highlight the SPH method. The basic principles of the formulations of the SPH method are also discussed. We have presented some open source parallel codes exploiting the SPH method. Examples of applications on problems related to fluid , structure and both in interactions are extracted from the literature to show the large interest that SPH method has experienced in the field of research and engineering.

2.1 Numerical simulation

Computational simulations or in other words numerical simulations using computers plays an important role for solving many practical problems in both engineering and science. A numerical simulation converts important aspects of a physical phenomenon into mathematical equations written in a discrete form, transfers the problem to computer in order to solve it, and inspects phenomena virtually following the requirements of the analysts. The advances in numerical analysis, coupled with the increasing power of computers, have greatly expanded the scope of numerical simulation.

Numerical simulation can be considered as a powerful tool for scientific investigation. It can reduce the expensive, time-consuming and in situ or in laboratory experiments. Numerical tools present advantages compared with classical experimental methods. It can provide complete information that is generally difficult to obtain through other means. Computational simulations play a principal role in providing a validation for theories, offers additional information on experimental results and helps in the interpretation or even the discovery of new phenomena. However, computational simulations are strongly interconnected to physical models and theoretical predictions as it is shown in figure 2.1 .

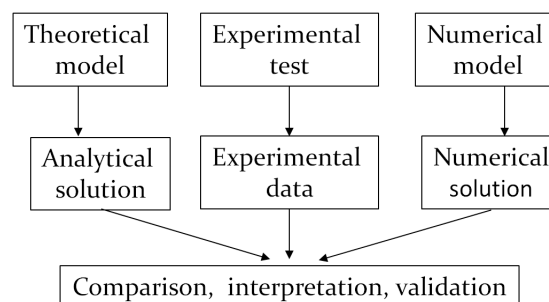


Figure 2.1 – Relation between the numerical simulations, theories and experiments.

Generally, numerical simulation techniques should follow a similar flow-chart as schematically shown in figure 2.2. Starting from the observed physical phenomena with a focus on

the aspects that need to be investigated, simplified mathematical models are established under some assumptions in the form of governing equations with proper limit conditions (initial conditions and boundary conditions). The governing equations are explicitly dependent of the nature of physical phenomena targeted for the investigation and can take several forms as: partial differential equations (PDE), ordinary differential equations (ODE), integration equations and so on.

In order to solve numerically the governing equations, the geometry of the problem that will be treated needs to be represented by interconnected discrete components. The domain discretization techniques may be different from a method to another. The step of domain discretization is followed by numerical discretization that provides means to obtain discrete representation of continuous forms of governing equations which correspond to the domain discretization technique. The last step is to translate the discrete form of governing equations into a computer code. The complete procedure of numerical simulation is summarized in figure 2.2.

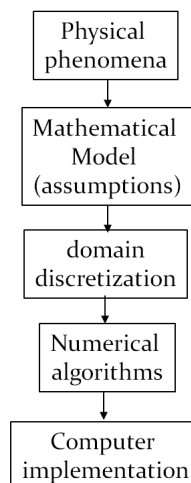


Figure 2.2 – Procedure of numerical simulation.

2.2 Grid based numerical methods

Grid based numerical methods adopt a computational domain which is composed of nodes, where the field of physical variables are evaluated, and their relations are predefined by a specific topography of nodal connectivity (mesh). The mesh cell size and the mesh patterns are the principal factors that define the accuracy of the numerical approximation. There are two fundamental descriptions in grid based methods: the Eulerian description

Lagrangian approach	Eulerian approach
The absence of convective term in the governing equation facilitate the numerical treatment phase.	The convective term should be handled in the simulation.
The ease of tracking the time-history of the physical variables at any point of material.	The difficulty of tracking the time-history of the physical variables at fixed point of material.
The ease of mesh adaption to complex and irregular geometries and description of material interfaces and moving boundaries.	A bad adaption of the mesh to complex geometries and difficulty in the determination of material interfaces and representation of moving boundaries.
The grid is needed only within the continuum.	the grid should be large enough in order to cover also the part of the space where the continuum can be moved.
A poor numerical accuracy due to the mesh distortion is presented when large deformation is occurring to the continuum.	The large deformation occurred to the continuum does not cause neither the mesh distortion nor infect the accuracy.
An expensive adaptive mesh algorithm is needed to overcome the previous problems.	No adaptive mesh numerical accuracy is needed.

Table 2.1 – Comparison of Lagrangian and Eulerian approaches (advantages and drawbacks).

and the Lagrangian description. The Eulerian description is a spatial description. Here the computational grid is assumed to be fixed on the physical space; the volume and shape of mesh cells remain unchanged during all the period of the computation while the materials are flowing across the mesh. The mass flux across mesh cell faces is simulated to compute the distribution of physical quantities in the problem domain. The finite difference method (FDM) is the typical example to represent the Eulerian description [164, 138, 350]. The Lagrangian description is a material description. Contrary to the Eulerian description, the grid is attached on the material and moves with it in the entire process of the computation. Here, there is no mass flux between adjacent cells because of the transportation of the mass with the movement of the mesh cells. The well-known and widely used method is the Finite Element Method (FEM) [361, 64]. Both description have advantages and suffer from drawbacks that are principally summarized in the table 2.1 .

In order to strengthen the advantages of Eulerian and Lagrangian approaches and avoid their drawbacks, combined approaches has been developed. The Coupled Eulerian Lagrangian (CEL) [213] and the Arbitrary Lagrange Eulerian (ALE) [26, 140, 24] methods are the most known methods belonging to this approach. However, the grid based methods are not well suited for situations where large deformations, moving material interfaces, large inhomogeneities, deformable boundaries and/or free surfaces are presented in the simulation

case. In the figure 2.3, the Lagrangian, Eulerian and Combined approaches are schematically illustrated.

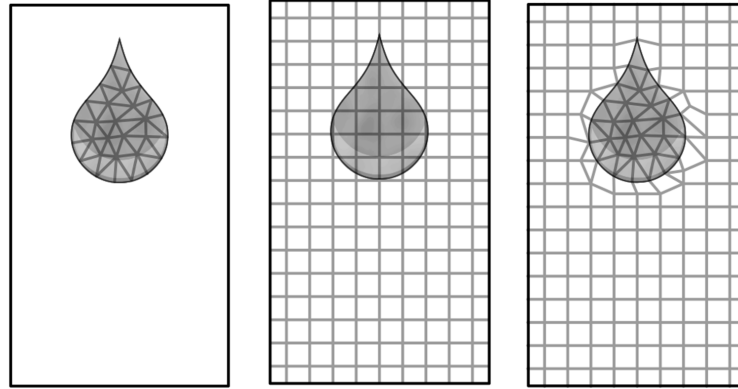


Figure 2.3 – Representation of Lagrangian, Eulerian and combined approaches of falling drop water. They are classed from the left to the right of the figure, respectively. This figure is reproduced from [59].

2.3 Meshfree numerical methods

For the purpose of avoiding all problems related to the connectivity between the nodes, another class of numerical methods so-called Meshfree methods was developed. The basic idea of the meshfree methods is to discretize the continuum into a set of nodes without presence of any connectivity between these nodes. This property makes treatment of large deformation problems, and representation of the free and moving interfaces an easier task while keeping a reasonable computational effort. When the nodes represent a massive element (particle) of the material domain and carrying its physical properties, the methods are so-called “meshfree particle methods (MPMs)” [198] (see figure 2.4). This kind of methods follows in general a Lagrangian approach.

The Meshfree Particle Methods (MPMs) include: lattice gas Cellular Automata (CA) [351, 167], Dissipative Particle Dynamics (DPD) [143, 96], Particle-in-Cell (PIC) [131, 132], Marker-and-Cell (MAC) [132], Fluid-In-Cell (FLIC) [114], Particle-Particle (PP), Particle-Mesh (PM), Particle-Particle-Mesh (P^M) [142], Moving Particle Semi-implicit (MPS) [176], Smoothed Particle Hydrodynamics (SPH) [210, 240] and other various meshfree particle methods. It is shown by Shao and Shao [301] and Souto-Iglesias et al [311] that the two last cited methods MPS and SPH are closely equivalent.

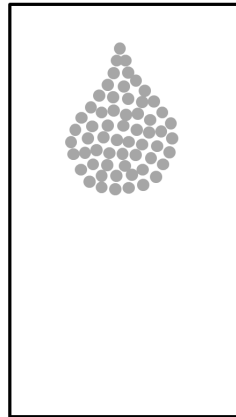


Figure 2.4 – Mesh free particle representation of the falling drop water.

2.4 Smoothed Particle Hydrodynamics (SPH) method

In this thesis, one of the most efficient and robust meshfree particle methods is highlighted. This method is called Smoothed particle hydrodynamics (SPH). It is a Lagrangian method for the numerical approximations of the governing equations solutions that works by replacing of continuum material with a set of particles in interaction. Generally, this method can be seen via two different points of view [245]:

- From the mathematicians point of view, the particles are considered as interpolation points from which properties of the continuum material can be approximated.
- From the physicists point of view, the SPH particles are also a continuum material particles that can be treated like any other material system.

The smoothed Particle Hydrodynamics (SPH) method was originally formulated by Lucy [210] and Gingold and Monaghan [118] for astrophysical applications. Since this seminal work, it has been successfully applied to a vast range of problems. These include astrophysical problems: galaxies formation and claps [249, 310], dusty gas dynamics [232, 259], stars and steller collisions [242, 27, 282]; Hydrodynamics and compressible flow problems: dam break [243, 72, 303], dam spillway [292, 189] fish pass [104], multiphase flow [254, 151], spersonic flow [102, 274], shock waves [235, 265], detonation and explosion [201, 202]; Bioengineering problems: swemming bodies [136, 168, 68], microfluidics [139, 11], heart valves [298], blood flows [22, 250]; heat transfer problems: [67, 348], structure problems; [66, 124, 137]; multi-physics problems [6, 332, 331], and many other applications.

2.5 Basics of SPH method

2.5.1 Kernel approximation

The highlight of the SPH method is related to its ability to represent numerical approximations for functions and their spatial derivatives without need to any topological connectivity between nodes (mesh).

Let us consider the sufficiently regular function field f , defined on the n -dimensional domain Ω and its border $\partial\Omega$. The field f may be defined at the position vector r_i ($f(r_i)$) from the following convolution product:

$$f(r_i) = \int_{\Omega} \delta(r_i - r_j) f(r_j) dr_j^n \quad (2.1)$$

Where dr_j^n is the elementary volume located at the position r_j , and term $\delta(r_i - r_j)$ denotes the Dirac or the delta function. Because the delta function is not regular (it lacks continuity and differentiability properties), it is replaced in the context of SPH method by an alternative well behaved function W called smoothing kernel function or simply kernel. Thus, the integral approximation in term of smoothing kernel function W reads as:

$$f(r_i) \approx \int_{\Omega(kh)} W(r_i - r_j, h) f(r_j) dr_j^n \quad (2.2)$$

Where, h represents the smoothing length, and it is usually defined as constant value proportional to the initial inter-particle distance Δx_0 [186]. The smoothing length h can be chosen variable for each individual particle in order to enhance the accuracy of SPH method. For more details about the variation of h , we advice the reader to refer to [242, 135].

In SPH, the kernel function is defined over a compact support of radius equal to kh where the particle of position r_i interacts only with neighboring particles r_j . Therefore, the global domain Ω is restricted to the compact support domain $\Omega(kh)$ which subsequently reduces the computation time. The constant k depends on the choice of the smoothing kernel function. More details are shown in figure 2.5.

The smoothing kernel function W should fulfill some properties [200]. The most general ones are summarized below :

- The smoothing function W should be a good approximation tof the Dirac delta function δ as $h \rightarrow 0$
- The smoothing function W should decrease monotonously from the position r_i .

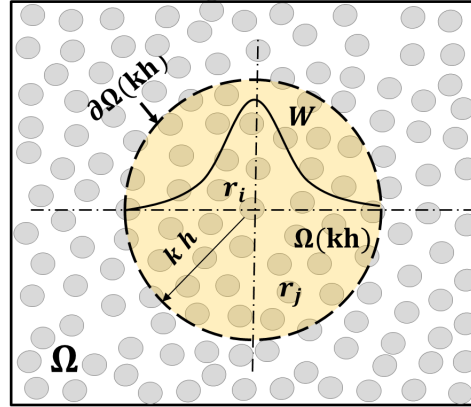


Figure 2.5 – Geometrical details of basics principles of SPH method. Ω is global domain that represent the continuum. W is the kernel function, $\Omega(kh)$ is the support compact of W centered at r_i . r_j are the neighboring particles of r_i within the support domain $\Omega(kh)$. Δx_0 is the initial inter-particles distance.

- The smoothing function W should be a spherically-symmetric even function: $W(r_i - r_j, h) = W(r_j - r_i, h) = W(r_{ij}, h)$. Here, the r_{ij} denotes the distance between the position vectors r_i and r_j ($r_{ij} = \|r_i - r_j\|$).

The gradient of kernel W is expressed as : $\nabla_{r_i} W(r_i - r_j, h) = \frac{\partial W(r, h)}{\partial r} \frac{r_i - r_j}{r} = -\nabla_{r_j} W(r_j - r_i, h)$

Where ∇ is the nabla operator (gradient).

- The smoothing function W should have a compact support $\Omega(kh)$: $W(r, h) = 0$ for $r \geq kh$
- The smoothing function W should satisfy the normalization condition:

$$\int_{\Omega(kh)} W(r_i - r_j, h) dr_j = 1$$
- The smoothing function W should be positive within the compact support area: $W(r_i - r_j, h) \geq 0$ for $r < kh$
- The smoothing kernel function W should be sufficiently smooth (differentiable).

2.5.2 Choice of the smoothing kernel function

The smoothing kernel function can be represented in a general form as :

$$W(r_{ij}, h) = W(r, h) = \frac{\eta_n}{h^n} Q\left(\frac{r}{h}\right) = \frac{\eta_n}{h^n} Q(q) \quad (2.3)$$

Where n is the number of space dimension, Q is function of dimensionless distance $q = \frac{r}{h}$, and η_n is constant depends of the choice of kernel function and the space dimension n . The letter r denotes the variable distance between two points ($r = r_{ij} = \|r_i - r_j\|$). In literature,

a several kernel functions which satisfy the list of conditions discussed above are treated in the context of SPH method. Some of the most frequently used kernel function are discussed as follows:

- The Gaussian kernel introduced by Gingold and Monaghan [118]. It is the simplest kernel whose spatial derivative is infinitely smooth and therefore exhibits good accuracy and stability properties especially for disordered particles (smoother kernel functions result generally in more stable SPH formulations [319, 253]). However, it lacks of a compact support (It never goes to zero theoretically), and it is computationally very expensive. Gaussian Kernel function follows the form of equation 2.3 where the function $Q(q)$ reads as

$$Q(q) = e^{-q^2} \quad (2.4)$$

With the constants $\eta_1 = \frac{1}{\sqrt{\pi}}$, $\eta_2 = \frac{1}{\pi}$ and $\eta_3 = \frac{1}{\pi\sqrt{\pi}}$ for 1, 2 and 3 dimensions, respectively.

- The B-spline kernel function or cubic spline kernel function [248]. It is the most commonly used kernel since it has a small compact support and resembles a Gaussian function. However, it is less stable than smoother kernels. The function $Q(q)$ is expressed as follows

$$Q(q) = \begin{cases} 1 - \frac{3}{2}q^2 + \frac{3}{4}q^3 & 0 \leq q < 1 \\ \frac{1}{4}(2 - q)^3 & 1 \leq q < 2 \\ 0 & q \geq 2 \end{cases} \quad (2.5)$$

With the constants $\eta_1 = \frac{2}{3}$, $\eta_2 = \frac{10}{7\pi}$ and $\eta_3 = \frac{10}{\pi}$ for 1, 2 and 3 dimensions, respectively.

- The Quartic and Quintic kernel functions are introduced by Morris [252, 253]. These kernels are higher order functions and have the advantage of smoother derivatives which more closely approximate the Gaussian kernel function and they are more stable. The functions $Q(q)$ are expressed for the Quartic and Quintic Kernel functions, respectively as:

$Q(q)$ of Quartic kernel function:

$$Q(q) = \begin{cases} (2.5 - q)^4 - 5(1.5 - q)^4 + 10(0.5 - q)^4 & 0 \leq q < 0.5 \\ (2.5 - q)^4 - 5(1.5 - q)^4 & 0.5 \leq q < 1.5 \\ (2.5 - q)^4 & 1.5 \leq q < 2.5 \\ 0 & q \geq 2.5 \end{cases} \quad (2.6)$$

With $\eta_1 = \frac{1}{24}$, $\eta_2 = \frac{96}{1199\pi}$ and $\eta_3 = \frac{1}{20\pi}$ for 1, 2 and 3 dimensions, respectively.
 $Q(q)$ of Quintic kernel function:

$$Q(q) = \begin{cases} (3 - q)^5 - 6(2 - q)^5 + 15(1 - q)^5 & 0 \leq q < 1 \\ (3 - q)^5 - 6(2 - q)^5 & 1 \leq q < 2 \\ (3 - q)^5 & 2 \leq q < 3 \\ 0 & q \geq 3 \end{cases} \quad (2.7)$$

With $\eta_1 = \frac{1}{120}$, $\eta_2 = \frac{7}{478\pi}$ and $\eta_3 = \frac{1}{120\pi}$ for 1, 2 and 3 dimensions, respectively.

- The Quartic smoothing function introduced by Liu et al [200]. This function fulfills the normalization condition, and has a common compact support with its first derivative. The Quartic kernel gives better results than cubic kernel function (equation (2.5)) since it has only one piece [200, 199]. The function $Q(q)$ reads as

$$Q(q) = \begin{cases} -\frac{5}{32}q^4 + \frac{19}{24}q^3 - \frac{9}{8}q^2 + \frac{2}{3} & 0 \leq q < 2 \\ 0 & q \geq 0 \end{cases} \quad (2.8)$$

With $\eta_1 = 1$, $\eta_2 = \frac{15}{7\pi}$ and $\eta_3 = \frac{315}{208\pi}$ for 1, 2 and 3 dimensions, respectively.

- The kernels of Wendland [347] are also often used. It is recommended by Robinson and Monaghan [286] since it reduces the SPH tensile instability [51]. Some $Q(q)$ functions of Wendland kernels are expressed as follows:

$Q(q)$ Wendland C2:

$$Q(q) = \left(1 - \frac{q}{2}\right)^4(2q + 1) \quad (2.9)$$

With $\eta_2 = \frac{7}{4\pi}$ and $\eta_3 = \frac{21}{16\pi}$ for 2 and 3 dimensions, respectively.

$Q(q)$ Wendland C4:

$$Q(q) = \left(1 - \frac{q}{2}\right)^6\left(\frac{35}{12}q^2 + 3q + 1\right) \quad (2.10)$$

With $\eta_2 = \frac{9}{4\pi}$ and $\eta_3 = \frac{495}{256\pi}$ for 2 and 3 dimensions, respectively.

$Q(q)$ Wendland C6:

$$Q(q) = \left(1 - \frac{q}{2}\right)^8 \left(4q^3 + \frac{25}{4}q^2 + 4q + 1\right) \quad (2.11)$$

With $\eta_2 = \frac{39}{14\pi}$ and $\eta_3 = \frac{1365}{512\pi}$ for 2 and 3 dimensions, respectively.

2.5.3 Kernel approximation of a function derivatives

When substituting gradient of the function field ∇f in kernel approximation formulation (2.2), the following is obtained:

$$\nabla f(r_i) \approx \int_{\Omega(kh)} \nabla f(r_j) W(r, h) dr_j^n \quad (2.12)$$

By applying the divergence theorem (Gauss theorem) in (2.12), it becomes:

$$\nabla f(r_i) \approx - \int_{\Omega(kh)} f(r_j) \nabla_{r_j} W(r, h) dr_j^n + \int_{\partial\Omega(kh)} f(r_j) W(r, h) n_{\partial\Omega} dr_j^{n-1} \quad (2.13)$$

The second integral on the right-hand side of the equation (2.13) is evaluated on the surface elements dr_j^{n-1} of the border $\partial\Omega(kh)$ of the domain $\Omega(kh)$. The vector $n_{\partial\Omega}$ is unit outward vector normal to $\partial\Omega(kh)$. As it is mentioned before among the list of conditions that the smoothing kernel function should satisfy, the domain $\Omega(kh)$ must be a support compact. In other words, the kernel value is equal to zero on the border $\partial\Omega(kh)$ inside the continuum domain. Therefore, the second integral of the formation (2.13) will vanish. When the border of kernel support $\partial\Omega(kh)$ intersects the border of continuum global domain $\partial\Omega$, the second integral of the formation (2.13) may be evaluated following [104, 192].

Because of $\nabla_{r_i} W(r_i - r_j, h) = -\nabla_{r_j} W(r_j - r_i, h)$ the formulation (2.13) can read as:

$$\nabla f(r_i) \approx \int_{\Omega(kh)} f(r_j) \nabla_{r_i} W(r, h) dr_j^n \quad (2.14)$$

Or simply:

$$\nabla f(r_i) \approx \int_{\Omega(kh)} f(r_j) \nabla W(r, h) dr_j^n \quad (2.15)$$

2.5.4 Accuracy of kernel approximation

The second order Taylor expansion of the function $f(r_j)$ around of r_i can read as

$$f(r_j) = f(r_i) + (r_j - r_i) \cdot \nabla f(r_i) + O(h^2) \quad (2.16)$$

When the Taylor expansion (2.16) is introduced in the right hand side of kernel approximation of equation (2.2)

$$\begin{aligned} \int_{\Omega(kh)} f(r_j) W(r, h) \, dr_j^n &= \int_{\Omega(kh)} \{f(r_i) + (r_j - r_i) \cdot \nabla f(r_i) + O(h^2)\} W(r, h) \, dr_j^n \\ &= f(r_i) \int_{\Omega(kh)} W(r, h) \, dr_j^n \\ &\quad + \nabla f(r_i) \cdot \int_{\Omega(kh)} (r_j - r_i) W(r, h) \, dr_j^n + O(h^2) \end{aligned} \quad (2.17)$$

From the mathematical development (2.17), it is clear that the kernel formulation of equation (2.2) is a second-order accurate approximation if :

$$\int_{\Omega(kh)} W(r, h) \, dr_j^n = 1 \quad (2.18)$$

and

$$\int_{\Omega(kh)} (r_i - r_j) W(r, h) \, dr_j^n = 0 \quad (2.19)$$

It is possible to obtain a higher order accuracy (k^{th} order) when all moments of W (until the k^{th} moment M_k) equal to zero [207, 23, 87, 88].

$$M_k = \int_{\Omega(kh)} (r_i - r_j)^k W(r, h) \, dr_j^n = 0 \quad (2.20)$$

If the Taylor expansion (2.16) is introduced in (2.15), the following expression is obtained

$$\begin{aligned}
\int_{\Omega(kh)} f(r_j) \nabla W(r, h) \, dr_j^n &= \int_{\Omega(kh)} \{f(r_i) + (r_j - r_i) \cdot \nabla f(r_i) + O(h^2)\} \nabla W(r, h) \, dr_j^n \\
&= f(r_i) \int_{\Omega(kh)} \nabla W(r, h) \, dr_j^n \\
&\quad + \nabla f(r_i) \cdot \int_{\Omega(kh)} (r_j - r_i) \otimes \nabla W(r, h) \, dr_j^n + O(h^2)
\end{aligned} \tag{2.21}$$

As it is concluded before for order of accuracy of the kernel approximation, and from the mathematical development (2.21), it is obvious that the gradient kernel approximation is second order accuracy if the following identities are satisfied

$$\int_{\Omega(kh)} \nabla W(r, h) \, dr_j^n = 0 \tag{2.22}$$

and

$$\int_{\Omega(kh)} (r_j - r_i) \otimes \nabla W(r, h) \, dr_j^n = I \tag{2.23}$$

Where I is the identity tensor.

2.5.5 Particle approximation

In SPH, the computational domain (continuum) is represented by a set of particles carrying all the generic variables (density, pressure, velocity ...). These particles are in interaction within a range controlled by the smoothing kernel function support called here $\Omega(kh)$ (see figure 2.5 for more details). The integrals under their continuous forms can be approximated with a summation applied on the finite number of neighboring particles with volume V_j . This process is the so-called particle approximation [112, 198, 200]. Therefore, the discrete form of the integral kernel approximation of the function f at position r_i (equation (2.2)) is obtained by using the surrounding particles r_j (the neighboring particles within the support domain of W centered at r_i) and can read as :

$$f(r_i) \approx \sum_j^{n_b} f(r_j) W_{ij} V_j \tag{2.24}$$

Where, n_b is the number of particles j in the neighborhood of the particle i , the volume V_j of particle j is defined as $V_j = \frac{m_j}{\rho_j}$, with m_j and ρ_j the mass and the density of the particle j , respectively. The notation W_{ij} denotes $W_{ij} = W(r_{ij}, h) = W(r_i - r_j, h)$.

With some mathematical manipulation, the discrete form of kernel approximation of the continuous gradient of the function field f can also be estimated as:

$$\nabla f(r_i) \approx \sum_j^{n_b} f(r_j) \nabla W_{ij} V_j \quad (2.25)$$

Alternative expressions for the gradient of the field function f can be obtained by considering the following two identities [242]:

$$\nabla f = \frac{1}{\rho} \{ \nabla(\rho f) - f \nabla \rho \} \quad (2.26)$$

$$\nabla f = \rho \left\{ \nabla \left(\frac{f}{\rho} \right) - \frac{f}{\rho^2} \nabla \rho \right\} \quad (2.27)$$

By substituting the equations (2.26) and (2.27) into the equation (2.25), the following paired particles forms of gradient function are obtained respectively

$$\nabla f(r_i) \approx \frac{1}{\rho_i} \sum_j^{n_b} m_j (f(r_j) - f(r_i)) \nabla W_{ij} \quad (2.28)$$

$$\nabla f(r_i) \approx \rho_i \sum_j^{n_b} m_j \left(\frac{f(r_j)}{\rho_j^2} + \frac{f(r_i)}{\rho_i^2} \right) \nabla W_{ij} \quad (2.29)$$

The equation (2.28) has a asymmetric form (as seen when particles i and j swap places). This formulation has the advantage over (2.25) since it returns exactly the derivative of a constant function (this formulation is called zeroth order consistency C^0), while the equation (2.29) has an symmetric form which it obeys the propriety of “the action is minus of the reaction”, thus, the conservative form is fulfilled whose use is favored in the discretization of the momentum equation [239]. Note, the divergence can be approximated using the same formulations as the gradient (2.28) and (2.29). The second order derivative of the field function f can be approximated by differentiating the equation (2.24) a twice :

$$\Delta f(r_i) = \nabla^2 f(r_i) = \nabla \cdot \nabla f(r_i) \approx \sum_j^{n_b} f(r_j) \nabla^2 W_{ij} V_j \quad (2.30)$$

This expression suffer from a lot of issues such as its strong sensitivity to the particle disorder and need and also it can results a large errors at low particle resolution, especially

when the employed kernel function is a low-order [43, 255]. To deal with this issues, a useful approach was proposed by Monaghan [231] in the context of heat conduction treatment, This approach reads as :

$$\Delta f(r_i) \approx 2 \sum_j^{n_b} \frac{f(r_i) - f(r_j)}{\|r_i - r_j\|^2} (r_i - r_j) \cdot \nabla W_{ij} V_j \quad (2.31)$$

This expression results from a hybrid combination between a finite difference derivative and a first-order SPH derivative. This formulation is also used by many researchers to discretize the second-order derivative [255, 67, 325] .

2.6 Performance optimization and open source codes of SPH method

One of the major problems presented in the use of smoothed particle hydrodynamics is its high cost in terms of computational time. This problem is communally found in all lagrangian methods for a many reasons. We can quote for instance, the cost of mathematical and physical proprieties calculations on each particle which is based on the interpolation with a considerable number of surrounding particles. Furthermore, the motion of particle involved the updating of search for new list of surrounding particles in each time step hold on each particle, unlike in the Eulerian methods, the connectivity of the nodes is known in advance and doesn't require any updating according to time. And also, the high number of iterations needed to simulate a given physical time. The last drawback is generally due to the explicitness of the integration scheme which requires a very small time step in order to preserve the numerical stability.

With performance growth presented in hardware architectures of the recent computers, a several contributions in the literature were done to make the SPH method cost-effective. In the context of shared memory architecture on both GPU and CPU, large parallelization techniques for WCSPH were developed in the literature thanks to the explicitness and independence of calculation tasks hold on each individual particle. For instance, in the framework of Dualphysics project : open source SPH solver [79], which is based on the Monaghan discretization scheme [242], a parallelism implementation both on GPU and CPU was progress in several works. Firstly it was implemented on a single GPU using the CUDA language [78]. This approach was limited for millions of particles due to the limitation of the device memory used in GPU cards. To deal with this problem, a multi-GPUs parallelization technique using message passing interface "MPI" paradigm is used to communicate between

several devices memories of Nvidia CUDA cards [335]. But this approach was not optimized regarding the fixed technique of interface communication between the memory devices of GPUs cards that causes a high computational time due to the amount of data transfer and its maladjusted with the particle motion that causing later a loss in load balancing. In the reference [90] an enhancement of the last method was done to optimize the communications between memory by sharing the particles between GPUs memory devices following the kinematic of particles flow. Later in reference [89] an optimized strategy was described which based on the keeping of the calculation tasks maximum as possible in GPU to minimize the CPU-GPU data transfer. In the last reference a multi-threading parallelization technique on CPU using the OpenCL library was proposed. Another free SPH Solver Parallel on GPU so-called AQUAgpusph was recently developed [53] to be widely supported in various cards architecture (Nvidia, AMD, IBM, Intel, etc...) thanks to OpenCL computing language which is not possible for CUDA language that works only on NVIDIA Cards technology.

Josephine is a parallel SPH code on CPU used to simulate free surface flow in open basin [60] using Colagrossi and Landrini [72] and Ferrari et al. [105] approaches. The principal of parallelism method used in the context of Josephine is based on a vertical decomposition domain with updating the interface separating between processes which define the buffer exchange zone to follow the kinetic of flow in order to guarantee a good load balancing between the processors by using a single way zone interaction based on the QuickSelect algorithm to determine the abscissa dividing the particles of interaction zone into tow subset.

2.7 Applications

Nowadays, SPH methods have gained a wide interest for application in research and engineering. Herein, some of its applications are addressed such as in fluid, structure and interactions.

2.7.1 Fluid applications

The dam break flow problem is one of the most known benchmarks used in the SPH framework [243, 36, 72, 204, 288, 339, 77, 105, 216]. It includes all the complexity that makes SPH a particularly well suited method for its simulation such as the presence of the free surface and its large deformation. Figure 2.6 shows the simulation sequences of the dam break realized by Marrone et al [216] in the context of diffusive scheme δ -SPH. The

comparison of pressure results with available experimental data made by Buchner [44] are presented in figure 2.7.

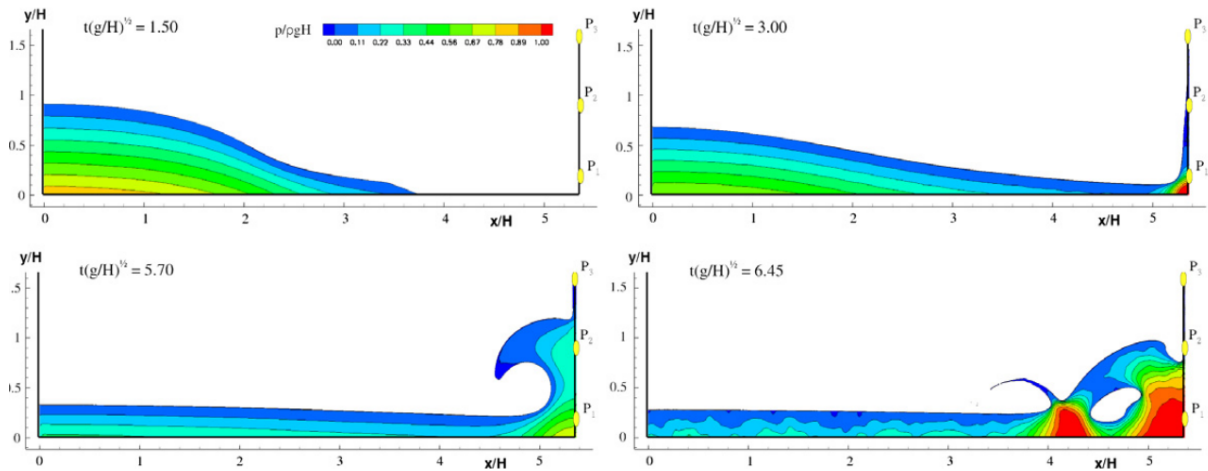


Figure 2.6 – Snapshots of the evolution of the dam-break flow against a vertical wall (Marrone et al [216]).

Lid-driven cavity flow has been widely used as a benchmarking test to validate numerical models in the context of confined fluid flow. For SPH applications, we can refer to [188, 357, 85, 5, 192]. We show via the Figure 2.8 the results obtained by Leroy et al [192] using incompressible SPH (ISPH) scheme with unified semi-analytical wall boundary conditions (USAW) compared with the Finite volume results (FV). While in figure 2.9 a comparison of the velocity profiles between the ISPH-USAW [192], SPH with the multiple boundary tangent method (SPH-MBT) [357], finites volumes, and the results of Ghia et al [116].

For multiphase fluid flows applications, the most popular investigated test is the Rayleigh–Taylor instability problem [80, 150, 128, 149, 238, 297, 58]. In figure 2.10 the positions of the SPH particles at dimensionless time 5 is taken from the work of Monaghan and Rafiee [238]. The results obtained are similar to that of Cummins and Rudman [80] and Grenier et al [128]. figure 2.11 show the ariation of the highest point of the low-density fluid for different particle resolutions compared with Layzer theory [307].

Many other applications can be quoted such as in aerodynamics [218] (see figure 2.12), bubbly flow and coalescence in framework of SPH interfacial multiphase method [129, 358], simulation with a high particle resolution (more than 10^9 particles) for large wave interacting with an off-shore oil rig platform [90] and so on.

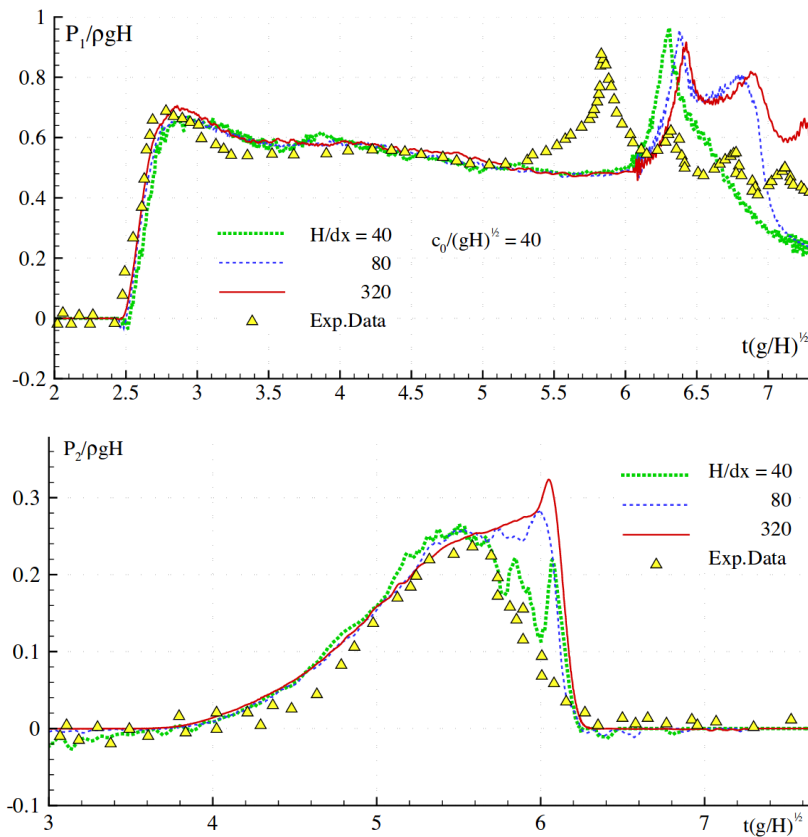


Figure 2.7 – Dam-break flow against a vertical wall. Comparison between the pressure loads measured experimentally by Buchner [44] and predicted by the numerical model at probes P_1 (top panel) and P_2 (bottom panel). Results are shown for three different space resolutions. (Marrone et al [216]).

2.7.2 Structure applications

The SPH method can be applied successfully to different problems behavior, such as elastic, plastic, and elasto-plastic behaviors.

Oscillating plate [124, 277, 359] and collision of two rubber rings [124, 206, 314] are two typical tests for simulation of elastic deformation of structure. figures 2.16 and 2.17 show the simulation sequences of the oscillating plate and the collision of two rubber rings, respectively. The convergence of SPH elastic model can be shown through the figure 2.18 that represents the time evolution of the vertical position of a point on the end of the plate for different resolution. all these figures are taken form the work of Gray and Monaghan [124].

The geomaterials can be considered as purely plastic materials. The SPH method offers a good advantage for the simulation of this kind of material via a Non-Newtonian fluid model that yields under a certain criterion (such as Mohr-Coulomb [227, 75] or Drucker–Prager

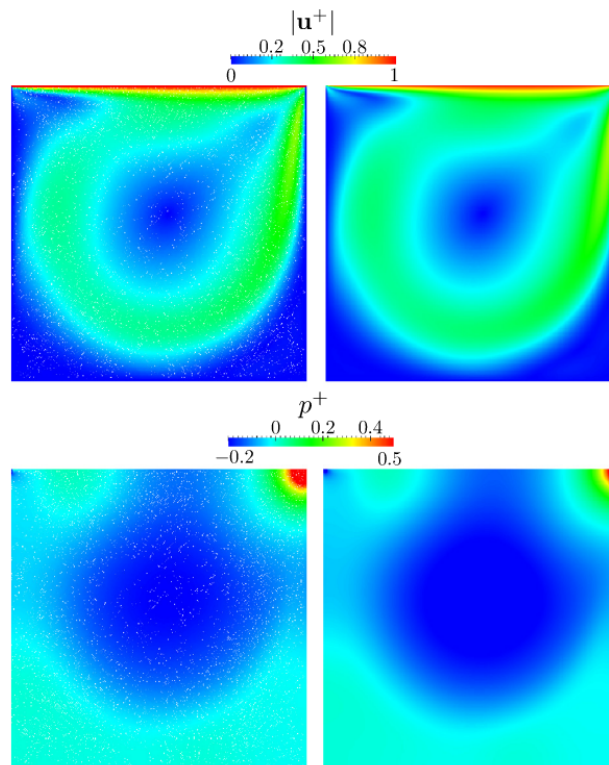


Figure 2.8 – Lid-driven cavity for Reynolds $R_e = 1000$: comparison of the results obtained after convergence with ISPH-USAW (left) and with FV (right). (Leroy et al [192])

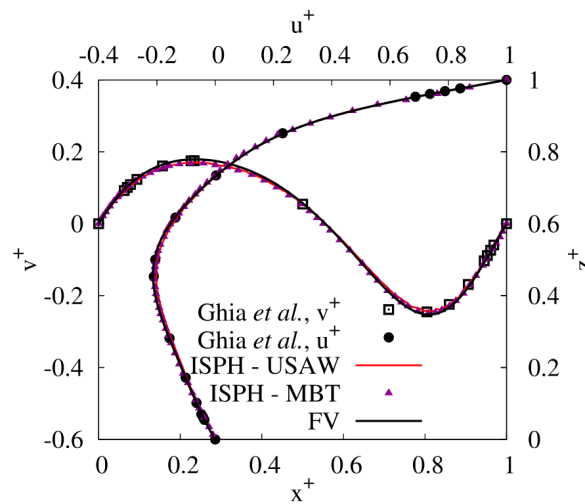


Figure 2.9 – Lid-driven cavity for $R_e = 100$. Comparison of the velocity profiles in $x^+ = 1/2$ and $z^+ = 1/2$ between ISPH-USAW, Incompressible SPH with the multiple boundary tangent (ISPH-MBT) [357], FV and the result of Ghia et al [116]. (Leroy et al [192])

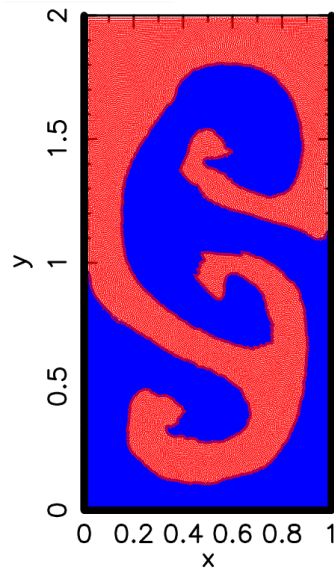


Figure 2.10 – The positions of the SPH particles at the dimensionless time 5 using 150×300 particles. The blue particles assign the light fluid.(Monaghan and Rafiee [238])

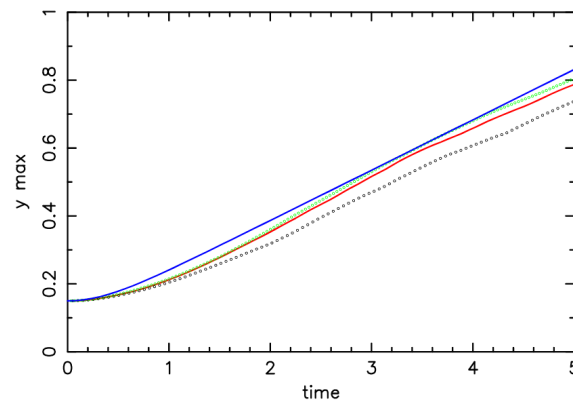


Figure 2.11 – The time evolution of the highest point of the low-density fluid. The Layzer theory is shown by the continuous blue line. The small open circles the results for 50×100 particles. Red line hews the results for 75×150 particles and green the results for the simulation with 150×300 particles.(Monaghan and Rafiee [238])

[93] yield criteria). This model is so-called visco-plastic model. A lot of applications of this method for the simulation of the flow behavior of granular materials can be found in the literature [13, 52, 153, 320]. Also the elasto-plastic constitutive models have also demonstrated that are suitable for simulation of granular materials [46, 49, 57, 260]. Figures 2.19 and 2.20 show the equilibrium state of 2D sediment dam break and the collapse of cylindrical sand column simulated using visco-plastic and elasto-plastic models, respectively. Douillet-Grellier et al [92] use Drucker-Prager and Grady-Kipp [28, 29] in the context of

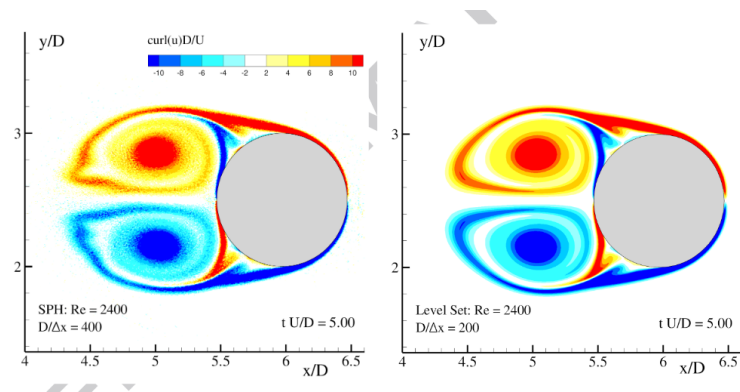


Figure 2.12 – WCSPH simulation of inviscid flow around a circular cylinder for $R_e = 2400$. Comparison of the predicted vorticity field between SPH (left) and Finite difference Navier-Stokes Solver (right) [74]. (Marrone et al [218])

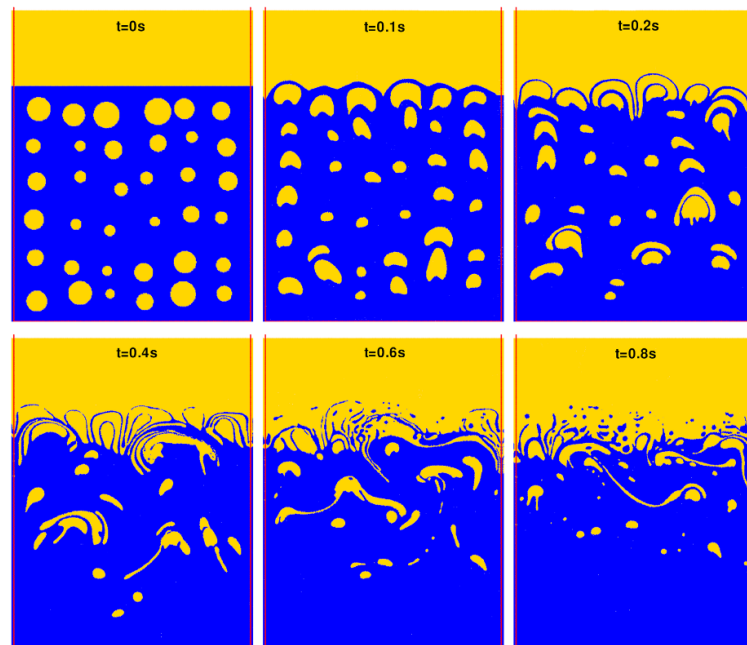


Figure 2.13 – Bubbly flow in a simplified closed oil-water separator. Density fields are shown at different times.(Grenier et al [129])

elasto-plastic SPH model to simulate the failure in uniaxial compression of gypsum samples that contain an angled flaw (see figure 2.21).

2.7.3 Fluid structure interactions

The deformation of an elastic plate subjected to time-dependent water pressure is a well-known benchmark proposed by Antoci et al [6] to validate the interaction between the

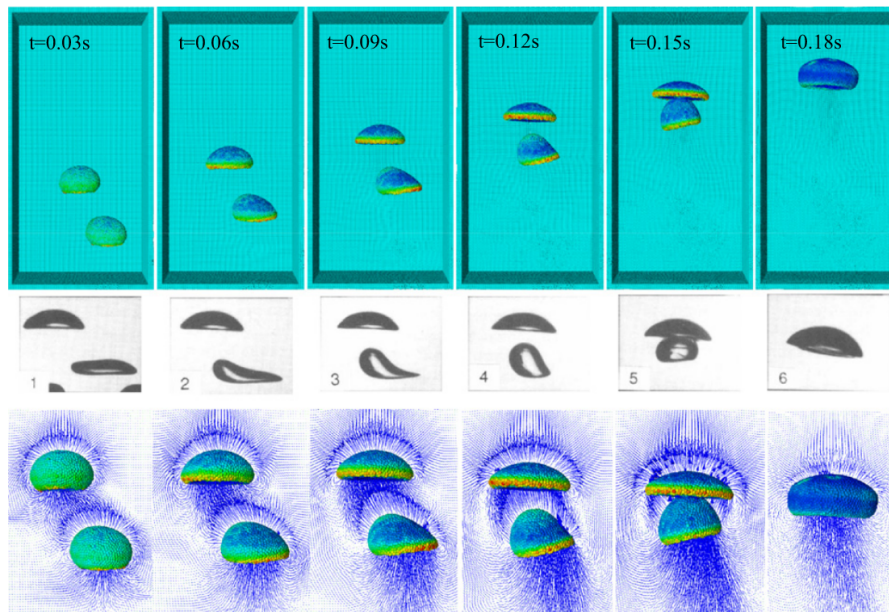


Figure 2.14 – The SPH snapshots of the oblique coalescence at some characteristic time instants (top); the experimental snapshots in Breuer and Korotney [42] (middle); the velocity field around the bubbles (bottom). (Zhang et al [358])

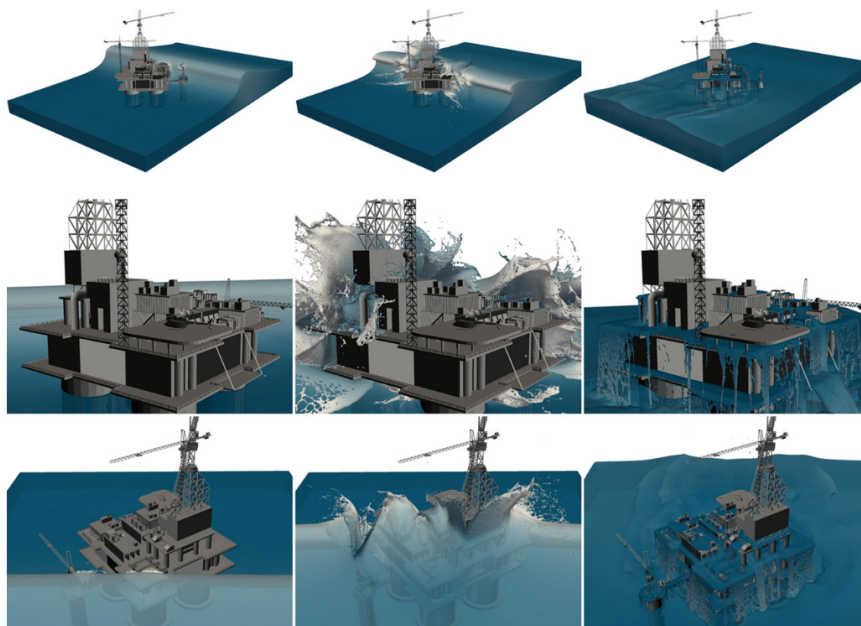


Figure 2.15 – Different instants $t = \{2.2, 3.2, 10\}$ [s] of the simulation of a large wave interacting with an off-shore oil rig platform using 10^9 Particles. (Dominguez et al [90])

fluid and elastic structures codes [6, 144, 277]. Figures 2.22 and 2.23 show comparative

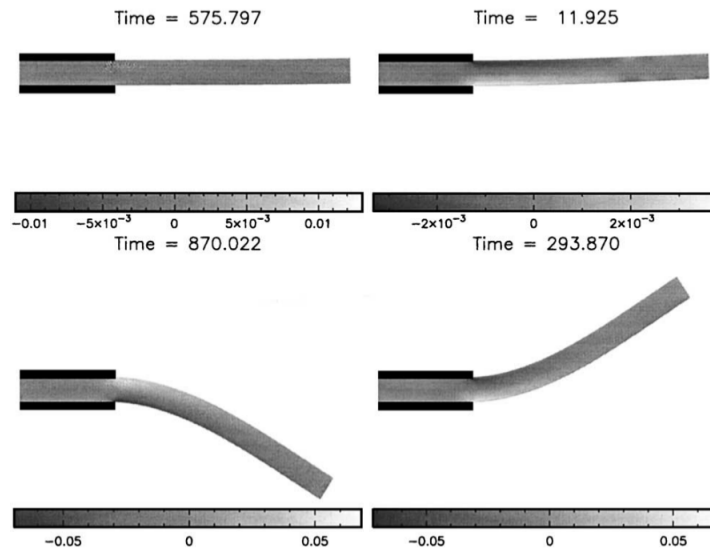


Figure 2.16 – Simulation sequences of the elastic plate oscillation. (Gray and Monaghan [124])

results between SPH and experimental tests for simulation sequences and the time-evolution of the horizontal and vertical displacements of the plate free end .

There is also another benchmark for modeling a breaking dam on hypoelastic baffle [277] compared with Particle Finite Element Method (PFEM) [157] that can be also used for the validation of fluid-elastic structures interactions codes. Figure 2.24 shows a comparison of simulation sequences of dam break interaction with hypoelastic baffle between two numerical method Particle Finite Element (PFE) and Smoothed Particle hydrodynamics methods (SPH) [277].

For fluid and land interactions, a classical simple example of numerical modeling of submarine landslide generated waves [275, 52, 353] can be used for the validation of SPH codes thanks to its available experimental data (Rzadkiewicz et al [290]). Figure 2.25 shows the position of fluid and land particles at the times $t = 0[s]$ and $t = 0.8[s]$, from the left to the right, respectively (Capone et al [52]). In the figure 2.26 comparison curves of the water free surface obtained with SPH method [52] and experimental data [290].

For fluid and rigid body interactions, a very good synthetic test case was proposed by Canelas et al [50] in order to simulate the impact of a violent water wave over a real geometry of container terminal of the Sines port (it is a big infrastructure on the Portuguese coast) to explore the possibilities of SPH method regarding complex, industrial scales. figure 2.27 shows four selected sequences of this application.

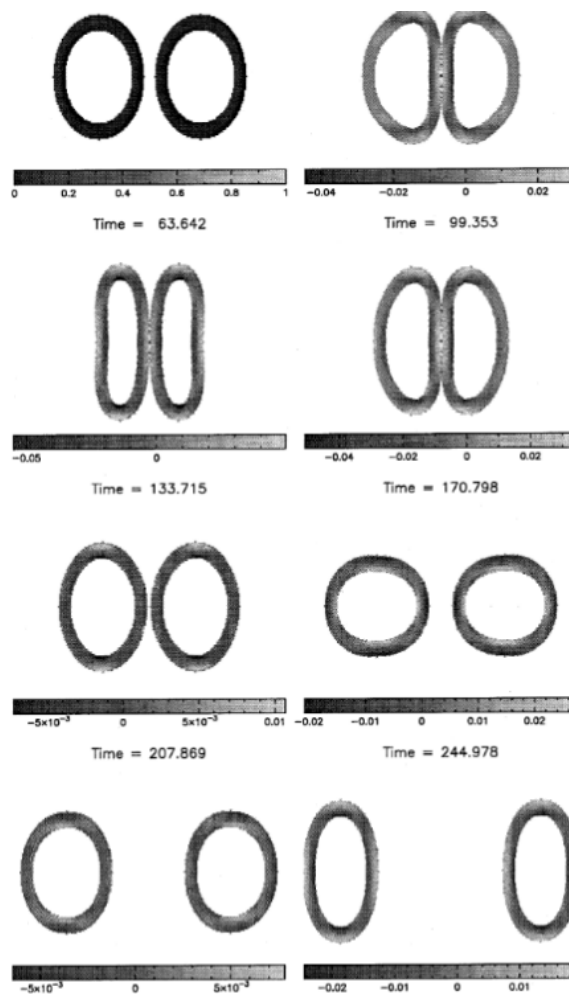


Figure 2.17 – Simulation sequences of the collision between two elastic rings . (Gray and Monaghan [124])

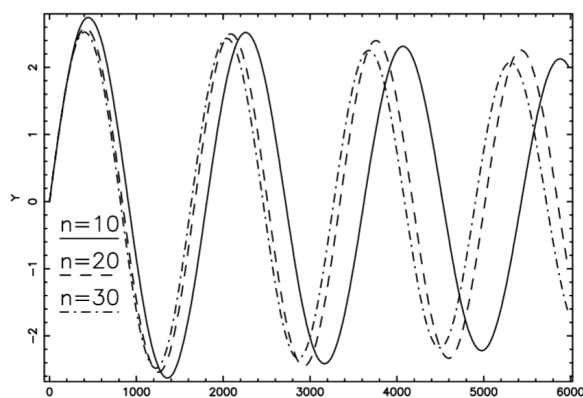


Figure 2.18 – Convergence study of the oscillating plate test case using three particle resolutions with $n = \{10, 20, 30\}$ particles towards the direction of the plate thickness . (Gray and Monaghan [124])

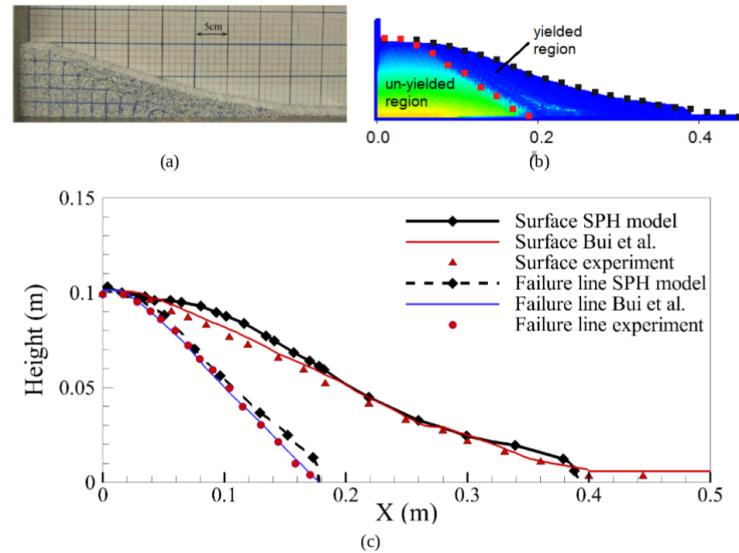


Figure 2.19 – The sediment dam break comparison between: (a) the experimental data of Bui et al [46], (b) Fourtakas and Rogers [108] results obtained via the visco-plastic model (c) comparison of the experimental profile and yielded surface of the sediment Bui et al.[46] and the Fourtakas and Rogers [108] model at the equilibrium state ($t=0.64s$) . (Fourtakas and Rogers [108])

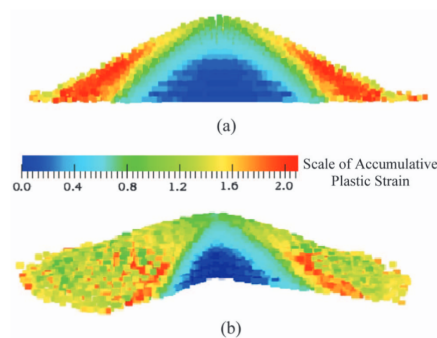


Figure 2.20 – Equilibrium state of collapse of a cylindrical sand column. The particles are colored with accumulative equivalent plastic strain. (a) side view; (b) isometric view. (Chen and Qiu [57])

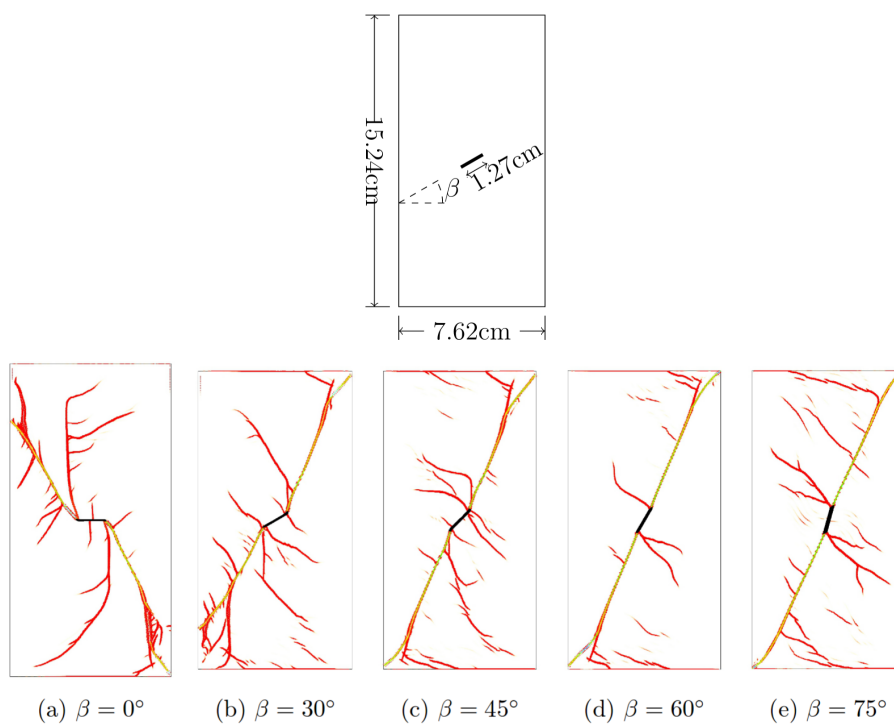


Figure 2.21 – Failure in uniaxial compression of gypsum sample with an angled flaw. The top figure shows the initial state of sample, while the bottom figures show the SPH crack simulation with considering several flaw angles.(Douillet-Grellier et al [92])

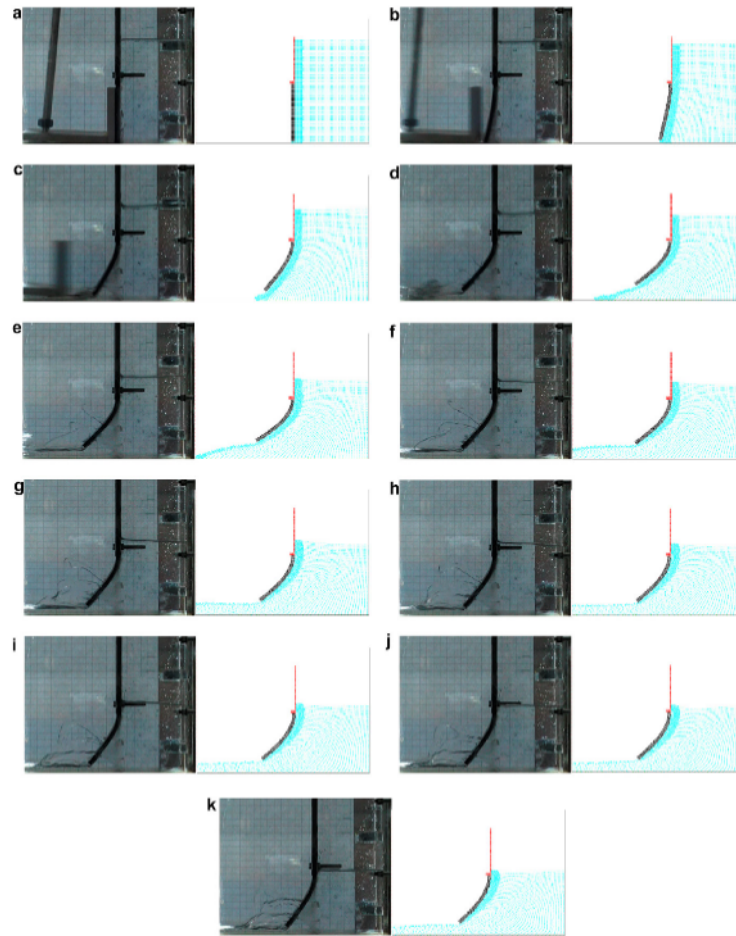


Figure 2.22 – Comparison between frames from the experiment and images of SPH particle positions [6] every 0.04s from $t = 0[s]$ (a) until $t = 0.4[s]$ (k). (Antoci et al [6])

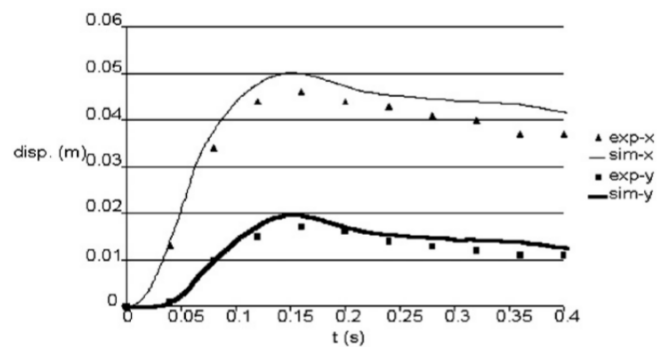


Figure 2.23 – Horizontal and vertical displacements of the free end of the plate. (Antoci et al [6])

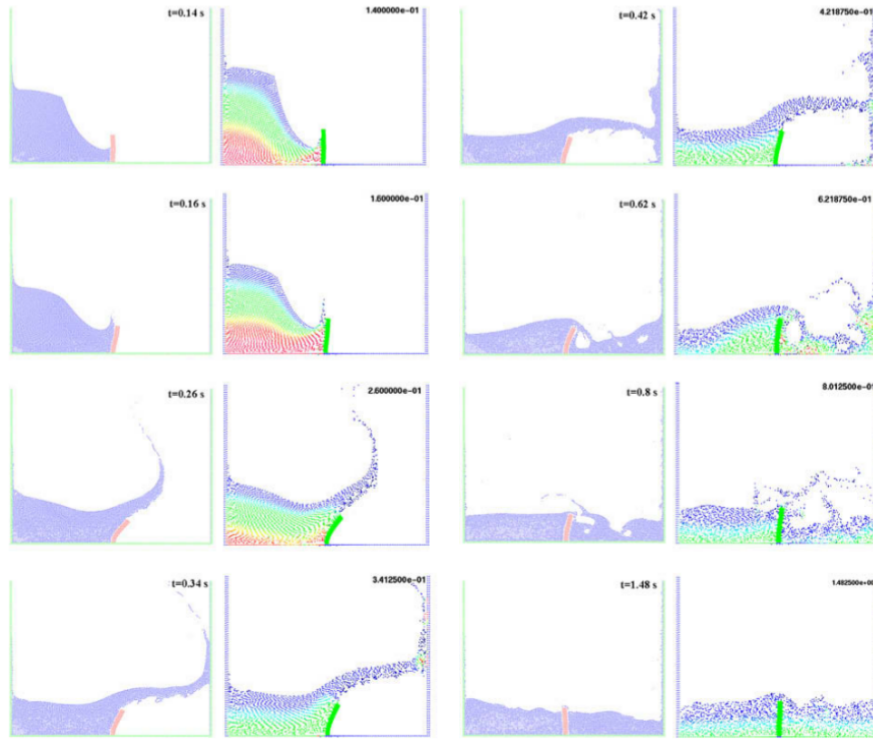


Figure 2.24 – Comparison between Particle Finite Element Method (PFEM) [157] results and SPH [277] simulations for dam break on a hypoelastic baffle. (Rafiee and Thiagarajan [277])

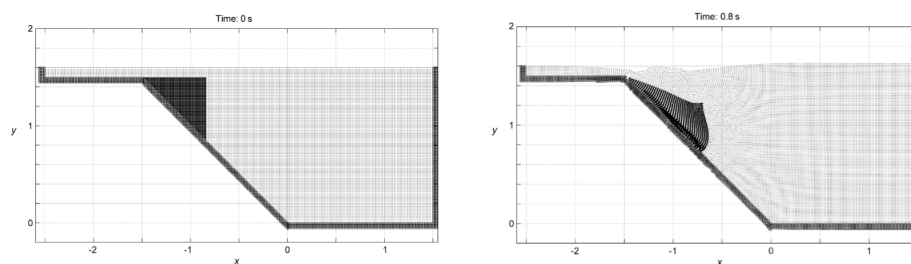


Figure 2.25 – Submarine landslide simulation: the left image represents the initial particles position of the land and the water (at $t = 0[s]$), while the right image is at $t = 0.8[s]$. (Capone et al [52])

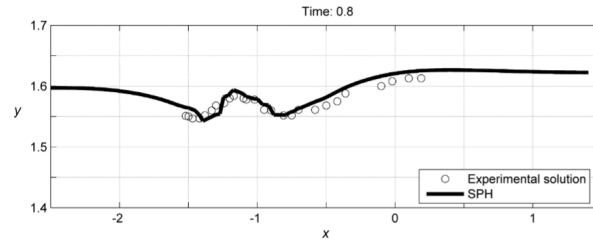


Figure 2.26 – Elevation of the water free surface at time $t = 0.8$ [8]: comparison between SPH [52] results and experimental data by Rzdakiewicz et al [290] . (Capone et al [52])

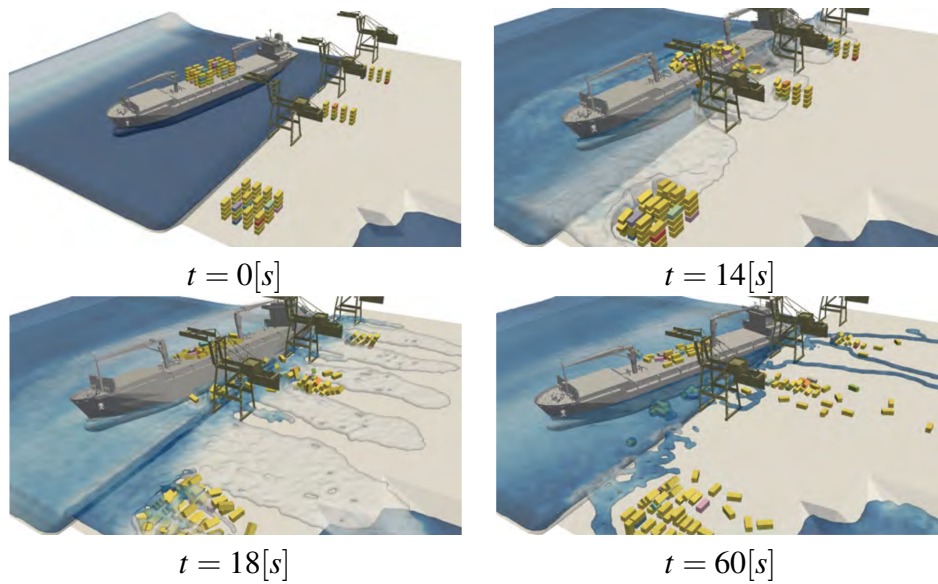


Figure 2.27 – Simulation of the impact of a violent water wave over Sines container terminal at times $t = \{0, 14, 18, 60\}$ [s]. (Canelas et al [50])

Chapter 3

SPH : Numerical development and governing equations discretization

Dans ce chapitre nous abordons les principales équations régissant le comportement d'un milieu continu (fluide et structure). Différentes formulations de discrétisation SPH extraits de la littérature sont discutées. Les principales méthodes utilisées pour la détermination de la pression afin de fermer le système des équations physique sont introduits. Nous donnons un aperçu théorique sur les différentes stratégies et méthodes de simulation des écoulements multiphasiques ainsi que les différentes formes de force de tension de surface utilisées dans le contexte de la méthode SPH. Les différentes stratégies de couplage multiphysiques entre le fluide et la structure sont brièvement discutées. Les méthodes de correction et amélioration de précision et stabilité de la méthode SPH sont présentées. La modélisation de différentes conditions aux limites, les schémas d'intégration en temps ainsi que les critères de stabilité dans le cadre de la méthode SPH sont aussi abordés.

In this chapter we present the governing equation describing the behaviour of a continuous medium (fluid and structure). Various SPH discretization formulations extracted from the literature are discussed. The main methods used to determine the pressure in order to close the governing equations system are introduced. We provide a theoretical overview of the different strategies and methods of multiphase flow simulation as well as the different forms of surface tension force used in the context of the SPH method. The different multiphysics coupling strategies between fluid and structure are given. Methods for correcting and improving the accuracy and stability of the SPH method are discussed. The modeling of different boundary conditions, time integration schemes and stability criteria in the framework of the SPH method are also presented.

3.1 Governing equations

Among the wide range of applications that can be dealt by the SPH method, we highlight in this work the physical phenomena generated from fluid, solid and their interactions. When the fluid and solid behave under isothermal conditions, their evolution can be described completely by the continuity, the momentum conservation and displacement equations. These equations are represented in Lagrangian form as follows:

$$\begin{cases} \frac{d\rho}{dt} = -\rho \nabla \cdot v \\ \frac{dv}{dt} = \frac{1}{\rho} \nabla \cdot \sigma + F^s + F^b \\ \frac{dr}{dt} = v \end{cases} \quad (3.1)$$

where $\frac{d(\cdot)}{dt} = \frac{\partial(\cdot)}{\partial t} + v \cdot \nabla(\cdot)$ represents the Lagrangian derivative (material derivative). ∇ is the nabla operator, ρ, v, r, F^s and F^b represent density, velocity vector, position vector, surface force vector and volumetric body force vector respectively. The surface and body forces can represent for instance the surface tension force, gravity force, electrical force and etc [150, 254, 278]. σ is the Cauchy stress tensor. For more details about the development of conservation equations of the system (3.1), we advise the reader to refer to [221, 283, 119]

The Cauchy stress tensor σ can be decomposed into two parts, the isotropic part ($-pI$) and deviatoric part (τ):

$$\sigma = -pI + \tau \quad (3.2)$$

With p and I denote the hydrostatic pressure (also called mean stress for solid mechanics with $p = -\frac{1}{n}tr(\sigma)$, where n is number of space dimensions and tr is the notation of trace

of square matrix) and the identity tensor, respectively. The notation of the deviatoric tensor (τ) is related to any continuum material, for the fluid material it can be called also viscous stress tensor. The deviatoric is often writing as a function of the rate of strain tensor D . This relation is called constitutive law.

By substituting the equation (3.2) into the momentum equation of the system (3.1), it becomes

$$\frac{dv}{dt} = -\frac{\nabla p}{\rho} + \frac{\nabla \cdot \tau}{\rho} + F^s + F^b \quad (3.3)$$

When the inertial forces are dominant over the viscous ones in the fluid material, it will be treated as inviscid or ideal fluid where the viscous forces are neglected in the computation ($\tau = 0$). For the Newtonian fluid flow, the stress tensor can not be neglected, and it is linearly proportional to the rate of strain tensor with a constant coefficient, the so-called dynamic viscosity (μ) [20, 269]. Thus, the viscous stress tensor (deviatoric tensor) for the Newtonian fluid flow can be expressed as

$$\tau = \mu D \quad (3.4)$$

Where D denotes the rate of strain tensor and it is defined as $D = \nabla v + (\nabla v)^T$, with ∇v represents the velocity gradient tensor, and the superscript T is the transpose tensor symbol. For incompressible Newtonian fluid, since $\nabla \cdot v = 0$, the divergence of the viscous tensor $\nabla \cdot \tau$ further reduces to

$$\tau = \mu \nabla^2 v \quad (3.5)$$

Where $\nabla^2 = \nabla \cdot \nabla = \Delta$ is the Laplacian operator.

All fluids that do not obey equation (3.4) are regrouped under one category so-called non-Newtonian [360, 124, 145, 61, 165]. The figure shows the three categories of non-Newtonian fluids classification: The purely viscous time- independent, time-dependent fluids and viscoelastic fluids [165].

The fluid belongs to the purely viscous time-dependent category, when the shear stress is a function only of the rate of strain but in different manner than described in equation (3.4). Figure 3.2 shows different models of viscous time-independent non-Newtonian fluids.

The pseudoplastic (shear thinning) [34] and dilatant (shear thickening) [17] models have their shear stress depend in a nonlinear way only on the shear rate. for both models, no initial stress is required to initiate yielding. The macromolecular and concentrated solids suspension fluids are examples of pseudoplastic and dilatant fluids, respectively [267].

The Bingham plastic model [33] (also called viscoplastic model) is one of the simplest and more commonly used among the viscous time-dependent category of fluids. In this model, when the yield stress limit (τ_y) is exceeded, the material behaves as Newtonian fluid. Otherwise, it behaves as a rigid body. The constitutive law for a Bingham Plastic can be written in tensorial form as

$$\begin{cases} \tau = \left\{ \frac{\tau_y}{\|D\|_F} + \mu \right\} D & \|\tau\|_F \geq \tau_y \\ D = 0 & \|\tau\|_F < \tau_y \end{cases} \quad (3.6)$$

The notation $\|\cdot\|_F$ refers to Frobenius norm (see equations (5.8) and (5.9)). In equation (5.7) the yielding criterion of soil materials is defined using the Von Mises criterion [226].

$$\|D\|_F = \left(\frac{1}{2} D : D \right)^{\frac{1}{2}} \quad (3.7)$$

$$\|\tau\|_F = \left(\frac{1}{2} \tau : \tau \right)^{\frac{1}{2}} \quad (3.8)$$

The formulation (5.7) can be written under a smooth form to avoid the numerical difficulties resulting from its discontinuous form. The exponential model [270] and the Bercovier and Engelman (BE) model [30] are used for instance to deal with this.

The typical example of Bingham plastic model is the toothpaste, which will not flow out only when certain stress is applied on the tube [281].

Under the Herschel–Bulkley model (also called a nonlinear viscoplastic model) [76], the fluid behaves exactly as with Bingham plastic model but after exceeding the yield stress they following the pseudoplastic model instead of the Newtonian one. Mud flow can be considered as a Herschel–Bulkley fluid [152].

The time-dependent fluids have a hysteresis loop which depends on the time-dependent rate at which the shear stress is applied. The pseudoplastic time-dependent fluid (thixotropic) [257] and the dilatant time-dependent fluid (rheopectic) are two models belonging to this category (see figure 3.2). The waxy crude oil [329] and Bentonite clay suspension [267] are the examples of thixotropic and rheopectic fluids, respectively .

Viscoelastic fluids [276], as can be understood from their name, they possess both viscous and elastic properties. The egg white and polymer melts are examples of Viscoelastic fluids [281].

For the study of the elastic dynamic behavior of any solid structure, the constitutive equation based on Hooke's formulation corrected by Jaumann rate [163] can be used [124]. It reads as

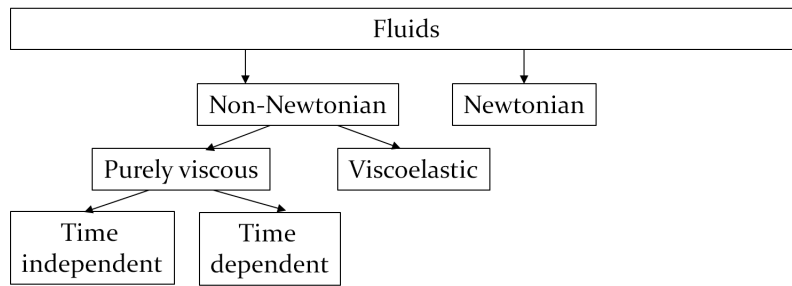


Figure 3.1 – Classification of fluids.(Reproduced from Johnson [165])

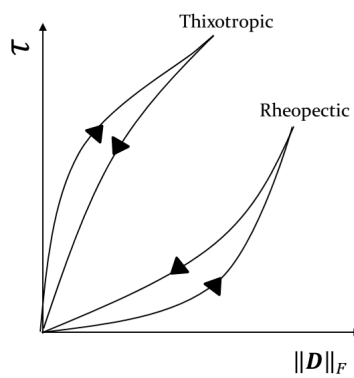


Figure 3.2 – Flow curves of shear stress as a function of shear rate for time-dependent fluids.(Reproduced from Johnson [165])

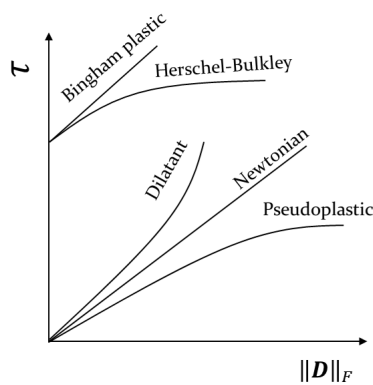


Figure 3.3 – Flow curves of shear stress as a function of shear rate for time-independent fluids.(Reproduced from Johnson [165])

$$\frac{d\tau}{dt} = G \left(D - \frac{1}{3}tr(D)I \right) + \tau\omega + \omega\tau \tag{3.9}$$

Where G is the shear modulus. For the isotropic materials, the shear modulus G can be written as a function of the Young's modulus E , the Poisson's ratio ν and the bulk modulus K [184].

$$G = \frac{E}{2(1 + \nu)} = \frac{3K(1 - 2\nu)}{2(1 + \nu)} \quad (3.10)$$

The tensor ω denotes the rotation-rate tensor that can be expressed as

$$\omega = \frac{1}{2} (\nabla v - (\nabla v)^T) \quad (3.11)$$

The notation $tr(D)$ presents the trace of the square matrix D .

There are other alternative laws for the time derivative of the deviatoric stress that can be used in the context of elastic behavior modeling as those proposed by Ellero et al [95] for studying viscoelastic flows.

Modeling of solid mechanics equations using SPH method has been largely employed thanks to the meshless nature of the method. It was firstly carried out by Libersky and Petschek [194] to simulate the fracture process in brittle solids. After that, it was extended by Randles and Libersky [279] and then Gray and Monaghan [124] to be applied on the elastic dynamics. The commonly used model for the study of plastic behavior of solids in the context of SPH model is the Drucker-Prager model [93]. It was used firstly by Bui et al [46] to study soil collapse and slope stability. Since that, it has been used in other applications, for instance: the study of the failure due to compression in a Brazilian test [86, 272], modeling large soil deformation [45, 47, 57, 260], and the study of the failure in uniaxial compression of gypsum samples [92]. For more details about the model, we refer the reader to consult the references [46, 92].

3.2 Determination of pressure

The system of equations (3.1) is open, and should be closed by the determination of pressure variable. Three principal approaches are commonly used for the pressure determination in the SPH method: Weakly compressible smoothed particle hydrodynamics (WCSPH), Truly incompressible smoothed particle hydrodynamics (ISPH), and explicit incompressible smoothed particle hydrodynamics (EISPH).

3.2.1 Weakly Compressible Smoothed Particle Hydrodynamics

In weakly compressible smoothed particle hydrodynamics (WCSPH) approach, the determination of pressure is done by using an explicit equation of state (EOS) that relates the pressure with particle density ρ and artificial speed of sound c_0 . The most commonly used EOS in the framework of WCSPH is the MacDonald [211] equation. It is also largely known as Tait equation of state in SPH community, This application is stated incorrect by Monaghan in [234]. The MacDonald equation of state is expressed as

$$p = p_r \left\{ \left(\frac{\rho}{\rho_0} \right)^\gamma - 1 \right\} + p_b \quad (3.12)$$

where ρ_0 , p_r and p_b denote the reference density, the reference pressure and background pressure, respectively. The reference density is related to the reference speed of sound c_0 by the following equation

$$p_r = \frac{\rho_0 c_0^2}{\gamma} \quad (3.13)$$

the parameter γ is generally set constant and equal 7 . In some references the $\gamma = 1.4$ is also used to simulate the air material [72, 128, 129, 358]. It is stated by Morris in [255] , that when the density fluctuations increases, small errors in density correspond to increasingly larger errors in pressure. Therefore, for lower Reynolds numbers, more accurate pressure estimates are obtained using SPH if $\gamma = 1$, since errors in density and pressure remain proportional. The linear equation of state (when $\gamma = 1$) is used in lot of references such as [254, 216].

The reference speed of sound c_0 in the case of fluid flow can be determined as [254, 308]

$$c_0^2 \approx \max \left\{ \frac{U_0^2}{\delta\rho}, \frac{\|g\|L_0}{\delta\rho}, \frac{\mu_{eff}U_0}{\rho_0 L_0 \delta\rho} \right\} \quad (3.14)$$

Where U_0 , L_0 , μ_{eff} and σ are the reference velocity, reference length, and effective dynamic viscosity (apparent viscosity), respectively. The term $\delta\rho$ represent the ratio of density variations about the initial density which is usually set equal to 1% ($\delta\rho = 0.01$) [243].

For numerical problems involving single-phase free surface fluid flows and also for solid dynamics, the background pressure is generally set to zero ($p_b = 0$). Furthermore, for simulations of single or multiphase confined fluid flows, the pressure is chosen as a positive value sufficient to guarantee the positivity of the calculated pressure field via the equation of state in order to avoid the tensile instability [218]. Several formulation of background

pressure are used in the literature such as: Marrone et al [218] use ($p_b = 3\rho_0 U_0^2$) for confined single fluid flow, and Krimi et al [178] use ($p_b \propto 0.05 p_r$) for the simulation of confined multi-phase flow.

In order to enhance the numerical stability of the multiphase fluid flow simulations, Colagrossi and Landrini [72] recommend the use a common reference pressure of all fluid phase.

In the case of the simulation of solid deformation, the linear equation of state (Equation (3.12) with $\gamma = 1$) is usually employed with a calculated artificial speed of sound using the following equation [124, 6, 293]

$$c_0^2 \approx \frac{K}{\rho_0} \quad (3.15)$$

Where K is the bulk modulus.

3.2.2 Incompressible Smoothed Particle Hydrodynamics

In Incompressible Smoothed Particle Hydrodynamics (ISPH) approach, the determination of pressure is done by solving the Poisson's equation via the projection method. This method is originally developed in the context of grid-based method by Chorin [62, 63], and implemented by Cummins and Rudman [80] to deal with incompressible SPH flow but without a free surface. The free surface condition was introduced in incompressible SPH model by Shao and Lo [303]. It has since been of great interest [302, 150, 355, 158]. In ISPH, the continuity equation of the system (3.1) is simplified to the divergence-free velocity by taking into account that the density is a constant parameter. It reads as

$$\nabla \cdot v = 0 \quad (3.16)$$

The original incompressible smoothed particle projection method [80, 188] is referred under the name of ISPH divergence-free velocity field (ISPH_DF method). Here, the density and mass of particles are constant and their positions r_i^n are advected with velocity v_i^n to an intermediate positions r_i^* as follows

$$r_i^* = r_i^n + \delta t v_i^n \quad (3.17)$$

At the position r_i^* , An intermediate velocity v_i^* is calculated based on all forces governing the movement of particle i at the time n except the pressure ones

$$v_i^* = v_i^n + \delta t \left(\frac{\nabla \cdot \tau}{\rho} + F^s + F^b \right) \quad (3.18)$$

Determination of pressure at time $n + 1$ by solving the following pressure Poisson equation (PPE) t

$$\nabla \cdot \left(\frac{1}{\rho} \nabla p^{n+1} \right)_i = \frac{1}{\delta t} \nabla \cdot v_i^* \quad (3.19)$$

The velocity at the final time-step $n + 1$ (v_i^{n+1}) will result from the projection of v_i^* . Thus,

$$v_i^{n+1} = v_i^* - \frac{\delta t}{\rho} \nabla p_i^{n+1} \quad (3.20)$$

The particle position at the final time-step is calculated by

$$r_i^{n+1} = r_i^n + \delta t \left(\frac{v_i^{n+1} + v_i^n}{2} \right) \quad (3.21)$$

The ISPH_DF scheme provides accurate and smooth pressure fields. However, it presents instabilities since it leads to highly anisotropic particles arrangements [197]. This problem can be avoided by using particle shifting algorithm as proposed by Xu et al [355] and improved by Lind et al [197] or the one proposed by Fatehi and Manzari [100].

Two alternative methods have been developed to enhance the accuracy and stability of the ISPH_DF method. The first method is referred as ISPH_DI (incompressible smoothed particle hydrodynamics based on keeping density invariance) [303], this method is similar to ISPH_DF for all steps except of the solving Poisson equation step. In ISPH_DI, the right hand side of Pressure Poisson equation is expressed with relative density difference instead of divergence of velocity in ISPH_DF. Therefore, the Pressure Poisson Equation can read as

$$\nabla \cdot \left(\frac{1}{\rho^*} \nabla p^{n+1} \right)_i = \frac{\rho_0 - \rho^*}{\rho_0 \delta t^2} \quad (3.22)$$

With ρ^* is the intermediate particle density approximated through the continuity equation.

As it is stated by Xu et al [355], the ISPH_DI scheme presents more stable simulations than with ISPH_DF one, but its accuracy is deteriorated. To benefit from both schemes ISPH_DF and ISPH_DI, Hu and Adams [150] proposed a combined a scheme which is referred as ISPH_DFDI. This scheme requires two pressure Poisson equations to be solved, and thus, computational cost becomes higher.

The main differences between weakly compressible smoothed particle hydrodynamics (WCSPH) and the incompressible smoothed particle hydrodynamics (ISPH) methods can be summarized by Table 3.1.

WCSPH	ISPH
Fully explicit nature of the scheme resolution	Semi-implicit nature of the scheme resolution
The pressure is calculated via an equation of state	The pressure is calculated via solving the Poisson equation
Suffer from a high frequency oscillations of pressure	Stable and smooth pressure
Free surface flow condition is maturely fulfilled	Imposition of free surface flow is required
Easy to program	More difficult to program than WCSPH
Small time step due to CFL condition related to the artificial speed of sound c_0	More important time step
Shifting particle algorithm is not needed (It presents good particles distribution)	Need for shifting algorithm in order to well distribute

Table 3.1 – Comparison between WCSPH and ISPH schemes.

3.2.3 Explicit Incompressible Smoothed Particle Hydrodynamics

The explicit incompressible smoothed particle hydrodynamics method (EISPH), is firstly developed by Hosseini et al [145] for the simulation of non-Newtonian fluid flow. It was employed after in other works as in [277, 14, 15]. This method uses the projection method as in ISPH [80] but relies on an explicit approximation of Poisson equation instead of solving it. Therefore, this method reduces the pressure oscillations and reduce the computational effort [82]. For more details about the formulations, we advise the reader to refer to [145, 82].

3.3 Discretization of governing equations

Generally, the asymmetric form of SPH first derivative (Equation 2.28) is employed to write the right hand side of the continuity equation of the system (3.1) (also called divergence equation [245]) in SPH discrete form. Thus, the discrete form at the particle i can be read as

$$\frac{d\rho_i}{dt} = \sum_j^{n_b} m_j v_{ij} \cdot \nabla W_{ij} \quad (3.23)$$

and also

$$\frac{d\rho_i}{dt} = \rho_i \sum_j^{n_b} \frac{m_j}{\rho_i} v_{ij} \cdot \nabla W_{ij} \quad (3.24)$$

With $v_{ij} = v_i - v_j$.

Otherwise, the density can be also directly approximated via the basic SPH interpolation (2.24) applied on the density ρ at the particle i . This summation form is expressed as

$$\rho_i = \sum_j^{n_b} \frac{m_j}{\rho_j} \rho_j W_{ij} = \sum_j^{n_b} m_j W_{ij} \quad (3.25)$$

The discrete formulation of the continuity equation (3.23) can be seen as the time derivative version of the summation form (3.25) [245].

The advantage of the density summation formulation (3.25) over the formulations (3.23) and 3.24 is that it conserves exactly the mass [242]. An alternative version of density summation formulation is presented by Hu et Adams [151] (equation (3.26)). This formulation conserves exactly the mass as well as (3.25), and in addition it allows for density discontinuities when the particle i interacts with the neighboring particles j that present a large particle-mass differences, for instance, it is well suited to dealing with multiphase fluid flow with large density ratio.

$$\rho_i = m_i \sum_j^{n_b} W_{ij} \quad (3.26)$$

The problem of the density summation formulations (3.25) and (3.26) is that it works badly in cases of free surface flows, because they can not reproduce a zero pressure in the free surface particle. While, with the use of the density divergence equations (3.23) or (3.25) the zero pressure in the free surface particle is reproduced naturally. The formulation (3.25) is recommended for use over equation (3.23) when the problem concerns multiphase fluid flow with high density ratio (≥ 2) [69, 245], because in the summation of the right hand side of the equation (3.23), the mass of neighboring particles affects the calculation, whereas with the formulation (3.24) it is the volumes that affects it.

In order to achieve the conservation of momentum, one of the following symmetric expression can be used for the calculation of divergence operator of the Cauchy stress tensor σ [242]

$$\frac{1}{\rho_i} \nabla \cdot \sigma_i = \sum_j^{n_b} m_j \left(\frac{\sigma_i}{\rho_i^2} + \frac{\sigma_j}{\rho_j^2} \right) \nabla W_{ij} \quad (3.27)$$

If the density varies significantly, Monaghan [234] has recommended to use another discrete symmetric form of Cauchy stress divergence [338]

$$\frac{1}{\rho_i} \nabla \cdot \sigma_i = \sum_j^{n_b} \frac{m_j}{\rho_i \rho_j} (\sigma_i + \sigma_j) \nabla W_{ij} \quad (3.28)$$

With σ_i is expressed as $\sigma_i = -p_i I + \tau_i$.

An asymmetric expression can be used to discretize the divergence of Cauchy stress tensor as it is used in [56, 279]

$$\frac{1}{\rho_i} \nabla \cdot \sigma_i = \sum_j^{n_b} \frac{m_j}{\rho_i \rho_j} (\sigma_j - \sigma_i) \nabla W_{ij} \quad (3.29)$$

The formulation is generally used with normalization technique of the kernel gradient explained in the section 3.7 (equation (3.67)) [56, 279].

The three formulation of the Cauchy stress tensor divergence $\nabla \cdot \sigma_i$ are usually employed in the context of solid mechanics, especially for modeling the elastic behavior where the deviatoric part τ is determined from time integration of a differential equation as equation (3.9) or as used in [95]. For fluid dynamics applications, the form of momentum equation (3.3) is preferred, where the gradient of pressure and the viscous tensor divergence τ are discretized separately in different ways.

The discretization of the pressure gradient follows the same three formulations [242, 338, 279]. Thus, they can be represented as

$$-\frac{1}{\rho_i} \nabla p_i = \begin{cases} -\sum_j^{n_b} m_j \left(\frac{p_i}{\rho_i^2} + \frac{p_j}{\rho_j^2} \right) \nabla W_{ij} \\ -\sum_j^{n_b} \frac{m_j}{\rho_i \rho_j} (p_i + p_j) \nabla W_{ij} \\ -\sum_j^{n_b} \frac{m_j}{\rho_i \rho_j} (p_j - p_i) \nabla W_{ij} \end{cases} \quad (3.30)$$

For the divergence of the viscous stress tensor. A hybrid formulation between the SPH gradient approximation and finite difference estimation of second derivative operator has been proposed by Morris [255] :

$$\frac{1}{\rho_i} \nabla \cdot \tau_i = \sum_j^{n_b} m_j \frac{(\mu_i + \mu_j)}{\rho_i \rho_j} \frac{r_{ij} \cdot \nabla W_{ij}}{r_{ij}^2} v_{ij} \quad (3.31)$$

This formulation (3.31) conserves linear momentum exactly, while preserving angular momentum approximately [19].

Violeau and Issa [339] have derived from the artificial viscosity term used in the the work of Monaghan and Gingold [235] the following formulation for the approximation of the divergence of viscous stress tensor

$$\frac{1}{\rho_i} \nabla \cdot \tau_i = \sum_j^{n_b} m_j \frac{8}{\rho_i + \rho_j} \left(\frac{\mu_i}{\rho_i} + \frac{\mu_j}{\rho_j} \right) \frac{r_{ij} \cdot v_{ij}}{r_{ij}^2 + \eta^2} \nabla W_{ij} \quad (3.32)$$

Another formulation for the calculation of viscous stress tensor divergence was introduced by Cleary [65] and can read as

$$\frac{1}{\rho_i} \nabla \cdot \tau_i = \sum_j^{n_b} m_j \frac{\xi}{\rho_i \rho_j} \frac{4\mu_i \mu_j}{\mu_i + \mu_j} \frac{r_{ij} \cdot v_{ij}}{r_{ij}^2 + \eta^2} \nabla W_{ij} \quad (3.33)$$

The parameter ξ was set as 4.96333 through calibration against known solutions in a Couette flow. Basa et al have stated in [19] that this value of ξ gives highly inaccurate velocities for the simulation of Poiseuille flow and the value of $\xi = 4.24$ provides much better results.

Note that the parameter η^2 is taken generally as small value ($\eta^2 = (0.1h)^2$) to prevent singularities (zero denominator) when two particles become too close.

For the multiphase fluid flow applications, Hu et Adams [151] have proposed approximations of spatial derivatives with particle-averaged in which the neighboring particles j of the particle i only contribute to the summation by their specific volumes and not their masses. This technique maintain exactly the mass conservation, and allows naturally for density discontinuities across phase interfaces. Therefore, the pressure gradient can be expressed as [151, 1]

$$-\frac{1}{\rho_i} \nabla p_i = -\frac{1}{m_i} \sum_j^{n_b} (V_i^2 p_i + V_j^2 p_j) \nabla W_{ij} \quad (3.34)$$

This expression is similar to the form of gradient pressure preferred by Monaghan [242]. This form conserves linear momentum exactly since exchanging of particle positions i and j within the sum results an opposite pressure force.

Another form of gradient pressure [2, 4]

$$-\frac{1}{\rho_i} \nabla p_i = -\frac{1}{m_i} \sum_j^{n_b} (V_i^2 + V_j^2) \widetilde{p}_{ij} \nabla W_{ij} \quad (3.35)$$

With \widetilde{p}_{ij} is the density-weighted inter-particle averaged pressure [150]

$$\widetilde{p}_{ij} = \frac{\rho_i p_j + \rho_j p_i}{\rho_i + \rho_j} \quad (3.36)$$

This form \widetilde{p}_{ij} (3.36) ensures that $\frac{1}{\rho} \nabla p$ is continuous even when a discontinuity is present in the density field.

While for the divergence of the viscous tensor is taken as

$$\frac{1}{\rho_i} \nabla \cdot \tau_i = \frac{1}{m_i} \sum_j^{n_b} (V_i^2 + V_j^2) \widetilde{\mu}_{ij} \frac{v_{ij}}{r_{ij}} \frac{\partial W}{\partial r_{ij}} \quad (3.37)$$

With $\widetilde{\mu}_{ij}$ is the inter-particle-averaged shear viscosity

$$\widetilde{\mu}_{ij} = \frac{2\mu_i\mu_j}{\mu_i + \mu_j} \quad (3.38)$$

This form of the viscous force (3.37) conserves linear momentum. The angular conservation of momentum can be achieved using other formulations, for instance the one used by Hu and Adam [148] which is extended for multiphase flow applications by Krimi et al [178]

$$\frac{1}{\rho_i} \nabla \cdot \tau_i = \frac{\zeta}{m_i} \sum_j^{n_b} (V_i^2 + V_j^2) \widetilde{\mu}_{ij} \frac{v_{ij} \cdot r_{ij}}{r_{ij}^2} \nabla W_{ij} \quad (3.39)$$

Where $\zeta = n + 2$, and n is the space dimension number.

Note that here the volume is calculated as $V_i = \frac{m_i}{\rho_i}$, with the mass m_i is taking as constant during all simulation time, and the density ρ_i is computed using the summation formulation (3.26).

Other principles of SPH discretization in the context of multiphase flow can be found in the literature. For instance, the work of Grenier et al [128], derives the governing equations following a Lagrangian variational principle that leads subsequently to an Hamiltonian system of particles. This formulation permits to model flows where both interfaces and a free surface are present. The details of these formulations are not discussed here, but can be found in [128, 127, 130, 129].

For modeling of Non-Newtonian fluids within the principle of Generalized Newtonian Fluids (GNL) technique [33, 343], other form of divergence of viscous stress tensor (deviatoric tensor) is usually found in literature [98, 352]

$$\frac{1}{\rho_i} \nabla \cdot \tau_i = \sum_j^{n_b} \frac{m_j}{\rho_j} \frac{\mu_i + \mu_j}{r_{ij}^2 + \eta^2} \{v_{ij} (r_{ij} \cdot \nabla W_{ij}) + r_{ij} (v_{ij} \cdot \nabla W_{ij})\} \quad (3.40)$$

Krimi et al [177] have extended this formulation to be applied to the Non-Newtonian multiphase fluid and/or fluid-like mass framework. It reads as

$$\frac{1}{\rho_i} \nabla \cdot \tau_i = \frac{1}{m_i} \sum_j^{n_b} \left\{ \frac{V_i^2 + V_j^2}{r_{ij}^2} \right\} \frac{\rho_i \mu_j + \rho_j \mu_i}{\rho_i + \rho_j} \{v_{ij} (r_{ij} \cdot \nabla W_{ij}) + r_{ij} (v_{ij} \cdot \nabla W_{ij})\} \quad (3.41)$$

3.4 Surface tension for multiphase fluids

As is stated by Monaghan [234], there are at least three ways to include the surface tension within the SPH framework.

The first one, is to assume that the SPH particle are real physical particles and introduce between them a forces in order to mimic the effects of surface tension [154, 324, 21, 262, 328].

The second way, the surface tension equations are modeled by including for SPH flows an extra energy term in the particle Lagrangian [236, 254].

The third way, is to use the surface tension force within transition region at the interface between the fluid phases (see figure 3.4) under well known forms : Continuum Surface Force (CSF) form or Continuum Surface Stress (CSS) form.

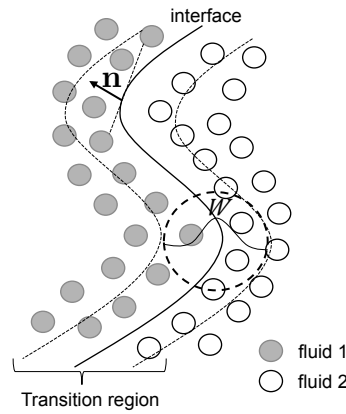


Figure 3.4 – Transition region of surface tension.

The Continuum Surface Force (CSF) formulation [40] describes the pressure-jump condition normal to the separation interface of the fluids. Assuming that the surface tension coefficient $\sigma^{(1-2)}$ is constant between two fluid phases (1 and 2), the expression of the force can be expressed as

$$F^{ST(1-2)} = \sigma^{(1-2)} \kappa n \delta_{\Sigma} \quad (3.42)$$

In equation (3.42), κ , n and δ_{Σ} denote the curvature, the unit normal vector to the interface (see figure 3.4) and the delta function, respectively. In the context of the SPH method, equation (3.42) reads as

$$F_i^{ST(1-2)} = -\sigma^{(1-2)} \nabla \cdot n_i \nabla C \quad (3.43)$$

where C is the color function that has a unit jump across the interface. It's equal to 1 in one particle fluid phase and 0 in its neighboring particle of other fluid phase.

Other alternative tensorial formulation of surface tension so-called the Continuum Surface Stress (CSS) [180] can be also used. It is equivalent to the CSF formulation given in equation (3.43)

$$F_i^{ST} = \nabla \cdot \Pi_i \quad (3.44)$$

where Π_i defines the immiscible mixture surface stress tensor of the particle i (capillary pressure tensor). Assuming that the particle i belongs to the l fluid phase, then the mixture surface stress can be expressed as

$$\Pi_i = \sum_{k \neq l} \Pi_i^{kl} \quad (3.45)$$

In equation (4.16), Π_i^{kl} is the fluid surface stress tensor between phases k and l , defined as

$$\Pi_i^{kl} = \frac{\sigma^{kl}}{\|\nabla C_i^{kl}\|} \left(\|\nabla C_i^{kl}\|^2 I - \nabla C_i^{kl} \otimes \nabla C_i^{kl} \right) \quad (3.46)$$

Moriss [254] employs both formulation (CSF) and (CSS) in the context of WSPH, The obtained results have been reasonable. Hu and Adams [151] used the CSS with introducing modification in order to have more stable results. Adami et al [2] use the CSF formulation by using new accurate divergence approximation to compute the curvature with good precision. Krimi et al [178] exploit the idea of Adami et al [2] and use it in the framework of CSS surface tension to simulate accurately the fluid problems including more than two phases.

3.5 Rigid body-fluid interaction

We consider a system of fluid containing a floating rigid body with center of mass R and the velocity at R is referred to V . The equation of motion of the center of mass of discretized rigid body can be expressed as

$$M \frac{dV}{dt} = \sum_k^{n_k} m_k f_k \quad (3.47)$$

Where k refer to k^{th} rigid particle constituting the global rigid body. The force f_k is the hydrodynamics force per unit mass acting on the boundary particle k , m_k is mass of rigid particle k and n_k is total number of rigid body particle. The force f_k is expressed as

$$f_k = \sum_l^{n_{FPS}} f_{kl} \quad (3.48)$$

Where f_{kl} is the force per unit mass exerted by the fluid particle l on the boundary particle k [316, 284, 316]

The equation of rotation of rigid body can read as

$$I \frac{d\Omega}{dt} = \sum_k^{n_k} m_k (r_k - R) \times f_k \quad (3.49)$$

Where Ω denotes angular velocity, I is the moment of inertia and r_k is the position of the rigid particle k . The mathematical notation \times refers to cross product.

The values of V and Ω are predicted by integrating the equations (3.47) and (3.49). The rigid body boundary particles move as part of the rigid body, thus, the position of boundary particle k is given by

$$\frac{dr_k}{dt} = v_k = V + \Omega \times (r_k - R) \quad (3.50)$$

The above described technique conserves both linear and angular momentum [237, 245]. Hashemi et al [133] use another approach for modeling body motion by employed surface integration on pressure and viscosity forces applied on the body elements.

3.6 Fluid-structure coupling strategies

In SPH method two ways of coupling strategies between the fluid and structure are possible: Weak coupling (also called partitioned) and strong coupling (also called monolithic) strategies.

For weak coupling between fluid and structure, either of the materials does not depend on the other, it can be analyzed first. Herein, the solution on each material will be done separately. For instance, as in the work of Shi et al [306], the fluid is solved first using a Navier-Stokes solver by considering that the structure is a rigid moving wall. Subsequently, the structure is solved using the assigned constitutive equation taking into consideration the storage forces applied on it by the fluid. The drawback of this technique is that it may allow for inter-penetration between the particle of both materials which leads to use a very time step for the simulation. This coupling strategy is largely employed to manage the interactions between fluid and rigid bodies [237, 245, 133, 174, 316, 284, 316], where the fluid considers the rigid body as a dynamic wall boundary, whereas for rigid bodies, their movement is determined from the forces applied by the fluid through the equations of motion

described in the section 3.5. The algorithms of coupling fluid-structure which are based on the use of explicit imposition of continuity conditions on the interface between fluid and structure (continuity of normal stress and velocity) may lead to a weak coupling because of the necessity to advance the solution from one material to another as it is realized in [181].

In the case of strong coupling of fluid and structure, both are solved simultaneously. The lagrangian nature of the SPH method allows this strategy to be the simplest for the application and the more robust one. It works just by introducing the contribution of all particles to the summation in the SPH discretized equations regardless of their nature. Here, the coupling conditions on the interface would be naturally satisfied [6, 277]. Among the works achieved in this context, we advice the reader to refer to [13, 52, 169, 299, 215, 108, 331, 345, 315].

The above description of fluid-structure coupling strategies concerns only the SPH-SPH applications (fluid and structure are modeled with SPH method). Several other numerical method can also be coupled in the fluid structure interactions framework such as SPH-FEM (SPH method for fluid and finites elements method for structure) [107, 356, 147, 209, 208]. This category of coupling is general classed as a weak (partitioned) because of the different natures of the methods and solvers.

3.7 Improvement in SPH method

The improvement of accuracy, stability and consistency of smoothed particle hydrodynamics method (SPH) can be seen via two general directions [296]: By improving the approximation of the kernel function with its derivatives and/or by recovering the SPH particle approximation of the governing equations.

3.7.1 Improvement in kernel approximation

The improvement of the kernel approximation can enhance significantly the SPH results specially when (i) the support of kernel is truncated with the boundaries (free surface or solid boundaries for instance), (ii) small number of particle are present within the kernel [67], (iii) the particles are not uniformly distributed [245].

Shepard formulation

Shepard formulation or also called Shepard filter [304] represents the simplest correction of the kernel approximation of the function f at the position r_i . It reads as

$$f(r_i) \approx \sum_j^{n_b} f(r_j) W_{ij}^S V_j \quad (3.51)$$

With

$$W_{ij}^S = \frac{W_{ij}}{\sum_j^{n_b} W_{ij}^S V_j} \quad (3.52)$$

Note that, the using of Shepard formulation guarantees the normalization condition even when the kernel support is not full (truncated by the free surface and/or solid boundaries) and presents 0^{th} order consistency C^0 . The Shepard formulation is usually employed to re-initialize the density in order to smooth pressure oscillations and stabilize the simulation [81, 122, 196], and also it is used for the measurement of physical proprieties at any given position [178].

damping technique

The imposition of initial conditions in the framework of the SPH method may cause spurious high-frequency oscillations due to artificial sound waves propagating through the simulation domain. Monaghan et al [247] proposed a damping technique applied during a predefined time period to reduce Such artefacts. This damping technique smoothes the particle distribution and otherwise accelerates particles. The damping time T_D defines the time period during which the acceleration due to the body force is mitigated by the factor $\xi_D(t)$. The factor $\xi_D(t)$ is defined as [4]

$$\xi_D(t) = \begin{cases} \left(\sin\left(\frac{t}{T_D} - 0.5\right) \pi + 1 \right) & t \leq T_D \\ 1 & t > T_D \end{cases} \quad (3.53)$$

MLS kernel

The Moving Least Square kernel (MLS) is developed by Dilts [87] and Belytschko et al [23]. It presents an approximation of first-order consistency C^1 or in other words, it can reproduce exactly a linear function. The function f can be approximated with MLS kernel at position r_i as follows

$$f(r_i) \approx \sum_j^{n_b} f(r_j) W_{ij}^{MLS} V_j \quad (3.54)$$

$$W_{ij}^{MLS} = (A^{-1} \cdot e) \cdot b W_{ij} \quad (3.55)$$

Assuming that the position r has in 3D space as coordinates $r^T = [x \ y \ z]$, the vector e , the vector b and the matrix A are expressed as

$$\begin{cases} b^T = [1, (x_j - x_i), (y_j - y_i), (z_j - z_i)] \\ e^T = [1, 0, 0, 0] \\ A = \sum_j^{n_b} (b \otimes b) W_{ij} V_j \end{cases} \quad (3.56)$$

The symbol \otimes represents the outer product.

The MLS approximation is used generally to smooth density in order to mitigate the spurious oscillations in pressure in the context of weakly compressible flow hypothesis [72, 268]. Colagrossi and Landrini [72] state that it is enough to use the MLS method to smooth the density only once for each 20 time iterations in order to make the computation time cost effective.

Kernel correction technique [36, 35]

The kernel correction technique [36, 35] is similar to MLS method [87]. It is based on the enforcement of a any linear field to be exactly evaluated through the kernel approximation formulation. Therefore, the function $f(r_i)$ is evaluated as

$$f(r_i) \approx \sum_j^{n_b} f(r_j) W_{ij}^C V_j \quad (3.57)$$

with,

$$W_{ij}^C = \alpha(r_i) [1 + \beta(r_i) \cdot (r_i - r_j)] W_{ij} \quad (3.58)$$

Where $\alpha(r_i)$ and $\beta(r_i)$ are the scalar and vector functions evaluated at the position r_i , respectively.

Assuming that $\phi(r_i)$ is a linear function ($\phi(r_i) = \phi_0 + \phi_1 r_i$). This function can be written via the formulation (3.57) as follows

$$\phi(r_i) = \phi_0 + \phi_1 r_i = \sum_j^{n_b} (\phi_0 + \phi_1 r_j) W_{ij}^C V_j \quad (3.59)$$

As ϕ_0 and ϕ_1 are arbitrary, the following relations (3.60) and (3.61) can be concluded from (3.59) as

$$\sum_j^{n_b} W_{ij}^C V_j = 1 \quad (3.60)$$

$$\sum_j^{n_b} (r_i - r_j) W_{ij}^C V_j = 0 \quad (3.61)$$

By substituting the formulation (3.58) into the relations (3.60) and (3.61), the parameters $\alpha(r_i)$ and $\beta(r_i)$ can be evaluated explicitly after simple algebra as follows

$$\beta(r_i) = \left[\sum_j^{n_b} (r_i - r_j) \otimes (r_i - r_j) W_{ij} V_j \right]^{-1} \sum_j^{n_b} (r_j - r_i) W_{ij} V_j \quad (3.62)$$

and,

$$\alpha(r_i) = \frac{1}{\sum_j^{n_b} [1 + \beta(r_i) \cdot (r_i - r_j)] W_{ij} V_j} \quad (3.63)$$

Gradient correction of the kernel function

A corrected form of kernel gradient of equation 2.28 is developed by Randles and Libersky [279] and since it presented in [36, 338, 55]. This corrected gradient can improve the accuracy of the asymmetric gradient formulation to the second order [264] and makes it a first-order consistent [99]. The principal idea is to enforce the fulfillment of the condition (2.23) to be satisfied in the context of gradient with asymmetric form (2.28). The Corrected gradient of the kernel function can be expressed as :

$$\nabla W_{ij}^C = L(r_i) \nabla \cdot W_{ij} \quad (3.64)$$

with $L(r_i)$ is the normalization matrix expressed as the inverse of the discretized version of the identity condition (2.23). It can read as

$$L(r_i) = \left(\sum_j^{n_b} (r_j - r_i) \otimes \nabla W(r, h) V_j \right)^{-1} \quad (3.65)$$

The corrected first-order consistent gradient operator of the function $f(r_i)$ is expressed in terms of $L(r_i)$ as follows :

$$\nabla f(r_i) \approx L(r_i) \sum_j^{n_b} f_{,ji} \nabla W_{ij} V_j \quad (3.66)$$

With $f_{ji} = f(r_j) - f(r_i)$.

The matrix $L(r_i)$ need to be firstly constructed and then inverted. To avoid this additional computational task , Adami et al [2] have proposed another simple explicit expression based on the two identities presented in Español and Revenga [97]. This formulation can be expressed as

$$\nabla W_{ij}^C = l(r_i) \nabla W_{ij} \quad (3.67)$$

Where $l(r_i)$ is a scalar function and it is expressed as

$$l(r_i) = \frac{n}{\sum_j^{n_b} (r_j - r_i) \cdot \nabla W_{ij} V_j} \quad (3.68)$$

With n is the number of spatial dimensions.

The corrected first-order consistent gradient operator of the function $f(r_i)$ is expressed in terms of the scalar $l(r_i)$ as follows :

$$\nabla f(r_i) \approx l(r_i) \sum_j^{n_b} f_{ji} \nabla W_{ij} V_j \quad (3.69)$$

Note that it is possible to use these gradients kernel correction ($L(r_i)$ and/or $l(r_i)$) into the asymmetric form of the equation 2.28.

Correction of the SPH Laplacian operator

The SPH Laplacian approximation (2.31) is only zero-order consistent, and making it higher order consistent via the kernel function correction is quite complex. Schwaiger [295] proposed a method more consistent than the last one, and can achieve an approximation of the second order consistency. Later on, Fatehi and Manzari [99] gave an new formulation that grantee exactly a second-order consistency. this technique requires the computation of a fourth-order tensor. This formulation of SPH Laplacian operator of the function $f(r_i)$ is then expressed as:

$$\nabla \cdot \nabla f(r_i) \approx B_i : [2 \sum_j^{n_b} V_j r_{ij} \otimes \nabla W_{ij} \left(\frac{f_{ij}}{r_{ij}^2} - \frac{r_{ij}}{r_{ij}^2} \cdot \nabla f(r_i) \right) .] \quad (3.70)$$

With $\nabla f(r_i)$ is the first order consistent gradient formulation given through the equation (3.66), and $B_i = B(r_i)$ is a fourth-order symmetric that can be determined from

$$B_i : \left\{ \sum_j^{n_b} V_j \frac{r_{ij}}{r_{ij}^2} \otimes r_{ij} \otimes r_{ij} \otimes \nabla W_{ij} + \left(\sum_j^{n_b} \frac{V_j}{r_{ij}^2} r_{ij} \otimes r_{ij} \otimes \nabla W_{ij} \right) \cdot L_i \cdot \left(\sum_j^{n_b} V_j r_{ij} \otimes r_{ij} \otimes \nabla W_{ij} \right) \right\} = -I \quad (3.71)$$

With $L_i = L(r_i)$ is the normalization matrix tensor given by the equation (3.65). The determination of the fourth order tensor B_i is done through solving the system (3.71) which makes this approach relatively expensive in terms of computation task.

3.7.2 Improvement by recovering the SPH particle approximation of the governing equations

Ferrari's diffusive term

Ferrari et al [105] proposed a diffusive term inspired from Riemann-based SPH schemes [338, 256, 25] by introducing the Rusanov flux into the continuity equation. This term improves the numerical stability of the SPH scheme without use of an artificial viscosity.

$$D_i^{Ferr} = \sum_j^{n_b} m_j \left(\frac{\max\{c_{0i}, c_{0j}\}}{\rho_j} (\rho_j - \rho_i) \right) e_{ij} \cdot \nabla W_{ij} \quad (3.72)$$

Where e_{ij} is the inter-particles unite vector that is expressed as $e_{ij} = \frac{r_{ij}}{r_{ij}}$.

Fatehi's diffusive term

Fatehi and Manzari [100] have been developed a diffusive term (D^{Fat}) to deal with non-physical oscillations in the pressure. This term is associated with the checkerboard problem [106] which is in the context of grid-based method. The use of this diffusive terms gives the advantageous of no need for neither artificial viscosity nor artificial stress for guarantee the stability of SPH scheme [100].

$$D_i^{Fat} = -\rho_i \delta t \left\{ \left\langle \nabla \cdot \left\langle \frac{\nabla p}{\rho} \right\rangle \right\rangle_i - \left\langle \nabla \cdot \frac{\nabla p}{\rho} \right\rangle_i \right\} \quad (3.73)$$

Where,

$$\left\langle \nabla \cdot \left\langle \frac{\nabla p}{\rho} \right\rangle \right\rangle_i = \sum_j^{n_b} V_j (\nabla \nabla W_{ij}) \cdot \left(\left\langle \frac{\nabla p}{\rho} \right\rangle_j - \left\langle \frac{\nabla p}{\rho} \right\rangle_i \right) \quad (3.74)$$

and

$$\left\langle \nabla \cdot \left\langle \frac{\nabla p}{\rho} \right\rangle \right\rangle_i = B_i : \left\{ 2 \sum_j^{n_b} V_j r_{ij} \otimes \nabla W_{ij} \left(\frac{p_i - p_j}{r_{ij}^2 \bar{\rho}_{ij}} - \frac{r_{ij}}{r_{ij}^2} \cdot \left\langle \frac{\nabla p}{\rho} \right\rangle_i \right) \right\} \quad (3.75)$$

Here, B_i denote the normalization matrix determined from solving of the system (3.71) and With $L_i = L(r_i)$ is the normalization matrix tensor given by the equation (3.65). The operation $\left\langle \frac{\nabla p}{\rho} \right\rangle_i$ is the first order consistent gradient formulation of the quantity $\left(\frac{p}{\rho}\right)$ given through the equation (3.66).

δ -SPH

δ -SPH term is an artificial diffusive term used in the context of weakly compressible SPH (WCSPH). It was first proposed by Molteni and Colagrossi [228], and has since been improved by Antuono et al [10] to deal better with free surface flow simulation, and then, it was applied in several works such as [9, 7, 216–218]. This term ($D^{\delta-SPH}$) is added into the right hand side of the continuity equation to reduce the spurious numerical high-frequency oscillations from the pressure field. The diffusive term $D^{\delta-SPH}$ is expressed at the particle i as

$$D_i^{\delta-SPH} = \delta h_i c_0 \sum_j^{n_b} \Psi_{ij} \nabla W_{ij} V_j \quad (3.76)$$

The vector Ψ_{ij} is written as

$$\Psi_{ij} = 2(\rho_i - \rho_j) \frac{r_{ij}}{r_{ij}^2} - \{ \langle \nabla \rho \rangle_i^L + \langle \nabla \rho \rangle_j^L \} \quad (3.77)$$

The symbol $\langle \nabla \rho \rangle_i^L$ denotes renormalized density gradient calculated through the equation (3.66).

The advantages and drawbacks of the using of the diffusive term $D^{\delta-SPH}$ into the SPH scheme are discussed in the work of Antuono et al. [8].

XSPH correction

The XSPH [230] is a simple method method used to prevent particle inter-penetration and to smooth the flow field in order to avoid a highly disordered configurations where negative pressures can be occurred. This is done by moving each particle with a velocity closer to the average one within its support kernel. The XSPH method modify the displacement equation of the governing equations system (3.1) as

$$\frac{dr_i}{dt} = v_i + \epsilon_{XSPH} \sum_j^{n_b} m_j \frac{v_{ji}}{\bar{\rho}_{ij}} W_{ij} \quad (3.78)$$

Where the constant ϵ_{XSPH} is taken within the range of 0 to 1. The commonly used value of ϵ is $\epsilon = 0.5$ [120, 293]. Liu and Liu [198] stated that $\epsilon = 0.3$ seems to be a good choice in simulating incompressible flows. $\bar{\rho}_{ij}$ denotes the average density between the particle i and j ($\bar{\rho}_{ij} = \frac{\rho_i + \rho_j}{2}$).

Artificial viscosity

The artificial viscosity is an additional term added to the momentum equation in order to improve the stability of numerical scheme. This term stops particles from approaching each other when they are very close or in other words, it prevents the inter-penetration of particles. This term was firstly introduced by Lucy [210] and then improved by Monaghan and Gingold [235] in order to ensure the linear and angular momentum conservation. The viscous term, denoted by Π_{ij} is added to the pressure terms in SPH momentum equations to give

$$\frac{dv_i}{dt} = - \sum_j^{n_b} m_j \left(\frac{p_i}{\rho_i^2} + \frac{p_j}{\rho_j^2} + \Pi_{ij} \right) \nabla W_{ij} \quad (3.79)$$

Or more generally

$$\frac{dv_i}{dt} = \sum_j^{n_b} m_j \left(\frac{\sigma_i}{\rho_i^2} + \frac{\sigma_j}{\rho_j^2} - \Pi_{ij} I \right) \nabla W_{ij} \quad (3.80)$$

Where I is the identity matrix and Π_{ij} is defined as

$$\Pi_{ij} = -\alpha \frac{\bar{h}_{ij} \bar{c}_{0ij}}{\bar{\rho}_{ij}} \left(\frac{v_{ij} \cdot r_{ij}}{r_{ij}^2 + \eta^2} \right) \quad (3.81)$$

Here $\eta^2 = (0.1h)^2$ is used to ensure a non-zero denominator, and $\bar{\rho}_{ij}$, \bar{h}_{ij} and \bar{c}_{0ij} denote the averages of the density, the smoothing length and the speed of sound of the particles i and j , respectively.

This artificial viscosity can be translated into a physical viscosity [245] in order to simulate viscous flows [247, 327, 4]. Therefore, The relation that links the physical kinematic viscosity ν and the parameters of artificial viscosity is given as

$$\nu = \frac{1}{2(n+2)} \alpha \bar{h}_{ij} \bar{c}_{0ij} \quad (3.82)$$

Where n represents the number of space dimensions.

It is found that the formulation of artificial viscosity Π_{ij} works well for shocks of moderate strength [235]. However, when Mach number becomes very high, this formulation will not serve the problem [245]. To deal with this problem, Monaghan [242] has added an extra term to the artificial viscosity (3.81)

$$\Pi_{ij} = \begin{cases} \frac{-\alpha \overline{c_{0ij}} \Phi_{ij} + \beta \Phi_{ij}^2}{\overline{\rho_{ij}}} & v_{ij} \cdot r_{ij} < 0 \\ 0 & v_{ij} \cdot r_{ij} \geq 0 \end{cases} \quad (3.83)$$

Where Φ_{ij} is read as

$$\Phi_{ij} = \frac{\overline{h_{ij}} v_{ij} \cdot r_{ij}}{r_{ij}^2 + \eta^2} \quad (3.84)$$

Here, α and β are free parameters that depend on the problem to be simulated. Good results have been obtained with the choice of $\alpha = 1$ and $\beta = 2$ [245]. This form is naturally deduced by considering the aspects of the dissipative term in shock solutions based on Riemann solvers [233]. It reads as

$$\Phi_{ij} = -K v_{sig} \frac{v_{ij} \cdot r_{ij}}{\overline{\rho_{ij}} r_{ij}} \quad (3.85)$$

With the parameter $K = 0.5$ and the v_{sig} denotes signal velocity and it is defined as

$$v_{sig} = c_{0i} + c_{0j} - \beta v_{ij} \cdot e_{ij} \quad (3.86)$$

Where $e_{ij} = \frac{r_{ij}}{r_{ij}}$ and $\beta = 4$.

Tensile instability and its correction

The tensile instability can be defined in the context of SPH method as a numerical artifact due to the attraction, clustering and clumping of the SPH particles. For WCSPH fluid simulation, the clumping of particle may be caused by the negative pressure resulting from the approximation of the equation of state [244, 255]. For the solid material simulation, the behavior of SPH particles mimic the one of the physical atoms of the solid material. Therefore, when the solid material is exposed to the compression, the SPH particles repel each other. Whereas, when the solid material is exposed to tension, the SPH particles form clumps which induce subsequently the tensile instability [255, 319]. Swegle et al [319] have performed Von-Neumann analysis to investigate the stability of SPH method. They concluded that the sufficient condition for an unstable growth is

$$W''\sigma > 0 \quad (3.87)$$

Where W'' is the second derivative of the kernel function W or also represents the slope of the first derivative of the kernel W' , and σ is particle stress that is by convention negative ($\sigma < 0$) in compression and positive in tension ($\sigma > 0$). The figure 3.5 summarizes schematically the stability regimes in the case of cubic B-spline kernel function. When the slope of the derivative of kernel function, the scheme is stable in tension and unstable in compression, and vis-versa.

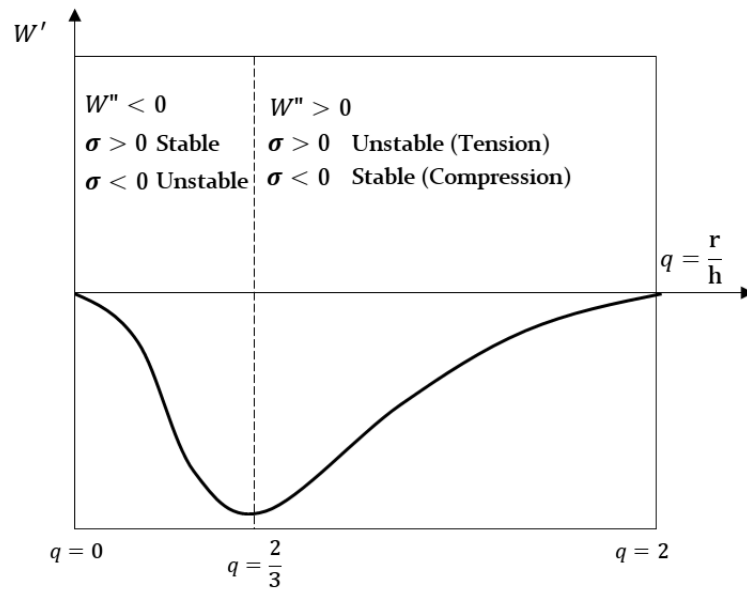


Figure 3.5 – Stability regimes for cubic spline kernel function.

several attempts have been made to remove the tensile instability using different approaches [55, 94, 280], the most successful one has been the artificial stress approach [244, 124]. The idea behind the artificial stress approach is to include small repulsive force between two neighboring particles when they are subjected to the attraction due to the tensile state in order to avoid the clumping and clustering of particles. By applying this approach, the momentum equation is modified from the equation (3.80) to the following one

$$\frac{dv_i}{dt} = \sum_j^{n_b} m_j \left(\frac{\sigma_i}{\rho_i^2} + \frac{\sigma_j}{\rho_j^2} - \Pi_{ij} I + f_{ij}^{n_{AS}} (R_i + R_j) \right) \nabla W_{ij} \quad (3.88)$$

Where n_{AS} is an exponent factor (is generally taken equal to 4) and f_{ij} is defined as

$$f_{ij} = \frac{W(r_{ij}, h)}{W(\Delta x_0, h)} \quad (3.89)$$

Where Δx_0 is the initial particles spacing. Assuming that computational problem is in 2D with planar Cartesian coordinates (x, y) , the components of the artificial stress tensor R are given by the following transformation expressions

$$\begin{cases} R_{xx} = R'_{xx} \cos^2 \theta + R'_{yy} \sin^2 \theta \\ R_{yy} = R'_{xx} \sin^2 \theta + R'_{yy} \cos^2 \theta \\ R_{xy} = \sin \theta \cos \theta (R'_{xx} - R'_{yy}) \end{cases} \quad (3.90)$$

Where R'_{xx} and R'_{yy} are the diagonal components of the stress tensor R' described in the coordinates frame (x', y') . The coordinates frame (x', y') are rotated with respect to (x, y) by an angle of θ which is given as

$$\tan 2\theta = \frac{2\sigma_{xy}}{\sigma_{xx} - \sigma_{yy}} \quad (3.91)$$

By this rotation, the stress tensor in the rotated frame becomes a diagonal tensor. Here, σ_{xx} , σ_{xy} and σ_{yy} denote the components of the Cauchy stress tensor wrote in the 2D original frame (x, y) . The diagonal component R'_{xx} of the artificial stress R' frame is given by [124]

$$R'_{xx} = \begin{cases} -\epsilon_{AS} \frac{\sigma'_{xx}}{\rho} & \text{if } \sigma'_{xx} > 0 \\ 0 & \text{otherwise} \end{cases} \quad (3.92)$$

Where ϵ_{AS} is a small parameter chosen as $0 < \epsilon_{AS} < 1$. The same rule applies for R'_{yy} with (xx) replaced by (yy) . The components of the Cauchy stress tensor σ' described in the rotated frame (x', y') can be expressed in terms of those in the original frame (σ) as follows

$$\begin{cases} \sigma'_{xx} = \cos^2 \theta \sigma_{xx} + 2 \cos \theta \sin \theta \sigma_{xy} + \sin^2 \theta \sigma_{yy} \\ \sigma'_{yy} = \sin^2 \theta \sigma_{xx} - 2 \cos \theta \sin \theta \sigma_{xy} + \cos^2 \theta \sigma_{yy} \end{cases} \quad (3.93)$$

3.8 Search neighboring particles

It is necessary to know the neighbors of any given particle i in order to approximate at that point the field of particle variables using SPH discretized formulations. The neighbors of the particle i are defined as all the particles j within the compact support $\Omega(kh)$ centered at that point. Since the connectivity between the computational particles does not exist, the distribution of particles changes in time as the continuum material evolves in space. Thus, the neighbors of all particles i requires to be searched continuously at each time step. The straightforward method to search the neighbors of any given particle i is to check its distance

with all other particles j and select those that have a distance less than or equal the radius of chosen kernel function (kh), in other words: j is neighbor of i only when $\|r_i - r_j\| \leq kh$. This searching method is so-called All-pair search [198]. This method has an algorithmic complexity of $O(N^2)$ which could be cost prohibitive in terms of computational time. Here N denotes the total number of particles within the global domain Ω .

The most popular alternative method to search particle neighbors is the so-called linked list method [229, 142]. This method is generally used when a constant smoothing length h is employed for all particles. In this method a temporary regular grid (square for 2D and cubic for 3D space) is overlaid on the problem domain. The size of grid cells is carefully selected to match with the radius of used kernel function kh . All particles are assigned to the corresponding cell via a linked list. This method restricts the search of the neighbors j of the particle i only in the surrounding cell of the particle i . This method is quite efficient in terms of computational time since it can present an algorithmic complexity of $O(N)$ [111]. The biggest difficulty with this problem is when a variable smoothing length h is used [117].

When a variable smoothing length is employed; the tree-algorithms for searching neighbors can be more efficient [111]. It works by creating ordered trees that correspond to the particle positions. Subsequently, the structure of trees will be used to find the neighboring particles. The complexity of this algorithm is of order $O(N \log(N))$ [135]. The operating principle of this algorithm is discussed in more detail in [12, 18, 134, 214].

3.9 Boundary conditions

3.9.1 Wall boundary conditions

The repulsive force technique proposed by Monaghan [243] is based on the use of Lennard-Jones forces between fluid particles and the walls. This technique is very simple to implement, however it may generate large numerical oscillation in the solid boundary [199, 205]. Later, softer version of repulsive force technique was developed by Rogers and Dalrymple [287] for modeling of tsunami waves with SPH method.

The Ghost Particles technique was first proposed by Libersky et al [195] to reflect a symmetrical condition using the opposite velocity on the reflecting image of particles. Colagrossi and Landrini [72] have extended this technique to be applied on rigid boundary by introducing into the ghost particles the density, pressure and velocity reflections. Morris et al [255] have proposed a technique to implement non-slip boundary conditions by introducing a virtual velocity into the ghost particles. This condition provides full compact support near

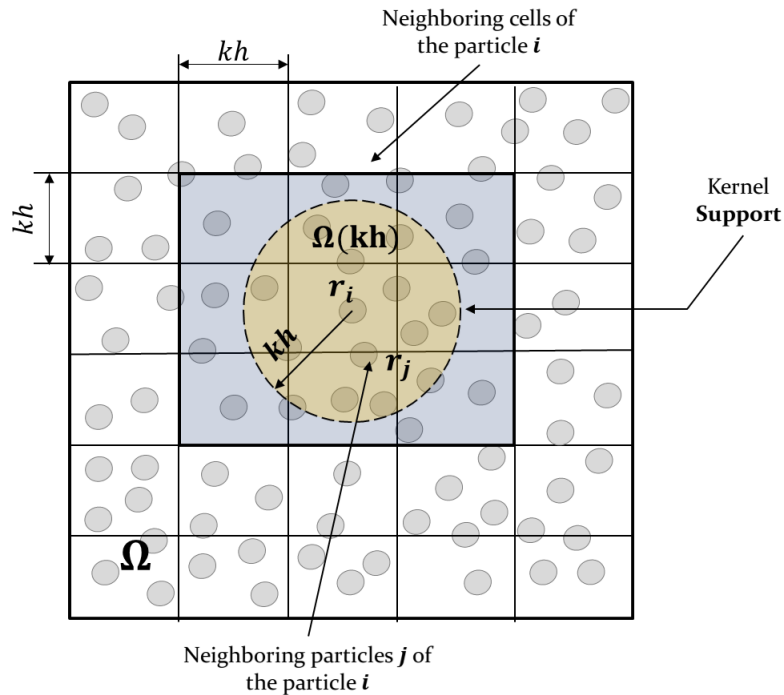


Figure 3.6 – The principle of linked list algorithm.

boundaries by using ghost particles. The drawback of this technique is presented in the treatment of complex geometries of boundaries (for instance the corners).

In the Dummy particles technique proposed by Takeda et al [322], fixed layers of particles are placed in order to represent the solid boundary on the one hand, and fill the compact support near it on the other hand. Comparing with Ghost Particle technique, this one can handle with complex geometrical shapes of boundaries. Issa et al [160] have extended this technique to investigate the turbulence modeling in the framework of SPH method. Adami et al [4] proposed a generalized formulations of the dummy particle technique by providing an accurate pressure approximation on the boundaries particles based on local force balance. Krimi et al [178] have extended this technique based on the work of Adami et al [4] to be applied in the context of multiphase fluid flow with different densities and viscosities.

The fixed Ghost Particles proposed by Marrone et al [216, 219], it is based on fixed layers of ghost particles placed around the of the solid boundary. On these particles the fluid properties are interpolated by using high order accuracy kernel function.

The coupled dynamic solid boundary treatment technique is introduced by [203], it consists of the use of two types of virtual particles, repulsive particles and fixed particles to represent the solid boundary in order to benefit from the advantages of each technique. The

repulsive particles are placed right on the solid boundary, whereas for the fixed particles are placed outside the solid boundary area.

A semi analytical wall boundary condition was developed in 2D by Ferrand et al [104] based on the works of Kulasegaram et al [179] and De Lefte et al [84]. In this method the wall boundaries are discretized using boundary elements (segments and vertices). This technique consists of overcoming the completeness of the kernel support near boundaries by computing surface integrals and using renormalization factor in the weakly compressible SPH (WCSPH) discrete interpolation. Macia et al [212] and Leroy et al [192] use this method in the context of incompressible SPH method (ISPH). Mayrhofer et [223, 222] extend this method to 3D applications. As it is stated by Valizadeh and Monaghan [336] this method gives a reasonable results, while it is difficult to be implemented and make the simulations more time consuming.

Fatehi and Manzari [100] have proposed a new technique for modeling wall boundary conditions with the use of one layers of solid particles, This condition is imposed in the accurate calculation of pressure on the wall to prevent the penetration of the particles in the wall. This technique performs well in situations of complex geometry. The method was successfully applied by Hashemi et al [133] in order to simulate the motion of rigid bodies in Newtonian fluid flows.

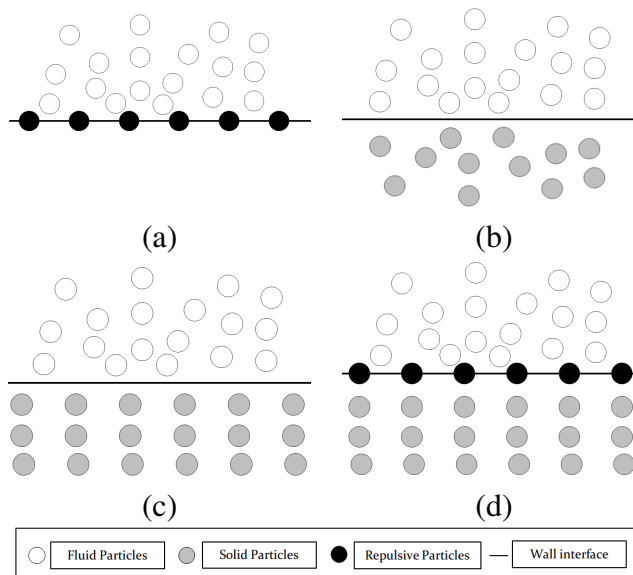


Figure 3.7 – Wall boundary conditions techniques: (a) repulsive force technique. (b) Ghost Particles technique. (c) Dummy particles Fixed Ghost Particles techniques. (d) Coupled dynamic boundary technique.

3.9.2 Inflow and OutFlow boundary conditions

Generally, the inflow and outflow boundary conditions are modeled using two buffer areas of particles placed alongside the inlets and outlets of the fluid domain [185, 146, 334, 101]. The width of the inflow and/or outflow buffer zones according to the flow direction is taken equal to or greater than the radius of support of the kernel function ($\geq kh$) in order to insure the completeness of support kernel (see figure 3.8).

As the particles within the inflow buffer zone move toward the fluid domain under prescribed velocities, they become fluid particle which evolve in accordance with the SPH equations. At the same time when the inflow particles enter the fluid domain, new alternative inflow particles are created in the inflow zone in a periodic way. Moreover, only the inflow particles effects fluid particles and not vice-versa.

In a similar manner , when fluid particles leave the fluid domain, they become outflow particles in outflow zone where the physical properties remained frozen in time except for their positions. The outflow particles will be deleted when they move out of outflow zone.

Leroy et al [191] and Ferrand et al [103] have extended the unified semi analytical wall boundary condition method [104] to be applied in the open boundaries conditions (inflow/outflow boundaries) in the framework of incompressible et weakly compressible SPH (ISPH and WCSPH). Here, no buffer zones are required for modeling inflow and outflow conditions. for more details about this method, we advise the reader to refer to [191, 103].

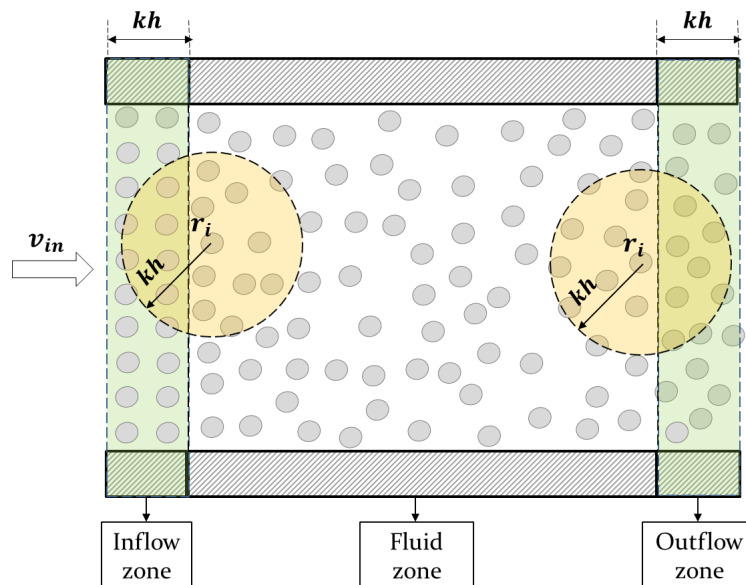


Figure 3.8 – Inflow and Outflow open boundary conditions.

3.9.3 Periodic boundary conditions

The periodic boundary condition is a classic open boundary condition in the fluid mechanics. This condition has a large range of applications in the context of SPH method as in [255, 4]. Particles near to a periodic boundary interact with the particles close to the complementary open periodic boundary on the other side of the domain. Therefore, the information is shared in both ways. Moreover, if a particle leaves the computational fluid domain through a periodic boundary, the same particle is reintroduced at the complementary boundary. When a support of kernel function of a particle is clipped by periodic open boundary, the SPH interpolation at this particle is recover by the remainder part of its clipped support applied at the complimentary open periodic boundary [121] (see figure 3.9). It is also possible to do the SPH interpolation by using buffer zones with a width equal to or greater than the radius of support kernel ($\geq kh$) at the open periodic boundaries that contain a mirror of computational fluid particles near of the complementary boundaries (see figure 3.10).

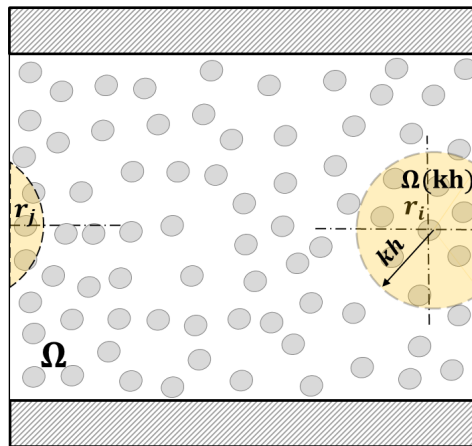


Figure 3.9 – Open periodic boundary condition with clipped kernel support method.

3.9.4 Free surface condition

The treatment of a free surface boundary requires the application of the kinetic and the dynamic boundary condition. The kinetic condition consists in ensuring that the initial free surface particles remain on the boundary, This condition is naturally fulfilled for both WCSPH and ISPH schemes, since the particles move according to their Lagrangian velocities [340]. The dynamic condition consists in imposing of null-pressure ($p = 0$) at the free surface. For WCSPH this condition is implicitly satisfied due to use of equation of state [70, 71, 263]. Wherese for the ISPH scheme, the free surface particles should first be detected correctly

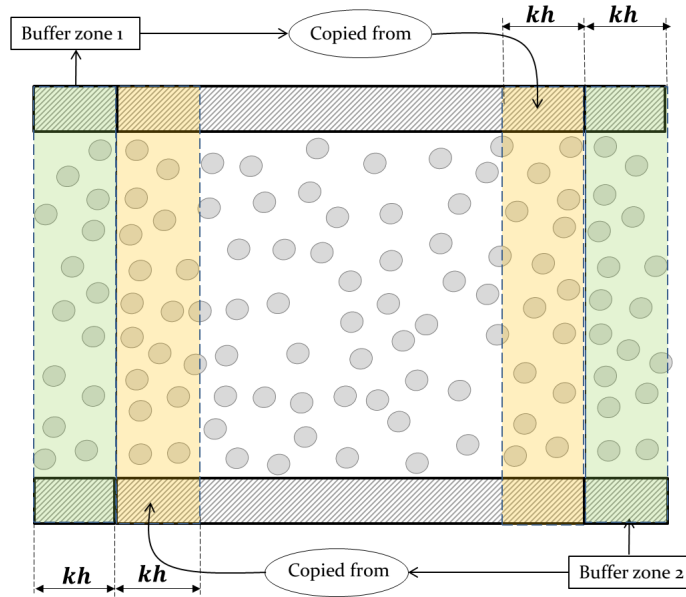


Figure 3.10 – Open periodic boundary condition with buffer zones method.

and thus imposed a null-pressure condition. Several methods have been used in the literature in order to detect the free surface particles. The traditional technique is done by evaluating the particle intermediate densities ρ^* , if the ($\rho_i^* < 0.99\rho_0$), then the particle i is at the free surface [303, 300, 171, 172, 170, 13]. A similar volume based technique was proposed in [295]. Other free surface detection technique was proposed in [188] based on the calculation of the divergence of particle position which is compared subsequently to a threshold value fixed accordingly to the number of space dimensions n . A simple purely geometrical-based technique was proposed in [16]. A more sophisticated and accurate free-surface detection algorithm based on SPH interpolations is proposed by Marrone [220]. The implementation of this algorithm does not require complex geometrical procedures.

3.10 Time integration algorithm

The SPH method transforms the physical continuum equations that are generally partial differential equations (PDEs) into ordinary differential equations (ODEs). Therefore, any time integration scheme of desired accuracy can be used. We can cite some algorithms among the most popular ones used in SPH, for instance : Predictor-Corrector algorithm [230]; velocity-Verlet algorithm [337, 4], Symplectic algorithm [245]; Leap-Frog algorithm [202, 48]; Runge–Kutta algorithm [161, 72, 60].

3.11 Stability conditions

In order to guarantee a stable SPH computation, several time-step criteria [242, 255, 80, 67] must be satisfied.

The CFL time-step condition for ISPH and EISPH [82] methods

$$\delta t \leq 0.25 \frac{h}{\max(\|v_i\|)} \quad (3.94)$$

The CFL time-step condition for WCSPH method

$$\delta t \leq 0.25 \frac{h}{\max(c_{0i}) + \max(\|v_i\|)} \quad (3.95)$$

When the artificial viscosity of equation (3.83) is taking into account, the time step will be subjected to new condition given by Monaghan [230]

$$\delta t \leq 0.3 \min \frac{h_i}{c_{0i} + 1.2(\alpha c_{0i} + \beta \max \phi_{ij})} \quad (3.96)$$

The viscous-diffusion condition

$$\delta t \leq 0.125 \frac{h^2}{\max(\frac{\mu_i}{\rho_{0i}})} \quad (3.97)$$

The body force condition

$$\delta t \leq 0.25 \left(\frac{h}{\|F^b\|} \right)^{1/2} \quad (3.98)$$

surface tension condition (in the case of interfacial multiphase SPH fluid flow) [40, 151]

$$\delta t \leq 0.25 \left(\frac{\min(\rho_k, \rho_l) h^3}{2\pi \sigma^{k-l}} \right)^{1/2} \quad (3.99)$$

Where σ^{k-l} denotes the surface tension coefficient between the fluid phases k and l .

The final time-step is taking as the minimum of all time-steps based on the above conditions.

Chapter 4

SPH : Modeling of interfacial multiphase fluid flows

Au cours des dernières décennies, la modélisation des écoulements de fluides multiphasiques a beaucoup intéressé les chercheurs, les scientifiques et les ingénieurs, en raison de sa large application dans le domaine industriel et dans la nature. Des modèles numériques utilisant le maillage ou sans le maillage sont disponibles pour traiter des problèmes de simulations des écoulements fluides multiphasiques via la discrétisation des équations de Navier-Stokes. Dans le contexte de l'approche avec maillage, des techniques de capture ou de suivi de l'interface entre les phases de fluide sont généralement requises. Les techniques les plus courantes comprennent la méthode VOF (Volume Of Fluid) [141], la méthode LS (level set) [266] et la méthode de suivi du front [261] [333]. Le principal inconvénient de ces techniques est la difficulté de prévoir l'évolution du mouvement de l'interface située entre les phases de fluide. La mauvaise prédiction de l'évolution de cette interface va causer par la suite une mauvaise approximation de sa courbure et son vecteur normal, ce qui provoque explicitement des erreurs en termes de forces de tension de surface. L'utilisation des algorithmes adaptés au raffinement du maillage [31] permettent de minimiser ces erreurs. Cependant, la génération d'une grande quantité de mailles conduit à un grand temps de calcul. La méthode SPH (Smoothed Particle Hydrodynamics) est une méthode sans maillage qui permet de gérer naturellement les interfaces entre les phases de fluide sans utiliser des algorithmes spécifiques. Cette méthode a été développée en 1977 pour réaliser des simulations en astrophysiques [118] [210]. Plus tard, en 1988, elle a été appliquée à la simulation des écoulements de fluides [241]. Depuis ce moment, la méthode SPH a reçu beaucoup d'attention et de grandes améliorations ont été développées.

Dans le contexte de la méthode SPH, plusieurs formulations de tension de surface ont été développées pour traiter les problèmes d'écoulement de fluides multiphasiques. La plupart

d'entre elles sont basées sur la méthode Continuum Surface Force (CSF) développée par Brackbill et al [40] ou avec sa variante, la méthode Continuum Stress Surface (CSS) [180].

Les méthodes CSF et CSS ont été initialement développées dans le cadre de méthodes numériques utilisant le maillage. Morris [254] a étendu ces formulations pour des applications aux méthodes sans maillage, notamment la méthode SPH. Cependant, Hu et Adams ont rapporté dans [151] qu'une contribution de pression négative à la contrainte de tension de surface peut apparaître lorsque la formulation CSS est explicitement appliquée. Cette contribution de pression négative pourrait causer des problèmes d'instabilité près de l'interface des fluides, et ils ont proposé une modification de la formulation CSS afin de l'éliminer. Par la suite, cette formulation a été appliquée à de nombreux cas de fluides multiphasiques [150, 149, 128, 258]. Néanmoins, la formulation CSS ne remplit pas le caractère tangential du tenseur des contraintes de surface (tenseur de la pression capillaire) [127]. Une formulation alternative de la tension de surface pour SPH a été présentée dans [154, 324, 326]. Cette formulation considère les particules SPH comme des vraies particules fluides avec des forces attractives / répulsives imbriquées entre elles. La définition de ces forces pour reproduire les effets de la tension de surface a permis d'obtenir des résultats prometteurs dans plusieurs cas de test impliquant des gouttes et des écoulements à travers des milieux fracturés.

Dans ce travail, nous présentons une extension de la formulation de tension de surface proposée par Adami et al [2] pour qu'elle soit applicable dans le cas de simulation de plus de deux phases de fluide. Cette formulation est basée sur la méthode Continuum Stress Surface (CSS) et présente trois majeurs avantages. Premièrement, elle améliore la stabilité en utilisant une approximation consistante de premier ordre pour calculer l'opérateur de divergence. Deuxièmement, la modification proposée respecte le caractère tangential physique de la tension de surface. Troisièmement, la formulation proposée bénéficie de tous les avantages de la formulation d'Adami et al [2], et de plus, elle peut être appliquée à des simulations avec plus de deux phases de fluide. Ces avantages font de notre formulation de tension de surface une bonne alternative à celle proposée par Adams et Hu [151], qui est largement utilisée dans le contexte de la méthode SPH [150, 149, 128, 258]. Malheureusement, et de manière similaire à la formulation de [2], notre formulation ne conserve pas exactement le moment. Afin de permettre l'application du modèle SPH développé pour des problèmes d'écoulement multiphasique avec présence de paroi rigides, nous présentons également une modification des conditions aux limites des parois généralisées [4].

À la fin, nous présentons une extension de la technique d'amortissement numérique (Damping) présentée dans [4] pour stabiliser la phase initiale transitoire de simulation d'écoulement de fluide multiphase gravitationnelle.

In recent decades, modeling of multiphase fluid flows has been attracted a large interest from researchers, scientists and engineers, due to its large applications in natural and industrial fields. Numerical models in both Mesh-based and Meshless approaches are available to deal with multiphase fluid flows simulations problems via the discretization of Navier-Stokes equations. In the context of grid-based approach techniques for capturing or tracking the phase interface are usually required. The most common techniques include the VOF (Volume Of Fluid) method [141], the LS (level set) method [266] and the front tracking method [261] [333]. The main drawback of these techniques is the difficulty in predicting the evolution of a moving interface. The inaccurate prediction of the evolution of interface causes subsequently a wrong approximation of its curvature and normal vector which explicitly causes errors in terms of surface tension forces. The use of adaptive mesh refinement algorithms [31] can minimize these errors. However, the generation of a large amount of grid cells in these methods leads to a large computational time. The Smoothed Particle Hydrodynamics (SPH) method, is a meshless method that has the ability to deal with moving interfaces naturally, without using any algorithm for interface tracking. This method was first developed in 1977 to treat astrophysical simulations [118] [210]. Later, in 1988 it was applied to the simulation of fluid flows [241]. Since then, the SPH method has received lots of attention and large improvements have been developed.

In the context of SPH method, several surface tension formulations have been developed to deal with multiphase fluid flows problems. Most of them are based on the Continuum Surface Force (CSF) method developed by Brackbill et al [40] or with its variant, the Continuum Stress Surface (CSS) method [180]. CSF and CSS methods were initially developed for mesh-based applications. Morris [254] extended these formulations to meshless applications in the framework of the SPH method. However, Hu and Adams reported in [151] that a negative pressure contribution to the surface stress may appear when the CSS formulation is applied. This negative pressure contribution might cause instability problems near to the fluids interface, and they proposed a modification to the CSS formulation in order to eliminate it. Afterwards, this formulation was applied to many multiphase fluid flows applications [150, 149, 128, 258]. However, the CSS formulation does not fulfill the tangential character of the surface stress tensor (capillary pressure tensor) [127]. An alternative formulation of the surface tension for SPH was presented in [154, 324, 326]. This formulation consider SPH particles as real fluid particles with attractive/repulsive forces among them. Defining these forces to reproduce the effects of surface tension has been obtained promising results in several test cases involving drops and flows through fractured media.

In this work, we present an extension of the surface tension formulation proposed by Adami et al [2] to be applicable in the case of more than two fluid phases simulations.

It is based on the Continuum Stress Surface formulation (CSS) and presents three major advantages. First, it enhances the stability by using a first-order consistency approximation to calculate the divergence operator. Second, the proposed modification respects the physical tangential character of the surface tension. Third, the proposed formulation benefits from all the advantages of the formulation of Adami et al [2], and in addition, it can be applied to simulations with more than two fluid phases. These advantages make our surface tension formulation as a good alternative to the one proposed by Adams and Hu [151] which is widely used in the context of SPH method [150, 149, 128, 258]. Unfortunately, and similarly to the original formulation of [2], the formulation does not conserve exactly the total momentum. In order to allow the application of the developed SPH method to multiphase fluid flow wall-bounded problems, we also present a modification of generalized wall boundary conditions [4].

Finally, we present an extension of the damping technique presented in [4] to smooth the initial transient phase of gravitational multiphase fluid flow simulations.

4.1 Multiphase model

4.1.1 Governing equations

In this work we assume a weakly compressible viscous fluid flow in isothermal conditions. Under these hypothesis, the Navier-Stokes and displacement equations expressed in Lagrangian form read as

$$\begin{cases} \frac{d\rho}{dt} = -\rho \nabla \cdot v \\ \frac{dv}{dt} = \frac{1}{\rho} (-\nabla p + F^{Vis} + F^{ST}) + g \\ \frac{dr}{dt} = v \end{cases} \quad (4.1)$$

where $\frac{d(\cdot)}{dt}$ represents the material derivative following an infinitesimal fluid element. ∇ is the nabla operator (gradient), ρ , p , v , r and g represent density, pressure, velocity vector, position vector, and the gravitational acceleration vector, respectively. F^{Vis} and F^{ST} denote the viscous and surface tension forces, respectively.

The weakly compressible smoothed particle hydrodynamics approach (WCSPH) was used in this work [243]. In order to close the system (4.1) it is required the use of an equation of state (EOS) which explicitly defines the pressure from the density instead to solve the Poisson equation. In this work the isothermal equation of state [254] is used which is expressed as

$$p = p_r \left\{ \left(\frac{\rho}{\rho_0} \right) - 1 \right\} + p_b \quad (4.2)$$

where ρ_0 , p_r and p_b denote the reference density, the reference pressure, and the background pressure, respectively. For the linear constitutive equation of state given by equation(5.2) the reference pressure is a function of the reference density and reference speed of sound c_0

$$p_r = \rho_0 c_0^2 \quad (4.3)$$

The use of the physical speed of sound as a reference leads to a very small time step according to the stability conditions explained in 4.1.4. It is then a common practice to use an artificial speed of sound as a reference. Thus, following [254] and [308] the value of c_0 is determined here as

$$c_0^2 \geq \max \left\{ \frac{U_0^2}{\delta\rho}, \frac{\|g\|L_0}{\delta\rho}, \frac{\sigma}{\rho_0 L_0 \delta\rho}, \frac{\mu U_0}{\rho_0 L_0 \delta\rho} \right\} \quad (4.4)$$

Where U_0 , L_0 , μ and σ are the reference velocity, reference length, dynamic viscosity and surface tension coefficient, respectively. $\delta\rho$ denote the dimensionless density variation which is set to 1% ($\delta\rho = 0.01$).

In the case of multiphase fluid flows, the reference pressure is chosen to be identical for all fluid phases, following [72]. Therefore, the speed of sound in each phase will be different in such a way that the reference pressure for all fluid phases is conserved.

$$p_r = p_{r_1} = \dots = p_{r_{N_f}} \quad (4.5)$$

$$p_r = \rho_{0_1} c_{0_1}^2 = \dots = \rho_{0_{N_f}} c_{0_{N_f}}^2. \quad (4.6)$$

where the subscript N_f denotes the number of fluid phases. This condition enhances the numerical stability of the computations [72]. Hence, the choice of the artificial speed of sound c_0 is taken in such a way that both equations (5.4) and (5.6) are satisfied in all fluid phases.

For numerical problems involving single-phase free surface fluid flows, the background pressure is generally set to zero ($p_b = 0$). Furthermore, for simulations of single or multiphase confined fluid flows, the pressure is chosen as a positive value sufficient to guarantee the positivity of the calculated pressure field via the equation of state in order to avoid the tensile instability [218]. In this work, the numerical experiments show that the ideal background

pressure p_b is chosen as a function of the reference pressure and it is proportional to $0.05p_r$ (i.e : $p_b \propto 0.05p_r$).

4.1.2 Discrete form of governing equations

The smoothed particle hydrodynamics is a meshless method. It discretizes the physical space into many discrete elements, usually called particles, without any connectivity among them. This method is based on the approximation of any physical scalar (or vector) field using the convolution formulation. Numerically, it is performed by replacing the Dirac delta function with a regular smooth function, which is called kernel. This function must satisfy some conditions such as symmetry (even function), normalization, compactness of its support, among others. We refer the interested reader to [200] for more details. The kernel function used in this work is the quintic spline [253] defined in equation (4.7). This kernel was selected since it prevents a high disorder in the particle distribution [?]. The kernel function depends on a parameter h , called the smoothing length, which defines the domain of influence of the kernel function. In this work, the smoothing length h is a constant which is chosen relative to the initial inter-particle distance δx_0 ($h = 1.33\delta x_0$). The initial particle volume is taken as $V_0 = \delta x_0^d$, with d is the space dimension number. The mass of each particle i of different fluid phases is chosen to be constant and equal to $m = \rho_{0_{phase}} V_0$ during all the simulation time.

$$W(r, h) = \alpha_d \begin{cases} (3 - \frac{r}{h})^5 - 6(2 - \frac{r}{h})^5 + 15(1 - \frac{r}{h})^5 & 0 \leq \frac{r}{h} < 1 \\ (3 - \frac{r}{h})^5 - 6(2 - \frac{r}{h})^5 & 1 \leq \frac{r}{h} < 2 \\ (3 - \frac{r}{h})^5 & 2 \leq \frac{r}{h} < 3 \\ 0 & \frac{r}{h} \geq 3 \end{cases} \quad (4.7)$$

where $\alpha_d = \frac{1}{120h}$, $\alpha_d = \frac{7}{478h^2\pi}$ and $\alpha_d = \frac{3}{359h^3\pi}$ for 1D, 2D and 3D cases, respectively. r is the distance between two neighboring particles i and j

Hu and Adams [151] developed a formulation that exactly guarantees mass conservation. In this formulation, the continuity equation of the Navier-Stokes system (4.1), can be replaced by the expression

$$\rho_i = m_i \sum_j^{n_b} W_{ij} \quad (4.8)$$

where ρ_i and m_i are the density and the mass of the particle i , respectively. $W_{ij} = W(r_{ij}, h)$ is the Kernel function, $r_{ij} = r_i - r_j$ is the distance between the particle i and its neighbours j . The number of particles in the neighborhood of particle i is denoted as n_b .

This formulation is widely used in SPH codes, and it works very well in the case of confined fluid flow simulations and allows the use of high values of the CFL number. However, this formulation is very sensitive to the particle disorder. Small variations of the particle positions cause high fluctuations in the particle density and thus in pressure, specially in the case of gravitational fluid flows. In practice, this problem can be alleviated by an adequate redistribution and acceleration of the initial particle positions and velocities by using a damping technique. This will be detailed in Section 4.1.5.

$$\frac{dv_i}{dt} = \frac{1}{\rho_i} \left(-\nabla p_i + F_i^{Vis} + F_i^{ST} \right) + g_i \quad (4.9)$$

Following [2], the acceleration of the particle i due to the gradient of pressure is approximated as

$$\frac{1}{\rho_i} \nabla p_i = \frac{1}{m_i} \sum_j^{n_b} (V_i^2 + V_j^2) \widetilde{p}_{ij} \nabla W_{ij} \quad (4.10)$$

Where $V_i = \frac{m_i}{\rho_i}$ is the volume of particle i . The term $\left(\nabla W_{ij} = \frac{\partial W}{\partial r_{ij}} e_{ij} \right)$ is the gradient of the kernel function, and $e_{ij} = \frac{r_{ij}}{r_{ij}} = \frac{r_i - r_j}{r_{ij}}$ is the unit inter-particle vector.

The term \widetilde{p}_{ij} is defined to ensure the continuity of pressure even for the case of discontinuous density between fluid particles (for example, when they belongs to different phases). Following [150] this term reads as

$$\widetilde{p}_{ij} = \frac{\rho_j p_i + \rho_i p_j}{\rho_i + \rho_j} \quad (4.11)$$

The acceleration due to the viscous forces can be expressed as in [2]

$$\frac{1}{\rho_i} F_i^{Vis} = \frac{1}{m_i} \sum_j^{n_b} (V_i^2 + V_j^2) \widetilde{\mu}_{ij} \frac{v_{ij}}{r_{ij}} \frac{\partial W}{\partial r_{ij}} \quad (4.12)$$

Where $v_{ij} = v_i - v_j$ is the relative velocity between the particle i and j . The term $\widetilde{\mu}_{ij}$ is the inter-particle-averaged dynamic viscosity which is defined as

$$\widetilde{\mu}_{ij} = \frac{2\mu_i \mu_j}{\mu_i + \mu_j} \quad (4.13)$$

In equation (4.13), μ_i is the dynamic viscosity of the particle i .

This form of viscous acceleration conserves the linear momentum [2], and performs well in the case of short-time simulations. In this work we have chosen an alternative formulation [148] which conserves both angular and linear momentum in order to perform long-time simulations. This alternative formulation reads as

$$\frac{1}{\rho_i} F_i^{Vis} = \frac{\zeta}{m_i} \sum_j^{n_b} (V_i^2 + V_j^2) \widetilde{\mu}_{ij} \frac{v_{ij} r_{ij}}{r_{ij}^2} \nabla W_{ij} \quad (4.14)$$

Where $\zeta = d + 2$, and d is the space dimension number.

The surface tension force:

In the case of a two-phase fluid, a Continuum Surface Force (CSF) formulation [40] may be used to represent the surface tension force. This formulation describes the pressure-jump condition normal to the separation interface of the fluids. However, if more than two phases are present in the flow, the explicit use of this formulation becomes impractical in the context of SPH method.

Thus, an alternative formulation should be used in these cases. The Continuum Surface Stress (CSS) [180] is a tensorial formulation of the surface tension force equivalent to the CSF formulation given in equation (B.2). The CSS formulation can be expressed as a body force applied through a transition region of finite thickness. The size of this finite thickness is equal to the diameter of Kernel function (see figure 4.1)

Using the CSS formulation, the surface tension force is defined as

$$F_i^{ST} = \nabla \cdot \Pi_i \quad (4.15)$$

where Π_i defines the immiscible mixture surface stress tensor of the particle i (capillary pressure tensor). Assuming that the particle i belongs to the l fluid phase, then the mixture surface stress can be expressed as

$$\Pi_i = \sum_{k \neq l} \Pi_i^{kl} \quad (4.16)$$

In equation (4.16) Π_i^{kl} is the fluid surface stress tensor between phases k and l , r is defined as ($r = r_{ij} = \|r_i - r_j\|$).

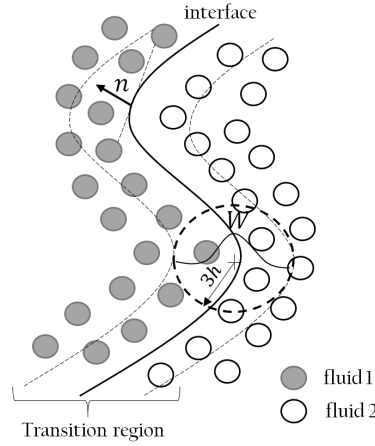


Figure 4.1 – Geometrical description of the principal parameter of surface tension formulation in the case of two immiscible fluids 1 and 2: interface, transition region, normal vector n . The thickness of the transition region is equivalent to the diameter of the kernel function ($6h$ for the quintic kernel function).

$$\Pi_i^{kl} = \frac{\sigma^{kl}}{\|\nabla C_i^{kl}\|} \left(\|\nabla C_i^{kl}\|^2 I - \nabla C_i^{kl} \otimes \nabla C_i^{kl} \right) \quad (4.17)$$

By assuming that the particle i belongs to the phase l , the gradient of the color function at the interface between two different phases k and l (∇C_i^{kl}) reads as [2]

$$\nabla C_i^{kl} = \frac{1}{V_i} \sum_j^{n_b} (V_i^2 + V_j^2) \widetilde{C}_{ij}^{kl} \nabla W_{ij} \quad (4.18)$$

The inter-particle-averaged color function \widetilde{C}_{ij}^{kl} is defined as

$$\widetilde{C}_{ij}^{kl} = \begin{cases} \frac{\rho_i}{\rho_i + \rho_j} & \text{if the particle } j \text{ belongs to the } k \text{ fluid phase} \\ 0 & \text{Otherwise} \end{cases} \quad (4.19)$$

The CSS formulation given by equations (4.16) and (4.17) is a variation of the CSF formulation (see Appendix ([Demonstration of the equivalence between CSS and CSF formulations](#))). In the CSS formulation, the interior efforts associated to the surface stress tensor Π are tangent to the interface, which is coherent with the propriety of surface tension force (the details are presented in the Appendix ([The internal forces associated to the surface stress tensor are tangent to the interface ?](#)))

Unfortunately, the direct application of the CSS formulation in the context of the SPH method, could lead to numerical instabilities [254, 151, 2]. In this work , we present a

modification to the CSS formulation in order to improve the stability of the CSS formulation in SPH methods. Based on the divergence formulation used in [2] for the calculation of the curvature of the interface, we modify the computation of the divergence of the capillary pressure tensor on equation (4.15). Thus, the modified discrete form of equation (4.15) is

$$F_i^{ST} = d \cdot \frac{\sum_j^{n_b} V_j \Pi_{ij} \nabla W_{ij}}{\sum_j^{n_b} V_j r_{ij} \frac{\partial W}{\partial r_{ij}}} \quad (4.20)$$

where we define the inter-particle surface stress tensor as $\Pi_{ij} = \Pi_i - \Pi_j$, d is the number of space dimensions and $r_{ij} = \|r_i - r_j\|$ is the inter-particle distance. Note that this formulation does not require a matrix inversion and gives a first-order consistency approximation to reproduce exactly the divergence of any linear field.

Note that with this formulation, the surface tension force does not exactly conserve the total momentum. However, It guarantees a good approximation even when a disordered particles distribution is presented or the support of the kernel function is not full with particles contained within the transition region. This force takes effect as a body one. This formulation takes all advantageous of the formulation proposed in [2], and in addition it can be applicable in the case of more than two-phases fluid flows simulation problems.

4.1.3 Wall boundary conditions

In this work, we also present a modification of the generalized wall boundary condition method proposed by [4] to deal with multiphase fluid flows. In this method, three layers of dummy particles must be added in the normal direction to the wall interface (see figure 5.4). The dummy particles are placed to represent the wall in such a way that it ensures the completeness of the support of kernel function, in order to obtain an accurate integration of the field variables near the wall interface. Free-slip or no-slip wall boundary conditions can be applied using this method. The free-slip boundary condition is applied by omitting the viscous interaction between the fluid particle with the adjacent dummy particles in the calculation of fluid viscous forces (equation 4.14). In the case of no-slip wall boundary condition, a virtual velocity v_w is imposed to the wall-dummy particle interacting with the fluid particle i in equation 4.14. This velocity is defined as

$$v_w = 2v_i - \tilde{v}_i \quad (4.21)$$

where v_i is the prescribed velocity of wall particle i and \tilde{v}_i denotes the interpolation of the smoothed velocity field of the fluid phase to the dummy particle position. The term n_f refers to the number of neighboring fluid particles j of the wall particle i .

$$\tilde{v}_i = \frac{\sum_j^{n_f} v_j W_{ij}}{\sum_j^{n_f} W_{ij}} \quad (4.22)$$

The pressure in the dummy-wall particle is calculated from the neighboring fluid particles j according to [4]

$$p_w = \frac{\sum_j^{n_f} p_j W_{wj} + (g - a_w) \sum_j^{n_f} \rho_j r_{wj} W_{wj}}{\sum_j^{n_f} W_{wj}} \quad (4.23)$$

where the term a_w represents a prescribed wall acceleration, if moving walls are present.

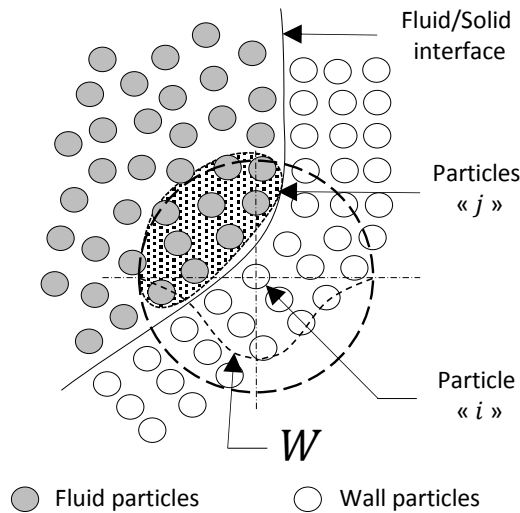


Figure 4.2 – Geometrical description of different parameters used in the generalized wall Boundary condition. Figure based on that presented in [4]

The method proposed in [4] computes the density of the dummy particle via the equation of state and is applicable for the case of single fluid with constant viscosity or in case of multiphase inviscid flows [235, 98, 273]. In the case of multiphase viscous flows where different viscosities are associated to each phase, this formulation becomes unusable because

of the ambiguity in the choice of the viscosity for the wall-dummy particles. This is specially noted when the neighboring particles belong to different fluid phases. Here we solve this ambiguity by using a method based on the fluid particle mirror similarity. We assume that each fluid particle *considers* all their wall-dummy neighbor particles as similar to it in terms of density, viscosity and volume. Using this approach we need to modify equations (5.31), (4.12) or (4.14) as follows

$$\frac{1}{\rho_i} \nabla p_i = \frac{1}{m_i} \sum_j^{n_b} \widetilde{\mathcal{P}}_{ij}^V \nabla W_{ij} \quad (4.24)$$

$$\frac{1}{\rho_i} F_i^{Vis} = \frac{1}{m_i} \sum_j^{n_b} \widetilde{\mu}_{ij}^V \frac{v_{ij}}{r_{ij}} \frac{\partial W}{\partial r_{ij}} \quad (4.25)$$

$$\frac{1}{\rho_i} F_i^{Vis} = \frac{\zeta}{m_i} \sum_j^{n_b} \widetilde{\mu}_{ij}^V \frac{v_{ij} r_{ij}}{r_{ij}^2} \nabla W_{ij} \quad (4.26)$$

Where $\widetilde{\mathcal{P}}_{ij}^V$ and $\widetilde{\mu}_{ij}^V$ are defined as

$$\widetilde{\mathcal{P}}_{ij}^V = \begin{cases} (V_i^2 + V_j^2) \frac{\rho_j p_i + \rho_i p_j}{\rho_i + \rho_j} & \text{if the particle } j \text{ is a fluid particle} \\ V_i^2 (p_i + p_j) & \text{if the particle } j \text{ is a wall particle} \end{cases} \quad (4.27)$$

$$\widetilde{\mu}_{ij}^V = \begin{cases} 2 (V_i^2 + V_j^2) \frac{\mu_i \mu_j}{\mu_i + \mu_j} & \text{if the particle } j \text{ is a fluid particle} \\ 2 V_i^2 \mu_i & \text{if the particle } j \text{ is a wall particle} \end{cases} \quad (4.28)$$

Note that the direct application of the proposed wall boundary conditions method can present spurious currents when the interfaces between the fluid phases includes a surface tension next to the wall boundaries. To deal with this issue, a special treatment as proposed in [3] can be added to this method. However, this problem is not addressed here since it is out of the scope of the present work.

4.1.4 Time integration

In this work a Predictor-Corrector scheme is proposed for time integration. An explicit Euler method is used to predict the velocity (\widetilde{v}_i^{n+1}) and the position (\widetilde{r}_i^{n+1}) of the particle i .

The corrected velocity at $n+1$ (v_i^{n+1}) is approximated by using the trapezoidal-rule, using predicted parameters $(\widetilde{\cdot})^{n+1}$ instead of the final ones $(\cdot)^{n+1}$. Note that, the density and pressure at time n (ρ^n, p^n) and the predicted values of velocity and position ($\widetilde{v}^{n+1}, \widetilde{r}^{n+1}$) are

used to predict the right hand-side of momentum equation $\left(\frac{d\tilde{v}_i}{dt}\right)^{n+1}$. The final position r_i^{n+1} is advected by the corrected velocity.

The following algorithm summarizes the prediction step.

$$\begin{cases} \tilde{v}_i^{n+1} = v_i^n + \delta t \left(\frac{dv_i}{dt}\right)^n \\ \tilde{r}_i^{n+1} = r_i^n + \delta t \left(\frac{dr_i}{dt}\right)^n \end{cases} \quad (4.29)$$

and the correction step is summarized as follows

$$\begin{cases} v_i^{n+1} = v_i^n + \frac{\delta t}{2} \left\{ \left(\frac{dv_i}{dt}\right)^n + \left(\frac{d\tilde{v}_i}{dt}\right)^{n+1} \right\} = \frac{1}{2} \{v_i^n + \tilde{v}_i^{n+1}\} + \frac{\delta t}{2} \left(\frac{d\tilde{v}_i}{dt}\right)^{n+1} \\ r_i^{n+1} = r_i^n + \delta t v_i^{n+1} \end{cases} \quad (4.30)$$

The final density (at time $n + 1$) is calculated as $\rho_i^{n+1} = m_i \sum_j^{n_b} W(\tilde{r}_{ij})^{n+1}$. Afterwards, the final pressure $p^{n+1} = p(\rho^{n+1})$ is calculated according to the equation of state (5.2), $p^{n+1} = p(\rho^{n+1})$.

The superscripts n and $n + 1$ refers to the time step, whereas $\{\tilde{\cdot}\}$ refers to the predicted physical parameter $\{\cdot\}$. For more details about the use of this scheme in the context of interfacial multiphase SPH model please see the Appendix ([Pseudo-code of SPH interfacial multiphase model](#)).

To ensure the stability of the method, the time step (δt) must be chosen to fulfill the kinetic, viscous, body force and surface tension conditions [246] [41]

$$\delta t = CFL \frac{h}{\max(c_{0_i}) + \max(\|v_i\|)} \quad (4.31)$$

$$\delta t \leq 0.125 \frac{h^2}{\max(\frac{\mu_i}{\rho_{0_i}})} \quad (4.32)$$

$$\delta t \leq 0.25 \left(\frac{h}{\|g\|}\right)^{1/2} \quad (4.33)$$

$$\delta t \leq 0.25 \left(\frac{\min(\rho_k, \rho_l) h^3}{2\pi\sigma^{k-l}}\right)^{1/2} \quad (4.34)$$

By using the density summation formulation (equation 4.8) with this time integration scheme, the simulations were stable with CFL numbers equal to one. In the numerical simulations presented here, a value of $CFL = 1$ is employed.

4.1.5 Damping strategy for multiphase fluid flow

In the framework of weakly compressible fluid flows, the accuracy on the determination of the pressure field using an equation of state depends on the density estimation. Here, the density of the particles is updated using the equation (4.8). It becomes obvious that a good estimation of the position of the particles is crucial to obtaining a good approximation of the pressure.

In this work, an initial regular lattice distribution of particles is chosen to perform the simulation. However, in the context of gravitational fluid flow problems, the use of the density summation formulation (equation (4.8)) to update density (and thus the pressure with equation (5.2)) in a regular distribution particles may spoil the imposed initial hydrostatic pressure and cause spurious high-frequency oscillations. In single fluid flow formulations, such artifacts can be reduced using a damping technique during the initial transient of simulations [4, 247]. This damping smooths both the distribution and the velocity of the particles to mitigate the oscillations. In fact, we introduce a mitigation factor ($\xi_D(t) \leq 1$) which acts as a multiplication factor on the body force in the momentum equation (4.9) as well as in the wall pressure equation 5.50, to obtain a gradual introduction of the gravity force. The mitigation factor is only activated during the time T_D (damping time), and is defined as

$$\xi_D(t) = \begin{cases} \left(\sin \left(\frac{t}{T_D} - 0.5 \right) \pi + 1 \right) & t \leq T_D \\ 1 & t > T_D \end{cases} \quad (4.35)$$

Note that other expressions are possible instead of 4.35, as for example, the Hill equation [115].

Unfortunately, these damping techniques [4, 247] are not applicable in the case of the simulation involving gravitational multiphase flows. This is due to the difference in density between the fluid phases (buoyancy force), which generates a considerable motion of the particles during the damping period. To extend the application of this technique to gravitational multiphase fluid flow simulations, a new strategy must be defined. In this work, all the physical properties of all fluid phases (reference density, viscosity, mass ...) are set to be equal to those of the heavier phase during the damping procedure, in order to avoid

any motion due to the different properties between the phases. This technique allows the particles to be slightly redistributed and accelerated in order to reach a good estimation of the initial hydrostatic pressure and velocity. After the damping time, the real physical properties must be assigned again to each phase, and the calculation procedure continues as usual. The reader is referred to the Appendix ([Pseudo-code of SPH interfacial multiphase model](#)) for more details about the use of this technique in the case of interfacial multiphase fluid flow simulations.

4.2 Conclusion

In this work, a consistent smoothed particle hydrodynamics model for multiphase flows is proposed. The model includes a surface tension formulation which ensures the tangential properties of the tensor surface stress and improves the stability of the numerical method. The numerical stability is improved through the use of a divergence operator with first-order consistency and also with a damping technique that avoids the numerical issues due to the transients on initial conditions. A modification of the generalized wall boundary conditions that allows its use for the simulation of wall-bounded multiphase fluid flows is also presented.

Chapter 5

SPH : Modeling of water-soil interactions using a multiphase approach

L'analyse des interactions sol-eau joue un rôle important dans l'évaluation et l'atténuation de nombreux problèmes environnementaux et géotechniques, tels que l'érosion des sols, l'érosion des structures offshore, les tsunamis générés par les glissements de terrain et leurs effets sur les structures adjacentes. La simulation numérique est considérée comme un outil puissant pour l'analyse de ces problèmes. Les problèmes d'interaction sol-eau sont de nature multi-composantes et se caractérisent généralement par des grandes déformations. Les méthodes numériques utilisant le maillage (éléments finis, volumes finis ou différences finies) sont difficilement applicables à ces problèmes en raison de l'enroulement, de la torsion et de la distorsion excessifs du maillage qui peuvent se produire.

Une autre méthode numérique dite la méthode Smoothed Particle Hydrodynamics (SPH) est peut être utilisée. Cette méthode sans maillage est largement utilisée pour simuler des problèmes à grandes déformation. La méthode SPH a été initialement développée en 1977 pour des applications astrophysiques [118] [210]. Plus tard, en 1988, elle a été appliquée à la simulation des écoulements de fluide [241]. Depuis, la méthode SPH a été largement utilisée et a connu beaucoup d'améliorations [234].

Dans le contexte de la méthode SPH, quatre approches sont généralement utilisées dans la littérature pour modéliser les interactions sol-eau. Dans chacune de ces quatre approches, l'écoulement fluide est modélisé en utilisant les équations de Navier-Stokes ou alternativement les équations d'Euler avec une viscosité artificielle. La différence entre les quatre approches repose sur la méthode utilisée pour la modélisation du sol.

Dans la première approche, le sol est considéré comme un solide rigide. Ceci est généralement utilisé lorsque le sol est moins exposé à la déformation, et également lorsque l'analyse se concentre uniquement sur le comportement de l'eau résultant du mouvement de

masse du sol. Les vagues impulsives générées par le glissement de terrain est le phénomène le plus modélisé en utilisant cette approche.

La deuxième approche est basée sur la modélisation du sol sous forme de fluide Newtonien (le sol est considéré comme un fluide à très haute viscosité) à l'aide des équations de Navier-Stokes. Cette approche peut donner des résultats acceptables seulement lorsqu'une valeur précise de viscosité est utilisée pour le sol. Cependant, les résultats donnés par cette approche ne sont pas très précis dans certains problèmes car aucune propriété physique du sol n'est introduite dans le modèle. Schwaiger et al [294] ont utilisé cette approche pour simuler le tsunami causé par glissement de terrain subaérien de 1958 à Lituya Bay (Alaska) [225].

Dans la troisième approche, un modèle de comportement élasto-plastique est utilisé pour décrire le sol. Le principal avantage de cette approche, comparée aux approches précédentes mentionnées ci-dessus, est que les propriétés physiques du sol utilisées dans ce modèle, comme le coefficient de Poisson ν , le module de Young E , la cohésion c , l'angle de frottement ϕ , sont réalistes. Cependant, le mouvement des particules de sol et d'eau est résolu séparément en utilisant différents modèles SPH (modèle de Navier-Stokes pour l'eau et un modèle de comportement élasto-plastique pour le sol) qui conduit à un couplage faible entre le sol et l'eau. Un traitement spécial est nécessaire pour le couplage. Cette approche a été appliquée à plusieurs problèmes géotechniques tels que les vagues d'eau générées par un glissement de terrain [306], des simulations de la fouille par un jet d'eau sur un sol sec et saturé, et l'érosion local sur des tumulus causée par un débordement d'eau provoqué par un tsunami [315].

La dernière approche est basée sur l'utilisation d'un modèle de fluide non Newtonien. Le sol est considéré comme une masse rigide au-dessous de certaine contrainte (appelée contrainte critique de déformation τ_y). Cette contrainte peut être une valeur constante égale à la cohésion du sol ($\tau_y = c$) pour les matériaux non frictionnels (Binghamiens / matériaux purement cohésifs) ou variable selon la pression, la cohésion c et l'angle de frottement (modèle rhéologique dépendant de la pression). Dans ce dernier cas, le sol est modélisé à l'aide de modèles de rupture plastique tels que les critères de Mohr-Coulomb [227] [75] ou Drucker-Prager [93]. Dans cette approche, le sol est considéré comme purement plastique avec une élasticité négligeable. L'avantage par rapport à tous les modèles précédents est le couplage fort entre le sol et l'eau, sans aucun traitement spécifique. Dans cette approche, les équations de Navier-Stokes sont utilisées pour les phases de l'eau et du sol. Cette approche a été utilisée pour simuler de nombreux problèmes géotechniques causés par les interactions sol-eau. Nous recommandons le lecteur à consulter [13, 52] pour des applications dans le

contexte de sol non frictionnel (matériau Binghamien) et [169, 299, 215, 108, 331, 345, 315] pour les applications qui se basent sur des modèles rhéologiques dépendant à la pression.

Dans ce travail, un modèle SPH faiblement compressible (WCSPH) a été développé pour traiter des problèmes d'écoulement multiphasiques. Le modèle est également capable de gérer les interactions sol-eau. Ici, le couplage entre le sol et l'eau est réalisé de manière forte et naturelle. Nous proposons un nouveau modèle rhéologique régulier dépendant de la pression, capable de simuler le comportement du sol (sol purement cohésif et frictionnel) et de l'eau (ou de tout autre fluide Newtonien). Le modèle proposé est nommé RBPMC - α_μ , il est basé sur une loi de comportement Binghamien plastique régularisée incluant le critère de rupture de Mohr-Coulomb. Ce modèle dépend d'un paramètre constant positif (α_μ), qui régularise le modèle ainsi qu'il permet de contrôler le pas de temps de la simulation.

De plus, nous proposons une version modifiée du terme diffusif artificiel ($D^{\delta-SPH}$) introduit dans [10] dans le contexte d'hypothèses d'écoulement faiblement compressible, pour atténuer les oscillations numériques à haute fréquence (parasitiques). Cette modification ($D^{\delta-MSPH}$) nous permet d'étendre la formulation $D^{\delta-SPH}$ à des problèmes des écoulements multiphasiques avec une loi de comportement incluant le critère de rupture de Mohr-Coulomb.

The analysis of soil-water interactions plays an important role for the assessment and mitigation of many environmental and geotechnical problems, such as soil erosion, scouring around offshore structures, landslide-generated tsunamis and their effect on reservoirs and adjacent structures ... and so on. Numerical simulation is considered as a powerful tool for the analysis of these problems. soil-water interaction problems are of a multi-component nature, and they are generally characterized by large deformations. Mesh-based numerical methods (Finite element, Finite Volume or Finite Difference) are hardly applicable in these problems due to the excessive winding, twisting and distortion of the mesh that may happen.

An alternative numerical method is the Smoothed Particle Hydrodynamics method (SPH). This meshless method is widely used to deal with the simulation of large deformation problems. SPH was first developed in 1977 for astrophysical applications [118] [210]. Later, in 1988 it was applied to the simulation of fluid flows [241]. Since then, the SPH method was widely used and got lots of improvement [234].

In the context of SPH method, four approaches are generally used in the literature to model soil-water interactions. In all of these four approaches, the water flow is modeled using Navier-Stokes equations or, alternatively, Euler equations with an artificial viscosity. The difference between the four approaches relies on the method used for soil modeling.

In the first approach, the soil is considered as a rigid solid. This is used generally when the soil is less exposed to the deformation, and also when the analysis is focused only on the water behavior resulting from the soil mass motion. The landslide generated impulsive water wave is the most modeled phenomenon using this approach [275, 346, 13] .

The second approach is based on the modeling of the soil as a Newtonian fluid (the soil is considered as a fluid with a very high viscosity) using Navier-Stokes equations. This approach can give acceptable results only when an appropriate Newtonian viscosity is used for the soil. However, the results given by this approach are not very accurate in some problems because no physical proprieties of soil is introduced to the model. Schwaiger et al [294] used this approach to simulate the 1958 subaerial landslide Tsunami at Lituya Bay (Alaska) [225].

In the third approach, an elasto-plastic constitutive model is used to describe the soil behavior. The main advantage of this approach, compared with the previous approaches mentioned above, is that the physical properties of soil used in the model, such as Poisson coefficient ν , Young modulus E , Cohesion c , angle of friction ϕ , are realistic. However, the motion of soil and water particles is solved separately using different SPH models (Navier-Stokes model for Water and an elasto-plastic constitutive model for soil) which leads to a weak coupling between the soil and water. A special treatment is needed for the coupling. This approach was applied on several geotechnical problems such as, the landslides generated

water wave [306], simulations of excavation by a water jet on dry and saturated soil [48] [344], and local scouring on rubble mound due to tsunami overflow [315].

Finally, the last approach is based on the use of a Non-Newtonian fluid model. The soil is considered as a rigid mass under certain stress (called yield stress τ_y). The yield stress can be a constant value equal to the cohesion of soil $\tau_y = c$ for non-frictional materials (Bingham/purely cohesive materials) or it can be variable depending on pressure, cohesion c and angle of friction (pressure-dependent rheology model). In the latter case, the soil is modeled using plastic strength models such as Mohr-Coulomb [227] [75] or Drucker-Prager [93] yield criteria. In this approach, the soil is considered as purely plastic with negligible elasticity. The advantage compared with all the previous models is the strong coupling between soil and water, without the need of any special treatment for the coupling. In this approach, the Navier Stokes equations are used for both water and soil phases. This approach has been used to simulate many geotechnical problems caused by soil-water interactions. We refer the reader to [13, 52] for applications in the context of non-frictional soil (Bingham soil) and to [169, 299, 215, 108, 331, 345, 315] for applications of the pressure-dependent rheology model.

In this work, a weakly compressible smoothed particle hydrodynamics (WCSPH) model for multiphase problems was developed. The model is also able to deal with soil-water interactions. Here, the coupling between the soil and water is achieved with a strong and natural manner. We propose a new regularized pressure-dependent rheology model that is capable of mimicking the behavior of soil (purely cohesive, and frictional soil) and water (or any other Newtonian fluid). The proposed model, named RBPMC- α_μ , is based on a Regularized Bingham Plastic constitutive law including Mohr-Coulomb failure criterion. This model depends on a positive constant parameter (α_μ), that regularizes the model and allows us to obtain greater time steps in the simulation.

Moreover, we propose a modified version of the artificial diffusive term ($D^{\delta-SPH}$) introduced in [10] in the context of weakly compressible flow hypothesis, for the mitigation of spurious numerical high-frequency oscillations. This modification ($D^{\delta-MSPH}$) allows us to extend the $D^{\delta-SPH}$ formulation to multiphase problems with constitutive law including Mohr-Coulomb failure criterion.

5.1 Governing equations and physical model

In this work, the soil material is assumed to be a fluid-like mass. The motion of soil and fluid phases are modeled using Navier-Stokes equations. It is assumed that the fluid phase is

weakly compressible, viscous and flow in isothermal conditions. With this assumptions, the Navier-Stokes and displacement equations can be written in a Lagrangian framework as

$$\begin{cases} \frac{d\rho}{dt} = -\rho \nabla \cdot v \\ \frac{dv}{dt} = \frac{1}{\rho} \left(\underbrace{-\nabla p + \nabla \cdot \tau}_{\nabla \cdot \sigma = \nabla \cdot (-pI + \tau)} \right) + g \\ \frac{dr}{dt} = v \end{cases} \quad (5.1)$$

where $\frac{d(\cdot)}{dt}$ represents the Lagrangian derivative. ∇ is the nabla operator, ρ , p , v , r and g represent density, pressure, velocity vector, position vector, and the gravitational acceleration vector, respectively. σ is the Cauchy stress tensor and τ is known as the deviatoric part of the Cauchy stress tensor (for any continuum material) or also called the viscous tensor (for fluids).

Under the weakly-compressible hypothesis, an explicit equation of state (EOS) is used to compute the pressure from the density. In this work we use the isothermal equation of state proposed in [254]

$$p = p_r \left\{ \left(\frac{\rho}{\rho_0} \right) - 1 \right\} \quad (5.2)$$

where ρ_0 and p_r denote the reference density and the reference pressure, respectively. The reference density is related to the reference speed of sound c_0 by the following equation

$$p_r = \rho_0 c_0^2 \quad (5.3)$$

The reference speed of sound c_0 can be determined as [254, 309]

$$c_0^2 \geq \max \left\{ \frac{U_0^2}{\delta\rho}, \frac{\|g\|L_0}{\delta\rho}, \frac{\mu_{eff}U_0}{\rho_0 L_0 \delta\rho} \right\} \quad (5.4)$$

Where U_0 , L_0 , μ_{eff} and σ are the reference velocity, reference length, and effective dynamic viscosity (apparent viscosity), respectively. The term $\delta\rho$ represent the ratio of density variation. In this work we set this value to 1% ($\delta\rho = 0.01$).

In the case of multiphase fluid flows, the reference speeds of sound are chosen to fulfill the equality of reference pressures for each fluid phase

$$p_r = p_{r_1} = \dots = p_{r_{N_f}} \quad (5.5)$$

$$p_r = \rho_{0_1} c_{0_1}^2 = \dots = \rho_{0_{N_f}} c_{0_{N_f}}^2. \quad (5.6)$$

where the subscript N_f denotes the number of fluid phases. This condition enhances the numerical stability of the computations [73].

The hypothesis of non-Newtonian fluids [360, 61] to model the behavior of geomaterials (soil, land, sediment, ...) is commonly accepted. A non-Newtonian fluid can withstand to deformation and remains rigid until a certain value of shear stress (called the yield stress (τ_y)) is reached. When this value is reached, these materials begin to flow.

The Bingham plastic model [33] is one of the simplest and more commonly used Non-Newtonian model. In this model, when the yield stress limit (τ_y) is exceeded, the material behaves as Newtonian fluid. Otherwise, it behaves as a rigid body. The constitutive law for a Bingham Plastic can be written in tensorial form as

$$\begin{cases} \tau = \left\{ \frac{\tau_y}{\|D\|_F} + \mu \right\} D & \|\tau\|_F \geq \tau_y \\ D = 0 & \|\tau\|_F < \tau_y \end{cases} \quad (5.7)$$

Where D is the rate of strain tensor and μ is the dynamic plastic viscosity which defines the viscosity of the fluid-like material (soil) after yielding.

The rate of strain tensor is defined as $D = \nabla v + (\nabla v)^T$, where ∇v denotes the velocity gradient tensor, and the superscript T denotes its transpose tensor.

The notation $\|\cdot\|_F$ refers to Frobenius norm. In equation (5.7) the yielding criterion of soil materials is defined using the Von Mises criterion [226]. Therefore, the quantities $\|D\|_F$ and $\|\tau\|_F$ can be expressed as follows

$$\|D\|_F = \left(\frac{1}{2} D : D \right)^{\frac{1}{2}} \quad (5.8)$$

$$\|\tau\|_F = \left(\frac{1}{2} \tau : \tau \right)^{\frac{1}{2}} \quad (5.9)$$

The discontinuity in the expression of the Bingham Plastic constitutive model (5.7) leads to considerable numerical difficulties; hence, smooth models are usually preferred and several different approaches have been used. For instance we cite the exponential model [270] and the Bercovier and Engelman (BE) model [30].

The Bingham model can be regularized using a control parameter ($\epsilon_r > 0$) for the approximation of the discontinuous model. The resulting model is similar to the one developed in [30].

$$\tau = \left\{ \frac{\tau_y}{\sqrt{\|D\|_F^2 + \varepsilon_r^2}} + \mu \right\} D \quad (5.10)$$

When $\varepsilon_r = 0$ in equation (5.10) with $\|D\|_F \neq 0$, we return to the original constitutive model (5.7). For this reason, the parameter ε_r must be chosen sufficiently small to insure the convergence between the regularized and original Bingham plastic models.

In the framework of Generalized Newtonian Fluids (GNL) [33, 343], the viscous stress tensor τ is given by the following constitutive equation:

$$\tau = \mu_{eff}(\|D\|_F)D \quad (5.11)$$

Where μ_{eff} is the effective viscosity.

From the equations (5.10) and (5.11) the effective viscosity can be expressed as:

$$\mu_{eff}(\|D\|_F) = \frac{\tau_y}{\sqrt{\|D\|_F^2 + \varepsilon_r^2}} + \mu \quad (5.12)$$

The choice of a stable simulation time step is related to the maximum value that the effective viscosity can reach in the rigid part of the material during the simulation period (see the viscous stability condition in section 5.2.3, equation (5.59)). The direct use of the model (5.10) or even the exponential [270] or the BE [30] models can greatly restrict the simulation time step.

In order to solve this problem, we propose a new regularized constitutive law that allows previously the choice and the control of the computational time step. Let us suppose that the maximum effective viscosity presented in the rigid region can be expressed linearly in terms of the yielding viscosity (plastic viscosity) μ as $\max(\mu_{eff}) = \alpha_\mu \mu$, with α_μ a positive constant.

It is obvious that the maximum value of μ_{eff} is reached in the undeformable regions ($\|D\|_F \rightarrow 0$). Therefore, from equation (5.12) the regularization parameter ε_r of the equation (5.10) results in $\varepsilon_r = \frac{\tau_y}{(\alpha_\mu - 1)\mu}$. Hence, we get

$$\tau = \left\{ \frac{\mu(\alpha_\mu - 1)\tau_y}{\sqrt{(\mu(\alpha_\mu - 1)\|D\|_F)^2 + \tau_y^2}} + \mu \right\} D \quad (5.13)$$

In figure 5.1, the regularized Bingham constitutive model (5.13) with different values of the constant $\alpha_\mu = \{10, 20, 100, 1000\}$ is plotted and compared with the discontinuous Bingham plastic model (5.7). We can clearly observe that the proposed regularized Bingham

plastic model converges to the original discontinuous model (5.7) when the constant α_μ is sufficiently large.

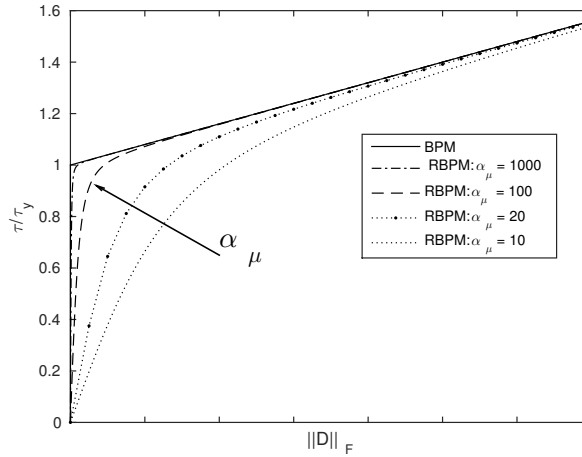


Figure 5.1 – Proposed Regularized Bingham Plastic Model (RBPM) with $\alpha_\mu = \{10, 20, 100, 1000\}$ and original Bingham Plastic Model (BPM) (solid line).

The regularized Bingham plastic model presented in this work (equation (5.13)) can be considered as the smooth version of the discontinuous bilinear model presented by Hosseini [145].

5.1.1 Determination of the yield stress

Now, the yield stress τ_y must be determined in order to close the model. At continuum level, the geomaterials are generally described using pressure-dependent yield criteria where the Von Mises criterion [226] cannot be satisfyingly represented because it does not include the pressure in its formulation. The Mohr-Coulomb [227] [75] or the Drucker-Prager [93] strength criteria are the most widely used for pressure sensitive materials. The difference between these criteria is that the Drucker-Prager criteria includes all the principal stresses (Three principal stresses in 3D space and two in 2D space) similarly to Von-Mises criterion, whereas the Mohr-Coulomb criterion includes only two principal stress (the maximum and minimum principal stress, similarly to Tresca criterion). Note that Mohr-Coulomb and Drucker-Prager criteria are identical in a two dimensional space.

The Mohr-Coulomb criterion is based on a linear failure envelope which combines the normal and shear stresses (σ, τ) on the failure plane by the relation

$$\tau = c - \sigma \tan \phi \quad (5.14)$$

Where c and ϕ denote the cohesion and the angle of internal friction (equivalent to the repose angle) of the material. Both parameters represent the physical properties of materials.

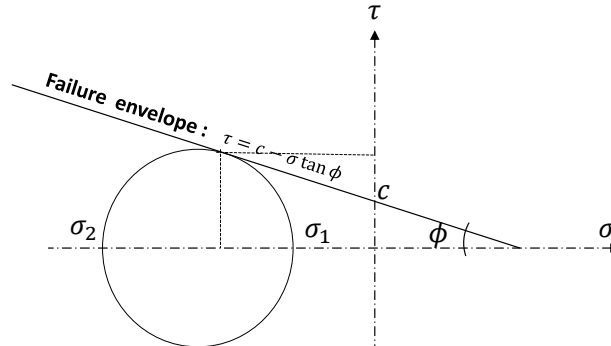


Figure 5.2 – Mohr-Coulomb yield criterion. The Mohr circle is based on the principal stresses σ_1 and σ_2 . The onset of yielding is occurring when the Mohr circle is tangent to the failure envelope.

The materials governed by the Mohr-Coulomb criterion for any given stress state fails (yields) when the Mohr's circle is tangent to the failure envelope (figure 5.2). By using trigonometric relations, an alternative form of the relation in terms of principal stresses can be expressed as

$$\frac{\sigma_1 - \sigma_2}{2} = -\frac{\sigma_1 + \sigma_2}{2} \sin \phi + c \cos \phi \quad (5.15)$$

The second invariant J_2 of the deviatoric stress tensor and the hydrostatic pressure p (negative mean stress) can be expressed in terms of principal stresses in two dimensions space as

$$\begin{aligned} J_2 &= \frac{1}{2} \tau : \tau \\ &= \frac{1}{2} tr(\tau^2) \\ &= \frac{1}{2} tr\left(\left\{\sigma - \frac{I_1}{2}I\right\}^2\right) \\ &= \frac{1}{2} \left(tr(\sigma^2) - \frac{I_1^2}{2}\right) \\ &= \frac{1}{4} (\sigma_1 - \sigma_2)^2 \end{aligned} \quad (5.16)$$

The notation $tr(A)$ presents the trace of the square matrix A . The terms σ_1 and σ_2 denote by convention the biggest and smallest principal stresses of the Cauchy stress tensor

σ ($\sigma_1 > \sigma_2$), respectively. While I_1 represents its first invariant that can be written in a two-dimensional space as

$$I_1 = \sigma_1 + \sigma_2 \quad (5.17)$$

The hydrostatic pressure p can be expressed in terms of the first invariant I_1 or principal stresses as

$$p = -\frac{I_1}{2} = -\frac{\sigma_1 + \sigma_2}{2} \quad (5.18)$$

Therefore, the Mohr-Coulomb criterion envelope can also be written in terms of hydrostatic pressure p and the second invariant J_2 as

$$\sqrt{J_2} = p \sin \phi + c \cos \phi \quad (5.19)$$

As explained previously, the Bingham Plastic material starts to yield under the Von Mises criterion when

$$\|\tau\|_F = \sqrt{J_2} = \tau_y \quad (5.20)$$

Hence, from the equations (5.20) and (5.19), the yielding stress τ_y of a material which yields under the Mohr-Coulomb criterion can be expressed as

$$\tau_y = p \sin \phi + c \cos \phi \quad (5.21)$$

Summarizing the previous developments, in this work the geomaterials have a Bingham Plastic behavior and yield under the Mohr-Coulomb criterion. This leads to a regularized constitutive law that we name RBPMC- α_μ

$$\tau = \left\{ \frac{\mu(\alpha_\mu - 1)(p \sin \phi + c \cos \phi)}{\sqrt{(\mu(\alpha_\mu - 1)\|D\|_F)^2 + (p \sin \phi + c \cos \phi)^2}} + \mu \right\} D \quad (5.22)$$

The use of the equation of state to determine the pressure from the density can lead to a negative pressure. For this reason an alternative positive pressure $\{p\}_+ = \max\{0, p\}$ is used instead of p . Thus, the RBPMC- α_μ model (5.23) reads as

$$\tau = \left\{ \frac{\mu(\alpha_\mu - 1)(\{p\}_+ \sin \phi + c \cos \phi)}{\sqrt{(\mu(\alpha_\mu - 1)\|D\|_F)^2 + (\{p\}_+ \sin \phi + c \cos \phi)^2}} + \mu \right\} D \quad (5.23)$$

The present RBPMC- α_μ constitutive law (equation (5.23)) can be specialized to other rheological models by changing the following parameters:

- Newtonian fluid (water, ...): set ($c = \phi = 0$) in equation (5.23) and use the Newtonian dynamic viscosity instead of μ ;
- Cohesionless or purely frictional materials: set $c = 0$ in equation (5.23) ;
- Bingham fluid (non-frictional/purely cohesive materials): use the value of yielding stress τ_y as material cohesion c ($\tau_y = c$) and set the frictional angle to zero ($\phi = 0$).

In this way, only the presented RBPMC- α_μ constitutive model is used to describe all fluid and/or fluid-like materials involved in the test cases presented here. Note that the flexibility of our formulation makes very easy its implementation in existing codes.

In some previous works [159, 251], the yielding stress of purely frictional materials is generally taken as $\tau_y = p \tan \phi$ which is equivalent to the presented model for small values of frictional angle ϕ . However, for greater values of ϕ this formulation becomes impractical and can distort the simulation results [91]. Note that this problem is avoided with the use of the formulation given by equation (5.23).

The effective viscosity can be expressed in term of pressure, cohesion, and frictional angle as

$$\mu_{eff}(\|D\|_F) = \frac{\mu(\alpha_\mu - 1) (\{p\}_+ \sin \phi + c \cos \phi)}{\sqrt{(\mu(\alpha_\mu - 1)\|D\|_F)^2 + (\{p\}_+ \sin \phi + c \cos \phi)^2}} + \mu \quad (5.24)$$

For the simulation of the granular materials the dynamic plastic viscosity can be calculated using the $\mu(I)$ rheology method [166] , as it is considered in [54, 159]. It is shown in the work of Ionescu et al [159] that the choice of constant value of the plastic viscosity does not change much the results if it is within the good interval comparing with those obtained from value of the $\mu(I)$ rheology [166]. In this work the plastic viscosity is chosen to be a constant value.

In the case of the modeling soil-water interactions ,the plastic viscosity is set equal to the viscosity of the water [291].

5.2 Discrete form of governing equations

We use as in previous chapter the quintic spline kernel function [253] to perform the SPH approximation of physical field. This kernel function prevents a high disorder in the particle distribution. The smoothing length h is chosen constant and relative to the initial inter-particle distance δx_0 ($h = 1.33\delta x_0$) as in previous chapter.

In this work, the discrete form of the continuity equation of system (5.1) is expressed as

$$\frac{d\rho_i}{dt} = \rho_i \sum_j^{n_b} V_j v_{ij} \nabla W_{ij} = \rho_i \sum_j^{n_b} \frac{m_j}{\rho_j} v_{ij} \nabla W_{ij} \quad (5.25)$$

Where $V_i = \frac{m_i}{\rho_i}$ is the volume of particle i . The term $(\nabla W_{ij} = \frac{\partial W}{\partial r_{ij}} e_{ij})$ is the gradient of the kernel function, and $e_{ij} = \frac{r_{ij}}{r_{ij}} = \frac{r_i - r_j}{r_{ij}}$ is the unit inter-particle vector. The initial particle volume is taken as $V_0 = \delta x_0^d$, with d is the space dimension number. The mass of each particle i of different fluid phases is chosen to be constant and equal to $m = \rho_{0_{Phase}} V_0$ during all the simulation time.

This formulation is accurate for the case of more than one fluid phase and specially with large density ratios as is reported in [69, 246].

In the context of a weakly compressible flow hypothesis, the determination of the hydrostatic pressure via the equation of state can originate numerical artifacts, in the form of spurious numerical high-frequency oscillations in the pressure field. This is specially critical when the Mohr-Coulomb criterion is used. In order to mitigate this, Molteni and Colagrossi [228] proposed the addition of an artificial diffusive term $\mathcal{D}^{\delta-SPH}$ to the right hand side of the continuity equation (5.25), resulting in

$$\frac{d\rho_i}{dt} = \rho_i \sum_j^{n_b} \frac{m_j}{\rho_j} v_{ij} \nabla W_{ij} + \mathcal{D}_i^{\delta-SPH} \quad (5.26)$$

with

$$\mathcal{D}_i^{\delta-SPH} = \delta h_i c_0 \sum_j^{n_b} \Psi_{ij} \nabla W_{ij} V_j \quad (5.27)$$

and Ψ_{ij} is defined as

$$\Psi_{ij} = 2 (\rho_i - \rho_j) \frac{r_{ij}}{r_{ij}^2} \quad (5.28)$$

Unfortunately, the use of $\mathcal{D}^{\delta-SPH}$ method with equation (5.27) for multiphase fluid flows can generate important numerical issues at the interface between the phases. These issues are principally caused by the repulsive forces generated by the difference in density between the phases. In order to alleviate these problems, Fourtakas and Rogers [108] proposed to use the $\mathcal{D}^{\delta-SPH}$ formulation in the fluid phase and sediment phase independently. That is, only particles belonging to the same fluid phase are considered in the computation of $\mathcal{D}^{\delta-SPH}$. However, this strategy does not completely solve the numerical issues, specially in the case of simulations that present a low motion.

In this work, we propose a modified version of the $\mathcal{D}^{\delta-SPH}$ term, that is able to deal with single and multiphase fluid applications. The principal idea is to assume that all particles j neighbors of the particle i are part of the same phase as i (that is, they have the same density reference ρ_{0_i}), but they also conserve their original particle density ratio $\beta_{\rho_j} = \frac{\rho_j}{\rho_{0_j}}$ (see figure 5.3). Applying this assumption on the equation (5.28), we get:

$$\Psi_{ij}^{MSPH} = 2 (\beta_{\rho_i} - \beta_{\rho_j}) \rho_{0_i} \frac{r_{ij}}{r_{ij}^2} \quad (5.29)$$

Then, the multiphase diffusive term can be written as

$$\mathcal{D}_i^{\delta-MSPH} = \delta h_i c_0 \sum_j^{n_b} \Psi_{ij}^{MSPH} \nabla W_{ij} V_j \quad (5.30)$$

The value of the dimensionless parameter δ is chosen as ($\delta = 0.1$). This value is used in this work for all examples.

Note that the formulation of multiphase diffusive term of equation (5.30) returns the classical form (equation (5.27)) in single fluid phase problems.

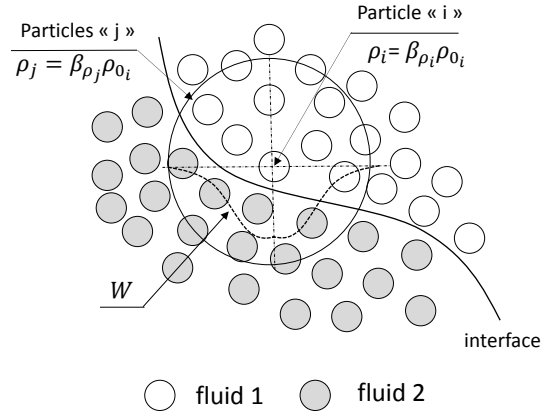


Figure 5.3 – The illustration of the hypothesis taken to calculate the diffusive term for multiphase fluid flow ($\mathcal{D}_i^{\delta-MSPH}$).

Using the modified formulation in equation (5.26), the value of the density, and thus of the pressure are significantly improved as demonstrated later via the example of Section 8.1.

The acceleration of the particle i due to the gradient of pressure is approximated following [2] as

$$\frac{1}{\rho_i} \nabla p_i = \frac{1}{m_i} \sum_j^{n_b} (V_i^2 + V_j^2) \widetilde{p}_{ij} \nabla W_{ij} \quad (5.31)$$

The term \widetilde{p}_{ij} is defined to ensure the continuity of pressure even for the case of discontinuous density between fluid particles (for example, when they belongs to different phases). Following [150] this term reads as

$$\widetilde{p}_{ij} = \frac{\rho_j p_i + \rho_i p_j}{\rho_i + \rho_j} \quad (5.32)$$

Using the same idea for the approximation of the divergence of the viscous tensor (deviatoric tensor) we obtain

$$\nabla \cdot \tau_i = \frac{1}{V_i} \sum_j^{n_b} (V_i^2 + V_j^2) \widetilde{\tau}_{ij} \nabla W_{ij} \quad (5.33)$$

where the inter-particle viscous tensor $\widetilde{\tau}_{ij}$ is defined as

$$\widetilde{\tau}_{ij} = \frac{\rho_i \tau_j + \rho_j \tau_i}{\rho_i + \rho_j} \quad (5.34)$$

The Taylor expansion of any quantity A around the position r_i can be expressed as

$$A(r_j) = A(r_i) + \nabla A(r_i)(r_j - r_i) + O(r_{ij}^2) \quad (5.35)$$

and ,

$$\nabla A(r_i) \approx \frac{A(r_i) - A(r_j)}{r_{ij}^2} (r_i - r_j) \approx \nabla A(r_j) \quad (5.36)$$

The rate of strain stress tensor is expressed in terms of the velocity gradient as $D = \nabla v + (\nabla v)^T$. Using equation (5.36) we conclude that

$$D(r_i) \approx D(r_j) \approx D \quad (5.37)$$

Equation (5.33) can be expressed using the equations (5.11) and (5.37) as follows:

$$\begin{aligned} \nabla \cdot \tau_i &= \frac{1}{V_i} \sum_j^{n_b} (V_i^2 + V_j^2) \frac{\rho_i \mu_{eff_j} D_j + \rho_j \mu_{eff_i} D_i}{\rho_i + \rho_j} \nabla W_{ij} \\ &= \frac{1}{V_i} \sum_j^{n_b} (V_i^2 + V_j^2) \frac{\rho_i \mu_{eff_j} + \rho_j \mu_{eff_i}}{\rho_i + \rho_j} D \nabla W_{ij} \end{aligned} \quad (5.38)$$

The term $(D \nabla W_{ij})$ can be simplified as :

$$\begin{aligned} D \nabla W_{ij} &= (\nabla v + (\nabla v)^T) \nabla W_{ij} \\ &= \frac{1}{r_{ij}^2} (v_{ij} \otimes r_{ij}) \nabla W_{ij} + \frac{1}{r_{ij}^2} (r_{ij} \otimes v_{ij}) \nabla W_{ij} \\ &= \frac{1}{r_{ij}^2} \{ v_{ij} (r_{ij} \cdot \nabla W_{ij}) + r_{ij} (v_{ij} \cdot \nabla W_{ij}) \} \end{aligned} \quad (5.39)$$

where \otimes denotes the outer product.

Finally, the divergence operator of the viscous tensor reads as

$$\nabla \cdot \tau_i = \frac{1}{V_i} \sum_j^{n_b} \left\{ \frac{V_i^2 + V_j^2}{r_{ij}^2} \right\} \frac{\rho_i \mu_{effj} + \rho_j \mu_{effi}}{\rho_i + \rho_j} \{ v_{ij} (r_{ij} \cdot \nabla W_{ij}) + r_{ij} (v_{ij} \cdot \nabla W_{ij}) \} \quad (5.40)$$

This obtained formulation is similar to that presented in [98, 352].

The effective viscosity is calculated using the equation (5.24). Assuming that the velocity vector in two-dimensional space is $v = [u \ w]^T$, the Frobenius norm of the rate strain $\|D\|_F$ can be expressed as

$$\|D\|_F = \sqrt{2 \left(\left(\frac{\partial u}{\partial x} \right)^2 + \left(\frac{\partial w}{\partial y} \right)^2 \right) + \left(\frac{\partial u}{\partial y} + \frac{\partial w}{\partial x} \right)^2} \quad (5.41)$$

In this work, the formulation developed by Adami and al [2] is adopted to approximate the space derivative of the velocity components. This formulation achieves a first order consistency approximation without the need for matrix inversion operations, contrary to the alternative version of Randles and Libersky [279]. The velocity components derivatives are expressed in 2D space as

$$\langle \nabla u \rangle = \left[\frac{\partial u}{\partial x} \ \frac{\partial u}{\partial y} \right]^T = 2 \frac{\sum_j^{n_b} V_j (u_i - u_j) \nabla W_{ij}}{\sum_j^{n_b} V_j r_{ij} \frac{\partial W}{\partial r_{ij}}} \quad (5.42)$$

$$\langle \nabla w \rangle = \left[\frac{\partial w}{\partial x} \ \frac{\partial w}{\partial y} \right]^T = 2 \frac{\sum_j^{n_b} V_j (w_i - w_j) \nabla W_{ij}}{\sum_j^{n_b} V_j r_{ij} \frac{\partial W}{\partial r_{ij}}} \quad (5.43)$$

The notation $\langle \cdot \rangle$ denotes the first order consistency approximation of the quantity $\{ \cdot \}$.

5.2.1 Modeling of the water suspended sediment

When water flows at a sufficient large velocity over a surface of sediment bed (soil), the sediment particles are picked up and transported on the surface, to be deposited again when the velocity of flow diminishes. This erosion process occurs when the shear stress generated by the frictional force of water flowing over the sediment overcomes the forces acting on the sediment grains (gravity, pressure, and viscosity forces). The simulation of this suspended load of sediment bed is not explicitly modeled using our immiscible multiphase SPH model detailed above. To deal with this problem, a transitional layer between the soil and water represented as a mixture phase are nested on the soil surface. The particles within this layer are treated as soil but with an altered mixture viscous proprieties. The easiest way to model this layer is to consider it as a Newtonian fluid. A simple relation is used to calculate the particle viscosity within the suspended sediment phase (ν_{mix}) [123, 299]

$$\nu_{mix} = \frac{\nu_l}{\sqrt{1 + c_s \frac{\rho_s}{\rho_l}}} \quad (5.44)$$

In equation (5.44), ν_l denotes the kinematic viscosity of the liquid (water) phase, whereas c_s , ρ_s and ρ_l present the volume fraction of the sediment phase, the density of sediment and liquid (water), respectively. Therefore, the dynamic viscosity of the mixture can be expressed as

$$\mu_{mix} = \frac{\mu_l (\rho_s c_s + (1 - c_s) \rho_l)}{\rho_l \sqrt{1 + c_s \frac{\rho_s}{\rho_l}}} \quad (5.45)$$

The volume fraction of the particle sediment i within the mixture phase c_{s_i} can be estimated as:

$$c_{s_i} = \frac{\sum_j^{n_b} k_s W_{ij}}{\sum_j^{n_b} W_{ij}} \quad (5.46)$$

Where $W_{ij} = W(r_{ij}, h)$ and k_s denotes the sediment particle indicator

$$k_s = \begin{cases} 0 & \text{if } j \text{ is a particle of the liquid phase} \\ 1 & \text{if } j \text{ is a particle of the sediment phase} \end{cases} \quad (5.47)$$

Note that the mixture viscosity μ_{mix} given by equation (5.45) is applied on the sediment particles of the mixture phase (suspended sediment load) when the sediment volumetric fraction $c_s < 1$. Otherwise, the viscosity of sediment particles is modeling using RBPMC- α_μ rheology explained above.

5.2.2 Wall boundary conditions

In this work, the rigid wall boundary condition method proposed by Krimi et al [178] is used. This method is presented as the modified version of generalized wall boundary condition method [4] to be well adapted with multiphase fluid flows. In this method, three layers of dummy particles must be added in the normal direction to the wall interface (see figure 5.4). The Free-slip or no-slip wall boundary conditions can be applied using this method. The free-slip boundary condition is applied by simply omitting the viscous interaction between the fluid particle with the adjacent dummy particles in the calculation of fluid viscous forces (equation (5.33)). In the case of no-slip wall boundary condition, a virtual velocity v_w is imposed to the wall-dummy particle interacting with the fluid particle i in equation (5.33). This velocity is defined as

$$v_w = 2v_i - \tilde{v}_i \quad (5.48)$$

where v_i is the prescribed velocity of wall particle i and \tilde{v}_i denotes the interpolation of the smoothed velocity field of the fluid phase to the dummy particle position. The term n_f refers to the of neighboring fluid particles j of the wall particle i .

$$\tilde{v}_i = \frac{\sum_j^{n_f} v_j W_{ij}}{\sum_j^{n_f} W_{ij}} \quad (5.49)$$

The pressure in the dummy-wall particle is calculated from the neighboring fluid particles j according to [4]

$$p_w = \frac{\sum_j^{n_f} p_j W_{wj} + (g - a_w) \sum_j^{n_f} \rho_j r_{wj} W_{wj}}{\sum_j^{n_f} W_{wj}} \quad (5.50)$$

where the term a_w represents a prescribed wall acceleration, if moving walls are present.

This method is based on the fluid particle mirror similarity, in other words it assumes that each fluid particle *considers* all their wall-dummy neighbor particles as similar to it in terms of density, viscosity and volume. Using this approach we need to modify equations (5.31), and (5.33) as follows

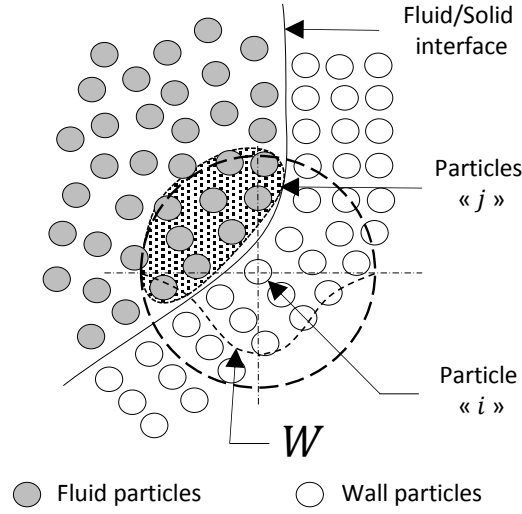


Figure 5.4 – Geometrical description of different parameters used in the generalized wall Boundary condition. Figure based on that presented in [4]

$$\frac{1}{\rho_i} \nabla p_i = \frac{1}{m_i} \sum_j^{n_b} \widetilde{\mathcal{P}}_{ij}^V \nabla W_{ij} \quad (5.51)$$

$$\nabla \cdot \tau_i = \frac{1}{V_i} \sum_j^{n_b} \frac{\widetilde{\mu}_{effij}^V}{r_{ij}^2} \{v_{ij} (r_{ij} \cdot \nabla W_{ij}) + r_{ij} (v_{ij} \cdot \nabla W_{ij})\} \quad (5.52)$$

Where \mathcal{P}_{ij}^V and $\widetilde{\mu}_{effij}^V$ are defined as

$$\widetilde{\mathcal{P}}_{ij}^V = \begin{cases} \left(V_i^2 + V_j^2 \right) \frac{\rho_j p_i + \rho_i p_j}{\rho_i + \rho_j} & \text{if the particle } j \text{ is a fluid particle} \\ V_i^2 (p_i + p_j) & \text{if the particle } j \text{ is a wall particle} \end{cases} \quad (5.53)$$

$$\widetilde{\mu}_{effij}^V = \begin{cases} \left(V_i^2 + V_j^2 \right) \frac{\rho_j \mu_{effi} + \rho_i \mu_{effj}}{\rho_i + \rho_j} & \text{if the particle } j \text{ is a fluid particle} \\ 2 V_i^2 \mu_{effi} & \text{if the particle } j \text{ is a wall particle} \end{cases} \quad (5.54)$$

5.2.3 Time integration

In this work a Predictor-Corrector scheme proposed by Krimi et al [178] is used for time integration. This scheme uses an explicit Euler method to predict the velocity (\widetilde{v}_i^{n+1}) and the position (\widetilde{r}_i^{n+1}) of the particle i .

Subsequently, the predicted velocities and positions are used to compute the final velocity at $n+1$ of the particle i (v_i^{n+1}), by using an implicit trapezoidal-rule to enhance its accuracy.

The position r_i^{n+1} is advected by the corrected velocity v_i^{n+1} . The density used for the velocity correction is the one approximated at the time step n . Finally, the density at time $n + 1$ (ρ^{n+1}) is computed from the predicted particles velocities (\tilde{v}^{n+1}) and positions (\tilde{r}^{n+1}) and also the density at previous time n (ρ^n) using equation (5.26).

The following algorithm summarizes the prediction step.

$$\begin{cases} \tilde{v}_i^{n+1} = v_i^n + \delta t \left(\frac{dv_i}{dt} \right)^n \\ \tilde{r}_i^{n+1} = r_i^n + \delta t \left(\frac{dr_i}{dt} \right)^n \end{cases} \quad (5.55)$$

and the correction step is summarized as follows

$$\begin{cases} v_i^{n+1} = \frac{1}{2} \{ v_i^n + \tilde{v}_i^{n+1} \} + \frac{\delta t}{2} \left(\frac{d\tilde{v}_i}{dt} \right)^{n+1} \\ r_i^{n+1} = r_i^n + \delta t v_i^{n+1} \\ \rho_i^{n+1} = \rho_i^n + \delta t \left(\rho_i^n \sum_j^{n_b} \frac{m_j}{\rho_j^n} \tilde{v}_i^{n+1} \nabla W(\tilde{r}_i^{n+1}) + \mathcal{D}_i^{\delta-MSPH}(\rho^n, \tilde{r}_i^{n+1}) \right) \end{cases} \quad (5.56)$$

The superscripts n and $n + 1$ refers to the time step, whereas $\{\tilde{\cdot}\}$ refers to the predicted physical parameter $\{\cdot\}$. Note that the term $\left(\frac{d\tilde{v}_i}{dt} \right)^{n+1}$ is computed using the predicted velocity \tilde{v}_i^{n+1} and the density of the previous time step ρ^n . This scheme is second order accurate as in [4, 243].

To ensure the stability of the method, the time step (δt) must be chosen to fulfill, the kinetic, the body force, and viscous conditions [245] [40]

$$\delta t \leq 0.25 \frac{h}{\max \{c_{0i} + \|v_i\|\}} \quad (5.57)$$

$$\delta t \leq 0.25 \left(\frac{h}{\|g\|} \right)^{1/2} \quad (5.58)$$

$$\delta t \leq C_\mu \frac{h^2}{\max \{v_{eff}\}} = C_\mu \frac{\rho_0 h^2}{\alpha_\mu \mu} \quad (5.59)$$

In previous works [352, 145, 303, 255], other authors assign the value of $C_\mu = 0.1$ in order to keep the simulation stable. In the present work, we have used the value $C_\mu = 0.2$, that preserves the stability and accuracy of the simulation when the viscous condition is

dominated. Thus, the use of the proposed formulation allows us the choice of a δt two times bigger than in previous SPH formulations.

The choice of the value of the positive constant α_μ depends on the applied efforts for each case. We select a value of α_μ as small as possible keeping the stability.

Note that the use of a very large value of the control parameter α_μ leads to a more accurate approximation of the rigid part of the soil, which is characterized by a maximum viscosity μ_{max} ($\mu_{max} = \alpha_\mu \mu$). However, this large value of α_μ leads to the use of a very small time step following the condition (5.59). Because of this, a good compromise for the value of α_μ must be found for each problem.

5.3 Conclusion

In this work, a weakly compressible multiphase Smoothed Particle Hydrostatic (SPH) model was developed in order to simulate soil, water (or any Newtonian fluid) and their interaction problems. A RBPMC- α_μ pressure-sensitive rheology model is proposed to model Newtonian fluids, purely frictional and cohesive (Binghamian) soils at the same time. Because of the developed rheology model is pressure-sensitive, a multiphase diffusive term called $D^{\delta-MSPH}$ is developed in order to damp the pressure oscillations due to the use of equation of state.

Chapter 6

Validation and application of SPH multiphase model

Ce chapitre est consacré à la démonstration de la capacité du modèle SPH présenté dans ce travail pour simuler des écoulements multiphasiques sous l'effet de gravité tout en négligeant la tension de surface. Les exemples abordés ici sont, l'évolution de deux phases de fluide stratifiées et l'instabilité de Rayleigh-Taylor. Le premier exemple n'est pas seulement fait pour examiner l'effet de stabilisation de la technique d'amortissement numérique (Damping), mais aussi pour valider les modifications proposées sur les conditions aux limites généralisées liées aux parois rigides lorsque les phases de fluide se rencontrent à la paroi. Le second exemple est fait pour comparer les résultats du modèle SPH multiphasique avec ceux utilisant la méthode Level-Set [128] et d'autres modèles SPH [238], ainsi qu'avec l'approche analytique présentée dans [187]. À la fin, nous présentons l'exemple de deux bulles montantes à travers une colonne d'eau en utilisant une résolution de particules plus élevée par rapport aux exemples précédents.

This chapter is devoted to demonstrating the ability of the presented SPH model for the simulation of multiphase flows under gravity effects neglecting surface tension. The examples addressed here are the evolution of the two-phase stratified fluid layers and the Rayleigh-Taylor instability (RTI). The first example is not only performed to examine the stabilization effect of the damping technique but also to validate the proposed modifications on generalized wall boundary conditions when the two fluid phases meet the solid boundaries. The second example, is done to compare the results of the presented SPH multiphase model with the ones using Level-Set [128] and other SPH [238] models, and also with the analytical approach presented in [187]. Finally, we present the example of two rising bubbles through a water column using a higher particle resolution than in the previous examples.

6.1 Vertical fluid column: Hydrostatic pressure condition

In this test, we set three configurations of two stratified fluid layers which have the same dimensions $([0, L] \times [0, 2L])$ (see figure 6.1) with different density ratio $\frac{\rho_2}{\rho_1} = 1$, $\frac{\rho_2}{\rho_1} = 2$ and $\frac{\rho_2}{\rho_1} = 4$ [190]. Each test case is investigated using three different particle resolutions $\{24 \times 49, 49 \times 99, 99 \times 199\}$. The subscripts 1 and 2 denote the upper and the lower fluids, respectively.

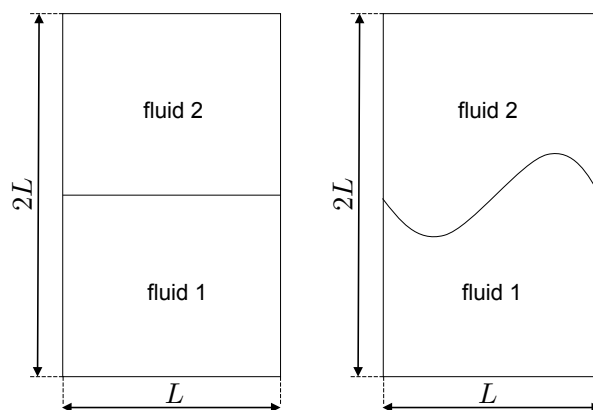


Figure 6.1 – Geometrical details of the initial configuration of vertical fluid column: The figure on the left describes the setup of the problem for the hydrostatic pressure condition. On the right, we show the initial state for the Rayleigh–Taylor instability test.

The half-length of the column is chosen as $L = 1$ [m], the interface between two fluids is located at the middle of the column (at height equals to L). The initial particle distribution is a regular lattice for each of the three resolutions considered. The density of the lighter fluid is $\rho_1 = 1$ [kg/m³]. The dynamic viscosity is chosen constant as $\mu_1 = \mu_2 = 0.1$ [Pas.s] for all phases in all the configurations. The vertical fluid column is assumed to be under the action

of an unit gravity ($g = (0, -1) [m/s^2]$). The reference speeds of sound are chosen according to the condition discussed in Section 4.1.2, resulting in the values of $c_{01} = 10 [m/s]$ for all configurations and $c_{02} = \{20, 14.142, 10\} [m/s]$ for the configurations of $\frac{\rho_2}{\rho_1} = 1$, $\frac{\rho_2}{\rho_1} = 2$ and $\frac{\rho_2}{\rho_1} = 4$, respectively. The background pressure is chosen as ($p_b = 0.05 p_r = 5 [Pa]$). The no-slip boundary condition is applied at all boundaries.

In order to show the efficiency of the damping technique to reach quickly the equilibrium state, the three configurations are tested with and without the damping technique for the coarsest particle resolution 24×49 . The value of the damping period is chosen as $T_D = 1 [s]$.

Figure 6.2 shows the effect of the damping technique on the simulation results for the pressure for the three configurations. We can see clearly that using the damping technique leads to lower amplitude of the pressure oscillations and to a faster convergence to the stabilized hydrostatic value. It is also observed that for the highest density ratio, the pressure has an important amplitude of oscillation. In this case, using the damping technique reduces the amplitude of the oscillations, but they are still important. This is principally due to the change of the physical parameters of the lighter fluid after the damping time. This change creates the jump in density, viscosity and mass and thus the pressure. Despite that, it converges faster and presents less oscillations than in the case of the simulation without using of the damping technique. A remedy to further reduce the oscillations is to increase the damping time (T_D). In the case of unit density ratio the oscillations of the pressure are very limited and reaches the stabilized value of the hydrostatic pressure very quickly.

After the stabilization of the pressure field using the damping technique, we compare the obtained pressure profiles using the present SPH model with the analytical ones for different density ratios and different particle resolutions (see figure 6.3). The numerical results agree well with the analytical ones.

In figure 6.4, we show the particle distribution and hydrostatic pressure at equilibrium for the three particle resolutions for the $\frac{\rho_2}{\rho_1} = 4$ case. Pressure isolines are plotted in order to check the hydrostatic pressure levels obtained with the three different resolutions. It is observed that the same pressure levels are reached for all the particle resolutions. This indicates the convergence of the presented numerical model for the simulation of gravitational multiphase fluid flows. Note that the background pressure $p_b = 5 [Pa]$ is included in the range of computed pressure variation.

From the results presented in figures 6.3 and 6.4 we can also conclude that the proposed modifications to the generalized wall boundary conditions method [4] (see section 4.1.3)

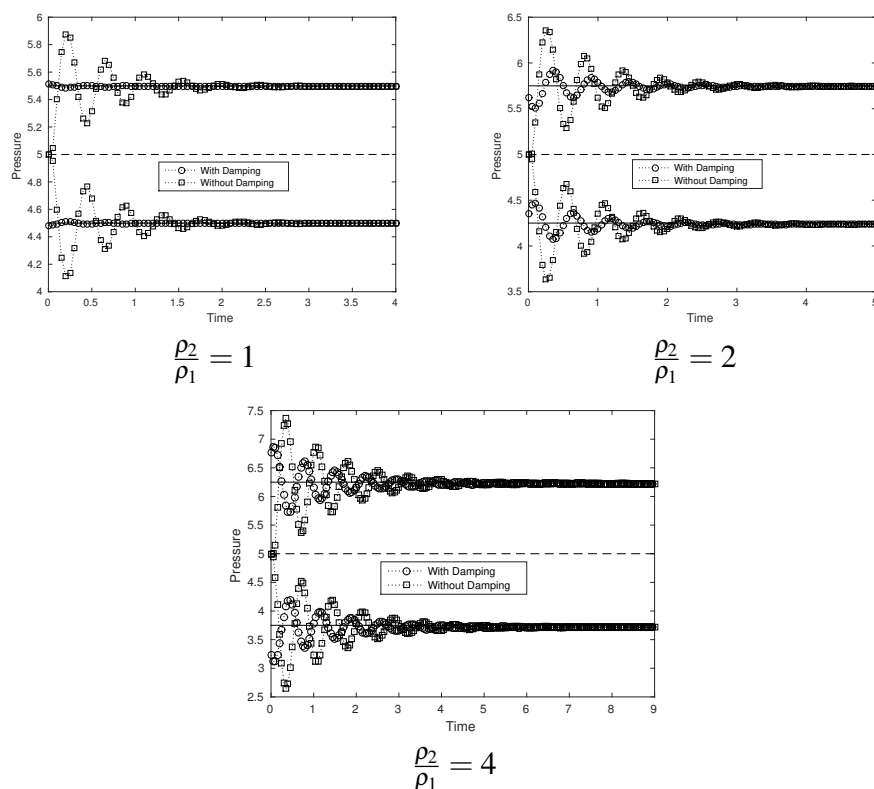


Figure 6.2 – Time-evolution of pressure at the point $(0.5, 0.5)$ (upper curves) and $(0.5, 1.5)$ (lower curves) with (Dotted line with small circle) and without (dotted line with small square) the damping technique. The solid lines represent the stabilized pressure, and the dashed line presents the background pressure.

give good results. In order to perform an additional analysis of the efficiency of this method, the same example was investigated under high density and viscosity ratios. The density ratio was chosen to be equal $\frac{\rho_2}{\rho_1} = 100$, with $\rho_2 = 100[\text{kg}/\text{m}^3]$ and $\rho_1 = 1[\text{kg}/\text{m}^3]$. While the viscosity ratio is taken as $\frac{\mu_2}{\mu_1} = 10$, with $\mu_1 = 0.01[\text{Pa}\cdot\text{s}]$ and $\mu_2 = 0.1[\text{Pa}\cdot\text{s}]$. The reference speed of sound of the fluid phase 2 is set to $c_{02} = 10[\text{m}/\text{s}]$ and $c_{01} = 100[\text{m}/\text{s}]$ for the phase 1 that give a reference pressure of $p_r = 10^4[\text{Pa}]$. The background pressure is taken as $p_b = 0.05p_r = 500[\text{Pa}]$. The simulation was performed using 49×99 particles, a damping period of $T_D = 1[\text{s}]$ and no-slip condition is applied on all wall boundaries.

After the damping period ($T_D = 1[\text{s}]$) the hydrostatic pressure field oscillates until it reaches the stabilized values at time $t = 18[\text{s}]$ as it is shown in the figure 6.5. When the pressure field stabilizes, we perform a comparison between the numerical and analytical hydrostatic pressure profiles taken from the centerline of the vertical fluid column. The results are shown in figure 6.6. A very satisfactory agreement is observed between the pressure results obtained with the present approach and analytical results. Figure 6.7 shows

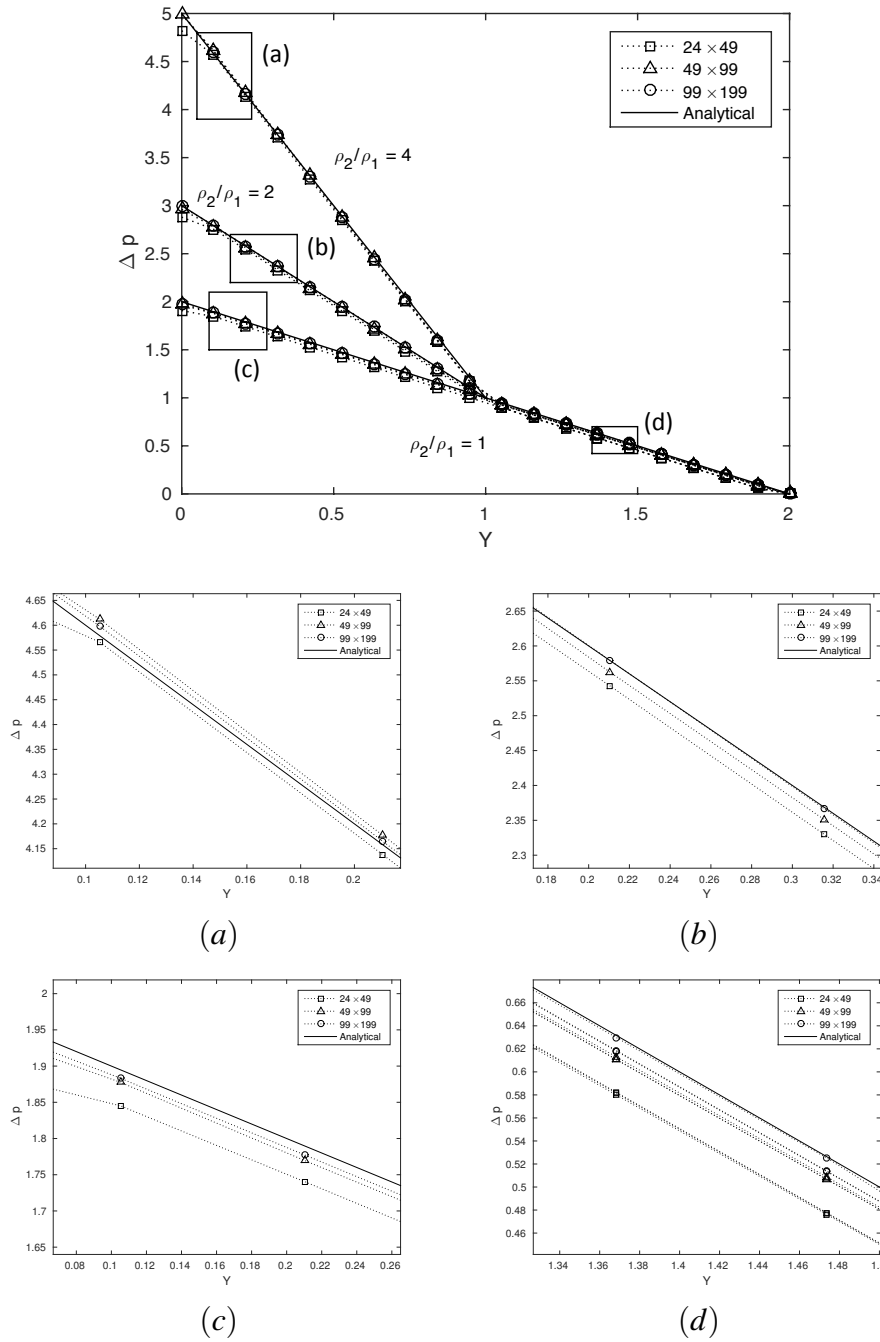


Figure 6.3 – Hydrostatic pressure variation $\Delta p = p - p_{min}$ for the three different density ratios $\frac{\rho_2}{\rho_1}$. Below, we plot a zoom of the selected zones (a) (b) (c) (d).

the vertical fluid column particles distribution at stabilized state. The fluid particles are colored with phases (gray for the fluid 2 and black for the fluid 1) in order to show that the interface between the two fluid phases that meet the vertical wall boundaries is stable. As it is shown in the center of the figure 6.7, there are spurious currents which present a maximum

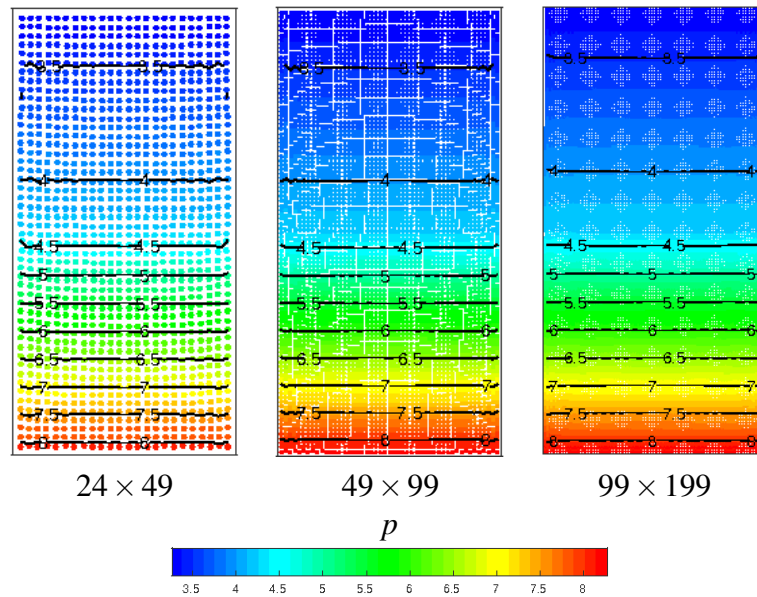


Figure 6.4 – The fluid column particles colored with normalized hydrostatic pressure for the density ratio $\frac{\rho_2}{\rho_1} = 4$ with the three particle resolutions 24×49 (left), 49×99 (center), 99×199 (right). It is also shown the pressure isolines in the range 3.5 to 8 [Pa].

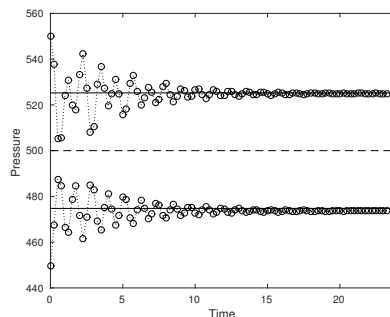


Figure 6.5 – Time-evolution of pressure at the point $(0.5, 0.5)$ (upper curves) and $(0.5, 1.5)$ (lower curves) after the damping period for the density and viscosity ratios of $\frac{\rho_2}{\rho_1} = 100$ and $\frac{\mu_2}{\mu_1} = 10$. The solid lines represent the stabilized pressure, and the dashed line presents the background pressure.

velocity magnitude of order $O(10^{-3})$. A smooth hydrostatic pressure field is observed via the right side of figure 6.7.

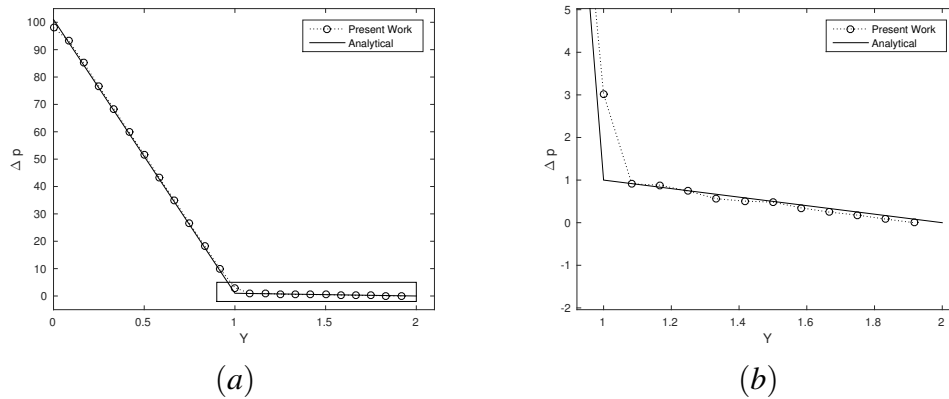


Figure 6.6 – Hydrostatic pressure variation $\Delta p = p - p_{min}$ for the density and viscosity ratios of $\frac{\rho_2}{\rho_1} = 100$ and $\frac{\mu_2}{\mu_1} = 10$. On the right we plot a zoom of the selected zone.

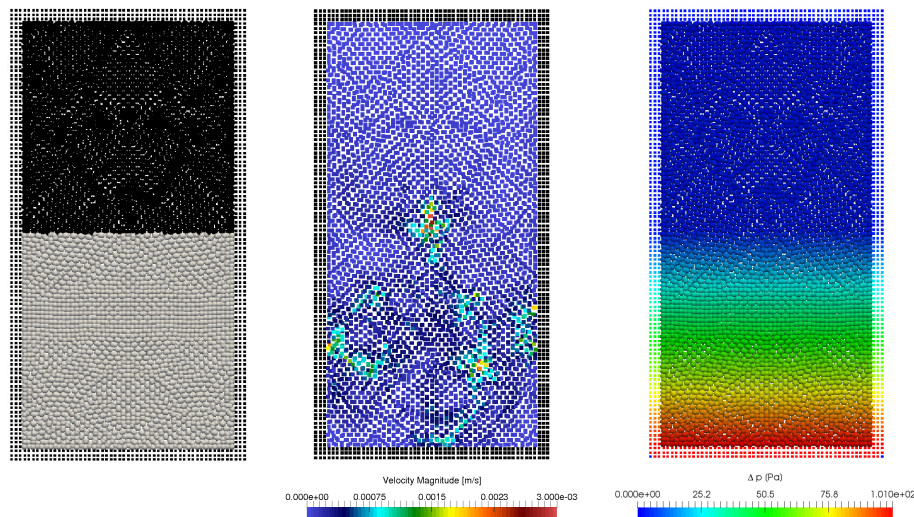


Figure 6.7 – The fluid column particles for the density and viscosity ratios of $\frac{\rho_2}{\rho_1} = 100$ and $\frac{\mu_2}{\mu_1} = 10$. The left figure represents the fluid particles colored with phase color (gray color for fluid 2, black color for fluid 1). The figure of the center show the velocity magnitude of every fluid particle. The right figure represents the fluid and wall particles colored with hydrostatic pressure field.

6.2 Rayleigh–Taylor instability

The Rayleigh–Taylor instability (RTI) is a widely used benchmark [80, 150, 128, 238] to test the accuracy of numerical methods for multiphase gravity flows. The Rayleigh–Taylor instability, occurs at an interface between two fluids of different densities when the lighter fluid pushes the heavier fluid. This phenomenon occurs in a multitude of physical (salt domes, weather inversions, etc) and industrial applications.

In this work a Rayleigh-Taylor with sinusoidal asymmetric interface perturbation is studied. The computational domain is $[0, L] \times [0, 2L]$ with $L = 1$ [m]. The computational domain is divided in two sub-domains by a sinusoidal interface $y(x) = 1 - 0.15 \sin(2\pi x)$ (see figure 6.1). The lower sub-domain is occupied by the lighter fluid (referred as phase 1) which has a density $\rho_1 = 1$ [kg/m³], while the upper sub-domain is occupied by the heavier fluid (referred as phase 2) with density $\rho_2 = 1.8$ [kg/m³]. The Reynolds number is defined here as $Re = \frac{\sqrt{\|g\|L^3}}{\nu}$, and a value of $Re = 420$ is chosen. In the previous definition, $\|g\| = 1$ [m/s²] is the modulus of the gravity acceleration vector, and $\nu = \nu_1 = \nu_2 = 0.0024$ [m²/s] is the kinematic viscosity which is chosen to be equal and constant for both fluids phases.

The particles have an initial regular lattice distribution. The RTI test is solved with three different particles resolutions $\{49 \times 99, 99 \times 199, 133 \times 267\}$. The reference speeds of sound are taken as $\{c_{01}, c_{02}\} = \{13.41, 10\}$ [m/s], for the lighter and heavier fluids, respectively. The reference pressure is chosen equal to 9 [Pa]. The no-slip boundary condition is applied on all solid boundaries.

In figure 6.8 we compare three different particle resolutions at three different times $t = 1$ [s], $t = 3$ [s], $t = 5$ [s]. Quantitatively, it's shown that the three particle resolutions are able to simulate substantially the same phenomena of RTI. Nevertheless, at the low resolution 49×99 the roll-up of the small structures at the mushroom-shaped head are not well reproduced. For the finer resolutions, all the small structure phenomena due to the development and roll-up of the mushroom-shaped heads are captured. The two finer resolutions (99×199 and 150×300) are very similar to each other in terms of the shape of the instability.

We also performed a comparison between the RTI interfaces reproduced with the proposed SPH model and two different numerical methods. In figure 6.9, we compare the results at time $t = 5$ [s] with the resolution of 150×300 particles with those of a Level-set method [128] and another SPH model [238]. There are some differences between the SPH method [238] and the method presented here. For instance in [238] a Wendland kernel function [347] and time-integration of continuity equation for the density are used instead of the quintic spline kernel 4.7 and summation-based density 4.8 used in the presented SPH method, respectively. The present SPH model can reproduce the RTI interface in good agreement with the other numerical models which have more resolution (Level-Set: a grid of 312×624 cells, and SPH model[238]: 150×300 particles). Globally, the RTI interface reproduced with the proposed SPH approach is closer to that reproduced with the SPH model of [238]. This is probably due to the same nature of both models. We note, however that in some places the interface with the proposed SPH method is closer to that obtained by the Level-set one [128]. These results are only of a qualitative nature. Monaghan et al [238] prefer to examine

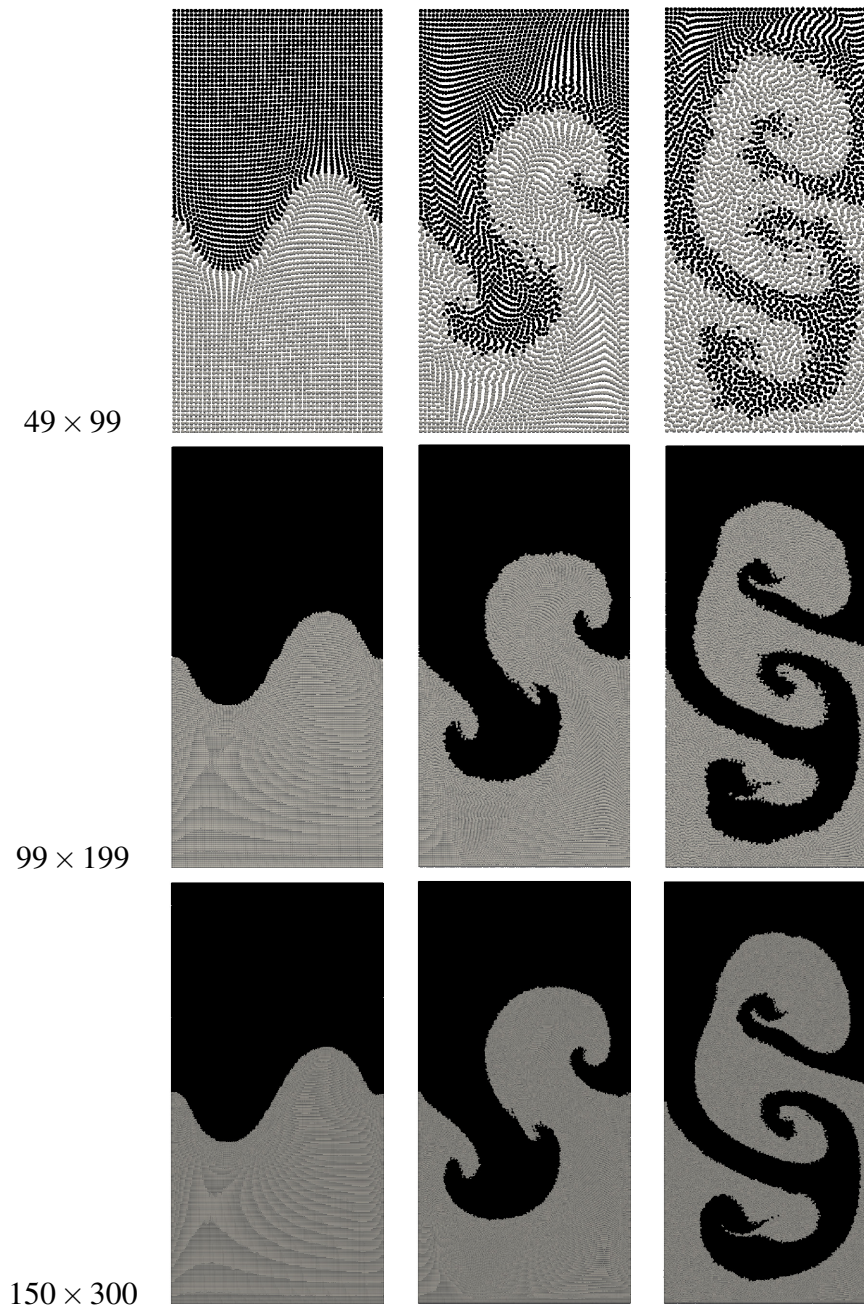


Figure 6.8 – Rayleigh–Taylor instability at three different times $t = 1$ [s] (left column), $t = 3$ [s] (center column), $t = 5$ [s] (right column) after the damping period, and three different resolutions: 49×99 particles (top), 99×199 particles (middle) and 150×300 particles (bottom).

the convergence by comparing the time evolution of the position of the Y –coordinate of the highest particle of the lighter fluid (phase 1) with that obtained from the Layzer’s theory [187, 83]. Thus, the highest point of the phase 1 fluid for the three particle resolutions

$\{49 \times 99, 99 \times 199, 150 \times 300\}$ is plotted in figure 6.10 together with the curve obtained using the Layzer's theory. The results are in good agreement with the Layzer theory. Note that the the Layzer theory is for a periodic domain, while the results are obtained from the simulation in a rectangular rigid domain with no-slip boundaries. This fact may explain some of the deviations of the numerical results from the theoretical line.

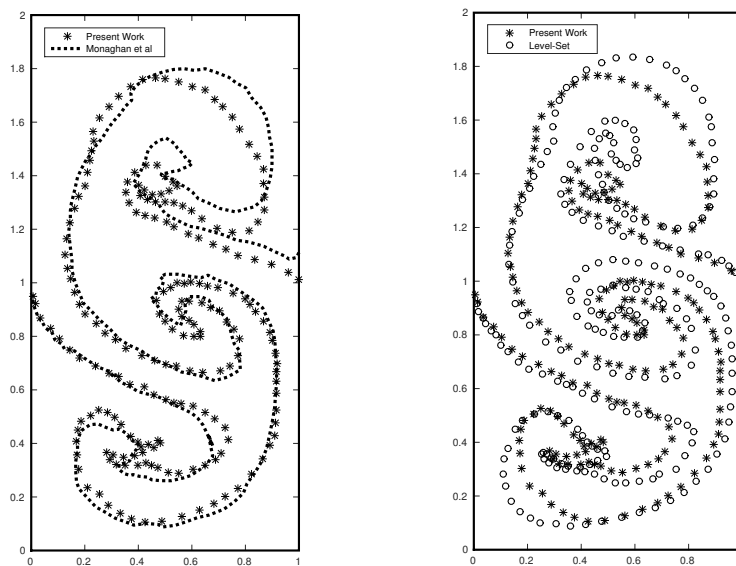


Figure 6.9 – Comparison between the fluid interfaces of the present work and the references. The left figure compares the fluid interface of present SPH model with that of SPH model developed by Monaghan et al [238]. The right figure compares the fluid interface of the present SPH method with that of Level-Set method [128].

6.3 Interaction of two rising bubbles through a fluid column

In this last test case we solve a case based on the one presented in [128]. Two bubbles are initially set close to each other and rise through a fluid column. The upper bubble is larger than the lower one. The smaller bubble has a radius $R = 0.1$ [m]. The geometrical setup of the problem is based on the radius of the smaller bubble and is detailed in figure 6.11. The physical parameters for the setup of this problem are given in Table 6.1, respectively.

We use here a discretization of 500×750 particles.

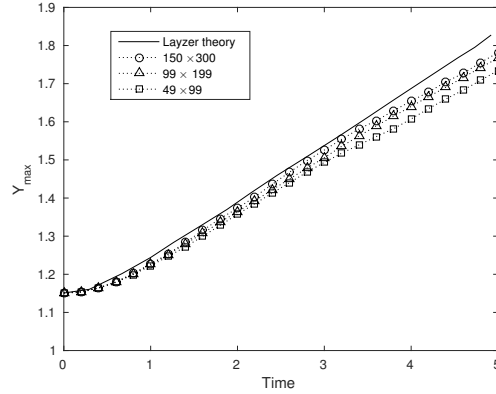


Figure 6.10 – Time-evolution for the highest point (Y_{max}) of the lighter fluid. Dotted line with small open triangles shows the results for the simulation with 99×199 particles, the small open square for 49×99 particles and the small open circles for 150×300 particles. Layzer’s theory curve is represented by the continuous solid line.

ρ_1 [kg/m^3]	ρ_2 [kg/m^3]	μ_1 [$Pa.s$]	μ_2 [$Pa.s$]	σ [N/m]	$\ g\ $ [m/s^2]	R_e	E_o	$\frac{\rho_1}{\rho_2}$	$\frac{\mu_1}{\mu_2}$
1000	100	0.156	0.078	0	2.9	1794	∞	10	2

Table 6.1 – Setup for the interaction of two rising bubbles through a fluid column test case. With Reynolds number $R_e = \frac{\rho_1 v_c L_c}{\mu_1}$ and Eötvös number $E_o = \frac{\rho_1 v_c^2 L_c}{\sigma}$.

The reference speeds of sound $\{c_{01}, c_{02}\} = \{9.32, 29, 47\}$ [m/s] are chosen for fluid water column and the fluid of the two bubbles, respectively. The simulation is damped for a period of $T_D = 0.25$ [s]. Left and right boundaries are set as free-Slip boundaries, whereas no-slip boundary conditions are set at top and bottom boundaries. The results for pressure variation $\widetilde{\Delta p} = p - p_{min}$, velocity magnitude of the fluid column and of the bubble are presented in figures 6.12 and 6.13.

During the evolution process of the two rising bubbles, the upper bubble covers the lower one. This generates more efforts over the lower bubble. Due to this forces, the lower bubble deforms. This deformation generates two fluid ejections that go thinner as the rising process continues. Finally, the two bubbles merge but this state is not stable and they split in two parts.

6.4 Conclusion

The accuracy, stability and applicability of the proposed SPH model to deal with gravitational multiphase fluid problems were shown. Using the proposed damping technique leads

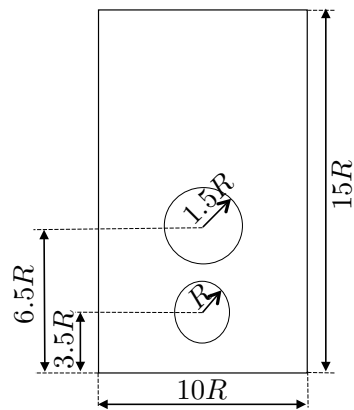


Figure 6.11 – Interaction of two rising bubbles through a fluid column: Geometrical setup.

to lower amplitude of the pressure oscillations. The modifications brought in this work to the generalized wall boundary conditions [4] for the multiphase applications is shown its efficiency to simulate gravitational multiphase fluid flow with high density ratio.

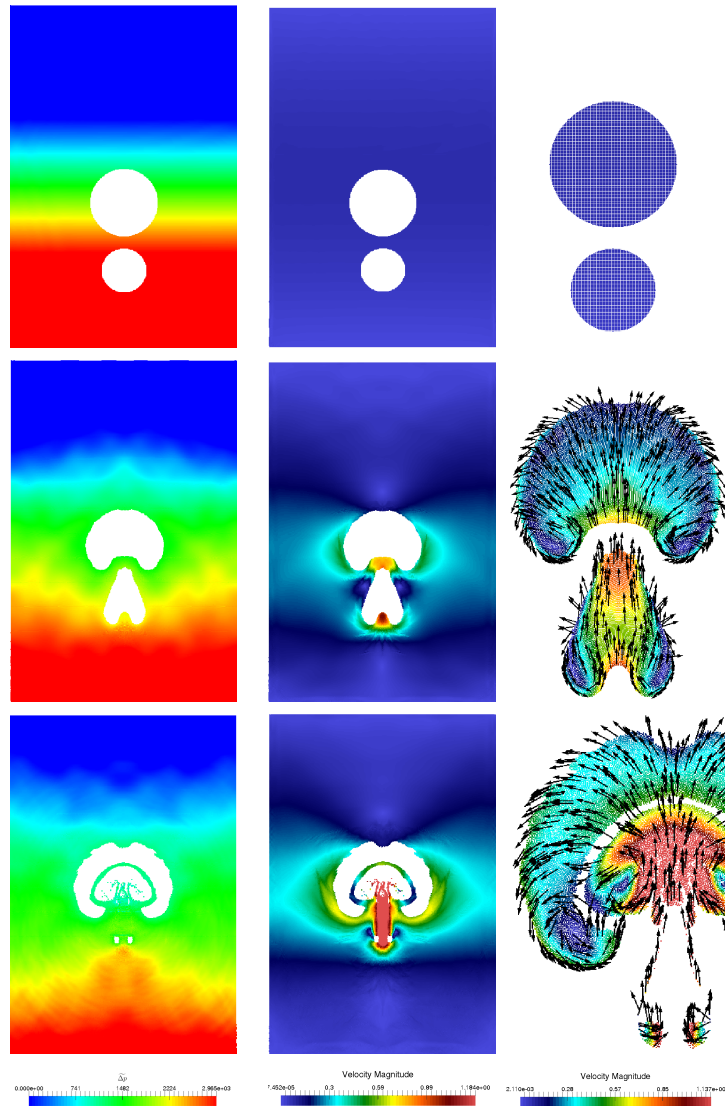


Figure 6.12 – Interaction of two rising bubbles through a fluid column First and second images columns represent the pressure and magnitude velocity, respectively. The third column presents the magnitude velocity with particle direction vector of isolated bubble. The simulations are presented in order at the times $t = \{0, 0.25, 0.5\}$ [s].

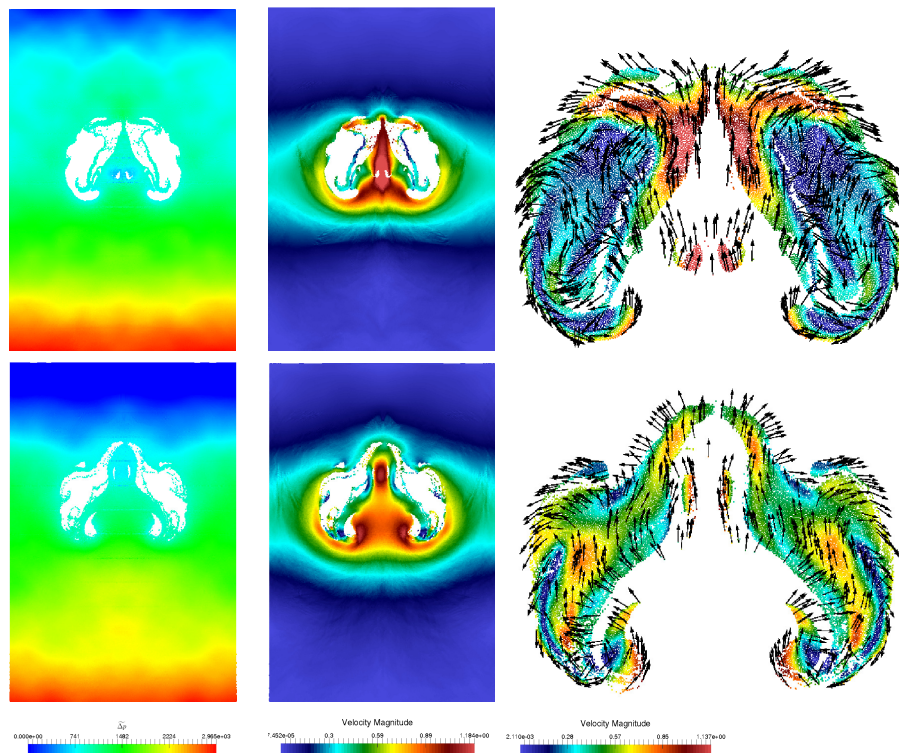


Figure 6.13 – Two rising bubbles through a fluid column. First and second images columns represent the pressure and magnitude velocity, respectively. The third column presents the magnitude velocity with particle direction vector of isolated bubble. The simulations are presented in order at the times $t = \{0.75, 1\}$ [s].

Chapter 7

Validation and application of SPH interfacial multiphase model

Ce chapitre est dédié à l'étude de la consistance et la convergence de la formulation non-conservatrice de la force de tension de surface proposée dans ce travail, dans le cas d'écoulement diphasique (deux phases) et triphasique (trois phases) avec présence de points de jonction triple. Ceci est fait par le biais de la comparaison avec des solutions analytiques disponibles. Les exemples abordés dans cette catégorie sont, la déformation d'une gouttelette carrée [2], l'étalement d'une goutte placée entre deux couches de fluide stratifiées [39] [193], et le test d'onde capillaire-visqueuse [254, 151, 150, 149, 2]. Par la suite, nous examinons l'effet des rapports de densité et de viscosité élevés. La montée d'une bulle d'air à travers une colonne d'eau de un seul fluide et de deux couches de fluide stratifiées est étudiée. Les résultats sont comparés à ceux obtenus avec d'autres méthodes numériques (Volume-Of-Fluid [155], Level-Set [318]) et aussi avec des résultats expérimentaux [37].

This chapter is dedicated to investigating the consistency and the convergence of the non-conservative formulation for the surface tension force proposed in this work, for the case of two and three phase flows with presence of triple junction points. This is done through the comparison with available analytical solutions. The examples addressed in this category are the square droplet deformation [2], the spreading lens between two stratified fluid layers [39] [193], and the capillary-viscous wave test [254, 151, 150, 149, 2]. Thereafter, we introduce high density and viscosity ratios effects. The rising of an air bubble through a water column and through two stratified fluid layers are investigated. The results obtained with the new method are compared to those obtained with other numerical methods (Volume-Of-Fluid [155], Level-Set [318]) and also with experimental results [37].

The simulations of the bubble rising behavior can be characterized by the Reynolds and the Eötvös dimensionless numbers [155] and also the density and viscosity ratio $(\frac{\rho_1}{\rho_2}, \frac{\mu_1}{\mu_2})$. The Reynolds number R_e gives the ratio of inertial to viscous effects and is expressed as

$$R_e = \frac{\rho_1 v_c L_c}{\mu_1}. \quad (7.1)$$

While the Eötvös number E_o compares buoyancy effects to capillary ones :

$$E_o = \frac{\rho_1 v_c^2 L_c}{\sigma}. \quad (7.2)$$

The subscripts 1 and 2 refer to the heavier and lighter fluid, respectively. The characteristic velocity is defined as $v_c = \sqrt{2R\|g\|}$ and $L_c = 2R$ refers to the characteristic length. R is initial radius of the bubble and $\|g\|$ is the magnitude of the gravity acceleration vector.

7.1 Square droplet deformation

In this first test case, the SPH method with CSS model of the surface tension force is applied to the simulation of the deformation of a square droplet under the action of the surface tension force. This example has already been investigated by Adami et al [2] using a SPH method with CSF model. The square droplet is defined by an edge length $l_d = 0.6$ [m] units. It is placed on the center of an square box with sides $L_s = 1$ [m]. The fluid within the square droplet is referred as phase 1 whereas the fluid outside the droplet is referred as phase 2 (see figure 7.1). The densities of the each fluid phases are chosen as $\rho_1 = \rho_2 = 1$ [Kg/m³] and the dynamic viscosity is taken as $\mu_1 = \mu_2 = 0.2$ [Pa.s]. The surface tension coefficient is $\sigma^{1-2} = 1$ [N/m].

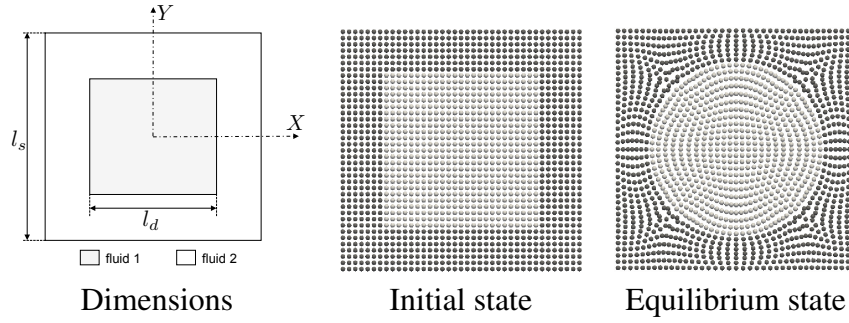


Figure 7.1 – The evolution of square droplet under the surface tension effort : The left figure describes the geometrical details. The middle figure shows the initial fluid particles at ($t = 0$ [s]) for the particle resolution $\frac{l_s}{40}$. The right figure describes droplet in equilibrium state after its evolution for the particle resolution $\frac{l_s}{40}$.

We investigate the evolution of the square droplet deformation using three different number of particles: $\frac{l_s}{40}$, $\frac{l_s}{80}$ and $\frac{l_s}{160}$. The smoothing length is chosen equal to $h = 1.33\delta x_0$. The reference speed of sound is set to ($c_0 = 10$ [m/s]) for all resolutions. A positive background pressure is taken as ($p_b = 5$ [Pa]). A non-slip boundary condition is applied on all sides of the square box.

The evolution of the kinetic energy of the particles inside the droplet ($E_k = \frac{1}{2} \sum_{i_d} m_{i_d} \|v_{id}\|^2$ where i_d refers to the droplet particles) is plotted in figure 7.2. The deformation of the square droplet starts at the corners because of a local high surface tension due to the high curvature at corners. This effect is reflected by the peak in the kinetic energy which evolves until the stabilization in a value close to zero for all resolutions.

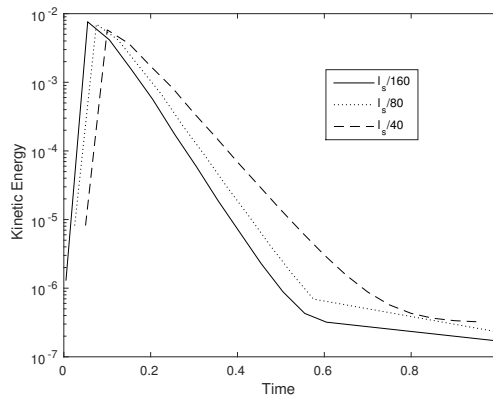


Figure 7.2 – Time evolution of droplet kinetic energy for particle resolutions $\frac{l_s}{40}$, $\frac{l_s}{80}$ and $\frac{l_s}{160}$.

At the stabilized state (equilibrium state) the particles are at rest, and the square droplet is totally transformed in a circular droplet. Under the fluid incompressibility hypothesis, both

phases must conserve their volumes (areas in 2D) during all the evolution process. Thus, the equality $\pi R^2 = l_d^2$ holds for the square droplet, and therefore the equilibrium radius is $R = \frac{l_d}{\sqrt{\pi}} \approx 0.338 [m]$. From Laplace's law, the pressure of the fluid particles inside the droplet (phase 1) must be higher than that of the surrounding particles (phase 2), and the jump of pressure between the two phases must satisfy the condition

$$\Delta p = \frac{\sigma^{1-2}}{R} \approx 2.954 [Pa] \quad (7.3)$$

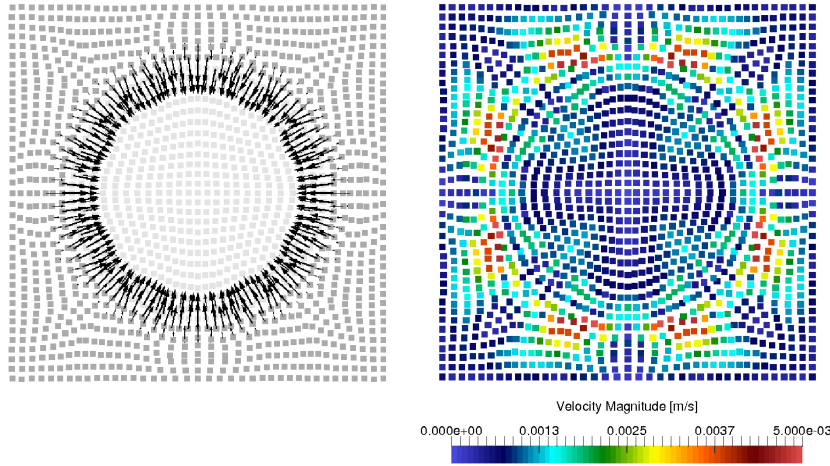


Figure 7.3 – Surface tension forces orientation (on the left) and magnitude of the velocity (on the right) of droplet at equilibrium state for the particle resolution $\frac{l_s}{40}$.

The surface tension forces orientation and the magnitude of the velocity are shown in figure 7.3. We observe that the surface tension force has a radial direction, oriented towards the center of droplet. This orientation corresponds to the direction of normal vectors to the interface between the fluid phases (see the left side of the figure 7.3). On the right side of the figure 7.3 the magnitude velocity of every particle is represented. The velocity magnitude is in the order of $O(10^{-3})$. When forces due to this spurious effect are comparable to other physical forces such as viscous, gravitational, and surface tension forces, errors will be greater.

In figure 7.4 we show the cut of pressure field at $Y = 0$ (X-axis) obtained in the simulations and also the analytical pressure predicted by Laplace's law. It is observed a good agreement between the numerical results and the theoretical pressure. These results show that the SPH method with the CSS non-conservative surface tension model is able to represent correctly the equilibrium state of this two phase flow problem.

When a low viscosity of $\mu_1 = \mu_2 = 0.001 [Pa.s]$ is used (small viscous forces) to simulate the square droplet deformation test case, the pressure profile at the equilibrium state is less

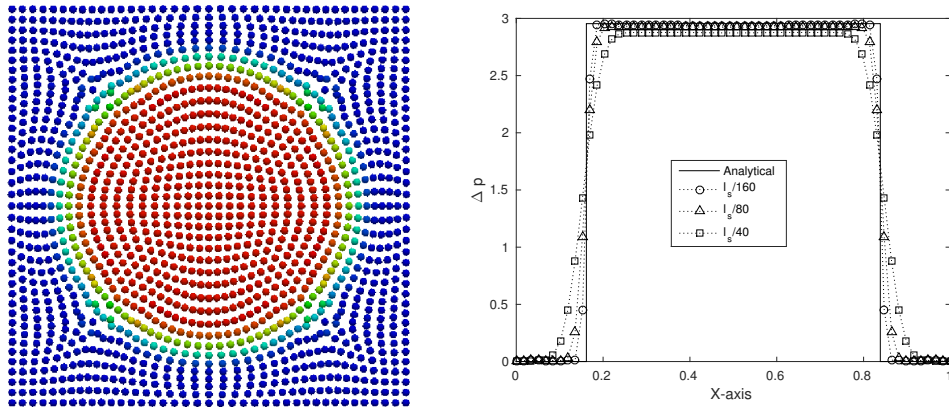


Figure 7.4 – Square droplet test case. The left figure plots the normalized pressure ($\frac{p-p_2}{p_1-p_2}$) at the final stabilized state. The figure on the right plots a cut of the pressure field at $Y = 0$ obtained by the numerical method and the theoretical solution for different particle resolutions $\frac{l_s}{160}$, $\frac{l_s}{80}$ and $\frac{l_s}{40}$.

accurate. This is because in this case viscosity forces are comparable with the forces due to the parasitic currents (see figures 7.5 and 7.6). Note however that the circular shape of droplet is well approximated. Parasitic currents are a numerical artifact suffered for numerical approaches of the surface tension based on the use of CSF or CSS formulations. The elimination of this effect is not addressed here. For more details about parasitic currents artifact and their elimination, please refer to [271, 330, 162].

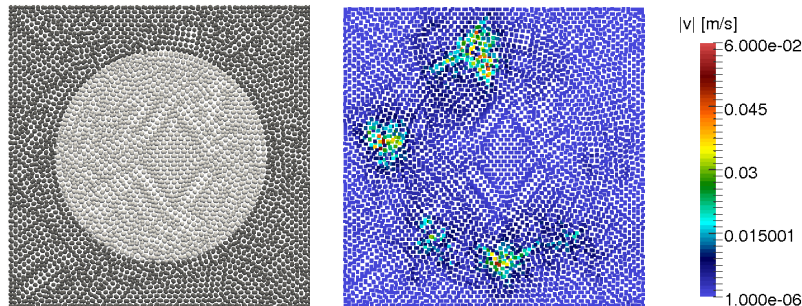


Figure 7.5 – Square droplet test case using low viscosity ($\mu_1 = \mu_2 = 0.001 [Pa.s]$) for the particle resolution of $\frac{l_s}{80}$. Particles colored with fluid phases (left). Magnitude velocity field (right).

Three density ratios $\frac{\rho_2}{\rho_1} = \{1, 10, 1000\}$ are investigated in order to show the influence of the variation of density ratios on the obtained pressure results. In figure 7.7, the pressure profiles at $Y = 0$ are plotted for three selected density ratios. Despite the obtained results of pressure are not as accurate as for the case of density ratio $\frac{\rho_2}{\rho_1} = 1$, we observe relatively a good agreement with the analytical solution for the density ratios of $\frac{\rho_2}{\rho_1} = 10$ and $\frac{\rho_2}{\rho_1} = 1000$.

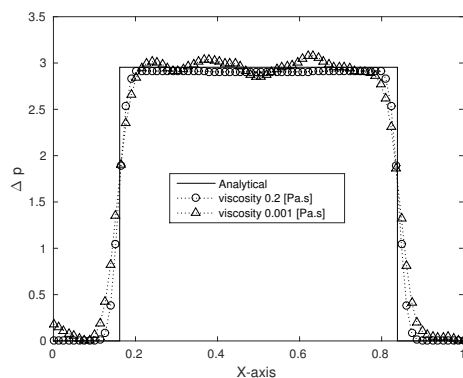


Figure 7.6 – A cut of the pressure field at $Y = 0$ obtained by the theoretical solution and the numerical method and numerical method with viscosity $\mu_1 = \mu_2 = 0.2 [Pa.s]$ (dotted line with small circles) and $\mu_1 = \mu_2 = 0.001 [Pa.s]$ (dotted line with small triangles) for the particle resolution of $\frac{l_s}{80}$.

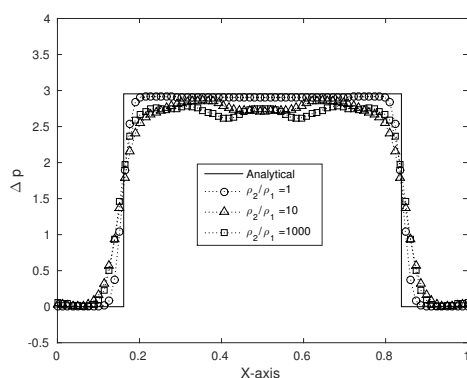


Figure 7.7 – A cut of the pressure field at $Y = 0$ obtained by the theoretical solution and the numerical method and numerical method with viscosity $\mu_1 = \mu_2 = 0.2 [Pa.s]$ and three density ratios $\frac{\rho_2}{\rho_1} = \{1, 10, 1000\}$ for the particle resolution of $\frac{l_s}{80}$.

7.2 Spreading lens between two stratified layers

This example aims to test if the presented SPH model can deal with triple junction points problems [193]. Thus, the classical test of the spreading of a lens between two stratified fluid layers is investigated. A circular lens of radius $\frac{1}{6} [m]$ is placed at the center of a square box with length sides ($l_b = 1 [m]$). The square box contains two different fluid phases in a stratified arrangement. These fluid phases are respectively referred as fluid phases 1 (the phase at the top of the stratification) and 2 (the phase at the lower part of the stratification arrangement) whereas the lens is referred as phase 3. Due to the effect of the surface tension,

the lens evolves until an equilibrium state (see figure 7.8). The contact angles at the triple junction point follows the Young's relation

$$\frac{\sin\theta_1}{\sigma^{2-3}} = \frac{\sin\theta_2}{\sigma^{1-3}} = \frac{\sin\theta_3}{\sigma^{1-2}} \quad (7.4)$$

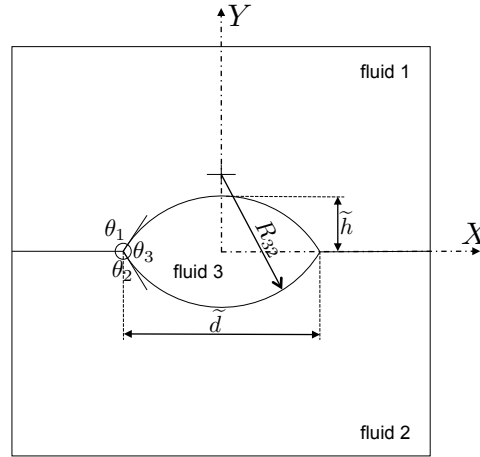


Figure 7.8 – Schematical representation of contact angles at a triple junction point.

Fluid densities are set as ($\rho_1 = \rho_2 = \rho_3 = 1 [Kg/m^3]$) for the three fluid phases. The dynamic viscosities are identical for the three fluid phases ($\mu_1 = \mu_2 = \mu_3 = 0.5 [Pas.s]$). The interfacial surface tension applied on all fluids interfaces is ($\sigma^{1-2} = \sigma^{2-3} = \sigma^{1-3} = 5 [N/m]$), in order to obtain a symmetric lens. The analytic solution is obtained from Laplace's law and Young's relation. The theoretical value of the pressure jump between phases (Δp) is obtained in 2D case from equation (7.5). The shape of the half lens (symmetric with respect to the X axis) at equilibrium state is assumed to be a circular segment with following parameters (see figure 7.8): The distance between the two triple junction points (\tilde{d}), the contact angles of the i^{th} phase (θ_i), the sagitta (the distance from the center of the arc to the center of its base) of the segment (\tilde{h}), the radius of the curvature of the interface between the phases i and j (R_{ij}) (in figure 7.8, we represent the curvature between the upper fluid of the stratification (1) and the fluid of the lens (3)).

$$\Delta p = p_i - p_j = \frac{\sigma^{i-j}}{R_{ij}} \quad (7.5)$$

At the equilibrium state the lens area A , the distance between triple junction points \tilde{d} , and the contact angles θ_i can be expressed follows the relation [173]

$$\tilde{d} = \left(\frac{1}{8A} \left(\frac{2(\pi - \theta_1) - \sin((\pi - \theta_1))}{\sin^2(\pi - \theta_1)} + \frac{2(\pi - \theta_2) - \sin((\pi - \theta_2))}{\sin^2(\pi - \theta_2)} \right) \right)^{-\frac{1}{2}} \approx 0.4617 [m] \quad (7.6)$$

Note that in this test case, the surface tension coefficients are taken identical. Then, the Young's relation (equation (7.4)) reads as $\theta_1 = \theta_2 = \theta_3 = \frac{2\pi}{3}$.

Geometrical consideration leads to the following results

$$R_{31} = R_{32} = \frac{\tilde{d}}{2 \sin \frac{\theta_3}{2}} \approx 0.2665 [m] \quad (7.7)$$

$$\tilde{h} = R_{32} \left(1 - \cos \frac{\theta_3}{2} \right) \approx 0.1333 [m] \quad (7.8)$$

All the particles are initially at rest. The no-slip boundary condition is applied on the upper and lower boundaries. On the left and right boundaries a periodic boundary condition is applied. The reference speed of sound and the background pressure are taken as ($(c_0 = 55 [m/s])$ and $p_b = 150 [Pa]$).

The time evolution of kinetic energy for three different resolutions $\frac{l_b}{40}$, $\frac{l_b}{80}$ and $\frac{l_b}{160}$ is plotted in the figure 7.9. The kinetic energy converges to approximate zero and reaches the equilibrium state. As it is observed, the magnitude of the velocity decreases considerably (order of $O(10^{-2})$; see figure 7.10) at later time for the three particle resolutions. This indicates that the parasitic currents do not create a serious effect on the obtained results.

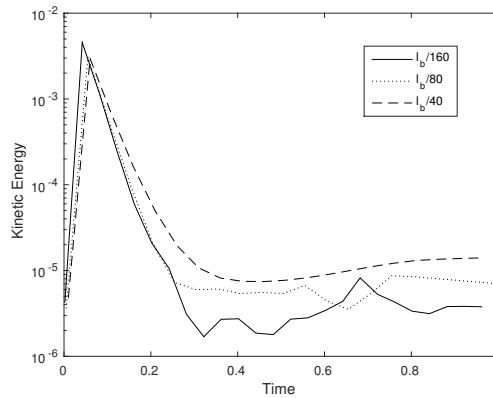


Figure 7.9 – Spreading lens between two stratified layers: Time-evolution of kinetic energy for three different particle resolutions.

Figure 7.10 shows the pressure field, the particle distribution of three phases stratification arrangement and magnitude of velocity filed at the equilibrium state. The initial circular shape of the lens evolved to an elliptical shape at the equilibrium state. The pressure jump profile along $X = 0$ and $Y = 0$ lines are plotted with the analytical solution obtained from equation (7.5), which gives $\Delta p = p_3 - p_1 = p_3 - p_2 \approx 18.7591 [Pa]$. Quantitatively a good agreement between the numerical solution and analytical one is observed for both pressure profiles (along the $X = 0$ and $Y = 0$ lines). A pressure instability appears near the triple junction points (following the X axis) for both resolutions (see figure 7.11). This instability tend to disappear with increasing of resolution (The instability in low resolution is more marked than in higher one). Note that for a higher particle resolution, the SPH numerical solution becomes closer to the analytical one in terms of pressure and geometrical details of lens which guarantees thereafter the convergence of the proposed SPH interfacial multiphase model to deal with a triple junction points problems.

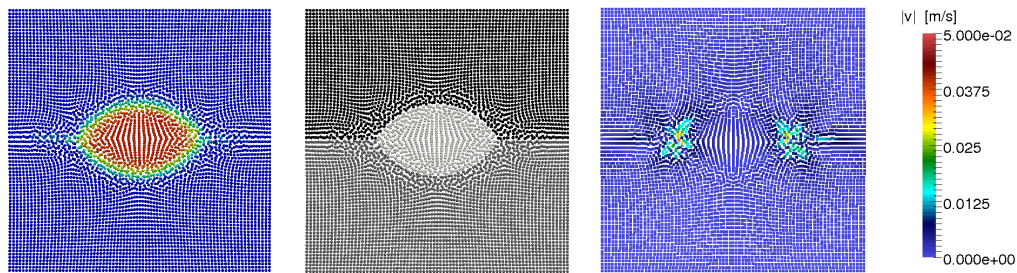


Figure 7.10 – Spreading lens between two stratified layers: pressure field (left), particle distribution of three-phases stratification arrangement (middle) and magnitude velocity filed (right).

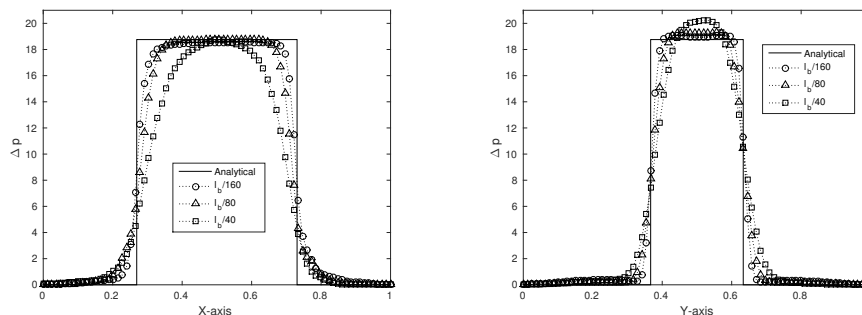


Figure 7.11 – Spreading lens between two stratified layers: pressure jump profile along $Y = 0$ (left) and $X = 0$ (right) lines.

The wettability of a fluid phase in contact with other two phases can occur either partially or totally, depending on the surface tensions between the three fluid interfaces. The degree

of wettability can be determined by the spreading parameter S_p [349]. If the spreading parameter is positive the fluid of this phase will spread completely on the interface between the other phases (total spreading). Here, in order to check if the proposed method reproduces accurately this phenomenon, we consider two different configurations following the work presented in [39].

We define the spreading parameter for the lens (S_{p_3}) and the upper fluid (S_{p_1}) phases as follows

$$S_{p_3} = \sigma^{1-2} - (\sigma^{1-3} + \sigma^{2-3}) \quad (7.9)$$

$$S_{p_1} = \sigma^{2-3} - (\sigma^{1-2} + \sigma^{1-3}) \quad (7.10)$$

The first configuration of the problem is defined by choosing the values of interfacial surface tensions as $\{\sigma^{1-2}, \sigma^{1-3}, \sigma^{2-3}\} = \{3, 1, 1\}$ [N/m] ($S_{p_3} = 1$ [N/m] > 0). This choice leads to the total spreading of the lens phase 3 on the interface phases 1-2

For the second configuration, the values of interfacial surface tensions are chosen as $\{\sigma^{1-2}, \sigma^{1-3}, \sigma^{2-3}\} = \{1, 1, 3\}$ [N/m] ($S_{p_1} = 1$ [N/m] > 0). This choice leads to the total spreading of the upper fluid phase 1 on the interface phases 2-3.

In figure 7.12 we show the evolution of the spreading until the equilibrium state is reached for the two configurations considered. In both cases, the triple points disappear and the equilibrium interfaces are plane in the first case and spherical in the second simulation case. The results obtained are in agreement with those obtained in [39].

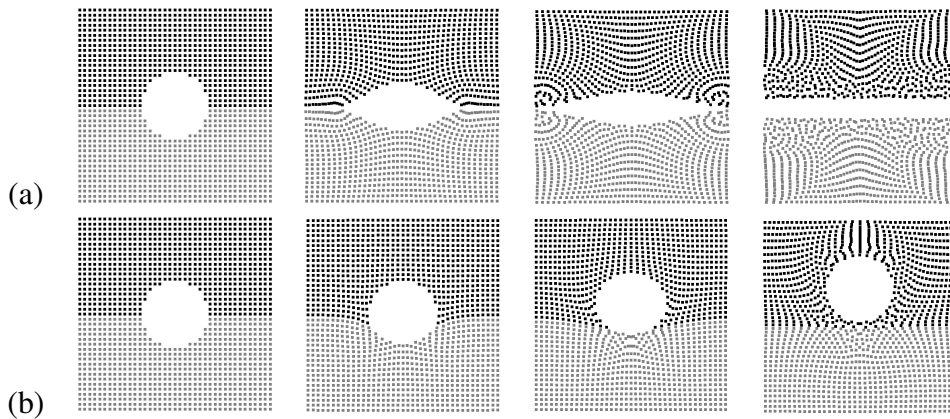


Figure 7.12 – Total spreading evolution of the fluid lens for the configurations : a) $\{\sigma^{1-2}, \sigma^{1-3}, \sigma^{2-3}\} = \{3, 1, 1\}$ [N/m] and b) $\{\sigma^{1-2}, \sigma^{1-3}, \sigma^{2-3}\} = \{1, 1, 3\}$ [N/m].

7.3 Capillary-viscous wave

In this example, the dynamic test case involving a liquid-droplet oscillation in a liquid phase under the action of capillary forces is investigated. This test was already simulated in the SPH framework in several works such as [254, 151, 150, 149, 2]. The liquid-droplet (referenced with a d subscript) has a radius of $R = 0.1875[m]$ and is surrounded with another liquid phase (referenced with a l subscript). Both fluids are placed at the center of a square box of size $L_x = L_y = 1[m]$. The densities and dynamic viscosities of the droplet and its surrounding fluid are considered the same and equal to $\rho_d = \rho_l = 1[Kg/m^3]$, $\mu_d = \mu_l = 0.05[Pa.s]$, respectively. The surface tension coefficient between the two phases is set as unity ($\sigma^{d-l} = 1[N/m]$). A divergence-free initial velocity field is assigned to all fluid particles and it reads as

$$v_x = v_0 \frac{x}{r_0} \left(1 - \frac{y^2}{r_0 r} \right) e^{-\frac{r}{r_0}} \quad (7.11)$$

$$v_y = -v_0 \frac{y}{r_0} \left(1 - \frac{x^2}{r_0 r} \right) e^{-\frac{r}{r_0}} \quad (7.12)$$

Where r denotes the distance between the particle position (x, y) and the droplet center. Terms v_0 and r_0 are the characteristic velocity and distance, and are taken as $v_0 = 10[m/s]$ and $r_0 = 0.05[m]$. We study the convergence properties using three different number of particles 900, 3600, 14400 particles. The reference speed of sound is chosen equal to $c_0 = 10 [m/s]$ for both fluid phases under all resolutions. A positive background pressure is set as ($p_b = 5 [Pa]$). A no-slip boundary condition is applied on the square box sides.

Figure 7.13 shows droplet particles positions at $t = \{0.0, 0.08, 0.16, 0.26\}[s]$, under the resolution of 14400 particles (about the same resolution used by Morris et al [254]). A good agreement is observed comparing with Morris et al [254] and also with Adami et al results (see figure 6 in [254]). Comparing these results with those of [254], it is observed that the present SPH model provides a more regular particle distribution and a smoother interface, with the consideration that the initial distribution of the particles are different.

Figure 7.14 shows the time evolution of the center of mass position of the upper right-quarter section of the droplet with different resolutions. It is observed that with increasing resolution the difference in results becomes less significant (the results with resolutions 3600 and 14400 particles are very close comparing with the lowest resolution of 900 particles).

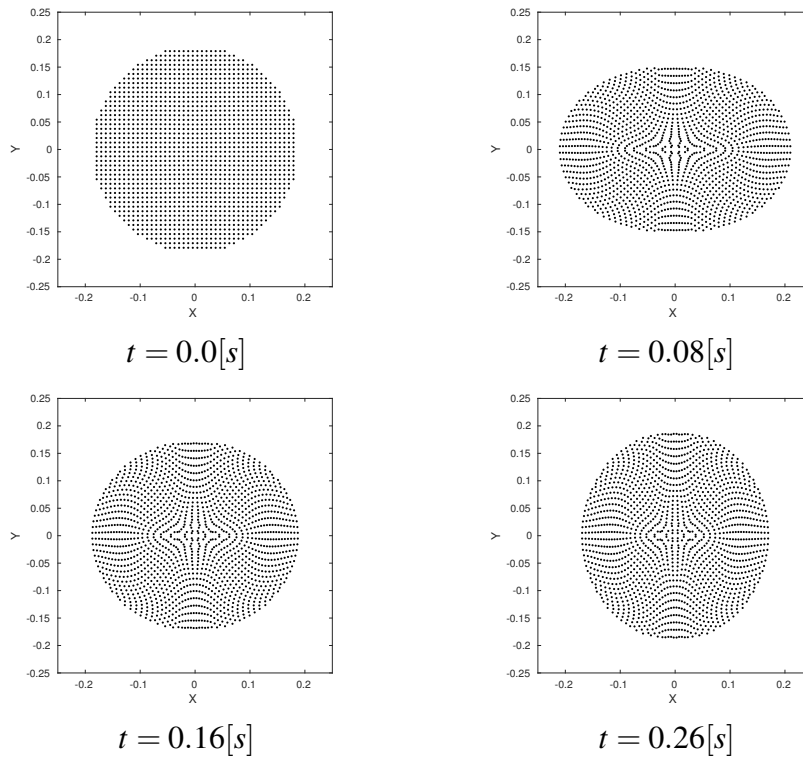


Figure 7.13 – Droplet oscillation : droplet particle positions at $t = \{0.0, 0.08, 0.16, 0.26\}[s]$.

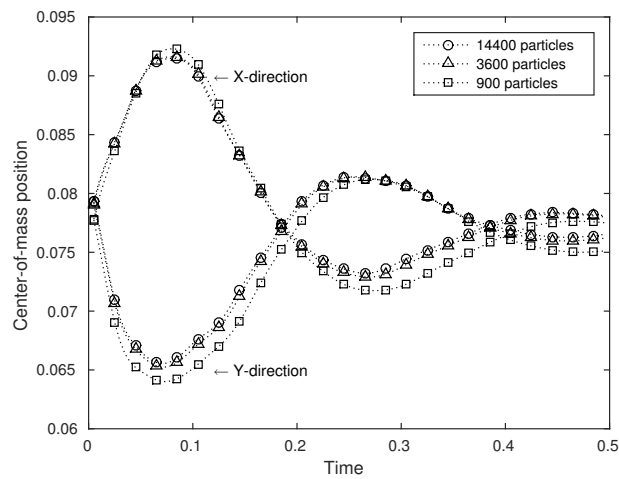


Figure 7.14 – Convergence test of droplet oscillation: Center of mass position of the upper right-quarter section of the droplet.

7.4 Single bubble rising through a vertical column of water

The purpose of this test is to show the efficiency of the present SPH model to simulate a two phase interfacial fluid flow with low and high density ratios. These tests are taken from the work of Hysing et al [155]. A single bubble rising in a vertical column due to gravity effect. The initial bubble position and dimensions of the vertical column are described related to the bubble radius R (see figure 7.15). The physical variables and parameters are summarized at Table 7.1 as Case 1.

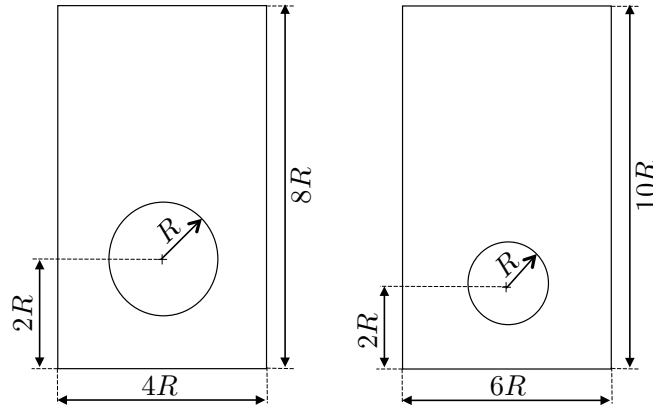


Figure 7.15 – Single bubble rising through a vertical column of water. Geometrical details of the initial setup. On the left it is schematically described the low-density ratio configuration (Case 1)[155] ($R = 0.25$ [m]) and on the right it is described the setup for the high-density ratio configuration (Case 2) [317] ($R = 0.025$ [m]).

This test is done with two different particle resolutions 66×133 and 133×267 . The damping technique is applied here with $T_D = 1$. The reference speeds of sound for the two phases are set to $\{c_{01}, c_{02}\} = \{5.7, 18\}$ [m/s]. No-slip boundary conditions are applied on the upper and lower solid boundaries, while free-slip boundary conditions are applied on the left and right boundaries.

The position of the gravity center GC_y of the bubble and its vertical velocity v_{GC} are computed as follows

$$GC_y = \frac{\sum i^{N_b} y_i}{N_b}. \quad (7.13)$$

$$v_{GC} = \frac{\sum i^{N_b} v_{yi}}{N_b}. \quad (7.14)$$

N_b denotes the number of particles in the bubble, and y_i is the Y coordinate of the particle i which belongs to the particle set of the bubble. The term v_{yi} denotes the vertical component of the velocity of the particle i .

In figure 7.16 we compare our results for the time evolution of the vertical position of the gravity center of the rising bubble and its vertical velocity with the ones obtained in [155] using the VOF method. Basically, a good agreement is found between our SPH numerical results and those of reference [155], even though a slight difference for the position of the gravity center is detected, and some oscillations are observed around the VOF velocity curve. However, the overall SPH results are in good agreement with the reference ones.

In figure 7.17, we also compare the shape and position of the bubble interfaces at time $t = 3$ [s]. We observe a perfect agreement in this case.

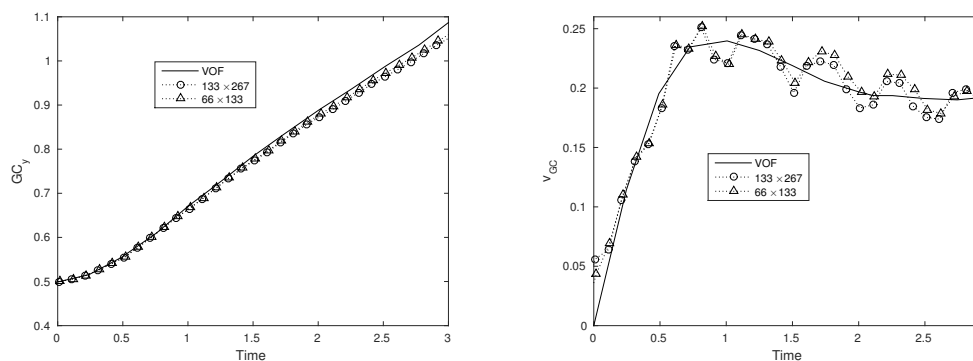


Figure 7.16 – Single bubble rising through a vertical column of water. Case 1: Time evolution of the position of the gravity center (left) and vertical velocity (right) of the rising bubble for different number of particles. The solid line represents the results obtained by VOF method [156].

Figure 7.18 shows the pressure and the magnitude velocity of the water column for two different particle resolutions at two different times $t = 1$ [s] and $t = 2$ [s]. Moreover, in figure 7.19 we show the direction of the velocity vector of the particles inside the bubble for the previous two resolutions at time $t = 1$ [s]. The results obtained for both particle resolutions are very similar, indicating the convergence of the numerical model.

Now we address the same case with a higher density ratio [317, 73, 128]. In this case, during the rising motion, the bubble undergoes a large deformation that subsequently splits it into three parts. The initial setup is presented in figure 6.1 and the physical variables and parameters for this test case are summarized at Table 7.1 as the Case 2.

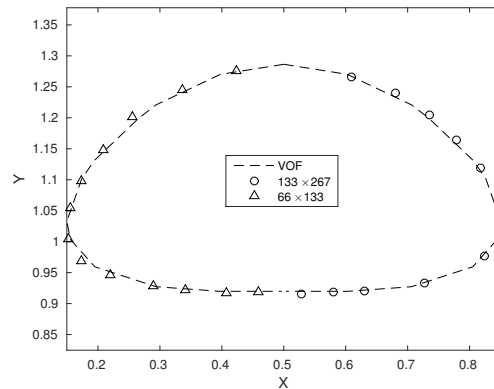


Figure 7.17 – Single bubble rising through a vertical column of water. Case 1: Comparison between the bubble interfaces at time $t = 3$ [s]: 66×133 SPH (Small triangles), 133×267 SPH (Small circles). Dashed line represent the interface obtained with the VOF method [155].

In this test we use a discretization of 240×400 particles. The reference speeds of sound are $\{c_{0_1}, c_{0_2}\} = \{7, 221.35\}$ [m/s]. The damping technique is used here with ($T_D = 0.05$ [s]). The boundary conditions are the same than for Case 1 of this section.

Figure 7.20 shows the velocity and relative pressure ($\widetilde{\Delta p} = p - p_{min}$) of the column of water at the dimensionless time $t \sqrt{\|g\|/R} = 3.6$. The bubble is strongly deformed and it is split in three parts during its evolution. The evolution of the bubble is presented in figure 7.21 at nine different instants. The particles inside the bubble are colored with the magnitude of the velocity. In figure 7.22 we compare the results obtained with the SPH method with those obtained using a Level-Set method [318]. The results of the SPH and Level-Set methods are in good agreement. During the rising process, the bubble deforms and takes a horseshoe shape. After that, the extremities roll-up until they undergo a big deformation which subsequently splits the bubble to form other small ones. The main difference between the results is that near to the symmetric axis the bubble obtained using the present SPH method is thicker than the one obtained by the level-Set method. The results for the width of the bubble remains in very good agreement during all the simulation period for both methods. We observe that in the Level-set solution the bubble splits in several very small bubbles that are not predicted by the present SPH method. Thereafter, these smaller bubbles disappear gradually from the Level-Set simulation.

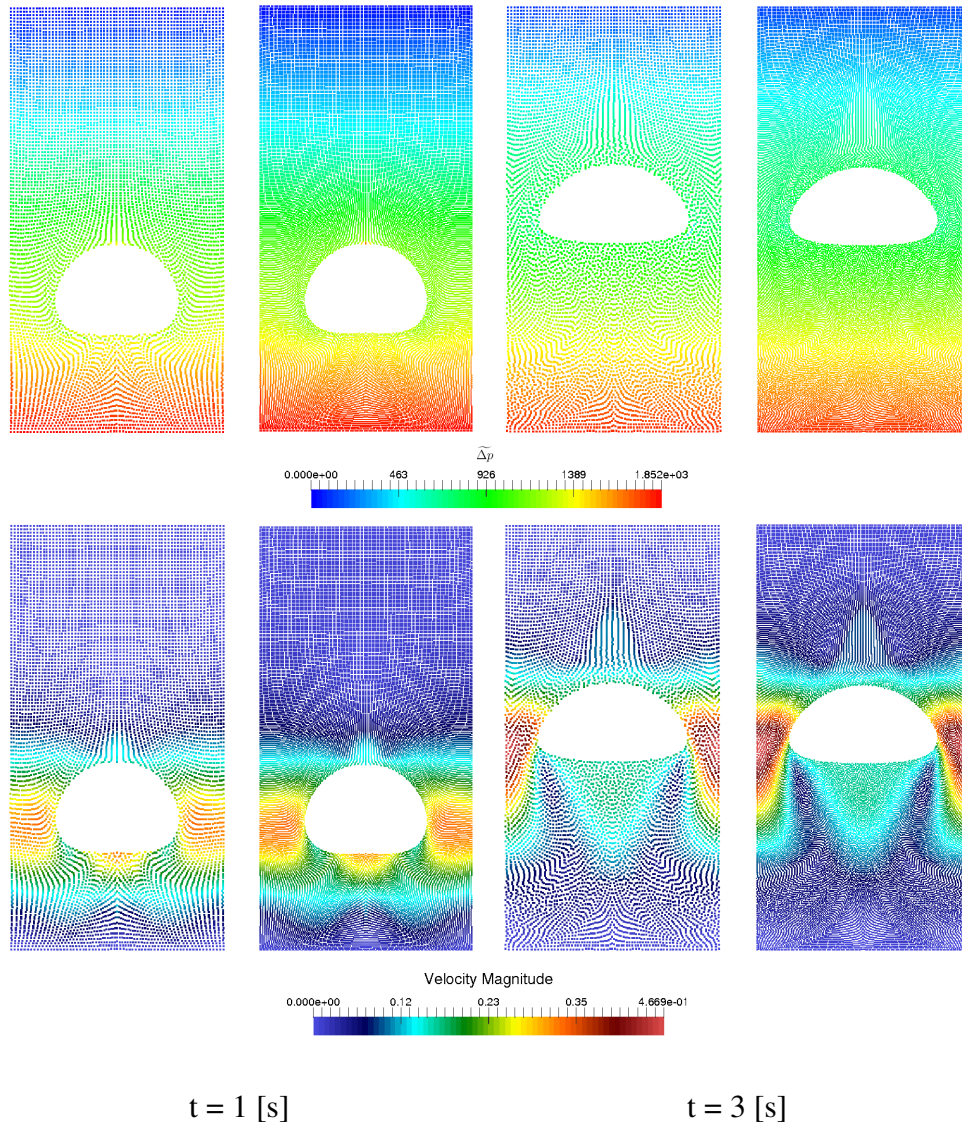


Figure 7.18 – Single bubble rising through a vertical column of water. Case 1: Pressure (top) and velocity (bottom) fields at times $t = 1$ [s] and $t = 3$ [s] for two different particle resolutions, 66×133 (left) and 133×267 (right).

Case	ρ_1 [kg/m^3]	ρ_2 [kg/m^3]	μ_1 [$Pa.s$]	μ_2 [$Pa.s$]	σ [N/m]	$\ g\ $ [m/s^2]	Re	E_o	$\frac{\rho_1}{\rho_2}$	$\frac{\mu_1}{\mu_2}$
1	1000	100	10	1	24.5	0.98	35	10	10	10
2	1000	1	0.035	0.0045	0.1226	9.81	1000	285.63	1000	7.77

Table 7.1 – Setup for Case 1 and Case 2 tests.

7.5 Gas bubble rising through two stratified fluid layers

This test example describes the behavior of a rising gas bubble through two stratified fluid layers (see figure 7.23). The gas bubble can cross the interface between layers with or

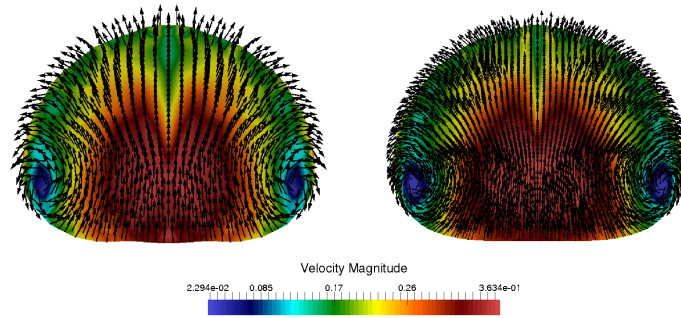


Figure 7.19 – Single bubble rising through a vertical column of water. Case 1: Direction of the velocity vector of the particles inside the bubble at $t = 1$ colored with magnitude velocity. On the left, results for 66×133 particles, and on the right we plot the results for the 133×267 particles case.

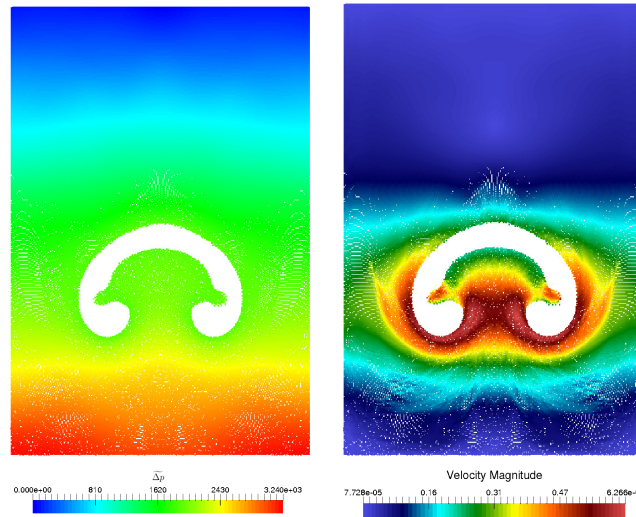


Figure 7.20 – Single bubble rising through a vertical column of water. Case 2: Relative pressure ($\widetilde{\Delta p} = p - p_{min}$) and magnitude of the velocity of the column of water at the dimensionless time $t\sqrt{\|g\|}/R = 3.6$

without entrainment of the heavier fluid into the lighter, or it could even remain trapped in it. Greene et al [125, 126] suggest a criterion on the bubble volume to predict this behavior based on a macroscopic balance between surface tension forces and buoyancy forces. Thus, if the bubble volume is greater than a critical volume V_c ($V_b > V_c$), the bubble will penetrate the interface layer and it will eventually entrain into the heavier fluid, otherwise the bubble will be trapped between the interface layers. The critical volume is calculated as follows

$$V_c = \left(\frac{2\pi \left(\frac{3}{4\pi}\right)^{1/3} \sigma^{2-3}}{(\rho_3 - \rho_1) \|g\|} \right)^{\frac{3}{2}} \quad (7.15)$$

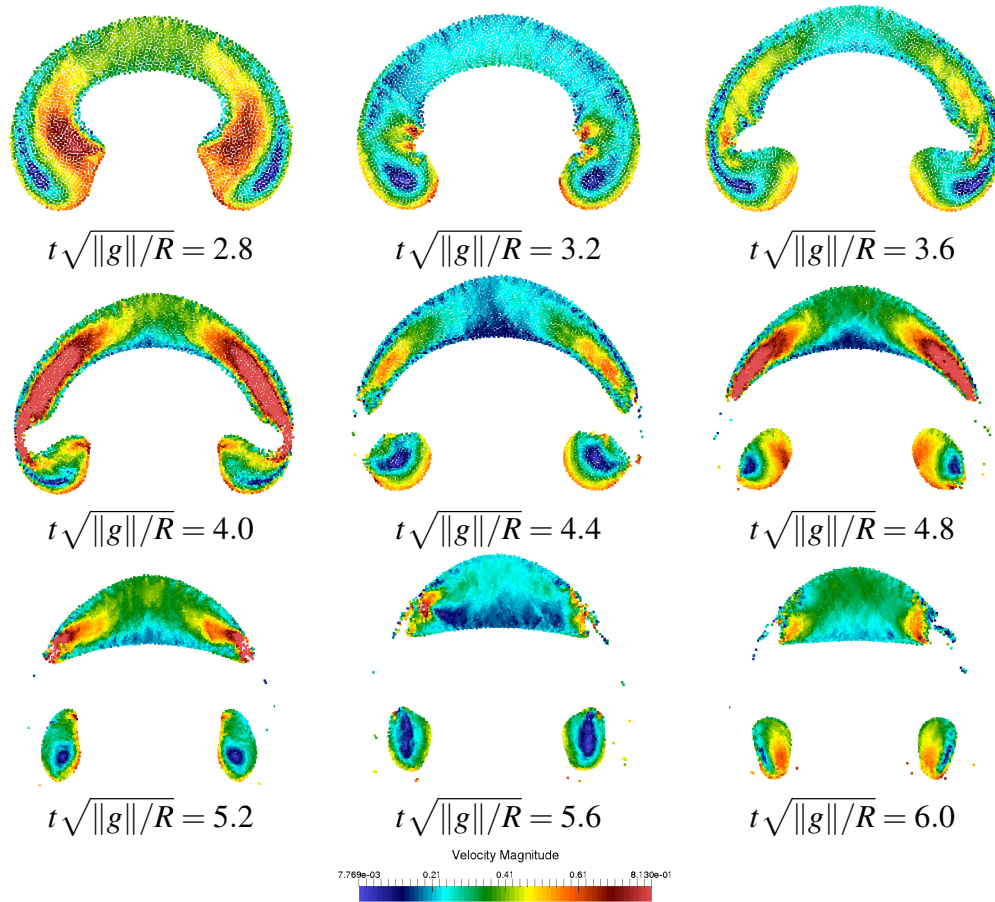


Figure 7.21 – Single bubble rising through a vertical column of water. Case 2: Evolution of the bubble at nine different instants. The Bubble is colored with velocity magnitude field.

In equation (7.15) the subscript(or superscript for surface tension) 1 corresponds to the lower fluid, 2 refers to the bubble, and 3 refers to the upper fluid.

This problem is very challenging from the numerical point of view since it involves high density and viscosity ratios and the presence of triple point junctions. The setup of the problem presented here is taken from [37]. The density and dynamic viscosity of fluid 1 (95% glycerin + water) are $\rho_1 = 1244 [kg/m^3]$, $\mu_1 = 550.1 \times 10^{-3} [Pa.s]$, in the case of the bubble (fluid 2) the chosen values are those of the air: $\rho_2 = 1.205 [kg/m^3]$ and $\mu_2 = 5 \times 10^{-3} [Pa.s]$. Note that the value of air bubble viscosity is chosen greater than the real one and equal $\mu_2 = 5 \times 10^{-3} [Pa.s]$ instead the use of the real gas viscosity with an artificial one to guarantee the stability of the algorithm [245]. Finally, for the fluid 3 (47V500 oil), the values are $\rho_3 = 965$. and $\mu_3 = 530.7 \times 10^{-3} [Pa.s]$. The surface tensions are $\sigma^{1-2} = 45.1613 \times 10^{-3} [N/m]$, $\sigma^{1-3} = 21 \times 10^{-3} [N/m]$, $\sigma^{2-3} = 28 \times 10^{-3} [N/m]$, and the speeds of sound are taken as $\{c_{01}, c_{02}, c_{03}\} = \{3.7, 118.88, 4.2\} [m/s]$. The radius of the

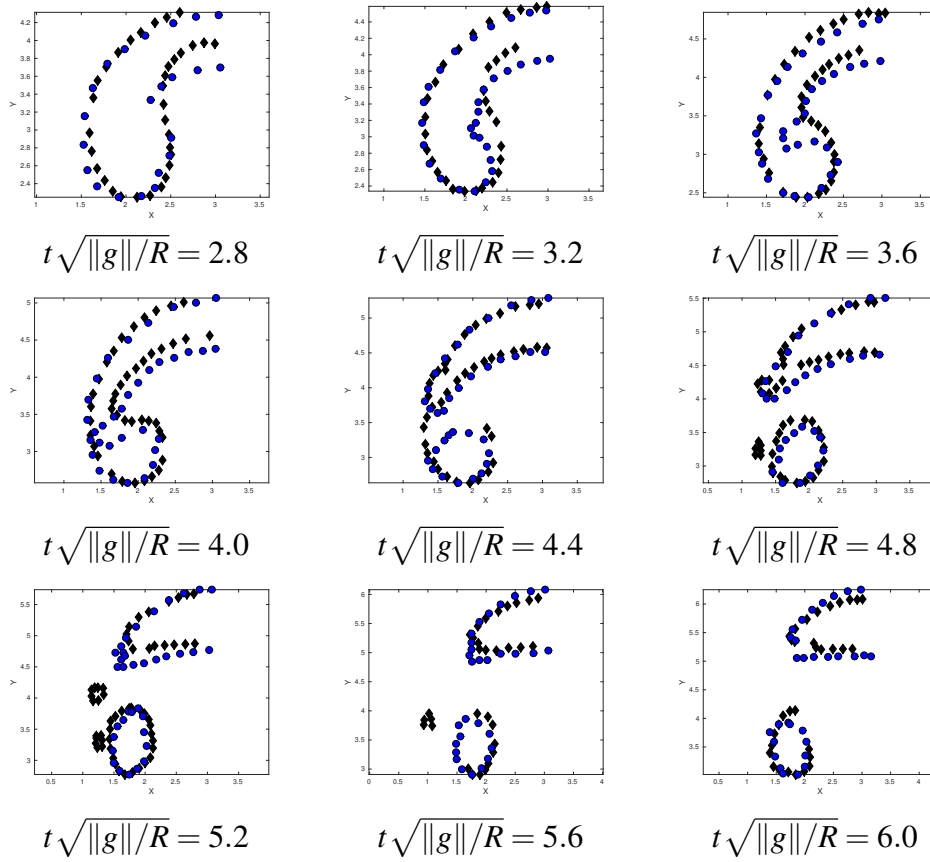


Figure 7.22 – Single bubble rising through a vertical column of water. Case 2: Evolution of the bubble at nine different instants. Results obtained with the present SPH method (blue circles) and with a Level-Set approach [318] (black diamonds).

air bubble is $R = 3.5 \times 10^{-3}$ [m]. These data correspond to a Reynolds number $Re \approx 4.15$ and Eötvös number $E_o \approx 13.24$. For the simulation, a regular lattice with 50×166 particles is employed. No-slip boundary conditions are applied on the top and bottom boundaries, and periodic boundary conditions are applied on the left and right edges of the domain. The dimensions of computational domain are detailed in figure 7.23. The damping technique is used with $T_D = 0.05$ [s].

The critical volume is computed using equation (7.15) which gives $V_c \approx 3.92 \times 10^{-8}$ [m³]. This implies a critical radius of $R_c \approx 0.021$ [m]. In this example, the initial radius of air bubble $R = 0.0035$ [m] is greater than the critical one which logically involves that the $V_c < V_{Bubble}$. With this values, the air bubble penetrates the interface fluid layers [38].

In figure 7.24 we show the numerical results for the relative hydrostatic pressure field $\widetilde{\Delta p} = p - p_{min}$, the magnitude of the velocity field and the distribution of the three different phases in different instants. The dimensionless interval between two images is taken equal to

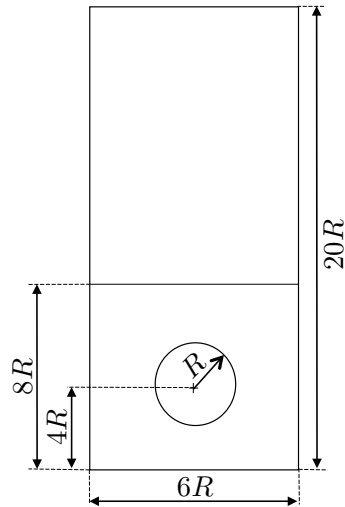


Figure 7.23 – Gas bubble rising through two stratified fluid layers. Geometrical details of the problem setup.

$\Delta t \sqrt{\|g\|/R} = 4.3$ [37]. In figure 7.25 we compare the numerical results with the experimental images obtained in [37]. The numerical results are in good agreement with the experimental ones. The differences between the numerical and experimental sequences are maybe due to uncertainties in the initial conditions of the experimental test and possibly to any 3D effect.

7.6 Conclusion

A series of numerical tests have been devoted in order to the validation of the accuracy and convergence of the surface tension formulation and achievement of the high ratio of density and viscosity of multiphase fluid flows. The obtained results are very satisfactory which demonstrate the consistency, stability and applicability of our proposed SPH interfacial multiphase fluids model including high density and viscosity ratios and triple junction points.

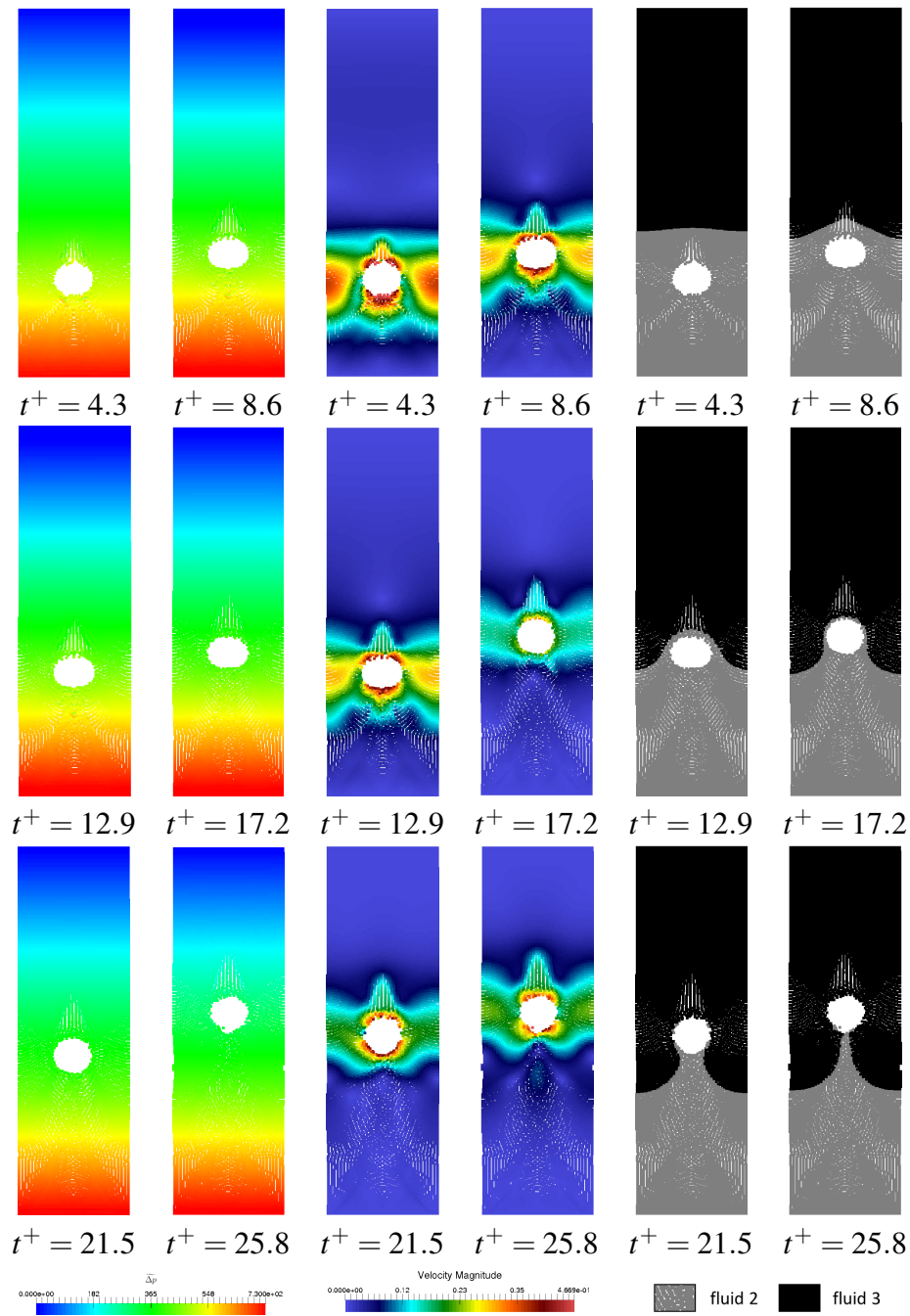


Figure 7.24 – Gas bubble rising through two stratified fluid layers. Starting from the left, first and second columns show the relative hydrostatic pressure field $\Delta \tilde{p} = p - p_{min}$ for different normalized times $t^+ = t\sqrt{\|g\|/R}$. Third and fourth columns present the magnitude of the velocity field. The last two columns show the fluid phases distribution.

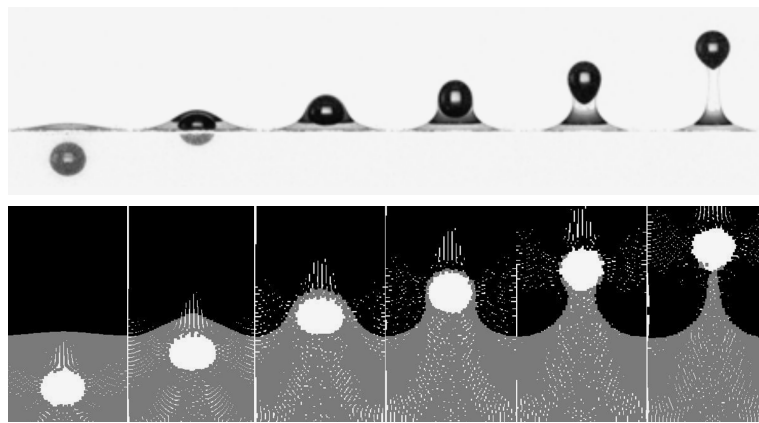


Figure 7.25 – Gas bubble rising through two stratified fluid layers. On the top, we show the experimental sequence taken from [37]. On the bottom we plot the results obtained using the proposed SPH method. The dimensionless interval between two images is taken equal to $\Delta t \sqrt{\|g\|/R} = 4.3$

Chapter 8

Validation and application of SPH water-soil interactions model

Dans ce chapitre, la robustesse, la précision et l'applicabilité de notre modèle multiphasique sont démontrées via plusieurs benchmarks. La validation de l'efficacité du terme diffusif multiphasique développé $D^{\delta-MSPH}$ est montré en utilisant l'exemple d'une colonne de deux couches de fluide Newtonien stratifiées en repos. L'applicabilité pour la simulation dynamique des matériaux granulaires est démontrée via les benchmarks de l'effondrement d'une colonne de fluide Binghamien et l'étalement d'une pile de matériau granulaire sur une surface horizontale. Tandis que pour la simulation des problèmes d'interactions eau-sol, les exemples de glissements de terrain sous-marins et subaériens sont consacrés. Un modèle de sédiments en suspension dans l'eau est imbriqué dans notre modèle SPH multiphasique pour bien capter les phénomènes d'érosion. Une simulation d'un écoulement de rupture de barrage sur un banc de sédiments érodables est utilisée pour démontrer l'efficacité du modèle de sédiment en suspension dans l'eau. À la fin, un benchmark démonstratif des phénomènes multiphysiques (le glissement de terrain subaérien générant des vagues d'eau impulsives, inondation et érosion) lié à l'interaction sol-eau est proposé pour montrer la capacité du modèle SPH multiphasique proposé dans ce travail.

In this chapter, the robustness, accuracy and applicability of our multiphase model is demonstrated via a several benchmarks. The validation of the efficiency of the developed multiphase diffusive term $D^{\delta-MSPH}$ is performed using the two stratified hydrostatics Newtonian fluid layers benchmark. The applicability on simulation of single phase of granular materials dynamics is demonstrated via the benchmarks of Bingham fluid dambreak and spreading of granular material pile on horizontal surface. Whereas for the simulation of the water-soil interactions problems, the submarine and subaerial landslides benchmarks are devoted. A suspended water sediment model is nested in our multiphase model to capture well the erosion phenomena. A simulation of a dambreak flows over erodible sediment bed benchmark is used for the demonstration of the efficiency of the added suspended water sediment model. Finally, a demonstrative benchmark of multi-physics phenomena (Subaerial landslide generated impulsive wave, flooding and scouring erosion) related to the soil-water interaction is proposed to show the capabilities of the newly proposed multiphase SPH model.

8.1 Two phases hydrostatic stratified column

The purpose of this test is to show the ability of multiphase diffusive terms $\mathcal{D}^{\delta-MSPH}$ of the present work comparing with $\mathcal{D}^{\delta-SPH}$ of equation (5.27) (applied with the procedure as in [108]) to reduce and smooth the oscillations of the computational pressure in the context of multiphase WCSPH. A two-dimensional (2D) tank of $0.6[m]$ long and $0.45[m]$ high is full with two stratified immiscible fluids (see figure 8.1). The upper fluid layer is considered as the lighter one with a density $\rho_1 = 1000[kg/m^3]$, while the lower layer is the heavier fluid with a density $\rho_2 = 2000[kg/m^3]$. The upper and lower fluids behave as Newtonian with a constant viscosity of $\mu_1 = 0.02[Pa.s]$ and $\mu_2 = 0.001[Pa.s]$, respectively. Both fluids are subjected to a vertical gravity acceleration of $-9.81[m/s^2]$.

We investigate the stability and convergence of the pressure field using our developed diffusive term $\mathcal{D}^{\delta-MSPH}$ and the classical one $\mathcal{D}^{\delta-SPH}$ applied separately on each fluid phase as in [108]. A resolution of 59×20 particles is chosen for this test case. The reference speeds of sound for the lighter and heavier fluids are chosen $c_{0_1} = 20 [m/s]$ and $c_{0_2} = 14.14 [m/s]$ in order to obtain the same reference pressure $p_r = \rho_1 c_{0_1}^2 = \rho_2 c_{0_2}^2 = 4 \times 10^5 [Pa]$.

Figure 8.2 shows the time evolution of the pressure calculated at three different points P_1 , P_{int} and P_2 (placed at locations as indicated in figure 8.1). Pressures at measurement points are approximated using the Shepard filter [305]). Thus, for the point P_1 the pressure is computed as

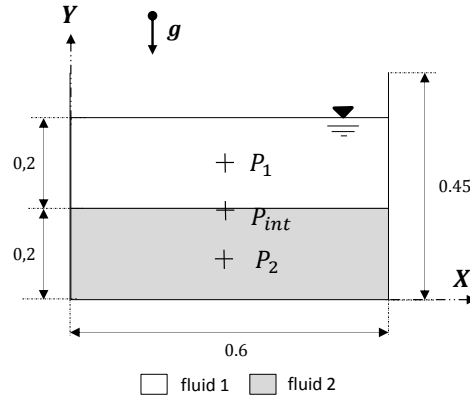


Figure 8.1 – Geometrical details of two phases hydrostatic stratified column configuration. $P_1 = (0.3, 0.5)$, $P_{int} = (0.3, 0.2)$, $P_2 = (0.3, 0.1)$ are the pressure measurement points located at the center of the layer of the fluid 1, the interface between the two fluids and the center of the fluid layer 2, respectively.

$$p(P_1) = \frac{\sum_i^n V_i p_i W(P_1 - r_i)}{\sum_i^n V_i W(P_1 - r_i)} \quad (8.1)$$

We observe that the calculated pressures at different points stabilize to approximate the hydrostatic pressure values after the time $t = 2.5[s]$ when the multiphase diffusive term $\mathcal{D}^{\delta-MSPH}$ is used as is shown in figure 8.2 (a).

In the case of classical diffusive term $\mathcal{D}^{\delta-SPH}$ the pressures remain relatively instable during all simulation period (7[s]) and present an important error specially at the interface between the fluid phases (as shown in figure 8.3 (b)). The pressure errors are generated accordingly to the instability of the interface between the phases as shown in the figure 8.3 (b). In figure 8.3 (a) it is observed the stability of the interface between the fluid phases and the smoothness of pressure distribution at later time after the stabilization (at $t = 7[s]$) when the formulation $\mathcal{D}^{\delta-MSPH}$ is used.

In order to analyze the results without taking into account the effect of the pressure filtration due to the use of Shepard filter (8.1), the pressure distribution on each particle is plotted against the analytical hydrostatics ones at the time $t = 7[s]$. This is shown in figure 8.4. It is observed that computed pressures using the multiphase diffusive term $\mathcal{D}^{\delta-MSPH}$ are in good agreement with the analytical values for both fluid layers and the interface between them (see figure 8.4 (a)). When the $\mathcal{D}^{\delta-SPH}$ model is used, pressure results do not match with the analytical ones specially at the interface, where we observe important differences (see Figure 8.4 (b)).

From this test, we can conclude that the use of $\mathcal{D}^{\delta-MSPH}$ diffusive terms in the context of the WCSPH method enhances significantly the stability and smoothness of computed pressure for the fluid phases.

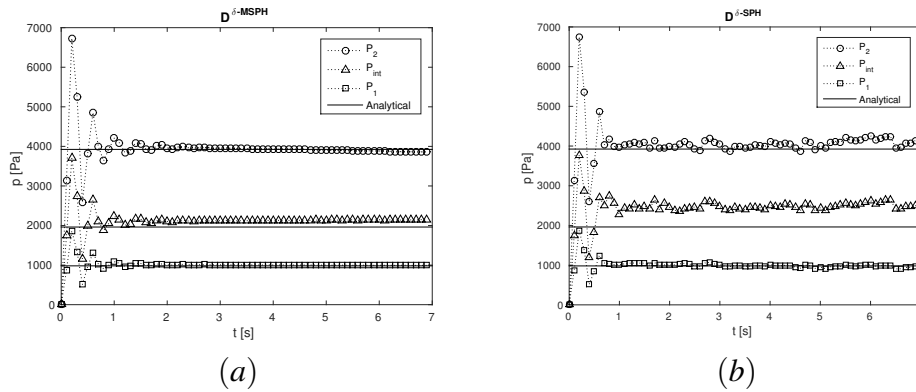


Figure 8.2 – Time evolution of pressure at the points P_1 , P_{int} and P_2 plotted against the analytical hydrostatic values represented in solid lines. The left figure represents the pressure results using the multiphase diffusive term $\mathcal{D}^{\delta-MSPH}$ of present work. The right figure represents the pressure results using the classical diffusive term $\mathcal{D}^{\delta-SPH}$ independently in each fluid phase.

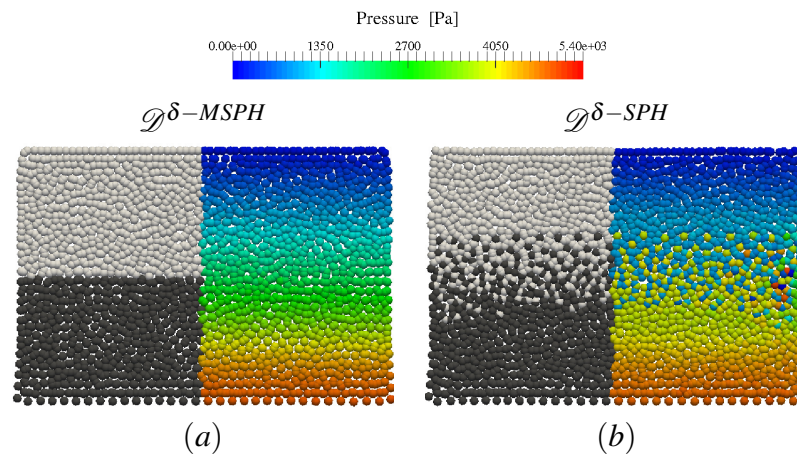


Figure 8.3 – Fluid phases distribution and hydrostatic pressure representation at $t = 7$ [s]. The gray color is chosen for the phase 1 and the black for the phase 2). The colored part shows the hydrostatic pressure field. Figure (a) shows the results using the multiphase diffusive term $\mathcal{D}^{\delta-MSPH}$ presented in this work, whereas figure (b) shows the results using the classical diffusive term $\mathcal{D}^{\delta-SPH}$. Notice the smooth distribution obtained with the proposed methodology.

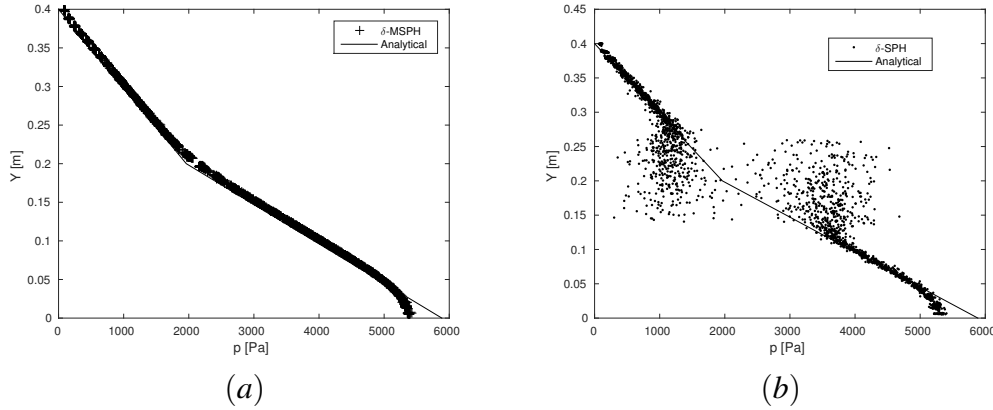


Figure 8.4 – Computed pressure values at all particles for all fluid phases at time $t = 7[s]$ plotted against the analytical hydrostatic pressure (solid black line). On the left it is shown the pressure computed using the multiphase diffusive term $\mathcal{D}^{\delta-MSPH}$ presented in this work. On the right, the results using the classical diffusive term $\mathcal{D}^{\delta-SPH}$.

8.2 Bingham fluid dam-break

This example is investigated in order to show that the proposed SPH model with the RBPMC- α_μ constitutive law (equation (5.23)) can accurately deal with Bingham materials (non-frictional materials: with $\phi = 0$ and $c = \tau_y$) in simulation problems in the context of Non-Newtonian free surface flow simulations.

The dam-break benchmark proposed by Komatina and Jovanovic [175] was reproduced numerically in this work. This benchmark was already investigated by other authors [352, 145] using SPH method.

A rectangular column of a single fluid with a height of $H = 0.1[m]$ and length of $L = 2[m]$ is confined between two fixed walls (at the left side and at the bottom) and a moving wall at the right side. The moving wall is removed and the fluid starts to flow under the effect of gravity $g = 9.81[m/s^2]$ (see figure 8.5). The fluid is considered as a water–clay mixture with a volume concentration of $C_v = 27.4\%$. The bulk density of the water–clay mixture is $\rho_{cw} = 1200kg/m^3$, and the fluid is considered as a Bingham Plastic. The plastic viscosity and the yielding shear stress area are estimated according to [175] as $\mu_{cw} = 0.621 \exp(0.173C_v) \approx 0.07 [Pa.s]$ and $\tau_y = 0.002 \exp(0.342C_v) \approx 25[Pa]$, respectively.

A distribution of 400×20 particles is used to discretize the rectangular fluid column. The speed of sound is ($c_0 = 10u_0 \approx 14 [m/s]$) with u_0 a reference velocity that is calculated following Torricelli's law ($u_0 = \sqrt{2Hg}$). Two values of the regularization parameter $\alpha_\mu = \{100, 1000\}$ are tested to investigate their influence on results.

In figure 8.6 the time-evolution of dimensionless front position ($X_F/H = (x - L)/H$) is plotted for the present SPH model using two values of control parameter $\alpha_\mu = \{100, 1000\}$, the incompressible non-Newtonian SPH model (INNSPH) of Xenakis et al [352], and the experimental results of Komatina and Jovanovic [175]. A good agreement between the present SPH formulation, the INNSPH model [352] and the experimental results are observed. In the case of the proposed method, the best results are obtained when a control parameter $\alpha_\mu = 1000$ is employed. It is also observed that the flow tends to stabilize at a rigid form (the so-called "freeze-point") with increasing time, since the shear stress at every computational particle do not exceed the yield stress τ_y . In figure 8.7 the results for the particle positions using the present SPH model with $\alpha_\mu = 10000$ at five different time steps $t = \{0.1, 0.3, 0.6, 1, 2\}[s]$ are presented. Fluid particles are colored with the hydrostatic pressure field. These results are used for a comparison between the free surfaces obtained with the present SPH model with $\alpha_\mu = 1000$, the INNSPH model [352], and the control volume finite element method (CVFEM) of [352] at two different time instants $t = \{0.6, 2\}[s]$. This comparison is presented in figure 8.8. The free surface obtained by the proposed WCSPH approach is between those of INNSPH and CVFEM.

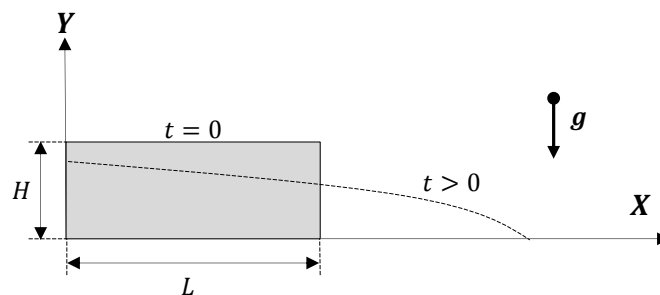


Figure 8.5 – Bingham fluid dam-break configuration.

8.3 Spreading of granular pile on horizontal plan

In order to show the efficiency of the proposed SPH model including the RPBMC- α_μ rheology for the simulation of cohesionless granular flow problems, the experimental benchmark proposed by [183] is reproduced. In this benchmark, a heap of dry granular material (glass beads) of length L and height of H (aspect ratio $a = \frac{H}{L}$) spreads on an horizontal roughness plane. The granular heap is initially blocked between a fixed glass wall at the left side a movable gate at the right side and a fixed rough wall at the bottom. The channel and the granular heap have the same uniform width ($W = 0.045[m]$) (see figure 8.9). The granular heap has a mass of $470[g]$, a height of $61[mm]$ ($H \approx 61[mm]$) and a

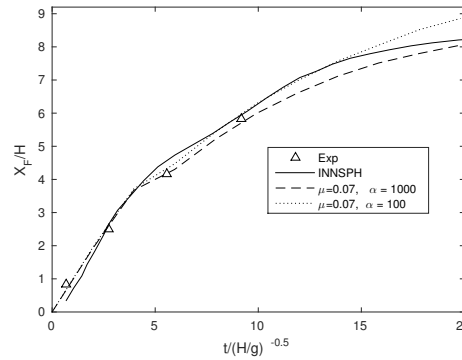


Figure 8.6 – Time-evolution of dimensionless Bingham dam-break front position ($X_F/H = (x_F - L)/H$). We compare the results obtained using the proposed method with a plastic viscosity ($\mu = 0.07$) and coefficients $\alpha_{mu} = 100$ (dotted line) $\alpha_{mu} = 1000$ (dashed line), with INNSPH(Incompressible Non-Newtonian SPH) [352] (solid line) and with the experimental results of Komatina and Jovanovic [175] (small triangles).

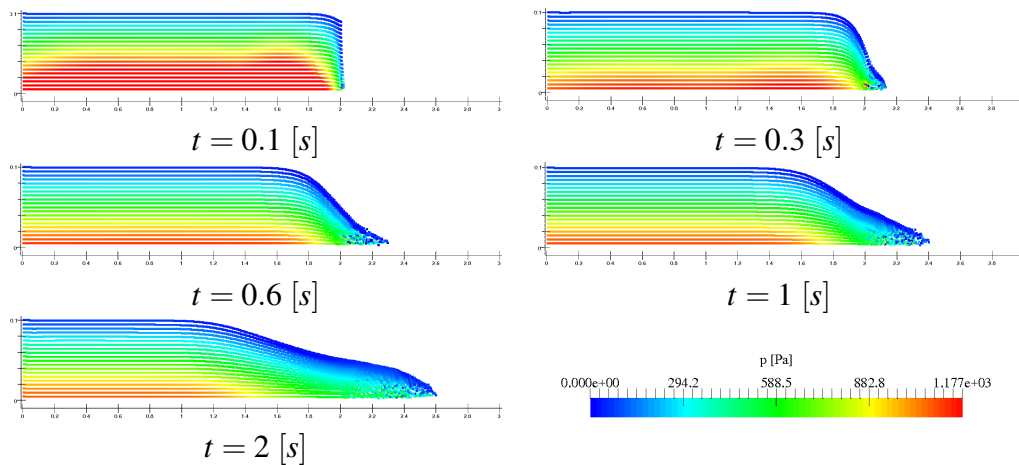


Figure 8.7 – Bingham dam-break flow at times $t = 0.1, 0.3, 0.6, 1, 2[s]$. The particles are colored with pressure values. The Y-axis is scaled by a factor of 5 for the sake of clarity.

length of $102[mm]$ ($L = 102[mm]$)(aspect ratio of $a = 0.6$). Since $L \gg W$ the behavior of three-dimensional granular flow can be considered as a two-dimensional one. Thus, in this work we consider only a two-dimensional configuration.

The glass bead is considered as a granular material with a grain density of $\rho_g = 2500[kg/m^3]$, and angle of repose $\phi_r \approx 22^{\pm 0.5}$ deg (it is equivalent to an internal friction angle $\phi \approx \phi_r \approx 22^{\pm 0.5}$ deg). The bulk density is approximated as $\rho_b \approx 1673[kg/m^3]$. This bulk density is calculated from the mass and volume of the granular heap by dividing the mass by the volume of pile ($\rho_b = \frac{Mass}{HLW}$) [182, 183].

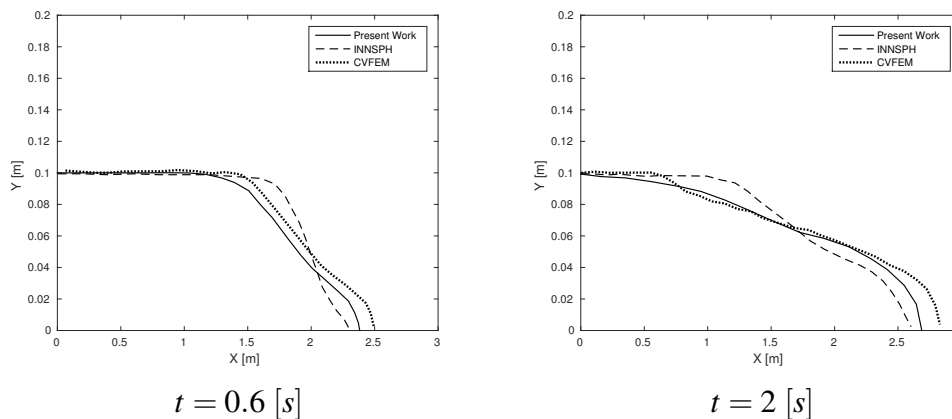


Figure 8.8 – Comparison between the free surface profiles of the present SPH method with a plastic viscosity ($\mu = 0.07$) and $\alpha_\mu = 1000$ (solid line), the INNSPH method [352] (dashed line) and CVFEM [352] (dotted line) at times $t = \{0.6, 2\}$ [s]

In this work the dynamic plastic viscosity of the glass beads is set to $\mu = 0.1$ [Pa.s] following [159]. Four values of control parameter of the RBPMC- α_μ ($\alpha_\mu = \{100, 1000, 2000, 3000\}$) were used. The results of our simulations were compared with the experimental results of [183].

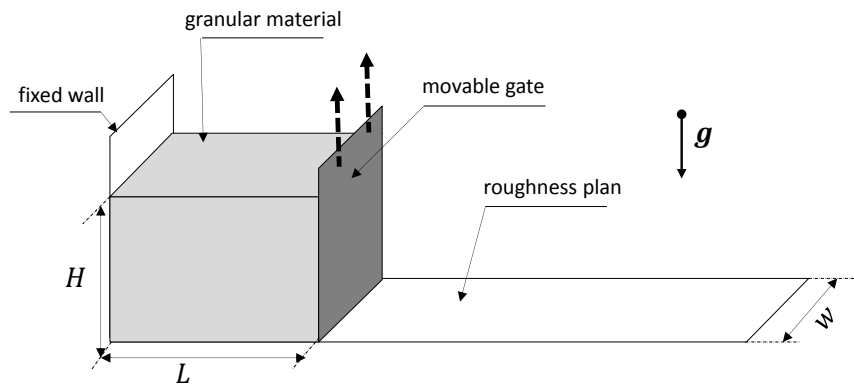


Figure 8.9 – Spreading of granular pile on horizontal plan: Schematics of the experimental configuration [183].

The granular column is represented by 50×30 particles (the initial inter-particle distance is $\delta_x = 0.002$ [m]). The reference speed of sound of the granular material is set to $c_0 = 11$ [m/s] (reference pressure $P_r = 202433$ [Pa]). A no-slip boundary condition is applied on the horizontal wall (rough wall), while free-slip boundary condition is applied on the vertical fixed wall.

In figure 8.10, the time evolution of the dimensionless front position ($X_F/H = (x - L)/H$) of the granular column is presented for the experimental and numerical results. A

disagreement between the numerical and experimental results is observed when the value $\alpha_\mu = 100$ is used. In this case, the numerical granular column continue to spread because of the low viscosity value assigned by the RBPMC- α_μ rheology model to the column ($\mu_{max} = 100\mu = 10[Pa.s]$). However, a very good agreement is observed when the value of α_μ is sufficiently higher ($\alpha_\mu = \{1000, 2000, 3000\}$). The best results are obtained by using $\alpha_\mu = 3000$.

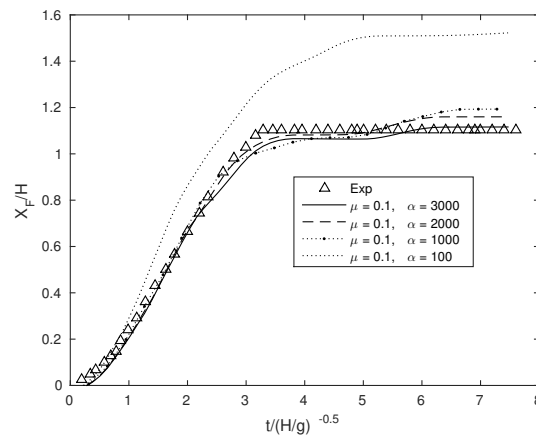


Figure 8.10 – Spreading of granular pile on horizontal plan: Time-evolution of the dimensionless front position of the glass beads pile. We plot the results of the proposed numerical method using $\alpha_\mu = 100$ (dotted line), $\alpha_\mu = 1000$ (dash-dot line), $\alpha_\mu = 2000$ (dashed line) and $\alpha_\mu = 3000$ (solid line), and the experimental data of Lajeunesse et al [183] (small triangles).

The shape evolution of the collapsing granular column profile for both experimental and numerical results is shown in figure 8.11 at times $t = \{0, 0.8, 0.16, 0.24, 0.32\}[s]$. A value of 3000 of the control parameter ($\alpha_\mu = 3000$) is used for the computation. The SPH particles are colored with the magnitude of the velocity in order to show the dynamic and the "freeze-point" of the collapsing column. The granular column stops spreading and takes the trapezoidal shape at $t = 0.32[s]$ for both numerical and experimental results. A very good agreement is observed between the numerical and experimental granular column profiles at different times. Nevertheless, a difference between the numerical and experimental granular column profiles is remarked at earlier stage at $t = 0.8[s]$. This is may be due to the process of moving the gate in the initial stage of the experiment that is not represented in the numerical simulation.

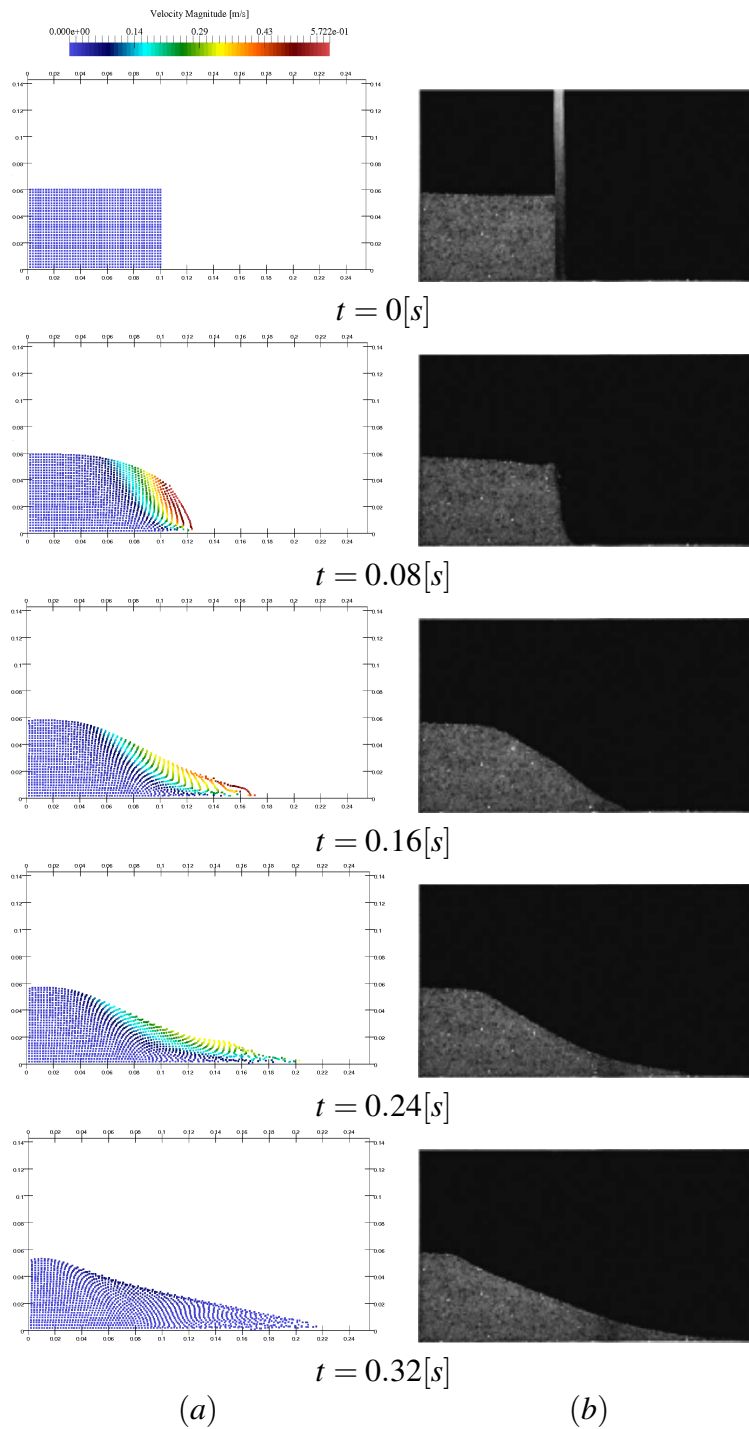


Figure 8.11 – Spreading of granular pile on horizontal plan: Sequences of the position of the granular material (glass beads) using the proposed SPH model with $\alpha_\mu = 3000$ (a) and experimental results of Lajeunesse et al [183] (b).

8.4 Landslide-generated wave

A landslide, also known as slope failure, slumps or landslip is a big mass of ground driven on a slope by gravity effort. Landslides can occur under-water (submarine) or upper-water (Subaerial). The potential energy of land sliding in the water bodies (oceans, seas, lakes and reservoirs) consequently generates an impulse wave that may potentially cause significant disasters. Papua New Guinea in 1998 [323] and Lituya Bay- Alaska in 1958 [224] tsunamis caused by a submarine and subaerial landslides, respectively, are demonstrations of the great destructive potential of these phenomena.

Submarine land-slide-generated water wave

In this example, we investigate the capability of the proposed multiphase SPH model to simulate water-land interactions related to submarine landslides. The land here is modeled as a purely cohesive material ($\phi = 0$, $c = \tau_y$). Here we reproduce the experiment of Rzadkiewicz et al [290, 289], and we compare our numerical results with those of [52]. This experiment examines the water waves generated by the sliding of sand mass along a slope of 45 deg . The dimensions of the channel are 2[m] high and 4[m] long. The initial profile of the sand mass has a triangular shape with a cross-section of 0.65[m] \times 0.65[m]. The sand mass has the same wide as the channel, so that the problem can be considered as two-dimensional. The density and viscosity of the water are set to $\rho_w = 1000[\text{kg}/\text{m}^3]$ and $\mu_w = 0.001[\text{Pa}\cdot\text{s}]$, respectively. The bulk density of the sand is 1950[kg/m^3]. The depth of the water is 1.6[m] and the top of triangular sand mas is initially located below the surface water by 0.1[m]. Figure 8.12 gives more geometrical details about the submarine landslide configuration.

In the work of Rzadkiewicz et al [290] the rheological parameters were not measured experimentally. They were chosen by numerical experience as $\tau_y = 1000[\text{Pa}]$ and $\mu = 0[\text{Pa}\cdot\text{s}]$. In this work we choose the same yielding stress, but a small value of plastic viscosity ($\mu = 0.001[\text{Pa}\cdot\text{s}]$) is chosen instead of zero. The reason is the necessity of using a non-null plastic viscosity in our rehological model RBPMC- α_μ . The control parameter is $\alpha_\mu = 10^6$.

The numerical simulations were carried out using a homogeneous resolution of 16819 particles (15916 particles for the water and 903 particles for the land mass), with an initial inter-particle spacing $\delta x = 0.0015[\text{m}]$ similarly to the work of Capone et al [52].

The speed of sound is chosen equal to $c_0 = 55[\text{m}/\text{s}]$ for the water phase which leads to a reference pressure of $P_r = 3.02510^6[\text{Pa}]$. The No-Slip boundary conditions are applied on all the rigid boundaries.

The numerical results of particles distribution for both land mass (dark gray color) and water (light grey color) are represented in the figure 8.13 at times $t = 0.4[\text{s}]$ and $t = 0.8[\text{s}]$.

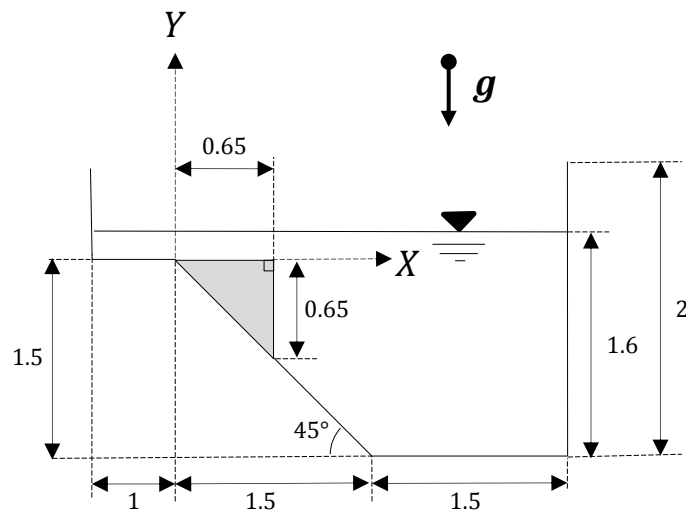


Figure 8.12 – Submarine land-slide-generated water wave: Geometrical details and setup of the problem.

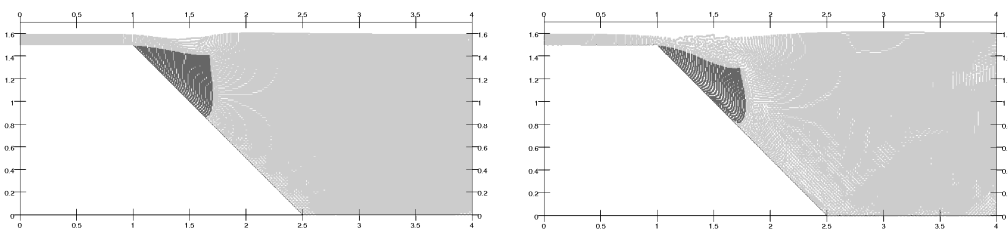


Figure 8.13 – Submarine land-slide-generated water wave: Particle distribution at times $t = 0.4[s]$ and $t = 0.8[s]$.

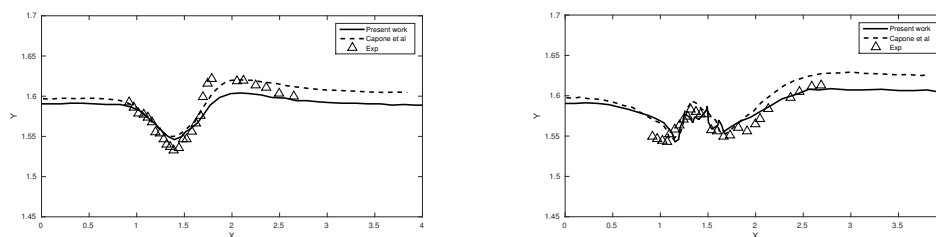


Figure 8.14 – Submarine land-slide-generated water wave: Comparison between the free surfaces at $t = 0.4[s]$ and $t = 0.8[s]$ obtained with the proposed SPH model, the SPH model of Capone et al. [52] and the experimental results of Rzdakiewicz et al [290, 289].

In the figure 8.14 the comparison between the water free-surface elevation at times $t = 0.4[s]$ and $t = 0.8[s]$ is represented between the current SPH model, the SPH model of Capone et al. [52] and the experiment of Rzdakiewicz et al [290, 289]. The SPH formulation presented in [52] is based on a bi-viscosity rheological model [32] considered within the artificial viscosity term presented by Monaghan [245]. Quantitatively, a good agreement

between our SPH model, Capone SPH model and experiment results is observed. At time $t = 0.4[s]$ the results given by the SPH model of Capone et al. is closer to the experiment than our current approach. However, for the time $t = 0.8[s]$ our multiphase SPH model gives more accurate results compared with the experimental results.

Sub-aerial land-slide-generated water wave

The purpose of this example is to investigate the efficiency of our multiphase SPH model to simulate a Sub-aerial land-slide-generated water wave. The land mass is modeled using a RBPMC- α_μ rheology where purely frictional/cohesionless ($c = 0$) model is considered (glass beads). Here, the experimental benchmark performed by Viroulet et al [342, 341] was reproduced numerically (see figure 8.15). It consists on the study of the interactions between the granular mass collapse and the water that generate impulse waves. A tank of $2.2[m]$ long, $0.4[m]$ high, and $0.20[m]$ wide includes an inclined plan at the left side with slop of 45 deg to allow slipping of the land mass (granular material). The tank is full initially with water of depth of $0.15[m]$. The land mass is blocked initially on the inclined plan and a vertical movable gate where the bottom of the land mass is located at the level of the free surface water (see figure 8.15). When the vertical gate is opened, the land impacts the surface water at a low velocity, generating impulse waves propagating along the tank. The evolution of the generated impulse waves and the granular flow shape are recorded experimentally with a high speed camera. The amplitudes and the propagation of the generated wave are measured with four resistive gauges located at four different distances $0.45, 0.75, 1.05,$ and $1.35[m]$ from the vertical movable gate. The granular material used for the land mass is composed of glass beads of density $\rho_s = 2500[kg/m^3]$, porosity of $n = 40\%$, frictional angle of $\phi = 23.3$ deg and the mass of $3[kg]$ (it gives $l = 0.2[m]$).

When the grain of the granular material slides at low velocity into the water, it mix with the water. Then, the bulk density is defined as a mix $\rho_b = (1 - n)\rho_s + n\rho_w = 1900[kg/m^3]$. The density and dynamic viscosity of the water are taken as $\rho_w = 1000[kg/m^3]$ and $\mu_w = 0.001[Pa.s]$, respectively. The Plastic viscosity of the land is taken to be equal to the water dynamic viscosity $\mu = \mu_w = 0.001[Pa.s]$, and the control parameter is set to $\alpha_\mu = 3 \times 10^7$.

The simulation is performed with a resolution of 32306 particles (31225 particles for the water and 1081 particles for the land mass), with initial spacing of $\delta x = 0.003[m]$. The reference speed of sound for water is taken $c_0 = 17[m/s]$ (it gives a reference pressure pressure of $2.89 \times 10^5[Pa]$). At tank walls and the inclined plan a no-slip boundary condition is used for the computation.

In figure 8.16, the elevation of the water free surface captured numerically and experimentally at four different position of wave gauges (G_1, G_2, G_3 and G_4) is plotted. A good

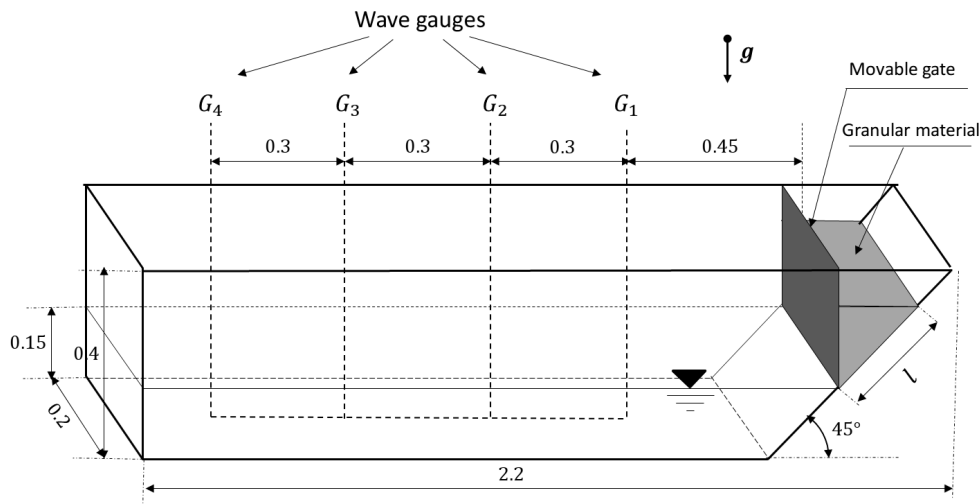


Figure 8.15 – Sub-aerial land-slide-generated water wave: Schematic view of the experimental setup and geometrical details.

agreement between the numerical simulation and experimental results during a period of 2[s] was observed. However, an amplitude shift between the numerical and experimental results is also observed. This can be a consequence of the use of the bulk density of the land mass that is fully mixed with water. However, very satisfactory results are observed concerning the water wave frequencies.

Quantitatively, a satisfactory agreement is observed between the experimental and numerical sliding granular mass into the water at three different time step $t = \{0.21, 0.43, 0.52\}$ [s] as is shown in figure 8.17. The water velocity field for the simulation and experimental results using the particle image velocimetry technique (PIV) is also shown in the same figure. At time $t = 0.21$ [s], the impact of the land mass on the water and beginning of the generated first wave are shown. Here, the elevated part of the water has a greater velocity and also we observe that the water region closer to the landslide head has high velocity. for the times $t = 0.43$ [s] and $t = 0.52$ [s], the slide starts to roll up creating a turbulent water region. Also we observe the onset of the second generated wave accompanied by the propagation of the first wave. The velocity is always greater at the more elevated part of the water the and at vicinity of the land front head. The roll up of the land head is more important in the experimental than in the numerical results. This issue is may be due to the low particle resolution that is used to simulate the granular mass. However, very satisfactory results are observed for the shape of the free surface water.

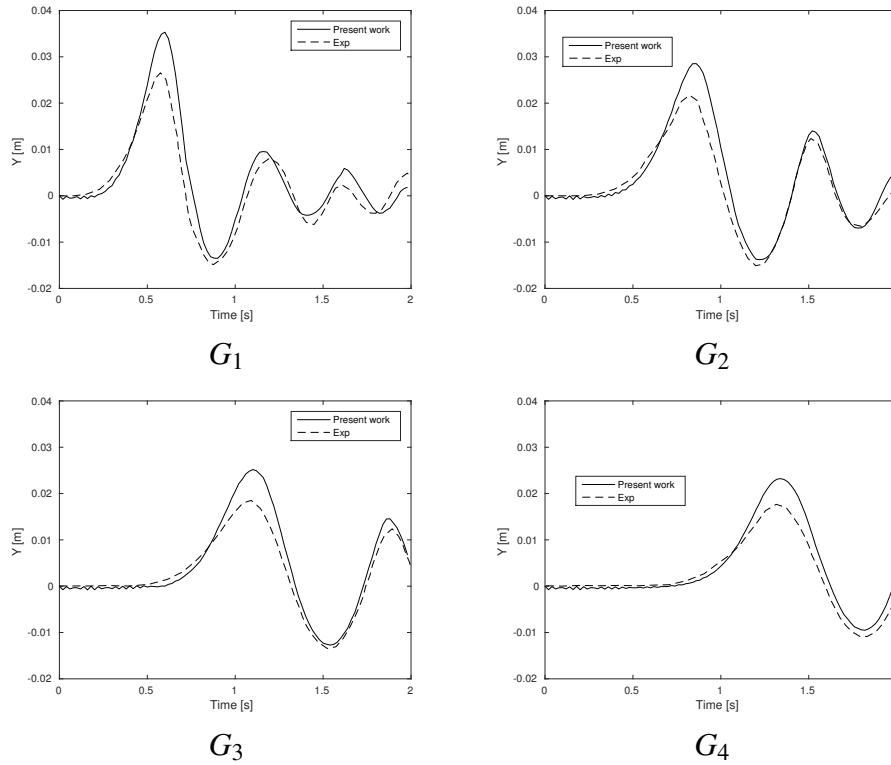


Figure 8.16 – Sub-aerial land-slide-generated water wave: Elevation of the free surface at each wave gauges G_1, G_2, G_3 and G_4 . The black solid line denotes the numerical results, while the dashed lines present the experimental results [342].

8.5 Dam-break flow over an erodible bed

This example aims to demonstrate the ability of our proposed model for the simulation of the erosion phenomena. Here, the proposed SPH model including the RBPMC- α_μ rheology is coupled with a suspended sediment layer modeled as it is explained in section 5.2.1.

Spinewine's [312] experiment of a dam-break induced sheet-flow is selected for this test. A tank is divided in two parts by a movable gate. A sediment layer of fully saturated sand material cover the lower part of the tank. There is a difference in the height of the sediment bed at both sides of the gate of 10[cm]. At one side of the gate, a water layer is contained over the sediment layer. When the movable gate is uplifted at very high speed, the water flows downstream and erodes the sand bed creating the a change in topography. Figure 8.18 gives more details about the geometry and the setup of the problem.

The properties of the bed material (saturated sand) are summarized in Table 8.1.

For the simulations, the density and viscosity of the water were taken equal to $\rho_w = 1000[\text{kg}/\text{m}^3]$ and $\mu_w = 0.001[\text{Pa}\cdot\text{s}]$. The plastic viscosity of the saturated sand is chosen

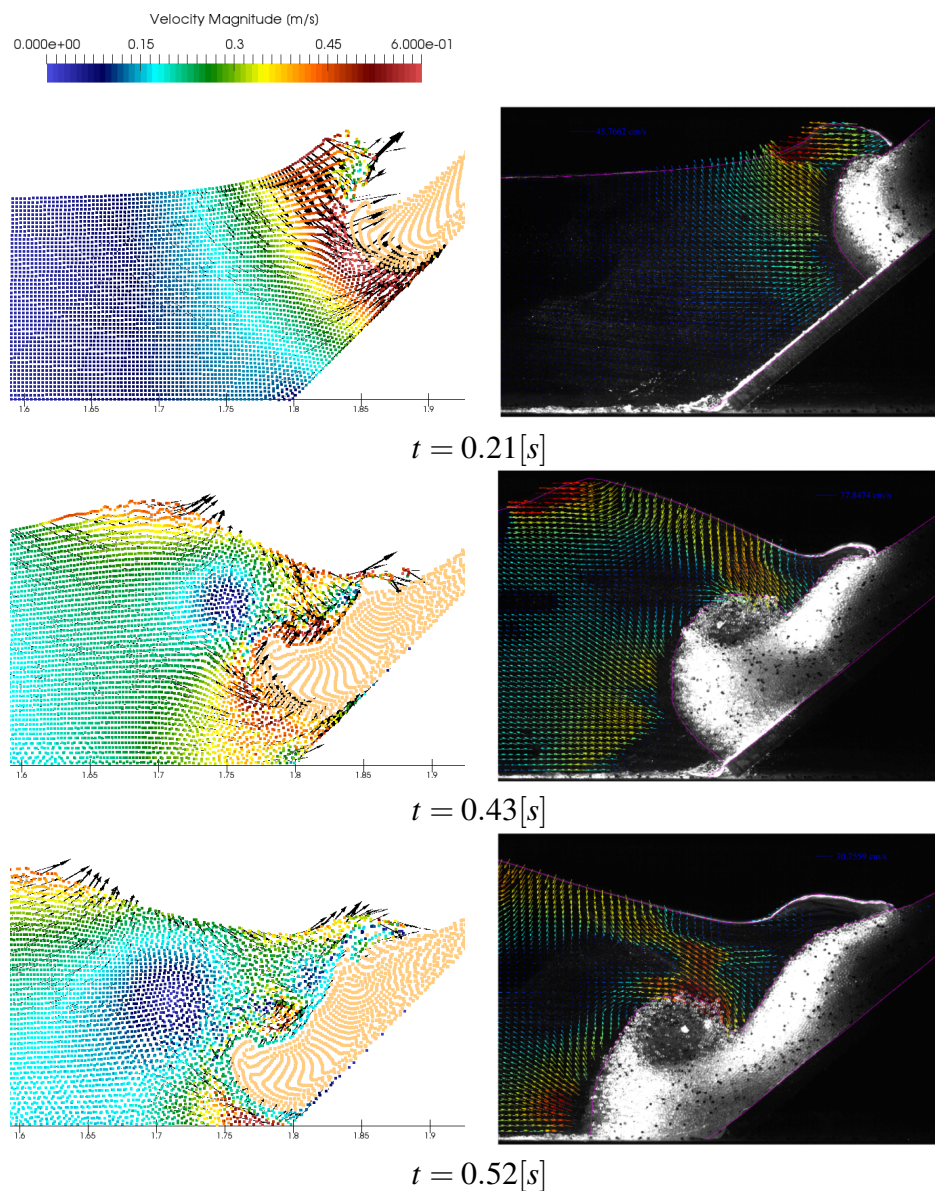


Figure 8.17 – Sub-aerial land-slide-generated water wave: Comparison between the numerical (left) and experimental (right) results at the times $t = \{0.21, 0.43, 0.52\} [s]$.

Material	Specific grain density [kg/m^3]	Granular volumetric fraction [-]	Bulk density [kg/m^3]	Friction angle [deg]
Sand	2680	0.53	1890.4	30

Table 8.1 – Properties of the sand material of the dam-break induced sheet-flow .

equal to that of the water $\mu = 0.001 [Pa.s]$ and the control parameter of the rheological model is taken as $\alpha_\mu = 10^6$.

The particles resolution used for this problem is 66000 particles (36000 sediment particles and 30000 water particles), with an initial inter-particle distance of $0.005 [m]$. The reference

speed of sound of water is set to $c_0 = 30[m/s]$ which leads to a reference pressure of $P_r = 9 \times 10^5 [Pa]$.

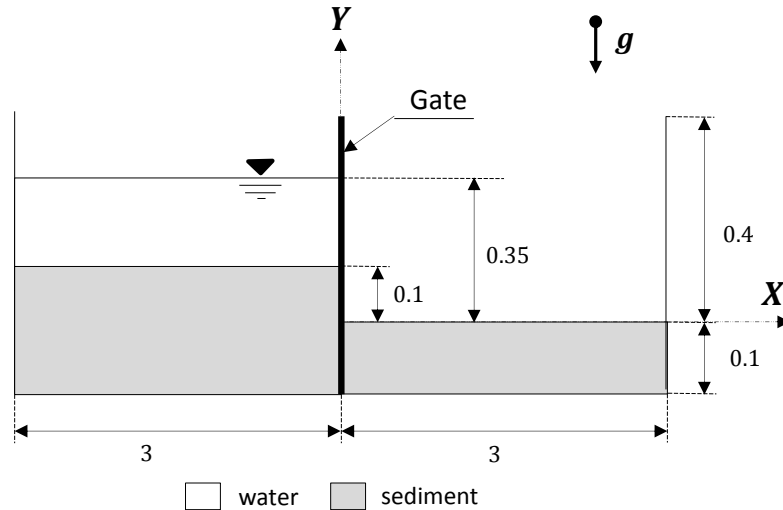


Figure 8.18 – Dam-break flow over an erodible bed: Geometrical details and setup of the problem.

Figures 8.19 and 8.20 show the sequence of the simulated dambreak, and the comparison with the experimental snapshots [312] at six different times $t = \{0.25, 0.5, 0.75, 1, 1.25, 1.5\} [s]$.

The water flow induces an erosion on the sediment bed. At the early stages, after removing the movable gate, it is observed that the water wave is propagated on the downstream bed, pikes up the particles material of bed and transports them. At late stages, the eroded particles will be gradually deposited due to the decrease in water velocity, and thus the shear stress.

Comparing the free surface water, surface of eroded bed and the position of the front water wave at three different times $t = \{0.25, 0.75, 1.25\} [s]$ (see figure 8.21), a good agreement between the numerical and experimental results is observed. However it is observed a small discrepancy between the numerical and experimental results, that is maybe due to the effects of the moving gate in the experiments that is absent in the numerical setup or to three dimensional effects.

8.6 Multi-physics numerical benchmark : subaerial landslide, flooding and scouring erosion

In this section , a new demonstrative numerical benchmark includes three coupled natural phenomena (Subaerial landslide, flooding and scouring erosion) is proposed in order to show

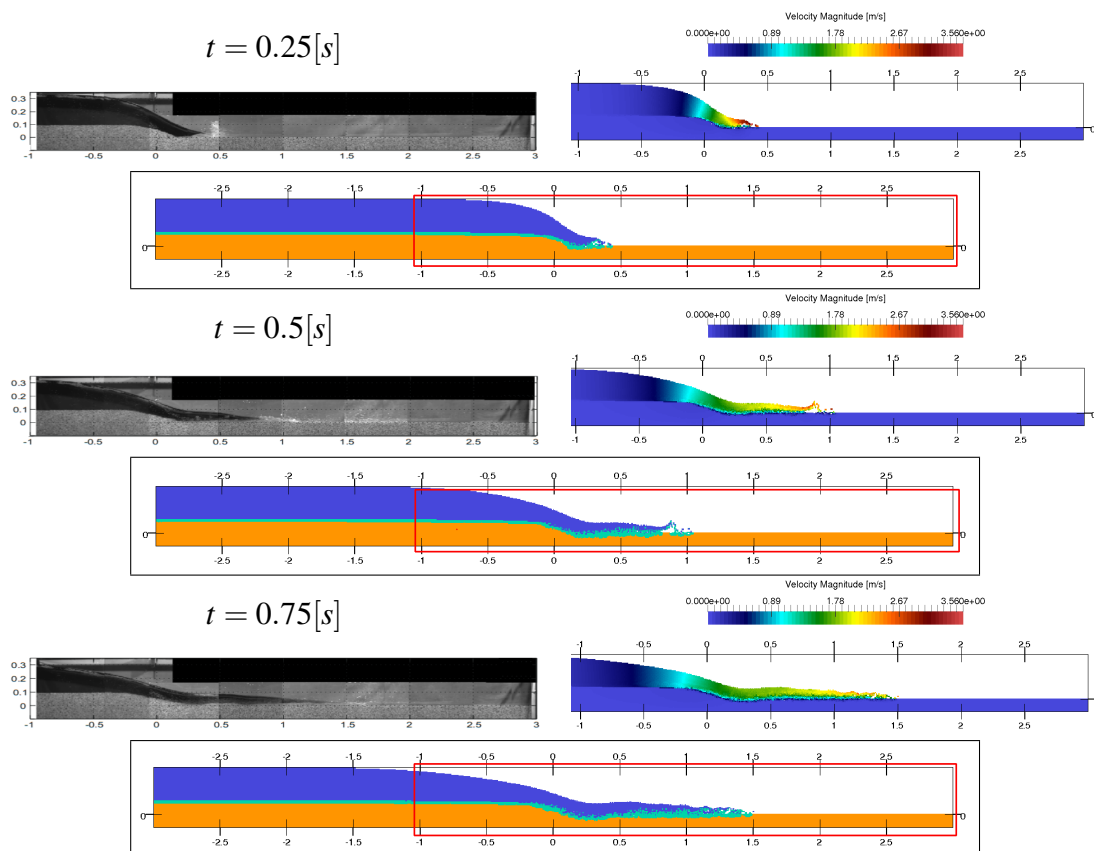


Figure 8.19 – Dam-break flow over an erodible bed: Flow sequences at times $t = \{0.25, 0.5, 0.75\} [s]$. The experimental results are on the left side (grey-scale image), the magnitude of the velocity field is plotted on the right side and a plot with the position of the different phases are centered below the previous plots for each time. The material phases are colored in blue for water particles, in orange for the rigid bed particles and in green for the suspended particles of the bed.

the capabilities and applicability of our proposed multiphase SPH model to simulate multiphysics problems resulting from the water-soil interactions. Figure 8.22 shows a schematic of three coupled phenomena. A rectangular mass of granular material ($GM1$) that has a length $L = 0.5[m]$ and height $H = 0.2[m]$ slides on slope of 45 deg. This mass was initially accelerated with a velocity of $v_0 = (\sqrt{2}, -\sqrt{2})[m/s]$. When the land impacts the water surface, a water wave will be generated and propagates until run-up and over-topping the dyke and subsequently floods on the other side of the dyke (on the bed of granular material $GM2$). The impact of the water jet induced from the flooding wave involves a scouring behind the dyke and erodes the bed granular material ($GM2$). We investigate the time evolution of the height of the over-topping above the dyke (at gauge wave G_2) as well as the wave height in the left tank at wave gauge G_1 and the maximum depth of scouring erosion behind the dyke

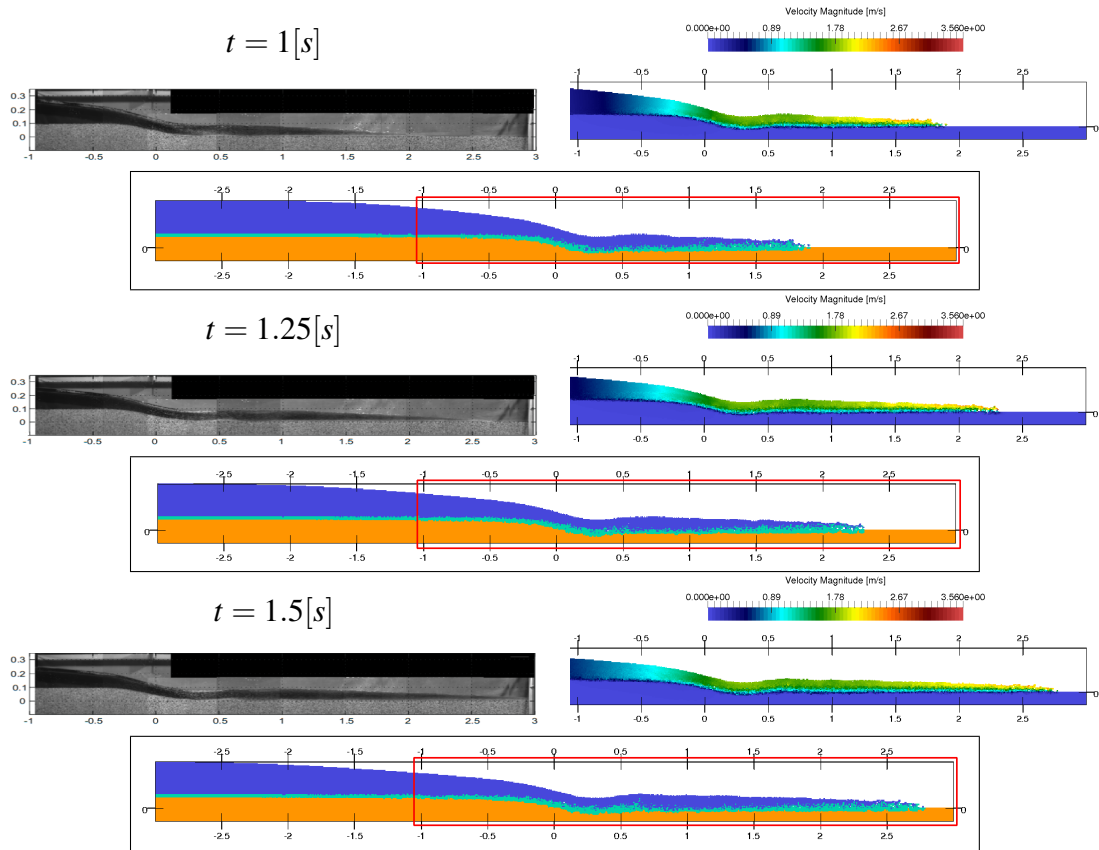


Figure 8.20 – Dam-break flow over an erodible bed: Flow sequences at times $t = \{1, 1.25, 1.5\}[s]$. The experimental results are on the left side (grey-scale image), the magnitude of the velocity field is plotted on the right side and a plot with the position of the different phases are centered below the previous plots for each time. The material phases are colored in blue for water particles, in orange for the rigid bed particles and in green for the suspended particles of the bed.

(at the right tank). The density and viscosity of the water is taken as $\rho_w = 1000[kg/m^3]$ and $\mu_w = 0.001[Pa.s]$, respectively. The bulk properties of granular materials $GM1$ and $GM2$ are taken as $\rho_{GM1} = 1600[kg/m^3]$, $\phi_{GM1} = 43 \text{ deg}$ and $\rho_{GM2} = 1200[kg/m^3]$, $\phi_{GM2} = 30 \text{ deg}$, respectively. While, the plastic viscosity for the both granular materials $GM1$ and $GM2$ is taken equal to the water dynamic viscosity $\mu = \mu_w = 0.001[Pa.s]$. The control parameter α_μ of our rheological model is taken equal to $\alpha_\mu = 6 \times 10^6$ for all granular materials.

This kind of numerical study can be very interesting for the design of the coastal protection structures (dykes, seawalls, Bulkheads, Breakwaters ...) and their foundations, because their damages are mainly caused by local scouring on the area behind them due to tsunami overflow [313, 321].

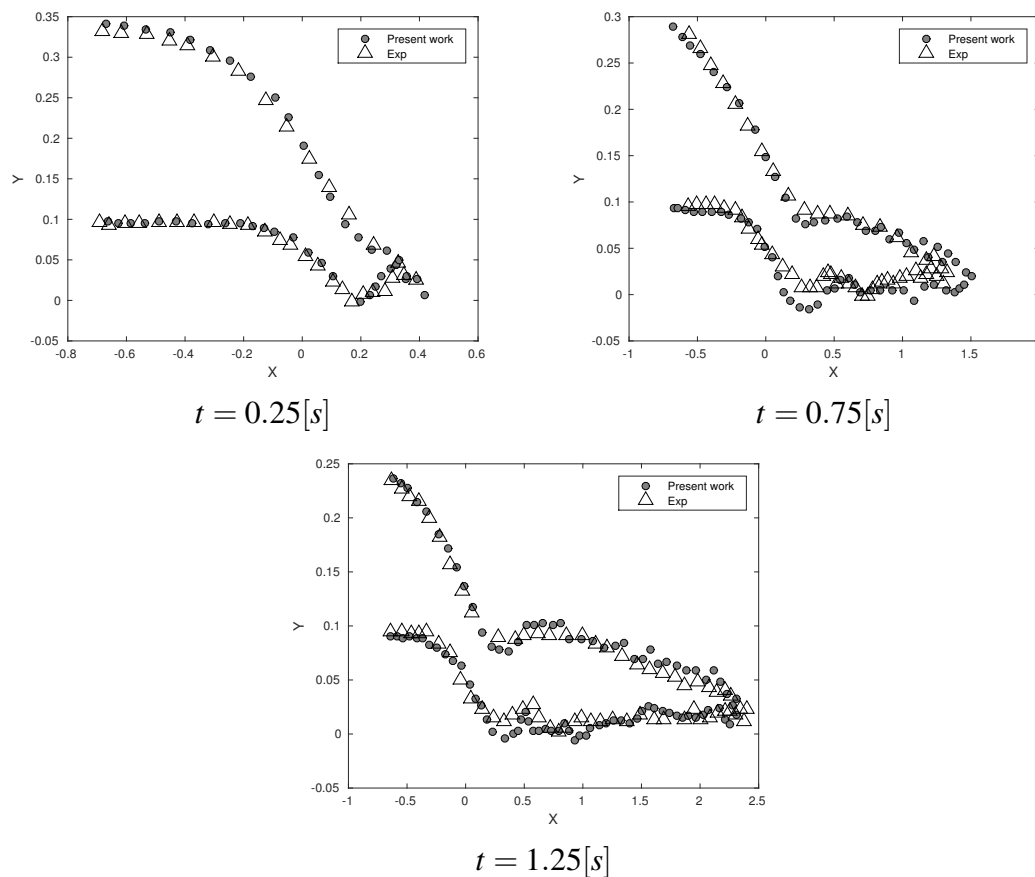


Figure 8.21 – Dam-break flow over an erodible bed: Water free surface and sediment surface positions results using the proposed numerical model and compared with the experiments of [312]

The numerical simulation is performed using an initial inter-particle spacing of $\delta x = 0.01[m]$ that leads to a total of 9465 particles, with 5020 particles devoted for the water and 1190, 3255 particles used for granular materials *GM1* and *GM2*, respectively. The water speed of sound is set equal $c_0 = 30[m/s]$ (it gives a reference pressure of $P_r = 9 \times 10^5[Pa]$). A no-slip boundary condition is applied on all horizontal surfaces (in the left and right tanks of figure 8.22). A free-slip condition is applied on the rest of surfaces (the slop, dyke and vertical walls). The total simulation time is of 7[s].

Snapshots of the results of numerical simulation for this benchmark are presented in the figures 8.23, 8.24, 8.25 and 8.26 at different times $t = \{0.3, 0.56, 1, 1.3, 1.7, 2, 2.5, 3, 5\}[s]$.

Figures 8.23 and 8.24 present the position of different material phases during all the period of the simulation. Water particles are colored in dark blue, whereas granular materials particles *GM1* and *GM2* are colored in cyan and brown, respectively. Yellow particles represent the particles of the granular material *GM2* mixed with water (suspended particles).

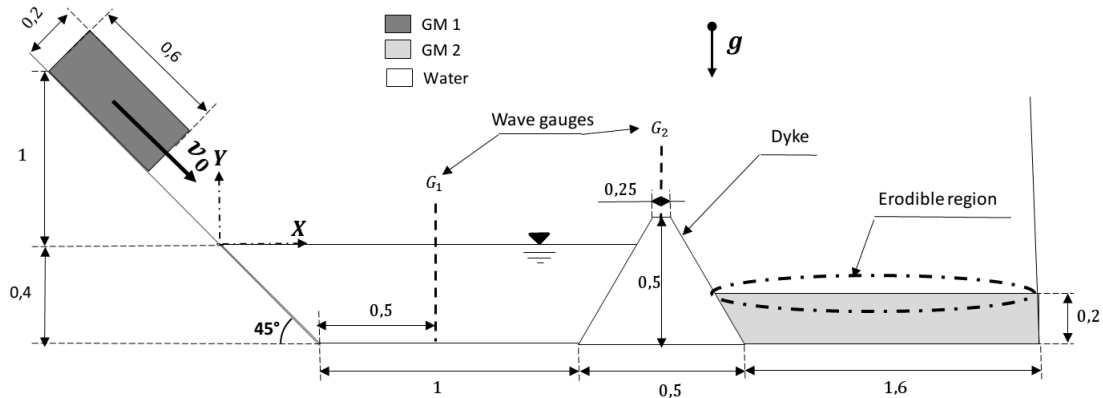


Figure 8.22 – Multi-physics numerical benchmark: Schematic view and geometrical details.

At $t = 0.3[s]$, the impact of granular material *GM1* on the surface water causes the formation of the first generated water wave. It reaches its maximum height at $t = 0.56[s]$. At time $t = 1[s]$ the granular material *GM1* stabilizes at rigid form (it reaches an effective viscosity of $\mu_{eff} = \mu_{max} = 6000[Pa.s]$) and at the same time the maximum height of the over-topping water is reached above the dyke structure. From this point the processes of dyke scour, erosion of the granular material *GM2*, and water run-up over the slope occurs. In figure 8.23 this is shown at $t = 1.3[s]$ and $t = 1.7[s]$. At $t = 2[s]$, a second wave is originated when the water flows downwards the slope. At the same time the granular material *GM2* reaches its maximum securing depth. At $t = 2.5[s]$ the soil particles starts to sediment and to cover the granular material (*GM2*). At $t = 3[s]$ the second wave flow over-tops above the dyke. At $t = 5[s]$, the granular material *GM2* reaches its rigid form (the maximum viscosity is reached everywhere in *GM2* except in the particles suspended in water) and the equilibrium is finally recovered.

Figures 8.25 and 8.26 show the evolution of the particle velocity, and the change in the behavior of the granular materials (switching from the rigid phase to the deformable phase and viceversa). Water particles are colored with the magnitude of the velocity, whereas the granular materials *GM1* and *GM2* are colored with the effective viscosity field (the Maximum viscosity $\mu_{max} = \alpha_{\mu}\mu = 60000[Pa.s]$ represents the rigid phase). The direction of the water particles is represented by arrows.

Figure 8.27 shows the time evolution of the relative height of the generated waves. This height is measured at the gauge G_1 (located at $x = 0.9[m]$ of the origin of the reference system axis (see figure 8.22)). The relative water height due to the over-topping flow above the dyke is also measured at the wave gauge G_2 (at $x = 1.65[m]$ of the origin) during all the

simulation period. In order to measure the erosion of the granular material *GM2*, figure 8.28 shows the time evolution of the maximum depth of the material bed *GM2*.

8.7 Conclusion

The robustness, accuracy and applicability of our multiphase model has been demonstrated. The validation of the efficiency of the developed multiphase diffusive term was performed using the benchmark of two stratified hydrostatics Newtonian fluid layers. The applicability on simulation of granular materials dynamics has been demonstrated via the benchmarks of Bingham fluid dambreak and spreading of granular material pile on horizontal surface. Whereas for the simulation of the water-soil interactions problems, the submarine and subaerial landslides benchmarks had been performed. A suspended water sediment model was nested in our multiphase model to capture well the erosion phenomena. A simulation of a dambreak flows over erodible sediment bed benchmark was used for the demonstration of the efficiency of the added suspended water sediment model. Finally, the capabilities of the newly proposed multiphase SPH model have been shown via a demonstrative benchmark of multi-physics phenomena (Subaerial landslide generated impulsive wave, flooding and scouring erosion) related to the soil-water interaction.

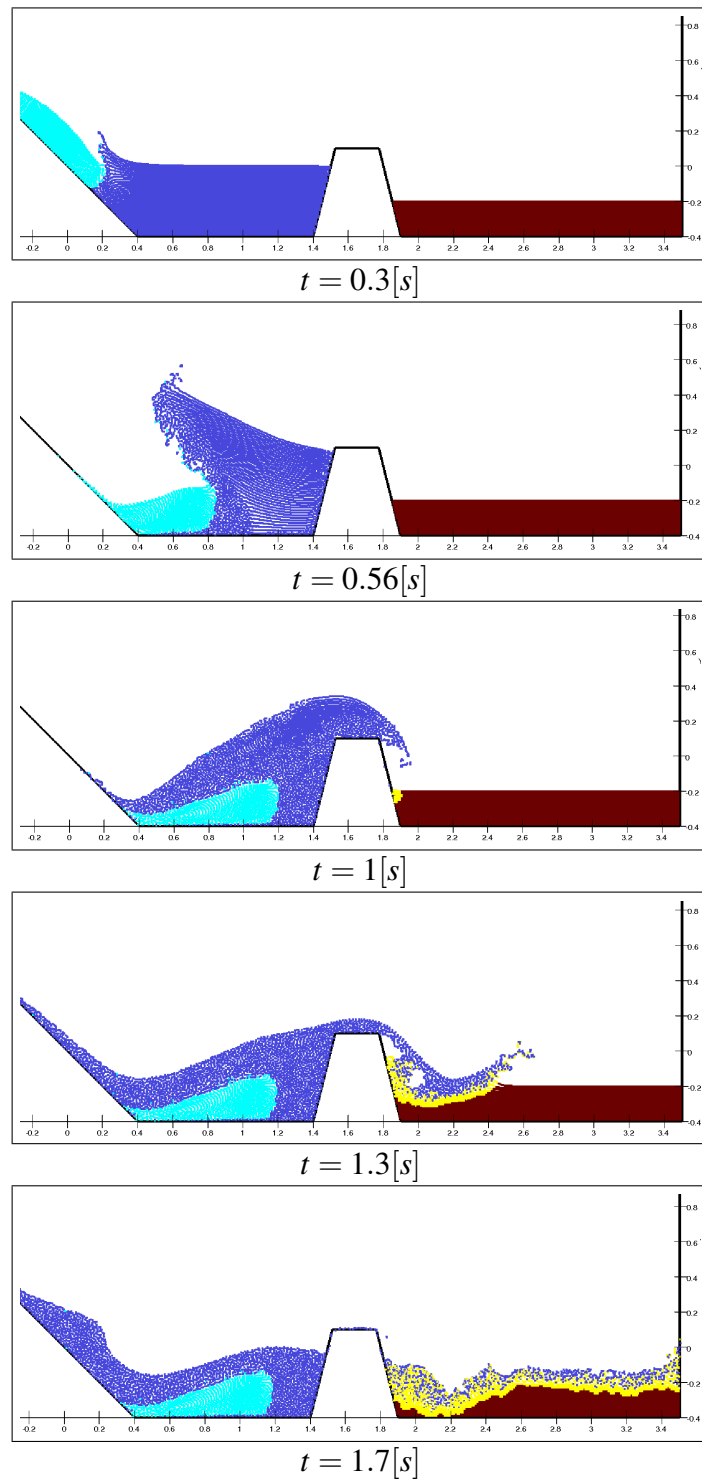


Figure 8.23 – Multi-physics numerical benchmark: simulation sequence. The different material phases are represented with different colors: Water is dark blue, the granular material *GM1* is cyan, the granular material *GM2* is brown and yellow is the suspended layer.

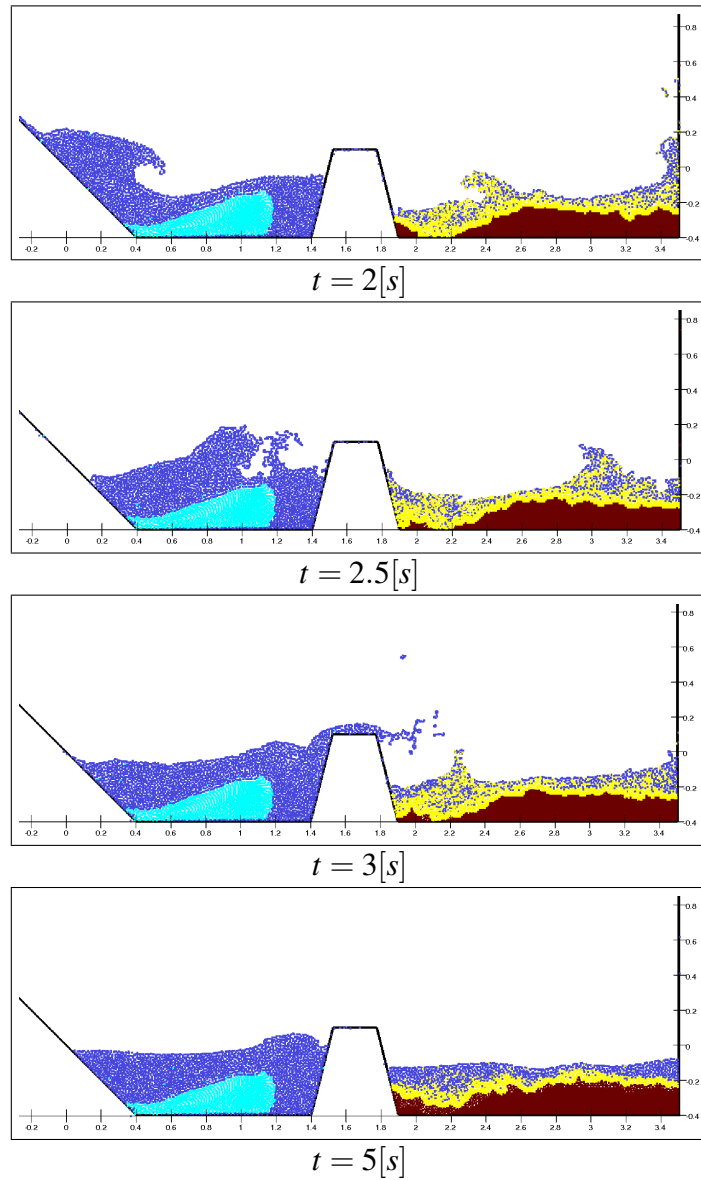


Figure 8.24 – Multi-physics numerical benchmark: simulation sequence. The different material phases are represented with different colors: Water is dark blue, the granular material *GM1* is cyan, the granular material *GM2* is brown and yellow is the suspended layer.

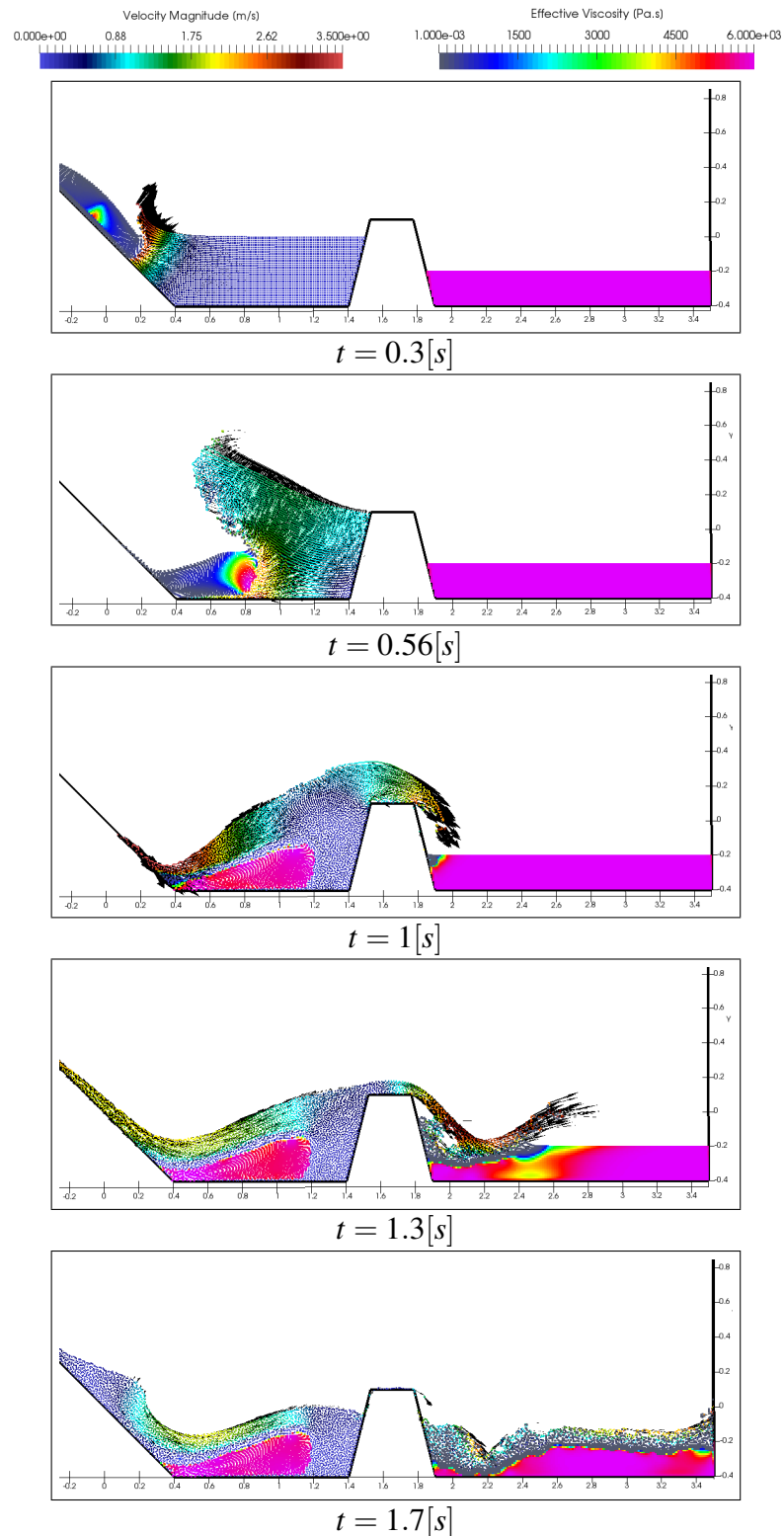


Figure 8.25 – Multi-physics numerical benchmark: Simulation sequences. The particles of soil material (*GM1*) and (*GM2*) are colored with the effective viscosity values. Water particles are colored with the magnitude of the velocity and the flow direction is represented by black arrows.

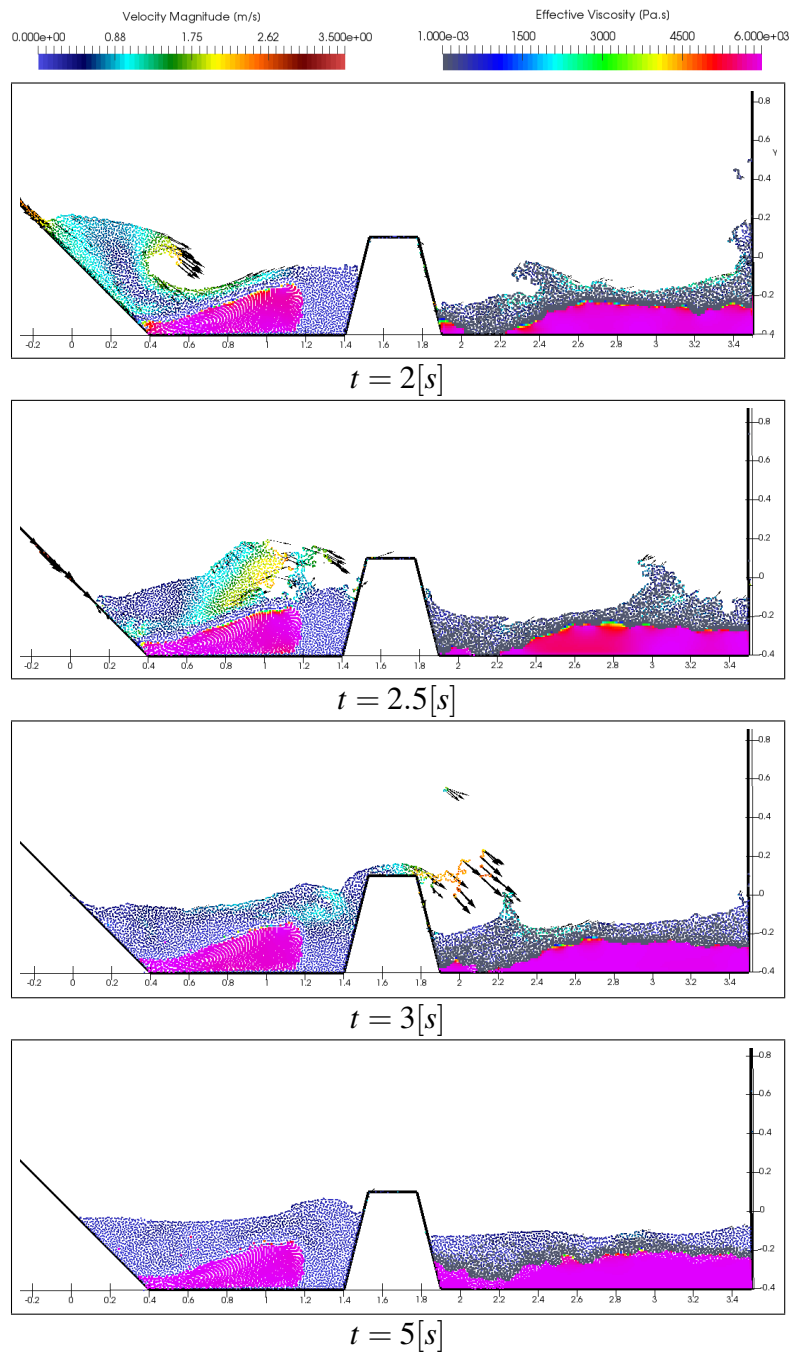


Figure 8.26 – Multi-physics numerical benchmark: Simulation sequences. The particles of soil material (GM1) and (GM2) are colored with the effective viscosity values. Water particles are colored with the magnitude of the velocity and the flow direction is represented by black arrows.

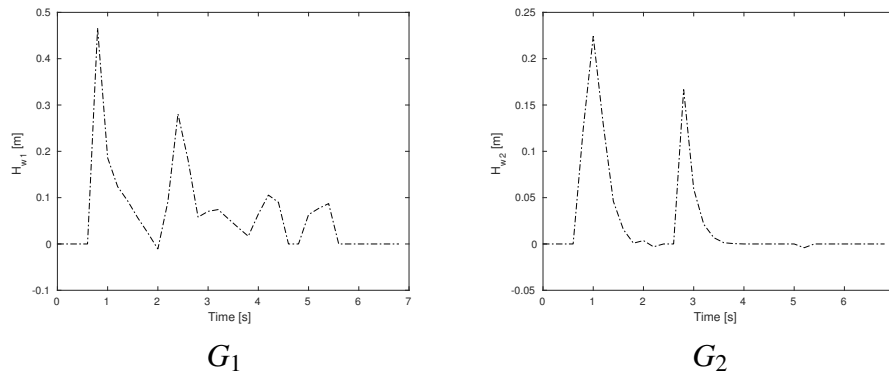


Figure 8.27 – Multi-physics numerical benchmark: Evaluation of the impulsive wave height for the left reservoir at $x = 0.9[m]$ (G_1 gauge) and height above the dyke (G_2 gauge) at $x = 1.65[m]$.

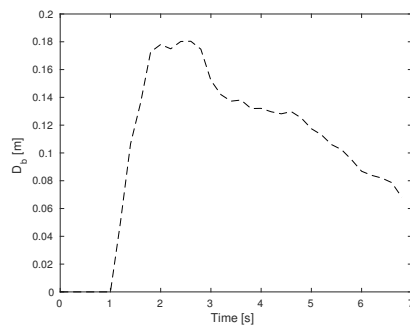


Figure 8.28 – Multi-physics numerical benchmark: Evaluation of maximum scouring depth on the granular material bed due to the over-topping flow.

Chapter 9

Conclusion

Un solveur SPH (Smoothed Particle Hydrodynamics) faiblement compressible (WCSPH) a été développé dans le cadre de cette thèse pour traiter les problèmes d'écoulement des fluides multiphasiques incluant différentes complexités d'écoulement (confiné, à surface libre, grande déformation, tension superficielle) et différents matériaux (fluides et sols). Une parallélisation sur CPUs en utilisant le paradigme MPI (Message Passing Interface) avec une technique de décomposition de domaine a été présentée dans l'annexe A. Des anciennes et récentes avancées ont été discutées pour les algorithmes d'amélioration et des schémas de discrétisation des équations physiques régissant le mouvement des particules dans le contexte de la méthode SPH. Un modèle SPH pour les écoulements multiphasiques a été proposé. Ce modèle comprend une formulation de tension de surface qui satisfait les propriétés tangentielles des contraintes de tension de surface et améliore la stabilité de la méthode numérique. La stabilité numérique est améliorée grâce à l'utilisation d'un opérateur de divergence consistant de premier ordre et une technique de d'amortissement (Damping) qui réduit les parasites numériques causées par la transition des conditions initiales. Des modifications sont apportées à la méthode des conditions aux limites généralisées liées aux parois solides pour étendre son application aux problèmes d'écoulement de fluide multiphasique. Le modèle SPH d'interactions eau-sol a été développé en utilisant une approche multiphasique. Ce modèle peut être utilisé pour simuler des sols (purements frictionnels et cohésifs), de l'eau (ou tout autres fluides Newtoniens) et leurs problèmes d'interaction. Ceci est réalisé grâce au modèle rhéologique RBPMC- α_μ sensible à la pression. Un terme diffusif multiphasique nommé ici $D^{\delta-MSPH}$ a également été développé pour amortir les oscillations de pression dues à l'utilisation d'une équation d'état. La précision, la stabilité et l'applicabilité du solveur SPH pour traiter les problèmes d'écoulement gravitationnel multiphasique, écoulement multiphasique avec présence de tension de surface et d'interaction eau-sol ont été

démontrées à travers une série de benchmarks. Ces benchmarks comprennent des cas-tests analytiques, numériques et expérimentaux.

9.1 Summary of Thesis Achievements

A weakly compressible smoothed particle hydrodynamics (WCSPH) solver has been developed in this thesis to deal with multiphase fluid flow problems including different complexities of flow (confined, free surface, large deformation, surface tension) and natures of materials (fluids and soils). This solver has been parallelized on CPUs (Central processing unit) using MPI (Message Passing Interface) paradigm with a domain decomposition technique as is shown in the appendix A. Past and recent advances in SPH method for improvement algorithms and different discretization schemes of governing equations are discussed. A consistent smoothed particle hydrodynamics model for multiphase flows has been proposed. This model includes a surface tension formulation which ensures the tangential properties of the tensor surface stress and improves the stability of the numerical method. The numerical stability is improved through the use of a divergence operator with first-order consistency and also with a damping technique that avoids the numerical issues due to the transients on initial conditions. Modifications are brought on the generalized wall boundary conditions to extends its application to multiphase fluid flow problems. Water-soil interactions SPH model has been developed using a multiphase approach. This model can be used to simulate soils (purely frictional and cohesive), water (or any other Newtonian fluid) and their interaction problems. This is done thanks to the RBPMC- α_μ pressure-sensitive rheology model. A multiphase diffusive term so-called herein $D^{\delta-MSPH}$ has been also developed to damp the pressure oscillations due to the use of equation of state in order to obtain more accurate results with using of such as pressure-sensitive model. The accuracy, stability and applicability of the proposed WCSPH solver to deal with gravitational multiphase fluid , interfacial multiphase fluid and water-soil interaction problems have been demonstrated via a series of benchmarks. Theses benchmarks include analytical, numerical and experimental test cases.

9.2 Applications

In this thesis, the applications cases have been classed under three category of tests:

The first category is devoted to the simulation of multiphase fluid flow evolved under gravity forces. The examples addressed here are the evolution of the two-phase stratified fluid layers and the Rayleigh-Taylor instability (RTI). The first example is not only performed to examine the stabilization effect of the damping technique but also to validate the proposed modifications on generalized wall boundary conditions when the two fluid phases meet the solid boundaries. The second example was carried out to compare the results of the presented

SPH multiphase model with the ones using Level-Set [128] and other SPH [238] models, and also with the analytical approach presented in [187]. Furthermore, the example of two rising bubbles through a water column is performed using a higher particle resolution.

The second category of test concerns the simulation of multiphase fluid flow with a surface tension formulation for the case of two and three phases flows with the presence of triple junction points. The examples addressed in this category are the square droplet deformation [2], the spreading lens between two stratified fluid layers [39] [193], and the capillary-viscous wave test [254, 151, 150, 149, 2]. Thereafter, high density and viscosity ratio effects have been introduced. The rising of an air bubble through a water column and through two stratified fluid layers are simulated.

The third category is devoted to validating multiphase WCSPH water-soil interaction model, where several benchmarks have been used. The validation of the efficiency of the developed multiphase diffusive term $D^{\delta-MSPH}$ was performed using the two stratified hydrostatics Newtonian fluid layers benchmark. The applicability on simulation of single phase of granular materials dynamics is demonstrated via the benchmarks of Bingham fluid dambreak and spreading of granular material pile on horizontal surface. For the simulation of the water-soil interactions problems, the submarine and subaerial landslides benchmarks are devoted. A suspended water sediment model was nested in our multiphase model to capture well the erosion phenomena. A simulation of a dambreak flows over erodible sediment bed benchmark was used for the demonstration of the efficiency of the added suspended water sediment model. Finally, a demonstrative benchmark of multi-physics phenomena (Subaerial landslide generated impulsive wave, flooding and scouring erosion) related to the soil-water interaction was proposed to show the capabilities of the newly proposed multiphase SPH model.

9.3 Future Work

As perspectives, several works are envisaged to make our SPH code more consistent and industrially exploitable such as:

- Extension of the following 2D code into 3D can achieve the simulations more complex and realistic.
- Parallelization on GPUs (Graphics processing unit) can be also shown more advantages in terms of computational cost and applications.
- Including the modeling of other physical natures such as a rigid bodies interact with water, elastic and elasto-plastic models to the code can for the simulation of multi-physics phenomena.

-
- A specific treatment of the contact line can be added to the modified wall boundary method to simulate the cases when the tension surface is nested at the interface between the fluid phases that meets the wall.
 - Using of incompressible and explicit incompressible smothered particle hydrodynamics (ISPH and EISPH) schemes in the developed code can be a good purpose for further investigation and comparison.

Bibliography

- [1] Adami, S., Hu, X., and Adams, N. (2010a). A conservative sph method for surfactant dynamics. *Journal of Computational Physics*, 229(5):1909–1926. [75](#)
- [2] Adami, S., Hu, X., and Adams, N. (2010b). A new surface-tension formulation for multi-phase sph using a reproducing divergence approximation. *Journal of Computational Physics*, 229(13):5011–5021. [75](#), [78](#), [84](#), [100](#), [101](#), [102](#), [105](#), [106](#), [107](#), [108](#), [128](#), [130](#), [151](#), [152](#), [161](#), [204](#)
- [3] Adami, S., Hu, X., and Adams, N. (2012a). Contact line hydrodynamics with sph. In *7th international SPHERIC workshop*. [110](#)
- [4] Adami, S., Hu, X., and Adams, N. (2012b). A generalized wall boundary condition for smoothed particle hydrodynamics. *Journal of Computational Physics*, 231(21):7057–7075. [16](#), [31](#), [75](#), [81](#), [87](#), [92](#), [95](#), [96](#), [100](#), [102](#), [108](#), [109](#), [112](#), [132](#), [133](#), [134](#), [139](#), [148](#)
- [5] Adami, S., Hu, X., and Adams, N. A. (2013). A transport-velocity formulation for smoothed particle hydrodynamics. *Journal of Computational Physics*, 241:292–307. [49](#)
- [6] Antoci, C., Gallati, M., and Sibilla, S. (2007). Numerical simulation of fluid–structure interaction by sph. *Computers & Structures*, 85(11):879–890. [15](#), [38](#), [53](#), [54](#), [59](#), [70](#), [80](#)
- [7] Antuono, M., Bouscasse, B., Colagrossi, A., and Lugni, C. (2012a). Two-dimensional modal method for shallow-water sloshing in rectangular basins. *Journal of Fluid Mechanics*, 700:419–440. [86](#)
- [8] Antuono, M., Colagrossi, A., and Marrone, S. (2012b). Numerical diffusive terms in weakly-compressible sph schemes. *Computer Physics Communications*, 183(12):2570–2580. [86](#)
- [9] Antuono, M., Colagrossi, A., Marrone, S., and Lugni, C. (2011). Propagation of gravity waves through an sph scheme with numerical diffusive terms. *Computer Physics Communications*, 182(4):866–877. [86](#)
- [10] Antuono, M., Colagrossi, A., Marrone, S., and Molteni, D. (2010). Free-surface flows solved by means of sph schemes with numerical diffusive terms. *Computer Physics Communications*, 181(3):532–549. [86](#), [117](#), [119](#)
- [11] Apfel, R. E., Tian, Y., Jankovsky, J., Shi, T., Chen, X., Holt, R. G., Trinh, E., Croonquist, A., Thornton, K. C., Sacco Jr, A., et al. (1997). Free oscillations and surfactant studies of superdeformed drops in microgravity. *Physical review letters*, 78(10):1912. [38](#)

- [12] Appel, A. W. (1985). An efficient program for many-body simulation. *SIAM Journal on Scientific and Statistical Computing*, 6(1):85–103. [91](#)
- [13] Ataie-Ashtiani, B. and Shobeyri, G. (2008). Numerical simulation of landslide impulsive waves by incompressible smoothed particle hydrodynamics. *International Journal for numerical methods in fluids*, 56(2):209–232. [52](#), [80](#), [96](#), [116](#), [118](#), [119](#)
- [14] Barcarolo, D., Le Touzé, D., and de Vuyst, F. (2012). Incompressible smoothed particle hydrodynamics: proposition and validation of a fully-explicit algorithm. In *Proc. Seventh International SPHERIC Workshop, Prato, Italy*. [72](#)
- [15] Barcarolo, D. A. (2013). *Improvement of the precision and the efficiency of the SPH method: theoretical and numerical study*. PhD thesis, Ecole Centrale de Nantes (ECN)(ECN)(ECN)(ECN). [72](#)
- [16] Barecasco, A., Terissa, H., and Naa, C. F. (2013). Simple free-surface detection in two and three-dimensional sph solver. *arXiv preprint arXiv:1309.4290*. [96](#)
- [17] Barnes, H. (1989). Shear-thickening (“dilatancy”) in suspensions of nonaggregating solid particles dispersed in newtonian liquids. *Journal of Rheology*, 33(2):329–366. [65](#)
- [18] Barnes, J. and Hut, P. (1986). A hierarchical o (n log n) force-calculation algorithm. *nature*, 324(6096):446–449. [91](#)
- [19] Basa, M., Quinlan, N. J., and Lastiwka, M. (2009). Robustness and accuracy of sph formulations for viscous flow. *International Journal for Numerical Methods in Fluids*, 60(10):1127–1148. [74](#), [75](#)
- [20] Batchelor, G. K. (2000). *An introduction to fluid dynamics*. Cambridge university press. [65](#)
- [21] Becker, M. and Teschner, M. (2007). Weakly compressible sph for free surface flows. In *Proceedings of the 2007 ACM SIGGRAPH/Eurographics symposium on Computer animation*, pages 209–217. Eurographics Association. [77](#)
- [22] Beg, O. A., Vasu, B., Sochi, T., and Prasad, V. (2013). Keller box and smoothed particle hydrodynamic numerical simulation of two-phase transport in blood purification auto-transfusion dialysis hybrid device with stokes and darcy number effects. *Journal of Advanced Biotechnology and Bioengineering*, 1(2):80–100. [38](#)
- [23] Belytschko, T., Krongauz, Y., Dolbow, J., and Gerlach, C. (1998). On the completeness of meshfree particle methods. *International Journal for Numerical Methods in Engineering*, 43(5):785–819. [44](#), [81](#)
- [24] Belytschko, T., Liu, W. K., Moran, B., and Elkhodary, K. (2013). *Nonlinear finite elements for continua and structures*. John wiley & sons. [36](#)
- [25] Ben Moussa, B. (2006). On the convergence of sph method for scalar conservation laws with boundary conditions. *Methods and applications of analysis*, 13(1):29–62. [85](#)
- [26] Benson, D. J. (1992). Computational methods in lagrangian and eulerian hydrocodes. *Computer methods in Applied mechanics and Engineering*, 99(2-3):235–394. [36](#)

- [27] Benz, W. (1988). Applications of smooth particle hydrodynamics (sph) to astrophysical problems. *Computer Physics Communications*, 48(1):97–105. [38](#)
- [28] Benz, W. and Asphaug, E. (1994). Impact simulations with fracture. i. method and tests. *Icarus*, 107(1):98–116. [52](#)
- [29] Benz, W. and Asphaug, E. (1995). Simulations of brittle solids using smooth particle hydrodynamics. *Computer physics communications*, 87(1-2):253–265. [52](#)
- [30] Bercovier, M. and Engelman, M. (1980). A finite-element method for incompressible non-newtonian flows. *Journal of Computational Physics*, 36(3):313–326. [66](#), [121](#), [122](#)
- [31] Berger, M. J. and Colella, P. (1989). Local adaptive mesh refinement for shock hydrodynamics. *Journal of computational Physics*, 82(1):64–84. [99](#), [101](#)
- [32] Beverly, C. and Tanner, R. (1992). Numerical analysis of three-dimensional bingham plastic flow. *Journal of non-newtonian fluid mechanics*, 42(1-2):85–115. [184](#)
- [33] Bird, R. B., Armstrong, R. C., and Hassager, O. (1987). Dynamics of polymer Fluid mechanics. [66](#), [76](#), [121](#), [122](#)
- [34] Bird, R. B., Stewart, W. E., and Lightfoot, E. N. (1960). Transport phenomena john wiley & sons. *New York*, page 413. [65](#)
- [35] Bonet, J. and Kulasegaram, S. (2000). Correction and stabilization of smooth particle hydrodynamics methods with applications in metal forming simulations. *International journal for numerical methods in engineering*, 47(6):1189–1214. [82](#)
- [36] Bonet, J. and Lok, T.-S. (1999). Variational and momentum preservation aspects of smooth particle hydrodynamic formulations. *Computer Methods in applied mechanics and engineering*, 180(1):97–115. [48](#), [82](#), [83](#)
- [37] Bonhomme, R., Magnaudet, J., Duval, F., and Piar, B. (2012a). Inertial dynamics of air bubbles crossing a horizontal fluid–fluid interface. *Journal of Fluid Mechanics*, 707:405–443. [20](#), [151](#), [152](#), [168](#), [170](#), [172](#)
- [38] Bonhomme, R., Magnaudet, J., Duval, F., and Piar, B. (2012b). Inertial dynamics of air bubbles crossing a horizontal fluid–fluid interface. *Journal of Fluid Mechanics*, 707:405–443. [169](#)
- [39] Boyer, F., Lapuerta, C., Minjeaud, S., Piar, B., and Quintard, M. (2010). Cahn–hilliard/navier–stokes model for the simulation of three-phase flows. *Transport in Porous Media*, 82(3):463–483. [151](#), [152](#), [160](#), [204](#)
- [40] Brackbill, J., Kothe, D. B., and Zemach, C. (1992a). A continuum method for modeling surface tension. *Journal of computational physics*, 100(2):335–354. [77](#), [97](#), [100](#), [101](#), [106](#), [134](#)
- [41] Brackbill, J., Kothe, D. B., and Zemach, C. (1992b). A continuum method for modeling surface tension. *Journal of computational physics*, 100(2):335–354. [111](#)
- [42] Brereton, G. and Korotney, D. (1991). Coaxial and oblique coalescence of two rising bubbles. *Dynamics of bubbles and vortices near a free surface, AMD*, 119. [14](#), [54](#)

- [43] Brookshaw, L. (1985). A method of calculating radiative heat diffusion in particle simulations. *Publications of the Astronomical Society of Australia*, 6(2):207–210. [47](#)
- [44] Buchner, B. (2002). Green water on ship-type offshore structures. [13](#), [49](#), [50](#)
- [45] Bui, H., Fukagawa, R., Sako, K., and Wells, J. (2011). Slope stability analysis and discontinuous slope failure simulation by elasto-plastic smoothed particle hydrodynamics (sph). *Géotechnique*, 61(7):565–574. [68](#)
- [46] Bui, H. H., Fukagawa, R., Sako, K., and Ohno, S. (2008a). Lagrangian meshfree particles method (sph) for large deformation and failure flows of geomaterial using elastic–plastic soil constitutive model. *International Journal for Numerical and Analytical Methods in Geomechanics*, 32(12):1537–1570. [14](#), [52](#), [57](#), [68](#)
- [47] Bui, H. H., Kodikara, J. K., Bouazza, A., Haque, A., and Ranjith, P. G. (2014). A novel computational approach for large deformation and post-failure analyses of segmental retaining wall systems. *International Journal for Numerical and Analytical Methods in Geomechanics*, 38(13):1321–1340. [68](#)
- [48] Bui, H. H., Sako, K., and Fukagawa, R. (2007). Numerical simulation of soil–water interaction using smoothed particle hydrodynamics (sph) method. *Journal of Terramechanics*, 44(5):339–346. [96](#), [119](#)
- [49] Bui, H. H., Sako, K., Fukagawa, R., and Wells, J. (2008b). Sph-based numerical simulations for large deformation of geomaterial considering soil–structure interaction. In *The 12th International Conference of International Association for Computer Methods and Advances in Geomechanics (IACMAG)*, volume 1, pages 570–578. [52](#)
- [50] Canelas, R., Ferreira, R., Domínguez, J., and Crespo, A. (2014). Modelling of wave impacts on harbour structures and objects with sph and dem. *Proceedings of the 9th SPHERIC*. [15](#), [55](#), [61](#)
- [51] Capone, T., Panizzo, A., Cecioni, C., and Darlymple, R. (2007). Accuracy and stability of numerical schemes in sph. In *2nd SPHERIC international workshop*. [42](#)
- [52] Capone, T., Panizzo, A., and Monaghan, J. J. (2010). Sph modelling of water waves generated by submarine landslides. *Journal of Hydraulic Research*, 48(S1):80–84. [15](#), [21](#), [52](#), [55](#), [60](#), [61](#), [80](#), [116](#), [119](#), [183](#), [184](#)
- [53] Cercos-Pita, J. L. (2015). Aquagpusph, a new free 3d sph solver accelerated with opencl. *Computer Physics Communications*, 192:295–312. [48](#)
- [54] Chauchat, J. and Médale, M. (2014). A three-dimensional numerical model for dense granular flows based on the μ (i) rheology. *Journal of Computational Physics*, 256:696–712. [126](#)
- [55] Chen, J., Beraun, J., and Carney, T. (1999a). A corrective smoothed particle method for boundary value problems in heat conduction. *International Journal for Numerical Methods in Engineering*, 46(2):231–252. [83](#), [89](#)
- [56] Chen, J., Beraun, J., and Jih, C. (1999b). An improvement for tensile instability in smoothed particle hydrodynamics. *Computational Mechanics*, 23(4):279–287. [74](#)

- [57] Chen, W. and Qiu, T. (2011). Numerical simulations for large deformation of granular materials using smoothed particle hydrodynamics method. *International Journal of Geomechanics*, 12(2):127–135. [15](#), [52](#), [57](#), [68](#)
- [58] Chen, Z., Zong, Z., Liu, M., Zou, L., Li, H., and Shu, C. (2015). An sph model for multiphase flows with complex interfaces and large density differences. *Journal of Computational Physics*, 283:169–188. [49](#)
- [59] Cherfils, J.-M. (2011). *Développements et applications de la méthode SPH aux écoulements visqueux à surface libre*. PhD thesis, Université du Havre. [13](#), [37](#)
- [60] Cherfils, J.-M., Pinon, G., and Rivoalen, E. (2012). Josephine: A parallel sph code for free-surface flows. *Computer Physics Communications*, 183(7):1468–1480. [48](#), [96](#)
- [61] Chhabra, R. P. (2010). Non-newtonian fluids: an introduction. In *Rheology of Complex Fluids*, pages 3–34. Springer. [65](#), [121](#)
- [62] Chorin, A. J. (1968). Numerical solution of the navier-stokes equations. *Mathematics of computation*, 22(104):745–762. [70](#)
- [63] Chorin, A. J. (1969). On the convergence of discrete approximations to the navier-stokes equations. *Mathematics of computation*, 23(106):341–353. [70](#)
- [64] Ciarlet, P. G. (2002). *The finite element method for elliptic problems*. SIAM. [36](#)
- [65] Cleary, P. W. (1998). Modelling confined multi-material heat and mass flows using sph. *Applied Mathematical Modelling*, 22(12):981–993. [75](#)
- [66] Cleary, P. W. and Das, R. (2008). The potential for sph modelling of solid deformation and fracture. In *IUTAM symposium on theoretical, computational and modelling aspects of inelastic media*, pages 287–296. Springer. [38](#)
- [67] Cleary, P. W. and Monaghan, J. J. (1999). Conduction modelling using smoothed particle hydrodynamics. *Journal of Computational Physics*, 148(1):227–264. [38](#), [47](#), [80](#), [97](#)
- [68] Cohen, R. C., Cleary, P. W., and Mason, B. R. (2012). Simulations of dolphin kick swimming using smoothed particle hydrodynamics. *Human movement science*, 31(3):604–619. [38](#)
- [69] Colagrossi, A. (2005). A meshless lagrangian method for free-surface and interface flows with fragmentation. *These, Universita di Roma*. [73](#), [127](#)
- [70] Colagrossi, A., Antuono, M., and Le Touzé, D. (2009). Theoretical considerations on the free-surface role in the smoothed-particle-hydrodynamics model. *Physical Review E*, 79(5):056701. [95](#)
- [71] Colagrossi, A., Antuono, M., Souto-Iglesias, A., and Le Touzé, D. (2011). Theoretical analysis and numerical verification of the consistency of viscous smoothed-particle-hydrodynamics formulations in simulating free-surface flows. *Physical Review E*, 84(2):026705. [95](#)

- [72] Colagrossi, A. and Landrini, M. (2003a). Numerical simulation of interfacial flows by smoothed particle hydrodynamics. *Journal of computational physics*, 191(2):448–475. [38](#), [48](#), [69](#), [70](#), [82](#), [91](#), [96](#), [103](#), [234](#)
- [73] Colagrossi, A. and Landrini, M. (2003b). Numerical simulation of interfacial flows by smoothed particle hydrodynamics. *Journal of Computational Physics*, 191(2):448–475. [121](#), [164](#)
- [74] Colicchio, G., Greco, M., and Faltinsen, O. (2006). Fluid-body interaction on a cartesian grid: dedicated studies for a cfd validation. *Proc. IWWFEB*, 6. [14](#), [53](#)
- [75] Coulomb, C. A. (1773). *Essai sur une application des regles de maximis & minimis a quelques problemes de statique: Relatifs a l'architecture*. publisher not identified. [50](#), [116](#), [119](#), [123](#)
- [76] Coussot, P. (1997). *Mudflow rheology and dynamics*. Balkema. [66](#)
- [77] Crespo, A., Gómez-Gesteira, M., and Dalrymple, R. A. (2007). Boundary conditions generated by dynamic particles in sph methods. *CMC-TECH SCIENCE PRESS-*, 5(3):173. [48](#)
- [78] Crespo, A. C., Dominguez, J. M., Barreiro, A., Gómez-Gesteira, M., and Rogers, B. D. (2011). Gpus, a new tool of acceleration in cfd: efficiency and reliability on smoothed particle hydrodynamics methods. *PloS one*, 6(6):e20685. [47](#)
- [79] Crespo, A. J., Domínguez, J. M., Rogers, B. D., Gómez-Gesteira, M., Longshaw, S., Canelas, R., Vacondio, R., Barreiro, A., and García-Feal, O. (2015). Dualsphysics: Open-source parallel cfd solver based on smoothed particle hydrodynamics (sph). *Computer Physics Communications*, 187:204–216. [47](#)
- [80] Cummins, S. J. and Rudman, M. (1999). An sph projection method. *Journal of computational physics*, 152(2):584–607. [49](#), [70](#), [72](#), [97](#), [143](#)
- [81] Dalrymple, R. and Rogers, B. (2006). Numerical modeling of water waves with the sph method. *Coastal engineering*, 53(2):141–147. [81](#)
- [82] Daly, E., Grimaldi, S., Bui, H. H., et al. (2016). Explicit incompressible sph algorithm for free-surface flow modelling: A comparison with weakly compressible schemes. *Advances in Water Resources*, 97:156–167. [72](#), [97](#)
- [83] Dalziel, S. (2001). Toy models for rayleigh taylor instability. In *8th International Workshop on the Physics of Compressible Turbulent Mixing*. [145](#)
- [84] De Leffe, M., Le Touzé, D., and Alessandrini, B. (2009). Normal flux method at the boundary for sph. In *4th Int. SPHERIC Workshop (SPHERIC 2009)*. [93](#)
- [85] De Leffe, M., Le Touzé, D., and Alessandrini, B. (2011). A modified no-slip condition in weakly-compressible sph. In *6th Int. SPHERIC Workshop (SPHERIC 2011)*. [49](#)
- [86] Deb, D. and Pramanik, R. (2013). Failure process of brittle rock using smoothed particle hydrodynamics. *Journal of Engineering Mechanics*, 139(11):1551–1565. [68](#)

- [87] Dilts, G. A. (1999). Moving-least-squares-particle hydrodynamics—i. consistency and stability. *International Journal for Numerical Methods in Engineering*, 44(8):1115–1155. [44](#), [81](#), [82](#)
- [88] Dilts, G. A. (2000). Moving least-squares particle hydrodynamics ii: conservation and boundaries. *International Journal for Numerical Methods in Engineering*, 48(10):1503–1524. [44](#)
- [89] Domínguez, J. M., Crespo, A. J., and Gómez-Gesteira, M. (2013a). Optimization strategies for cpu and gpu implementations of a smoothed particle hydrodynamics method. *Computer Physics Communications*, 184(3):617–627. [48](#)
- [90] Domínguez, J. M., Crespo, A. J., Valdez-Balderas, D., Rogers, B. D., and Gómez-Gesteira, M. (2013b). New multi-gpu implementation for smoothed particle hydrodynamics on heterogeneous clusters. *Computer Physics Communications*, 184(8):1848–1860. [14](#), [48](#), [49](#), [54](#)
- [91] Domnik, B. (2013). *Multiscale Modelling and Simulation of Rapid Granular Flows*. PhD thesis, Bonn, Rheinische Friedrich-Wilhelms-Universität Bonn, Diss., 2013. [126](#)
- [92] Douillet-Grellier, T., Jones, B. D., Pramanik, R., Pan, K., Albaiz, A., and Williams, J. R. (2016). Mixed-mode fracture modeling with smoothed particle hydrodynamics. *Computers and Geotechnics*, 79:73–85. [15](#), [52](#), [58](#), [68](#)
- [93] Drucker, D. C. and Prager, W. (1952). Soil mechanics and plastic analysis or limit design. *Quarterly of applied mathematics*, 10(2):157–165. [52](#), [68](#), [116](#), [119](#), [123](#)
- [94] Dyka, C. and Ingel, R. (1995). An approach for tension instability in smoothed particle hydrodynamics (sph). *Computers & structures*, 57(4):573–580. [89](#)
- [95] Ellero, M., Kröger, M., and Hess, S. (2002). Viscoelastic flows studied by smoothed particle dynamics. *Journal of Non-Newtonian Fluid Mechanics*, 105(1):35–51. [68](#), [74](#)
- [96] Espanol, P. (1998). Fluid particle model. *Physical Review E*, 57(3):2930. [37](#)
- [97] Espanol, P. and Revenga, M. (2003). Smoothed dissipative particle dynamics. *Physical Review E*, 67(2):026705. [84](#)
- [98] Fan, X.-J., Tanner, R., and Zheng, R. (2010). Smoothed particle hydrodynamics simulation of non-newtonian moulding flow. *Journal of Non-Newtonian Fluid Mechanics*, 165(5):219–226. [76](#), [109](#), [130](#)
- [99] Fatehi, R. and Manzari, M. (2011). Error estimation in smoothed particle hydrodynamics and a new scheme for second derivatives. *computers & Mathematics with Applications*, 61(2):482–498. [83](#), [84](#)
- [100] Fatehi, R. and Manzari, M. (2012). A consistent and fast weakly compressible smoothed particle hydrodynamics with a new wall boundary condition. *International Journal for Numerical Methods in Fluids*, 68(7):905–921. [71](#), [85](#), [93](#)
- [101] Federico, I., Marrone, S., Colagrossi, A., Aristodemo, F., and Antuono, M. (2012). Simulating 2d open-channel flows through an sph model. *European Journal of Mechanics-B/Fluids*, 34:35–46. [94](#)

- [102] Federrath, C., Banerjee, R., Clark, P. C., and Klessen, R. S. (2010). Modeling collapse and accretion in turbulent gas clouds: implementation and comparison of sink particles in amr and sph. *The Astrophysical Journal*, 713(1):269. [38](#)
- [103] Ferrand, M., Joly, A., Kassiotis, C., Violeau, D., Leroy, A., Morel, F.-X., and Rogers, B. D. (2017). Unsteady open boundaries for sph using semi-analytical conditions and riemann solver in 2d. *Computer Physics Communications*, 210:29–44. [94](#)
- [104] Ferrand, M., Laurence, D., Rogers, B. D., Violeau, D., and Kassiotis, C. (2013). Unified semi-analytical wall boundary conditions for inviscid, laminar or turbulent flows in the meshless sph method. *International Journal for Numerical Methods in Fluids*, 71(4):446–472. [38](#), [43](#), [93](#), [94](#)
- [105] Ferrari, A., Dumbser, M., Toro, E. F., and Armanini, A. (2009). A new 3d parallel sph scheme for free surface flows. *Computers & Fluids*, 38(6):1203–1217. [48](#), [85](#)
- [106] Ferziger, J. H. and Perić, M. (2002). Solution of the navier-stokes equations. In *Computational Methods for Fluid Dynamics*, pages 157–216. Springer. [85](#)
- [107] Fourey, G., Oger, G., Le Touzé, D., and Alessandrini, B. (2010). Violent fluid-structure interaction simulations using a coupled sph/fem method. In *IOP conference series: materials science and engineering*, volume 10, page 012041. IOP Publishing. [80](#)
- [108] Fourtakas, G. and Rogers, B. (2016). Modelling multi-phase liquid-sediment scour and resuspension induced by rapid flows using smoothed particle hydrodynamics (sph) accelerated with a graphics processing unit (gpu). *Advances in Water Resources*, 92:186–199. [14](#), [57](#), [80](#), [117](#), [119](#), [127](#), [174](#)
- [109] Frising, T., Noik, C., and Dalmazzone, C. (2006). The liquid/liquid sedimentation process: from droplet coalescence to technologically enhanced water/oil emulsion gravity separators: a review. *Journal of Dispersion Science and Technology*, 27(7):1035–1057. [27](#), [29](#)
- [110] Fritz, H. M., Mohammed, F., and Yoo, J. (2009). Lituya bay landslide impact generated mega-tsunami 50th anniversary. *Pure and Applied Geophysics*, 166(1-2):153–175. [13](#), [30](#)
- [111] Fulk, D. A. (1994). A numerical analysis of smoothed particle hydrodynamics. Technical report, AIR FORCE INST OF TECH WRIGHT-PATTERSON AFB OH. [91](#)
- [112] Fulk, D. A. and Quinn, D. W. (1996). An analysis of 1-d smoothed particle hydrodynamics kernels. *Journal of Computational Physics*, 126(1):165–180. [45](#)
- [113] Gao, Y., Yin, Y., Li, B., Wang, W., Zhang, N., Yang, C., and Zuo, X. (2017). Investigation and dynamic analysis of the long runout catastrophic landslide at the shenzhen landfill on december 20, 2015, in guangdong, china. *Environmental Earth Sciences*, 76(1):13. [13](#), [27](#), [29](#)
- [114] Gentry, R. A., Martin, R. E., and Daly, B. J. (1966). An eulerian differencing method for unsteady compressible flow problems. *Journal of Computational Physics*, 1(1):87–118. [37](#)

- [115] Gesztelyi, R., Zsuga, J., Kemeny-Beke, A., Varga, B., Juhasz, B., and Tosaki, A. (2012). The hill equation and the origin of quantitative pharmacology. *Archive for history of exact sciences*, 66(4):427–438. [112](#)
- [116] Ghia, U., Ghia, K. N., and Shin, C. (1982). High-re solutions for incompressible flow using the navier-stokes equations and a multigrid method. *Journal of computational physics*, 48(3):387–411. [14](#), [49](#), [51](#)
- [117] Gingold, R. and Monaghan, J. (1982). Kernel estimates as a basis for general particle methods in hydrodynamics. *Journal of Computational Physics*, 46(3):429–453. [91](#)
- [118] Gingold, R. A. and Monaghan, J. J. (1977). Smoothed particle hydrodynamics: theory and application to non-spherical stars. *Monthly notices of the royal astronomical society*, 181(3):375–389. [38](#), [41](#), [99](#), [101](#), [115](#), [118](#)
- [119] Godunov, S. K. and Romenskii, E. (2013). *Elements of continuum mechanics and conservation laws*. Springer Science & Business Media. [64](#)
- [120] Gómez-Gesteira, M. and Dalrymple, R. A. (2004). Using a three-dimensional smoothed particle hydrodynamics method for wave impact on a tall structure. *Journal of waterway, port, coastal, and ocean engineering*, 130(2):63–69. [87](#)
- [121] Gomez-Gesteira, M., Rogers, B. D., Crespo, A. J., Dalrymple, R. A., Narayanaswamy, M., and Dominguez, J. M. (2012). Sphysics—development of a free-surface fluid solver—part 1: Theory and formulations. *Computers & Geosciences*, 48:289–299. [95](#)
- [122] Gomez-Gesteira, M., Rogers, B. D., Dalrymple, R. A., and Crespo, A. J. (2010). State-of-the-art of classical sph for free-surface flows. *Journal of Hydraulic Research*, 48(S1):6–27. [81](#)
- [123] Gotoh, H. and Fredso/e, J. (2001). Lagrangian two-phase flow model of the settling behavior of fine sediment dumped into water. In *Coastal Engineering 2000*, pages 3906–3919. [131](#)
- [124] Gray, J., Monaghan, J., and Swift, R. (2001). Sph elastic dynamics. *Computer methods in applied mechanics and engineering*, 190(49):6641–6662. [14](#), [38](#), [50](#), [55](#), [56](#), [65](#), [66](#), [68](#), [70](#), [89](#), [90](#)
- [125] Greene, G. A., Chen, J. C., and Conlin, M. T. (1988). Onset of entrainment between immiscible liquid layers due to rising gas bubbles. *International Journal of Heat and Mass Transfer*, 31(6):1309–1317. [167](#)
- [126] Greene, G. A., Chen, J. C., and Conlin, M. T. (1991). Bubble induced entrainment between stratified liquid layers. *International journal of heat and mass transfer*, 34(1):149–157. [167](#)
- [127] Grenier, N. (2009). *Modélisation numérique par la méthode SPH de la séparation eau-huile dans les séparateurs gravitaires*. PhD thesis, Ecole Centrale de Nantes (ECN)(ECN)(ECN)(ECN). [76](#), [100](#), [101](#)

- [128] Grenier, N., Antuono, M., Colagrossi, A., Le Touzé, D., and Alessandrini, B. (2009). An hamiltonian interface sph formulation for multi-fluid and free surface flows. *Journal of Computational Physics*, 228(22):8380–8393. [17](#), [49](#), [69](#), [76](#), [100](#), [101](#), [102](#), [137](#), [138](#), [143](#), [144](#), [146](#), [164](#), [204](#)
- [129] Grenier, N., Le Touzé, D., Colagrossi, A., Antuono, M., and Colicchio, G. (2013a). Viscous bubbly flows simulation with an interface sph model. *Ocean Engineering*, 69:88–102. [14](#), [27](#), [29](#), [49](#), [53](#), [69](#), [76](#)
- [130] Grenier, N., Le Touzé, D., Colagrossi, A., Colicchio, G., and Antuono, M. (2013b). Sph multiphase simulation of bubbly flows: Towards oil and water separation. In *ASME 2013 32nd International Conference on Ocean, Offshore and Arctic Engineering*, pages V007T08A083–V007T08A083. American Society of Mechanical Engineers. [76](#)
- [131] Harlow, F. H. (1962). The particle-in-cell method for numerical solution of problems in fluid dynamics. Technical report, Los Alamos Scientific Lab., N. Mex. [37](#)
- [132] Harlow, F. H. (1964). The particle-in-cell computing method for fluid dynamics. *Methods Comput. Phys.*, 3:319–343. [37](#)
- [133] Hashemi, M., Fatehi, R., and Manzari, M. (2012). A modified sph method for simulating motion of rigid bodies in newtonian fluid flows. *International Journal of Non-Linear Mechanics*, 47(6):626–638. [79](#), [93](#)
- [134] Hernquist, L. (1990). Vectorization of tree traversals. *Journal of Computational Physics*, 87(1):137–147. [91](#)
- [135] Hernquist, L. and Katz, N. (1989). Treesph—a unification of sph with the hierarchical tree method. *The Astrophysical Journal Supplement Series*, 70:419–446. [39](#), [91](#)
- [136] Hieber, S. E. and Koumoutsakos, P. (2008). An immersed boundary method for smoothed particle hydrodynamics of self-propelled swimmers. *Journal of Computational Physics*, 227(19):8636–8654. [38](#)
- [137] Hiermaier, S., Könke, D., Stilp, A., and Thoma, K. (1997). Computational simulation of the hypervelocity impact of al-spheres on thin plates of different materials. *International Journal of Impact Engineering*, 20(1-5):363–374. [38](#)
- [138] Hirsch, C. (2007). *Numerical computation of internal and external flows: The fundamentals of computational fluid dynamics*. Butterworth-Heinemann. [36](#)
- [139] Hirschler, M., Kunz, P., Huber, M., Hahn, F., and Nieken, U. (2016). Open boundary conditions for isph and their application to micro-flow. *Journal of Computational Physics*, 307:614–633. [38](#)
- [140] Hirt, C., Amsden, A. A., and Cook, J. (1974). An arbitrary lagrangian-eulerian computing method for all flow speeds. *Journal of computational physics*, 14(3):227–253. [36](#)
- [141] Hirt, C. W. and Nichols, B. D. (1981). Volume of fluid (vof) method for the dynamics of free boundaries. *Journal of computational physics*, 39(1):201–225. [99](#), [101](#)

- [142] Hockney, R. W. and Eastwood, J. W. (1988). *Computer simulation using particles*. crc Press. 37, 91
- [143] Hoogerbrugge, P. and Koelman, J. (1992). Simulating microscopic hydrodynamic phenomena with dissipative particle dynamics. *EPL (Europhysics Letters)*, 19(3):155. 37
- [144] Hosseini, S. and Amanifard, N. (2007). Presenting a modified sph algorithm for numerical studies of fluid-structure interaction problems. *Int. J. Eng. Trans. B*, 20:167–178. 54
- [145] Hosseini, S., Manzari, M., and Hannani, S. (2007). A fully explicit three-step sph algorithm for simulation of non-newtonian fluid flow. *International Journal of Numerical Methods for Heat & Fluid Flow*, 17(7):715–735. 65, 72, 123, 134, 177
- [146] Hosseini, S. M. and Feng, J. J. (2011). Pressure boundary conditions for computing incompressible flows with sph. *Journal of Computational physics*, 230(19):7473–7487. 94
- [147] Hu, D., Long, T., Xiao, Y., Han, X., and Gu, Y. (2014). Fluid–structure interaction analysis by coupled fe–sph model based on a novel searching algorithm. *Computer Methods in Applied Mechanics and Engineering*, 276:266–286. 80
- [148] Hu, X. and Adams, N. (2006a). Angular-momentum conservative smoothed particle dynamics for incompressible viscous flows. *Physics of Fluids*, 18(10):101702. 76, 106
- [149] Hu, X. and Adams, N. (2009). A constant-density approach for incompressible multi-phase sph. *Journal of Computational Physics*, 228(6):2082–2091. 49, 100, 101, 102, 151, 152, 161, 204
- [150] Hu, X. and Adams, N. A. (2007). An incompressible multi-phase sph method. *Journal of computational physics*, 227(1):264–278. 49, 64, 70, 71, 75, 100, 101, 102, 105, 129, 143, 151, 152, 161, 204
- [151] Hu, X. Y. and Adams, N. A. (2006b). A multi-phase sph method for macroscopic and mesoscopic flows. *Journal of Computational Physics*, 213(2):844–861. 38, 73, 75, 78, 97, 100, 101, 102, 104, 107, 151, 152, 161, 204
- [152] Huang, X. and Garcia, M. H. (1998). A herschel–bulkley model for mud flow down a slope. *Journal of fluid mechanics*, 374:305–333. 66
- [153] Huang, Y., Zhang, W., Mao, W., and Jin, C. (2011). Flow analysis of liquefied soils based on smoothed particle hydrodynamics. *Natural hazards*, 59(3):1547–1560. 52
- [154] Hunter, J. (1992). *Surface tension in smoothed particle hydrodynamics*. PhD thesis, Honours thesis, Mathematics Department, Monash University, Melbourne, Australia. 77, 100, 101
- [155] Hysing, S.-R., Turek, S., Kuzmin, D., Parolini, N., Burman, E., Ganesan, S., and Tobiska, L. (2009a). Quantitative benchmark computations of two-dimensional bubble dynamics. *International Journal for Numerical Methods in Fluids*, 60(11):1259–1288. 19, 151, 152, 163, 164, 165

- [156] Hysing, S.-R., Turek, S., Kuzmin, D., Parolini, N., Burman, E., Ganesan, S., and Tobiska, L. (2009b). Quantitative benchmark computations of two-dimensional bubble dynamics. *International Journal for Numerical Methods in Fluids*, 60(11):1259–1288. [19](#), [164](#)
- [157] Idelsohn, S. R., Marti, J., Limache, A., and Oñate, E. (2008). Unified lagrangian formulation for elastic solids and incompressible fluids: application to fluid–structure interaction problems via the pfem. *Computer Methods in Applied Mechanics and Engineering*, 197(19):1762–1776. [15](#), [55](#), [60](#)
- [158] Ihmsen, M., Cornelis, J., Solenthaler, B., Horvath, C., and Teschner, M. (2014). Implicit incompressible sph. *IEEE Transactions on Visualization and Computer Graphics*, 20(3):426–435. [70](#)
- [159] Ionescu, I. R., Mangeney, A., Bouchut, F., and Roche, O. (2015). Viscoplastic modeling of granular column collapse with pressure-dependent rheology. *Journal of Non-Newtonian Fluid Mechanics*, 219:1–18. [126](#), [180](#)
- [160] Issa, R., Violeau, D., Lee, E., and Flament, H. (2010). Modelling nonlinear water waves with rans and les sph models. *Advances in numerical simulation of nonlinear water waves*, 11. [92](#)
- [161] Jameson, A., Schmidt, W., Turkel, E., et al. (1981). Numerical solutions of the euler equations by finite volume methods using runge-kutta time-stepping schemes. *AIAA paper*, 1259:1981. [96](#)
- [162] Jamet, D., Torres, D., and Brackbill, J. (2002). On the theory and computation of surface tension: the elimination of parasitic currents through energy conservation in the second-gradient method. *Journal of Computational Physics*, 182(1):262–276. [155](#)
- [163] Jaumann, G. (1911). Geschlossenes system physikalischer und chemischer differentialgesetze (i. mitteilung). *Sitzungsber. der kaiserliche Akad. der Wissenschaften in Wien, CXVII (Mathematisch IIa)*, 385. [66](#)
- [164] John, D. and Anderson, J. (1995). Computational fluid dynamics: the basics with applications. *P. Perback, International ed., Published*. [36](#)
- [165] Johnson, R. W. (2016). *Handbook of fluid dynamics*. Crc Press. [15](#), [65](#), [67](#)
- [166] Jop, P., Forterre, Y., and Pouliquen, O. (2006). A constitutive law for dense granular flows. *Nature*, 441(7094):727–730. [126](#)
- [167] Kadanoff, L. P., McNamara, G. R., and Zanetti, G. (1989). From automata to fluid flow: comparisons of simulation and theory. *Physical Review A*, 40(8):4527. [37](#)
- [168] Kajtar, J. and Monaghan, J. J. (2008). Sph simulations of swimming linked bodies. *Journal of Computational Physics*, 227(19):8568–8587. [38](#)
- [169] Khanpour, M., Zarrati, A., Kolahdoozan, M., Shakibaeinia, A., and Amirshahi, S. (2016). Mesh-free sph modeling of sediment scouring and flushing. *Computers & Fluids*, 129:67–78. [80](#), [117](#), [119](#)

- [170] Khayyer, A. and Gotoh, H. (2009). Modified moving particle semi-implicit methods for the prediction of 2d wave impact pressure. *Coastal Engineering*, 56(4):419–440. [96](#)
- [171] Khayyer, A., Gotoh, H., and Shao, S. (2008). Corrected incompressible sph method for accurate water-surface tracking in breaking waves. *Coastal Engineering*, 55(3):236–250. [96](#)
- [172] Khayyer, A., Gotoh, H., and Shao, S. (2009). Enhanced predictions of wave impact pressure by improved incompressible sph methods. *Applied Ocean Research*, 31(2):111–131. [96](#)
- [173] Kim, J. (2005). A diffuse-interface model for axisymmetric immiscible two-phase flow. *Applied mathematics and computation*, 160(2):589–606. [157](#)
- [174] Koh, C., Luo, M., Gao, M., and Bai, W. (2013). Modelling of liquid sloshing with constrained floating baffle. *Computers & Structures*, 122:270–279. [79](#)
- [175] Komatina, D. and Jovanovic, M. (1997). Experimental study of steady and unsteady free surface flows with water-clay mixtures. *Journal of Hydraulic Research*, 35(5):579–590. [20](#), [177](#), [178](#), [179](#)
- [176] Koshizuka, S., Nobe, A., and Oka, Y. (1998). Numerical analysis of breaking waves using the moving particle semi-implicit method. *International Journal for Numerical Methods in Fluids*, 26(7):751–769. [37](#)
- [177] Krimi, A., Khelladi, S., Nogueira, X., Deligant, M., Ata, R., and Rezoug, M. (3001forthcomingr). Multiphase smoothed particle hydrodynamics approach for modeling soil-water interactions. *Submitted to Advances in Water Resources*. [76](#)
- [178] Krimi, A., Rezoug, M., Khelladi, S., Nogueira, X., Deligant, M., and Ramírez, L. (2018). Smoothed particle hydrodynamics: A consistent model for interfacial multiphase fluid flow simulations. *Journal of Computational Physics*, 358:53–87. [70](#), [76](#), [78](#), [81](#), [92](#), [132](#), [133](#)
- [179] Kulasegaram, S., Bonet, J., Lewis, R., and Profit, M. (2004). A variational formulation based contact algorithm for rigid boundaries in two-dimensional sph applications. *Computational Mechanics*, 33(4):316–325. [93](#)
- [180] Lafaurie, B., Nardone, C., Scardovelli, R., Zaleski, S., and Zanetti, G. (1994). Modelling merging and fragmentation in multiphase flows with surfer. *Journal of Computational Physics*, 113(1):134–147. [78](#), [100](#), [101](#), [106](#)
- [181] Lahooti, M., Pischevar, A., and Saidi, M. (2011). A novel 2d algorithm for fluid solid interaction based on the smoothed particle hydrodynamics (sph) method. *Scientia Iranica*, 18(3):358–367. [80](#)
- [182] Lajeunesse, E., Mangeney-Castelnau, A., and Vilotte, J. (2004). Spreading of a granular mass on a horizontal plane. *Physics of Fluids*, 16(7):2371–2381. [179](#)
- [183] Lajeunesse, E., Monnier, J., and Homsy, G. (2005). Granular slumping on a horizontal surface. *Physics of fluids*, 17(10):103302. [21](#), [178](#), [179](#), [180](#), [181](#), [182](#)

- [184] Landau, L. D. and Lifshitz, E. (1986). Theory of elasticity, vol. 7. *Course of Theoretical Physics*, 3:109. [68](#)
- [185] Lastiwka, M., Basa, M., and Quinlan, N. J. (2009). Permeable and non-reflecting boundary conditions in sph. *International journal for numerical methods in fluids*, 61(7):709–724. [94](#)
- [186] Lavrov, A., Skjetne, P., Lund, B., Bjønnes, E., Bjørnson, F. O., Busklein, J. O., Coudert, T., Klebert, P., Lye, K. O., Olsen, J. E., et al. (2015). Density-consistent initialization of sph on a regular cartesian grid: Comparative numerical study of 10 smoothing kernels in 1, 2 and 3 dimensions. *Procedia IUTAM*, 18:85–95. [39](#)
- [187] Layzer, D. (1955). On the instability of superposed fluids in a gravitational field. *The astrophysical journal*, 122:1. [137](#), [138](#), [145](#), [204](#)
- [188] Lee, E.-S., Moulinec, C., Xu, R., Violeau, D., Laurence, D., and Stansby, P. (2008). Comparisons of weakly compressible and truly incompressible algorithms for the sph mesh free particle method. *Journal of computational physics*, 227(18):8417–8436. [49](#), [70](#), [96](#)
- [189] Lee, E.-S., Violeau, D., Issa, R., and Ploix, S. (2010). Application of weakly compressible and truly incompressible sph to 3-d water collapse in waterworks. *Journal of Hydraulic Research*, 48(S1):50–60. [38](#)
- [190] Lee, H. G., Kim, K., and Kim, J. (2011). On the long time simulation of the rayleigh–taylor instability. *International Journal for Numerical Methods in Engineering*, 85(13):1633–1647. [138](#)
- [191] Leroy, A., Violeau, D., Ferrand, M., Fratter, L., and Joly, A. (2016). A new open boundary formulation for incompressible sph. *Computers & Mathematics with Applications*, 72(9):2417–2432. [94](#)
- [192] Leroy, A., Violeau, D., Ferrand, M., and Kassiotis, C. (2014). Unified semi-analytical wall boundary conditions applied to 2-d incompressible sph. *Journal of Computational Physics*, 261:106–129. [13](#), [14](#), [43](#), [49](#), [51](#), [93](#)
- [193] Li, J. (2013). An arbitrary lagrangian eulerian method for three-phase flows with triple junction points. *Journal of Computational Physics*, 251:1–16. [151](#), [152](#), [156](#), [204](#)
- [194] Libersky, L. D. and Petschek, A. (1991). Smooth particle hydrodynamics with strength of materials. In *Advances in the free-Lagrange method including contributions on adaptive gridding and the smooth particle hydrodynamics method*, pages 248–257. Springer. [68](#)
- [195] Libersky, L. D., Petschek, A. G., Carney, T. C., Hipp, J. R., and Allahdadi, F. A. (1993). High strain lagrangian hydrodynamics: a three-dimensional sph code for dynamic material response. *Journal of computational physics*, 109(1):67–75. [91](#)
- [196] Lind, S., Stansby, P., and Rogers, B. D. (2016). Incompressible–compressible flows with a transient discontinuous interface using smoothed particle hydrodynamics (sph). *Journal of Computational Physics*, 309:129–147. [81](#)

- [197] Lind, S., Xu, R., Stansby, P., and Rogers, B. D. (2012). Incompressible smoothed particle hydrodynamics for free-surface flows: A generalised diffusion-based algorithm for stability and validations for impulsive flows and propagating waves. *Journal of Computational Physics*, 231(4):1499–1523. [71](#)
- [198] Liu, G.-R. and Liu, M. B. (2003). *Smoothed particle hydrodynamics: a meshfree particle method*. World Scientific. [37](#), [45](#), [87](#), [91](#)
- [199] Liu, M. and Liu, G. (2010). Smoothed particle hydrodynamics (sph): an overview and recent developments. *Archives of computational methods in engineering*, 17(1):25–76. [42](#), [91](#)
- [200] Liu, M., Liu, G., and Lam, K. (2003a). Constructing smoothing functions in smoothed particle hydrodynamics with applications. *Journal of Computational and applied Mathematics*, 155(2):263–284. [39](#), [42](#), [45](#), [104](#)
- [201] Liu, M., Liu, G., Lam, K., and Zong, Z. (2003b). Meshfree particle simulation of the detonation process for high explosives in shaped charge unlined cavity configurations. *Shock Waves*, 12(6):509–520. [38](#)
- [202] Liu, M., Liu, G., Zong, Z., and Lam, K. (2003c). Computer simulation of high explosive explosion using smoothed particle hydrodynamics methodology. *Computers & Fluids*, 32(3):305–322. [38](#), [96](#)
- [203] Liu, M., Shao, J., and Chang, J. (2012). On the treatment of solid boundary in smoothed particle hydrodynamics. *Science China Technological Sciences*, 55(1):244–254. [92](#)
- [204] Liu, M., Xie, W., and Liu, G. (2005). Modeling incompressible flows using a finite particle method. *Applied mathematical modelling*, 29(12):1252–1270. [48](#)
- [205] Liu, M.-B. and Liu, G.-R. (2015). *Particle methods for multi-scale and multi-physics*. World Scientific. [91](#)
- [206] LIU, M.-b., SHAO, J.-r., and LI, H.-q. (2013). Numerical simulation of hydro-elastic problems with smoothed particle hydrodynamics method. *Journal of Hydrodynamics, Ser. B*, 25(5):673–682. [50](#)
- [207] Liu, W. K., Jun, S., and Zhang, Y. F. (1995). Reproducing kernel particle methods. *International journal for numerical methods in fluids*, 20(8-9):1081–1106. [44](#)
- [208] Long, T., Hu, D., Wan, D., Zhuang, C., and Yang, G. (2017). An arbitrary boundary with ghost particles incorporated in coupled fem–sph model for fsi problems. *Journal of Computational Physics*, 350:166–183. [80](#)
- [209] Long, T., Hu, D., Yang, G., and Wan, D. (2016). A particle-element contact algorithm incorporated into the coupling methods of fem–isph and fem–wcsph for fsi problems. *Ocean Engineering*, 123:154–163. [80](#)
- [210] Lucy, L. B. (1977). A numerical approach to the testing of the fission hypothesis. *The astronomical journal*, 82:1013–1024. [37](#), [38](#), [87](#), [99](#), [101](#), [115](#), [118](#)

- [211] Macdonald, J. R. (1966). Some simple isothermal equations of state. *Reviews of Modern Physics*, 38(4):669. [69](#)
- [212] Macia, F., González, L. M., Cercos-Pita, J. L., and Souto-Iglesias, A. (2012). A boundary integral sph formulation: consistency and applications to isph and wcsph. *Progress of Theoretical Physics*, 128(3):439–462. [93](#)
- [213] Mair, H. U. (1999). Hydrocodes for structural response to underwater explosions. *Shock and Vibration*, 6(2):81–96. [36](#)
- [214] Makino, J. (1990). Vectorization of a treecode. *Journal of Computational Physics*, 87(1):148–160. [91](#)
- [215] Manenti, S., Sibilla, S., Gallati, M., Agate, G., and Guandalini, R. (2011). Sph simulation of sediment flushing induced by a rapid water flow. *Journal of Hydraulic Engineering*, 138(3):272–284. [80](#), [117](#), [119](#)
- [216] Marrone, S., Antuono, M., Colagrossi, A., Colicchio, G., Le Touzé, D., and Graziani, G. (2011a). δ -sph model for simulating violent impact flows. *Computer Methods in Applied Mechanics and Engineering*, 200(13):1526–1542. [13](#), [48](#), [49](#), [50](#), [69](#), [86](#), [92](#), [234](#)
- [217] Marrone, S., Bouscasse, B., Colagrossi, A., and Antuono, M. (2012). Study of ship wave breaking patterns using 3d parallel sph simulations. *Computers & Fluids*, 69:54–66.
- [218] Marrone, S., Colagrossi, A., Antuono, M., Colicchio, G., and Graziani, G. (2013). An accurate sph modeling of viscous flows around bodies at low and moderate reynolds numbers. *Journal of Computational Physics*, 245:456–475. [14](#), [49](#), [53](#), [69](#), [70](#), [86](#), [103](#)
- [219] Marrone, S., Colagrossi, A., Antuono, M., Lugni, C., and Tulin, M. (2011b). A 2d+t sph model to study the breaking wave pattern generated by fast ships. *Journal of Fluids and Structures*, 27(8):1199–1215. [92](#)
- [220] Marrone, S., Colagrossi, A., Le Touzé, D., and Graziani, G. (2010). Fast free-surface detection and level-set function definition in sph solvers. *Journal of Computational Physics*, 229(10):3652–3663. [96](#)
- [221] Mase, G. T., Smelser, R. E., and Mase, G. E. (2009). *Continuum mechanics for engineers*. CRC press. [64](#)
- [222] Mayrhofer, A., Ferrand, M., Kassiotis, C., Violeau, D., and Morel, F.-X. (2015). Unified semi-analytical wall boundary conditions in sph: analytical extension to 3-d. *Numerical Algorithms*, 68(1):15–34. [93](#)
- [223] Mayrhofer, A., Rogers, B. D., Violeau, D., and Ferrand, M. (2013). Investigation of wall bounded flows using sph and the unified semi-analytical wall boundary conditions. *Computer Physics Communications*, 184(11):2515–2527. [93](#)
- [224] Miller, D. (1960a). Giant waves in lituya bay, alaska. *U.S. Geological Survey Professional Paper 354-C*, pages 51–86. [183](#)
- [225] Miller, D. (1960b). Giant waves in lituya bay, alaska, geological survey professional paper 354-c. *US Government Printing Office, Washington DC*. [116](#), [118](#)

- [226] Mises, R. v. (1928). Mechanik der plastischen formänderung von kristallen. *ZAMM-Journal of Applied Mathematics and Mechanics/Zeitschrift für Angewandte Mathematik und Mechanik*, 8(3):161–185. [66](#), [121](#), [123](#)
- [227] Mohr, O. (1906). *Abhandlungen aus dem gebiete der technischen mechanik...* [50](#), [116](#), [119](#), [123](#)
- [228] Molteni, D. and Colagrossi, A. (2009). A simple procedure to improve the pressure evaluation in hydrodynamic context using the sph. *Computer Physics Communications*, 180(6):861–872. [86](#), [127](#)
- [229] Monaghan, J. (1985). Particle methods for hydrodynamics. *Computer Physics Reports*, 3(2):71–124. [91](#)
- [230] Monaghan, J. (1989). On the problem of penetration in particle methods. *Journal of Computational physics*, 82(1):1–15. [86](#), [96](#), [97](#)
- [231] Monaghan, J. (1995). Heat conduction with discontinuous conductivity. *Applied Mathematics Reports and Preprints*, 95(18):7–1. [47](#)
- [232] Monaghan, J. (1997a). Implicit sph drag and dusty gas dynamics. *Journal of Computational Physics*, 138(2):801–820. [38](#)
- [233] Monaghan, J. (1997b). Sph and riemann solvers. *Journal of Computational Physics*, 136(2):298–307. [88](#)
- [234] Monaghan, J. (2012). Smoothed particle hydrodynamics and its diverse applications. *Annual Review of Fluid Mechanics*, 44:323–346. [69](#), [73](#), [77](#), [115](#), [118](#)
- [235] Monaghan, J. and Gingold, R. (1983). Shock simulation by the particle method sph. *Journal of computational physics*, 52(2):374–389. [38](#), [74](#), [87](#), [88](#), [109](#)
- [236] Monaghan, J. and Kocharyan, A. (1995). Sph simulation of multi-phase flow. *Computer Physics Communications*, 87(1-2):225–235. [77](#)
- [237] Monaghan, J., Kos, A., and Issa, N. (2003). Fluid motion generated by impact. *Journal of waterway, port, coastal, and ocean engineering*, 129(6):250–259. [79](#)
- [238] Monaghan, J. and Rafiee, A. (2013). A simple sph algorithm for multi-fluid flow with high density ratios. *International Journal for Numerical Methods in Fluids*, 71(5):537–561. [14](#), [17](#), [49](#), [52](#), [137](#), [138](#), [143](#), [144](#), [146](#), [204](#)
- [239] Monaghan, J. J. (1982). Why particle methods work. *SIAM Journal on Scientific and Statistical Computing*, 3(4):422–433. [46](#)
- [240] Monaghan, J. J. (1988a). An introduction to sph. *Computer physics communications*, 48(1):89–96. [37](#)
- [241] Monaghan, J. J. (1988b). An introduction to sph. *Computer physics communications*, 48(1):89–96. [99](#), [101](#), [115](#), [118](#)
- [242] Monaghan, J. J. (1992). Smoothed particle hydrodynamics. *Annual review of astronomy and astrophysics*, 30(1):543–574. [38](#), [39](#), [46](#), [47](#), [73](#), [74](#), [75](#), [88](#), [97](#)

- [243] Monaghan, J. J. (1994). Simulating free surface flows with sph. *Journal of computational physics*, 110(2):399–406. [38](#), [48](#), [69](#), [91](#), [102](#), [134](#), [234](#)
- [244] Monaghan, J. J. (2000). Sph without a tensile instability. *Journal of Computational Physics*, 159(2):290–311. [88](#), [89](#)
- [245] Monaghan, J. J. (2005a). Smoothed particle hydrodynamics. *Reports on progress in physics*, 68(8):1703. [38](#), [72](#), [73](#), [79](#), [80](#), [87](#), [88](#), [96](#), [134](#), [168](#), [184](#)
- [246] Monaghan, J. J. (2005b). Smoothed particle hydrodynamics. *Reports on progress in physics*, 68(8):1703. [111](#), [127](#)
- [247] Monaghan, J. J. and Kajtar, J. B. (2009). Sph particle boundary forces for arbitrary boundaries. *Computer Physics Communications*, 180(10):1811–1820. [81](#), [87](#), [112](#)
- [248] Monaghan, J. J. and Lattanzio, J. C. (1985). A refined particle method for astrophysical problems. *Astronomy and astrophysics*, 149:135–143. [41](#)
- [249] Monaghan, J. J. and Lattanzio, J. C. (1991). A simulation of the collapse and fragmentation of cooling molecular clouds. *The Astrophysical Journal*, 375:177–189. [38](#)
- [250] Moreno, N., Vignal, P., Li, J., and Calo, V. M. (2013). Multiscale modeling of blood flow: coupling finite elements with smoothed dissipative particle dynamics. *Procedia Computer Science*, 18:2565–2574. [38](#)
- [251] Moriguchi, S., Borja, R. I., Yashima, A., and Sawada, K. (2009). Estimating the impact force generated by granular flow on a rigid obstruction. *Acta Geotechnica*, 4(1):57–71. [126](#)
- [252] Morris, J. P. (1995). A study of the stability properties of sph. *arXiv preprint astro-ph/9503124*. [41](#)
- [253] Morris, J. P. (1996). *Analysis of smoothed particle hydrodynamics with applications*. Monash University Australia. [41](#), [104](#), [126](#)
- [254] Morris, J. P. (2000). Simulating surface tension with smoothed particle hydrodynamics. *International journal for numerical methods in fluids*, 33(3):333–353. [38](#), [64](#), [69](#), [77](#), [78](#), [100](#), [101](#), [102](#), [103](#), [107](#), [120](#), [151](#), [152](#), [161](#), [204](#)
- [255] Morris, J. P., Fox, P. J., and Zhu, Y. (1997). Modeling low reynolds number incompressible flows using sph. *Journal of computational physics*, 136(1):214–226. [47](#), [69](#), [74](#), [88](#), [91](#), [95](#), [97](#), [134](#)
- [256] Moussa, B. B., Lanson, N., and Vila, J. P. (1999). Convergence of meshless methods for conservation laws applications to euler equations. In *Hyperbolic Problems: Theory, Numerics, Applications*, pages 31–40. Springer. [85](#)
- [257] Mujumdar, A., Beris, A. N., and Metzner, A. B. (2002). Transient phenomena in thixotropic systems. *Journal of Non-Newtonian Fluid Mechanics*, 102(2):157–178. [66](#)
- [258] Neethling, S. J. and Barker, D. J. (2016). Using smooth particle hydrodynamics (sph) to model multiphase mineral processing systems. *Minerals Engineering*, 90:17–28. [100](#), [101](#), [102](#)

- [259] Nelson, R. P. and Langer, W. D. (1997). The dynamics of low-mass molecular clouds in external radiation fields. *The Astrophysical Journal*, 482(2):796. [38](#)
- [260] Nguyen, C. T., Nguyen, C. T., Bui, H. H., Nguyen, G. D., and Fukagawa, R. (2017). A new sph-based approach to simulation of granular flows using viscous damping and stress regularisation. *Landslides*, 14(1):69–81. [52](#), [68](#)
- [261] Nishida, T., Sugihara, K., and Kimura, M. (2007). Stable marker-particle method for the voronoi diagram in a flow field. *Journal of Computational and Applied Mathematics*, 202(2):377–391. [99](#), [101](#)
- [262] Nugent, S. and Posch, H. (2000). Liquid drops and surface tension with smoothed particle applied mechanics. *Physical Review E*, 62(4):4968. [77](#)
- [263] Oger, G. (2006). *Aspects théoriques de la méthode SPH et applications à l'hydrodynamique à surface libre*. PhD thesis, Nantes. [95](#)
- [264] Oger, G., Doring, M., Alessandrini, B., and Ferrant, P. (2007). An improved sph method: Towards higher order convergence. *Journal of Computational Physics*, 225(2):1472–1492. [83](#)
- [265] Omang, M. and Trulsen, J. (2014). Multi-phase shock simulations with smoothed particle hydrodynamics (sph). *Shock Waves*, 24(5):521–536. [38](#)
- [266] Osher, S. and Fedkiw, R. P. (2001). Level set methods: an overview and some recent results. *Journal of Computational physics*, 169(2):463–502. [99](#), [101](#)
- [267] Pal, R., Yan, Y., and Masliyah, J. (1992). Rheology of emulsions. ACS Publications. [65](#), [66](#)
- [268] Panizzo, A. (2004). Physical and numerical modelling of subaerial landslide generated waves. *Ph. D thesis. Università degli Studi di L'Aquila*. [82](#)
- [269] Panton, R. L. (2006). *Incompressible flow*. John Wiley & Sons. [65](#)
- [270] Papanastasiou, T. C. (1987). Flows of materials with yield. *Journal of Rheology*, 31(5):385–404. [66](#), [121](#), [122](#)
- [271] Popinet, S. and Zaleski, S. (1999). A front-tracking algorithm for accurate representation of surface tension. *International Journal for Numerical Methods in Fluids*, 30(6):775–793. [155](#)
- [272] Pramanik, R., Douillet-Grellier, T., Pan, K., Jones, B., Albaiz, A., Williams, J., Du, J., Pourpak, H., Deb, D., et al. (2016). An sph approach to the simulation of hydraulic fracture propagation in naturally fractured rock medium. In *50th US Rock Mechanics/Geomechanics Symposium*. American Rock Mechanics Association. [68](#)
- [273] Price, D. J. (2010). Smoothed particle magnetohydrodynamics–iv. using the vector potential. *Monthly Notices of the Royal Astronomical Society*, 401(3):1475–1499. [109](#)
- [274] Price, D. J., Federrath, C., and Brunt, C. M. (2010). The density variance–mach number relation in supersonic, isothermal turbulence. *The Astrophysical Journal Letters*, 727(1):L21. [38](#)

- [275] Qiu, L.-C. (2008). Two-dimensional sph simulations of landslide-generated water waves. *Journal of Hydraulic Engineering*, 134(5):668–671. [55](#), [118](#)
- [276] Rafiee, A., Manzari, M., and Hosseini, M. (2007). An incompressible sph method for simulation of unsteady viscoelastic free-surface flows. *International Journal of Non-Linear Mechanics*, 42(10):1210–1223. [66](#)
- [277] Rafiee, A. and Thiagarajan, K. P. (2009). An sph projection method for simulating fluid-hypoelastic structure interaction. *Computer Methods in Applied Mechanics and Engineering*, 198(33):2785–2795. [15](#), [50](#), [54](#), [55](#), [60](#), [72](#), [80](#)
- [278] Rahmat, A., Tofighi, N., Shadloo, M., and Yildiz, M. (2014). Numerical simulation of wall bounded and electrically excited rayleigh–taylor instability using incompressible smoothed particle hydrodynamics. *Colloids and Surfaces A: Physicochemical and Engineering Aspects*, 460:60–70. [64](#)
- [279] Randles, P. and Libersky, L. (1996). Smoothed particle hydrodynamics: some recent improvements and applications. *Computer methods in applied mechanics and engineering*, 139(1-4):375–408. [68](#), [74](#), [83](#), [130](#)
- [280] Randles, P. and Libersky, L. (2000). Normalized sph with stress points. *International Journal for Numerical Methods in Engineering*, 48(10):1445–1462. [89](#)
- [281] Rashaïda, A. A. (2005). *Flow of a non-Newtonian Bingham plastic fluid over a rotating disk*. PhD thesis. [66](#)
- [282] Rasio, F. A. and Lombardi, J. C. (1999). Smoothed particle hydrodynamics calculations of stellar interactions. *Journal of Computational and Applied Mathematics*, 109(1):213–230. [38](#)
- [283] Reddy, J. N. (2010). *Principles of continuum mechanics: a study of conservation principles with applications*. Cambridge University Press. [64](#)
- [284] Ren, B., He, M., Dong, P., and Wen, H. (2015). Nonlinear simulations of wave-induced motions of a freely floating body using wcsph method. *Applied Ocean Research*, 50:1–12. [79](#)
- [285] Ren, B., Yan, X., Yang, T., Li, C.-f., Lin, M. C., and Hu, S.-m. (2016). Fast sph simulation for gaseous fluids. *The Visual Computer*, 32(4):523–534. [27](#), [29](#)
- [286] Robinson, M. and Monaghan, J. (2008). Forced two-dimensional wall-bounded turbulence using sph. In *3th ERCOFTAC SPHERIC workshop on SPH simulatons, June*, pages 4–6. [42](#)
- [287] Rogers, B. D. and Dalrymple, R. A. (2008). Sph modeling of tsunami waves. *Advanced numerical models for simulating tsunami waves and runup*, 10:75–100. [91](#)
- [288] Roubtsova, V. and Kahawita, R. (2006). The sph technique applied to free surface flows. *Computers & Fluids*, 35(10):1359–1371. [48](#)
- [289] Rzadkiewicz, S. A., Mariotti, C., and Heinrich, P. (1996). Modelling of submarine landslides and generated water waves. *Physics and Chemistry of the Earth*, 21(1-2):7–12. [21](#), [183](#), [184](#)

- [290] Rzadkiewicz, S. A., Mariotti, C., and Heinrich, P. (1997). Numerical simulation of submarine landslides and their hydraulic effects. *Journal of Waterway, Port, Coastal, and Ocean Engineering*, 123(4):149–157. [15](#), [21](#), [55](#), [61](#), [183](#), [184](#)
- [291] Salazar, F., Irazábal, J., Larese, A., and Oñate, E. (2015). Numerical modelling of landslide-generated waves with the particle finite element method (pfem) and a non-newtonian flow model. *International Journal for Numerical and Analytical Methods in Geomechanics*. [126](#)
- [292] Saunders, K., Prakash, M., Cleary, P. W., and Cordell, M. (2014). Application of smoothed particle hydrodynamics for modelling gated spillway flows. *Applied Mathematical Modelling*, 38(17):4308–4322. [38](#)
- [293] Schäfer, C., Riecker, S., Maindl, T. I., Speith, R., Scherrer, S., and Kley, W. (2016). A smooth particle hydrodynamics code to model collisions between solid, self-gravitating objects. *Astronomy & Astrophysics*, 590:A19. [70](#), [87](#)
- [294] Schwaiger, H. and Higman, B. (2007). Lagrangian hydrocode simulations of the 1958 lituya bay tsunamigenic rockslide. *Geochemistry, Geophysics, Geosystems*, 8(7). [116](#), [118](#)
- [295] Schwaiger, H. F. (2008). An implicit corrected sph formulation for thermal diffusion with linear free surface boundary conditions. *International journal for numerical methods in engineering*, 75(6):647–671. [84](#), [96](#)
- [296] Shadloo, M., Oger, G., and Le Touzé, D. (2016). Smoothed particle hydrodynamics method for fluid flows, towards industrial applications: Motivations, current state, and challenges. *Computers & Fluids*, 136:11–34. [80](#)
- [297] Shadloo, M., Zainali, A., and Yildiz, M. (2013). Simulation of single mode rayleigh–taylor instability by sph method. *Computational Mechanics*, pages 1–17. [49](#)
- [298] Shahriari, S., Maleki, H., Hassan, I., and Kadem, L. (2011). Smoothed particle hydrodynamics simulation of flow through a bileaflet mechanical heart valve: Advantages and prospects. *METHODOLOGY*, 10:11. [38](#)
- [299] Shakibaeinia, A. and Jin, Y.-C. (2011). A mesh-free particle model for simulation of mobile-bed dam break. *Advances in Water Resources*, 34(6):794–807. [80](#), [117](#), [119](#), [131](#)
- [300] Shao, S. (2006). Incompressible sph simulation of wave breaking and overtopping with turbulence modelling. *International Journal for Numerical Methods in Fluids*, 50(5):597–621. [96](#)
- [301] Shao, S. and Gotoh, H. (2005). Turbulence particle models for tracking free surfaces. *Journal of Hydraulic Research*, 43(3):276–289. [37](#)
- [302] Shao, S., Ji, C., Graham, D. I., Reeve, D. E., James, P. W., and Chadwick, A. J. (2006). Simulation of wave overtopping by an incompressible sph model. *Coastal Engineering*, 53(9):723–735. [70](#)
- [303] Shao, S. and Lo, E. Y. (2003). Incompressible sph method for simulating newtonian and non-newtonian flows with a free surface. *Advances in water resources*, 26(7):787–800. [38](#), [70](#), [71](#), [96](#), [134](#)

- [304] Shepard, D. (1968a). A two-dimensional interpolation function for irregularly-spaced data. In *Proceedings of the 1968 23rd ACM national conference*, pages 517–524. ACM. [80](#)
- [305] Shepard, D. (1968b). A two-dimensional interpolation function for irregularly-spaced data. In *Proceedings of the 1968 23rd ACM National Conference*, ACM '68, pages 517–524, New York, NY, USA. ACM. [174](#)
- [306] Shi, C., An, Y., Wu, Q., Liu, Q., and Cao, Z. (2016). Numerical simulation of landslide-generated waves using a soil–water coupling smoothed particle hydrodynamics model. *Advances in Water Resources*, 92:130–141. [79](#), [116](#), [119](#)
- [307] Singh, S. and Hans, H. (1966). Magnetic viscosity and the stability of superposed fluids in a magnetic field. *Nuclear Fusion*, 6(1):6. [49](#)
- [308] Sivanapillai, R., Falkner, N., Hartmaier, A., and Steeb, H. (2016a). A csf-sph method for simulating drainage and imbibition at pore-scale resolution while tracking interfacial areas. *Advances in Water Resources*, 95:212–234. [69](#), [103](#)
- [309] Sivanapillai, R., Falkner, N., Hartmaier, A., and Steeb, H. (2016b). A csf-sph method for simulating drainage and imbibition at pore-scale resolution while tracking interfacial areas. *Advances in Water Resources*, 95:212–234. [120](#)
- [310] Sommer-Larsen, J., Gelato, S., and Vedel, H. (1999). Formation of disk galaxies: feedback and the angular momentum problem. *The Astrophysical Journal*, 519(2):501. [38](#)
- [311] Souto-Iglesias, A., Macià, F., González, L. M., and Cercos-Pita, J. L. (2013). On the consistency of mps. *Computer Physics Communications*, 184(3):732–745. [37](#)
- [312] Spinewine, B. et al. (2005). Two-layer flow behaviour and the effects of granular dilatancy in dam-break induced sheet-flow. *Hydraulic Structures. University of Catholic the Louvain*. [22](#), [187](#), [189](#), [192](#)
- [313] Sugano, T., Nozu, A., Kohama, E., Shimosako, K.-i., and Kikuchi, Y. (2014). Damage to coastal structures. *Soils and Foundations*, 54(4):883–901. [191](#)
- [314] Sugiura, K. and Inutsuka, S.-i. (2017). An extension of godunov sph ii: Application to elastic dynamics. *Journal of Computational Physics*, 333:78–103. [50](#)
- [315] SULIANTO, A. A. and MURAKAMI, K. (2015). Sph simulation of local scouring on rubble mound due to tsunami overflow. *strain*, 2(2):4. [80](#), [116](#), [117](#), [119](#)
- [316] Sun, P., Ming, F., and Zhang, A. (2015). Numerical simulation of interactions between free surface and rigid body using a robust sph method. *Ocean Engineering*, 98:32–49. [79](#)
- [317] Sussman, M., Smereka, P., and Osher, S. (1994a). A level set approach for computing solutions to incompressible two-phase flow. *Journal of Computational physics*, 114(1):146–159. [19](#), [163](#), [164](#)
- [318] Sussman, M., Smereka, P., and Osher, S. (1994b). A level set approach for computing solutions to incompressible two-phase flow. *Journal of Computational physics*, 114(1):146–159. [19](#), [151](#), [152](#), [165](#), [169](#)

- [319] Swegle, J., Hicks, D., and Attaway, S. (1995). Smoothed particle hydrodynamics stability analysis. *Journal of computational physics*, 116(1):123–134. [41](#), [88](#)
- [320] Szewc, K. (2017). Smoothed particle hydrodynamics modeling of granular column collapse. *Granular Matter*, 19(1):3. [52](#)
- [321] Takahashi, H., Sassa, S., Morikawa, Y., Takano, D., and Maruyama, K. (2014). Stability of caisson-type breakwater foundation under tsunami-induced seepage. *Soils and Foundations*, 54(4):789–805. [191](#)
- [322] Takeda, H., Miyama, S. M., and Sekiya, M. (1994). Numerical simulation of viscous flow by smoothed particle hydrodynamics. *Progress of Theoretical Physics*, 92(5):939–960. [92](#)
- [323] Tappin, D. R., Watts, P., and Grilli, S. T. (2008). The Papua New Guinea tsunami of 17 July 1998: anatomy of a catastrophic event. *Natural Hazards and Earth System Science*, 8(2):243–266. [183](#)
- [324] Tartakovsky, A. and Meakin, P. (2005a). Modeling of surface tension and contact angles with smoothed particle hydrodynamics. *Physical Review E*, 72(2):026301. [77](#), [100](#), [101](#)
- [325] Tartakovsky, A. M., Ferris, K. F., and Meakin, P. (2009). Lagrangian particle model for multiphase flows. *Computer Physics Communications*, 180(10):1874–1881. [47](#)
- [326] Tartakovsky, A. M. and Meakin, P. (2005b). A smoothed particle hydrodynamics model for miscible flow in three-dimensional fractures and the two-dimensional rayleigh–taylor instability. *Journal of Computational Physics*, 207(2):610–624. [100](#), [101](#)
- [327] Tartakovsky, A. M., Pan, W., and Monaghan, J. J. (2012). Sph non-newtonian model for ice sheet and ice shelf dynamics. Technical report, Pacific Northwest National Laboratory (PNNL), Richland, WA (US). [87](#)
- [328] Tartakovsky, A. M. and Panchenko, A. (2016). Pairwise force smoothed particle hydrodynamics model for multiphase flow: surface tension and contact line dynamics. *Journal of Computational Physics*, 305:1119–1146. [77](#)
- [329] Teng, H. and Zhang, J. (2013). A new thixotropic model for waxy crude. *Rheologica Acta*, 52(10-12):903–911. [66](#)
- [330] Torres, D. and Brackbill, J. (2000). The point-set method: front-tracking without connectivity. *Journal of Computational Physics*, 165(2):620–644. [155](#)
- [331] Ulrich, C., Leonardi, M., and Rung, T. (2013). Multi-physics sph simulation of complex marine-engineering hydrodynamic problems. *Ocean Engineering*, 64:109–121. [38](#), [80](#), [117](#), [119](#)
- [332] Ulrich, C. and Rung, T. (2010). Multiphysics sph for harbor and ocean engineering hydrodynamics. In *V European Conference on Computational Fluid Dynamics ECCOMAS CFD*. [38](#)

- [333] Unverdi, S. O. and Tryggvason, G. (1992). A front-tracking method for viscous, incompressible, multi-fluid flows. *Journal of computational physics*, 100(1):25–37. [99](#), [101](#)
- [334] Vacondio, R., Rogers, B., Stansby, P., and Mignosa, P. (2011). Sph modeling of shallow flow with open boundaries for practical flood simulation. *Journal of Hydraulic Engineering*, 138(6):530–541. [94](#)
- [335] Valdez-Balderas, D., Domínguez, J. M., Rogers, B. D., and Crespo, A. J. (2013). Towards accelerating smoothed particle hydrodynamics simulations for free-surface flows on multi-gpu clusters. *Journal of Parallel and Distributed Computing*, 73(11):1483–1493. [48](#)
- [336] Valizadeh, A. and Monaghan, J. J. (2015). A study of solid wall models for weakly compressible sph. *Journal of Computational Physics*, 300:5–19. [93](#)
- [337] Verlet, L. (1967). Computer" experiments" on classical fluids. i. thermodynamical properties of lennard-jones molecules. *Physical review*, 159(1):98. [96](#)
- [338] Vila, J. (1999). On particle weighted methods and smooth particle hydrodynamics. *Mathematical models and methods in applied sciences*, 9(02):161–209. [73](#), [74](#), [83](#), [85](#)
- [339] Violeau, D. and Issa, R. (2007). Numerical modelling of complex turbulent free-surface flows with the sph method: an overview. *International Journal for Numerical Methods in Fluids*, 53(2):277–304. [48](#), [74](#)
- [340] Violeau, D. and Rogers, B. D. (2016). Smoothed particle hydrodynamics (sph) for free-surface flows: past, present and future. *Journal of Hydraulic Research*, 54(1):1–26. [95](#)
- [341] Viroulet, S., Sauret, A., and Kimmoun, O. (2014). Tsunami generated by a granular collapse down a rough inclined plane. *EPL (Europhysics Letters)*, 105(3):34004. [185](#)
- [342] Viroulet, S., Sauret, A., Kimmoun, O., and Kharif, C. (2013). Granular collapse into water: toward tsunami landslides. *J. Visualization*, 16(3):189–191. [21](#), [185](#), [187](#)
- [343] Vola, D., Babik, F., and Latché, J.-C. (2004). On a numerical strategy to compute gravity currents of non-newtonian fluids. *Journal of computational physics*, 201(2):397–420. [76](#), [122](#)
- [344] Wang, C., Wang, Y., Peng, C., and Meng, X. (2016a). Smoothed particle hydrodynamics simulation of water-soil mixture flows. *Journal of Hydraulic Engineering*, 142(10):04016032. [119](#)
- [345] Wang, D., Li, S., Arikawa, T., and Gen, H. (2016b). Isph simulation of scour behind seawall due to continuous tsunami overflow. *Coastal Engineering Journal*, 58(03):1650014. [80](#), [117](#), [119](#)
- [346] Wang, W., Chen, G.-q., Zhang, H., Zhou, S.-h., Liu, S.-g., Wu, Y.-q., and Fan, F.-s. (2016c). Analysis of landslide-generated impulsive waves using a coupled dda-sph method. *Engineering Analysis with Boundary Elements*, 64:267–277. [118](#)

- [347] Wendland, H. (1995). Piecewise polynomial, positive definite and compactly supported radial functions of minimal degree. *Advances in computational Mathematics*, 4(1):389–396. [42](#), [144](#)
- [348] Whitehouse, S. C. and Bate, M. R. (2004). Smoothed particle hydrodynamics with radiative transfer in the flux-limited diffusion approximation. *Monthly Notices of the Royal Astronomical Society*, 353(4):1078–1094. [38](#)
- [349] Widom, B. (1982). Molecular theory of capillarity. [160](#)
- [350] Wilkins, M. L. (2013). *Computer simulation of dynamic phenomena*. Springer Science & Business Media. [36](#)
- [351] Wolfram, S. (1983). Cellular automata. *Los Alamos Science*, 9:2–27. [37](#)
- [352] Xenakis, A., Lind, S., Stansby, P., and Rogers, B. (2015a). An incompressible sph scheme with improved pressure predictions for free-surface generalised newtonian flows. *Journal of Non-Newtonian Fluid Mechanics*, 218:1–15. [20](#), [21](#), [76](#), [130](#), [134](#), [177](#), [178](#), [179](#), [180](#)
- [353] Xenakis, A. M., Lind, S. J., Stansby, P. K., and Rogers, B. D. (2015b). An isph scheme with shifting for newtonian and non-newtonian multi-phase flows. In *Proceedings of the 10th International SPHERIC Workshop*, pages 84–91. [55](#)
- [354] Xing, A., Yuan, X., Xu, Q., Zhao, Q., Huang, H., and Cheng, Q. (2017). Characteristics and numerical runout modelling of a catastrophic rock avalanche triggered by the wenchuan earthquake in the wenjia valley, mianzhu, sichuan, china. *Landslides*, 14(1):83–98. [27](#), [29](#)
- [355] Xu, R., Stansby, P., and Laurence, D. (2009). Accuracy and stability in incompressible sph (isph) based on the projection method and a new approach. *Journal of Computational Physics*, 228(18):6703–6725. [70](#), [71](#)
- [356] Yang, Q., Jones, V., and McCue, L. (2012). Free-surface flow interactions with deformable structures using an sph–fem model. *Ocean engineering*, 55:136–147. [80](#)
- [357] Yildiz, M., Rook, R., and Suleman, A. (2009). Sph with the multiple boundary tangent method. *International journal for numerical methods in engineering*, 77(10):1416–1438. [14](#), [49](#), [51](#)
- [358] Zhang, A., Sun, P., and Ming, F. (2015). An sph modeling of bubble rising and coalescing in three dimensions. *Computer Methods in Applied Mechanics and Engineering*, 294:189–209. [14](#), [27](#), [29](#), [49](#), [54](#), [69](#)
- [359] Zhang, C., Hu, X. Y., and Adams, N. A. (2017). A generalized transport-velocity formulation for smoothed particle hydrodynamics. *Journal of Computational Physics*, 337:216–232. [50](#)
- [360] Zienkiewicz, O., Jain, P., and Onate, E. (1978). Flow of solids during forming and extrusion: some aspects of numerical solutions. *International Journal of Solids and Structures*, 14(1):15–38. [65](#), [121](#)
- [361] Zienkiewicz, O. C. and Taylor, R. L. (2005). *The finite element method for solid and structural mechanics*. Butterworth-heinemann. [36](#)

Appendix A

Parallelization technique on CPU of our SPH code

The parallelism of the SPH code on CPU is performed using the Domain decomposition method. This method is based on the principle of division of the physical computational domain Ω (in our case the fluid domain) into N_d subdomains Ω_i which are initially load-balanced $\Omega_1 \approx \Omega_2 \approx \dots \approx \Omega_{N_d}$ and $\bigcup_{i=1}^{N_d} \Omega_i = \Omega$.

For a demonstration, we assume that the global domain is divided into 4 sub-domains $\Omega = \Omega_1 \cup \Omega_2 \cup \Omega_3 \cup \Omega_4$. For each subdomain Ω_i a process of rank $Proc_i$ is designated to handle its task of calculation. The physical domain is considered as a continuous medium, meaning that the subdomains are dependent in term of physical computing properties. For this reason, the MPI (Message Passing Interface) paradigm is used to exchange data between subdomains. The Lagrangian movement of the fluid flow imposes the use of specific method. This method must ensure a balanced partitioning of computation loads on each process. In this work, an average position interface detection method was used. This method is based on the calculation of the maximum particle position x_{maxi} that belongs to the x-axis of the subdomain Ω_i and the minimum particle position x_{maxi+1} that belongs to the x-axis of the subdomain Ω_{i+1} for each iteration. The new position of the interface is determined in the middle of these positions (x_{maxi}, x_{maxi+1}) that can express as $In_i = \frac{x_{maxi} + x_{maxi+1}}{2}$. A new distribution of particles on the subdomains Ω_i and Ω_{i+1} must be done in order that all the particles which have an abscissa coordinate less than or equal to the interface position will be transferred to subdomain Ω_i , and the particles which have abscissa coordinate greater than the same interface will be transferred to the subdomain Ω_{i+1} . The communication between the processes using MPI paradigm is done in a way that the process of even rank send the informations held in buffers zones to the odd rank process and they receive them from the odd

processors. While the odd processes receive the information from the process of even rank after they send to the process of odd rank. This strategy ensures sufficient buffer memory to guarantee the continuity of communication as well as optimizing the performance of parallelism.

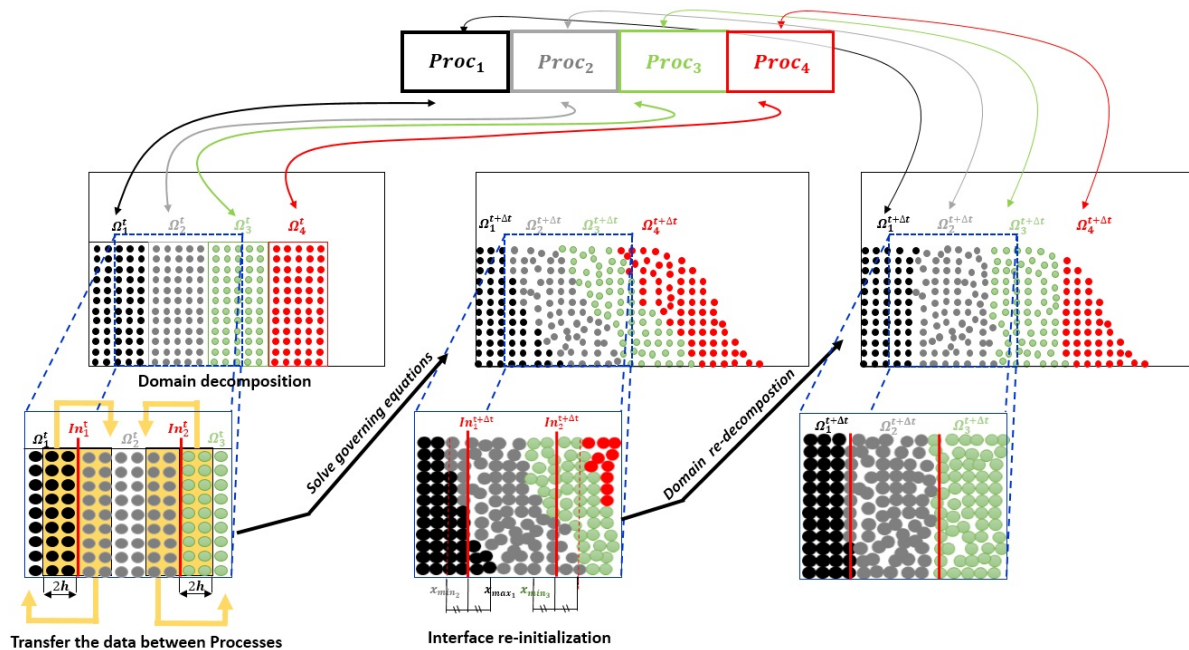


Figure A.1 – Parallelization technique of SPH code on CPU using MPI library.

The parallelization technique was tested on the famous dam break benchmark [243, 72, 216] using different particle resolutions.

The following figure A.3 shows the time-evolution of work loads on four processors, Work loads are computed using the number of particles in each processors divided by the total number of particles. Along the time a very good load balancing was achieved through the proposed parallelism technique. An imbalance of order less than 1% was observed from the moment $t\sqrt{\frac{g}{H}} = 6$. This small imbalance is due to the sudden increase of the fluid velocity caused by the impact of the wave shown at the moment $t\sqrt{\frac{g}{H}} = 6$.

The computing Cloud of the Institute of Research in Constructability of ESTP school was used to perform calculations. The machine is equipped with 32 processors type Intel Xeon Processor E7-4850 frequency 2 GHz and 24 MB cache memory, and has a RAM of 96 GB. In figure A.4, a Sub-linear evolution of the speed-up relative to the number of processors was observed at 8192 particles. This sub-linearity is mainly due to the communication time between the processors that exceeds the computational time on each one. from 25,088 particles the speed-up evolution with processors number becomes super-linear due to the

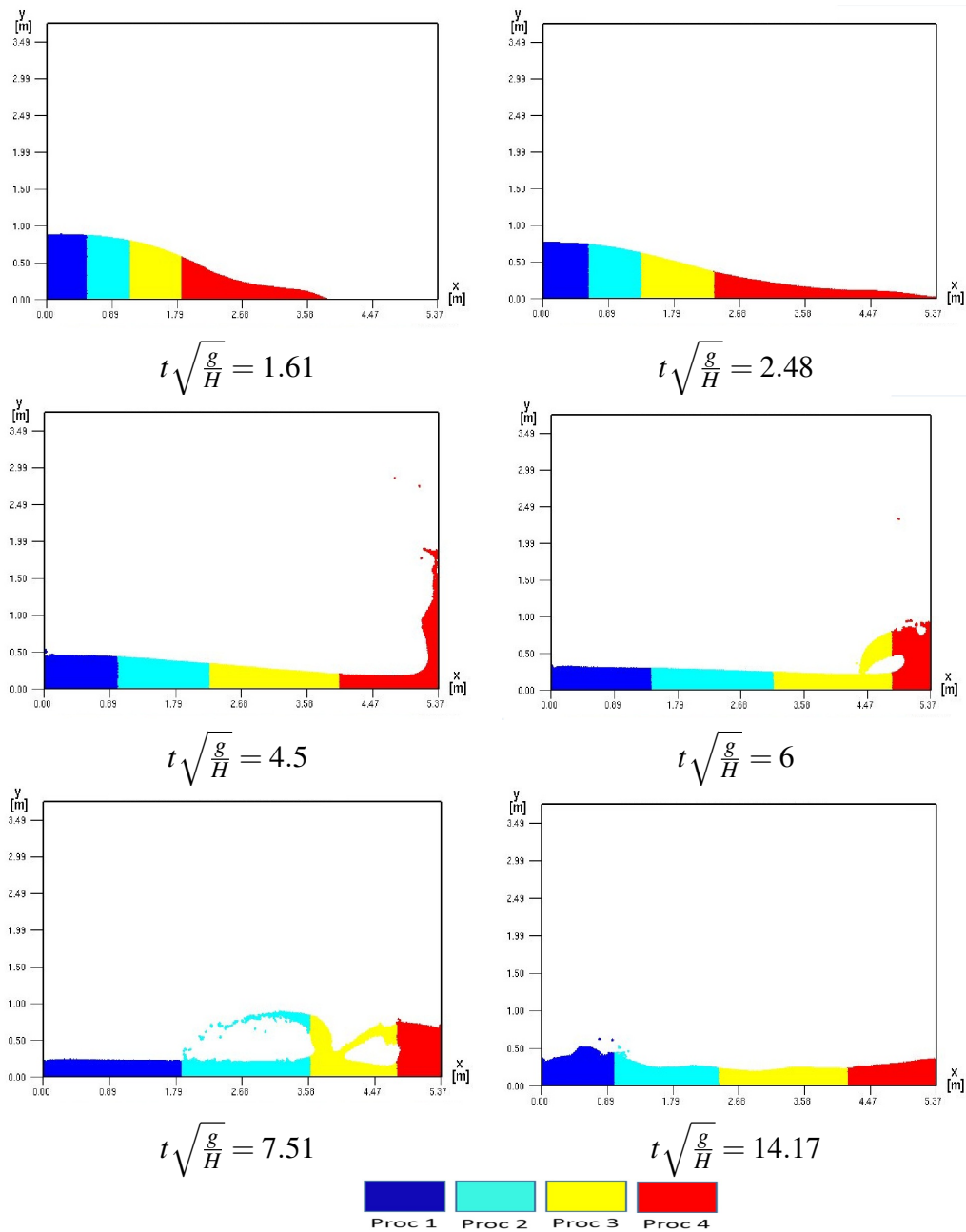


Figure A.2 – The time-evolution flows of particles loads on four processors for 20,000 particles.

ability of caches memories to store the data of the problem, and the speed of their access to the processor.

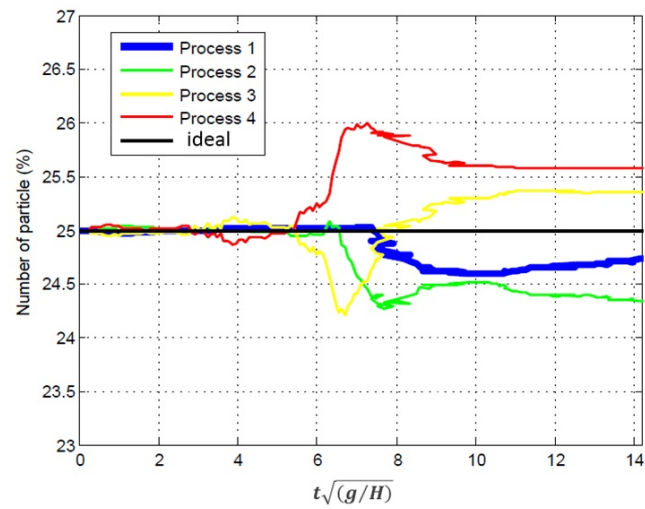


Figure A.3 – The time evolution of load percentage on four processors for 20,000 particles.

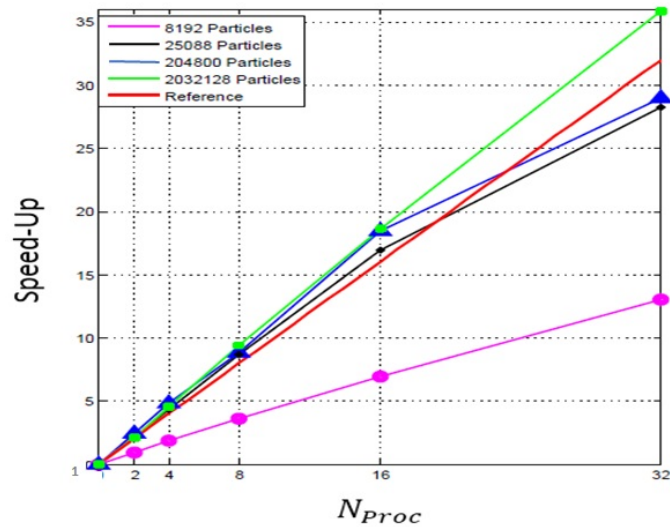


Figure A.4 – Speed-Up of parallel SPH code

Appendix B

Demonstration of the equivalence between CSS and CSF formulations

In this Appendix we show the relation between CSS and CSF formulations. We first recall the CSF formulation. Assuming that the surface tension coefficient $\sigma^{(1-2)}$ is constant between two fluid phases (1 and 2), the expression of the force can be expressed as

$$\mathbf{F}^{ST(1-2)} = \sigma^{(1-2)} \kappa \mathbf{n} \delta_{\Sigma} \quad (\text{B.1})$$

In equation (B.1), κ , \mathbf{n} and δ_{Σ} denote the curvature, the unit normal vector to the interface (see figure 4.1) and the delta function, respectively. In the context of the SPH method, equation (B.1) reads as

$$\mathbf{F}_i^{ST(1-2)} = -\sigma^{(1-2)} \nabla \cdot \mathbf{n}_i \nabla C \quad (\text{B.2})$$

where C is the color function that has a unit jump across the interface. It's equal to 1 in one particle fluid phase and 0 in its neighboring particle of other fluid phase.

Now, the Continuum Surface Stress (CSS) formulation reads

$$\mathbf{F}^{ST} = \nabla \cdot \Pi \quad (\text{B.3})$$

Replacing the stress tensor Π by its formulation in the equation (B.3) we get:

$$\mathbf{F}^{ST} = \nabla \cdot \left(\underbrace{\sigma \|\nabla C\| \mathbf{I}}_{(I)} - \underbrace{\sigma \frac{\nabla C}{\|\nabla C\|} \otimes \nabla C}_{(II)} \right) \quad (\text{B.4})$$

The divergence of the first part (*I*) of the equation (B.4) can be modified as

$$\nabla \cdot (\|\nabla C\| \mathbf{I}) = \nabla (\|\nabla C\|) = \left(\frac{\nabla C}{\|\nabla C\|} \cdot \nabla \right) \nabla C. \quad (\text{B.5})$$

Whereas the divergence of the second part (*II*) can be written as

$$\nabla \cdot \left(\frac{\nabla C}{\|\nabla C\|} \otimes \nabla C \right) = \nabla \cdot \left(\frac{\nabla C}{\|\nabla C\|} \right) \nabla C + \left(\frac{\nabla C}{\|\nabla C\|} \cdot \nabla \right) \nabla C. \quad (\text{B.6})$$

By subtracting the equation (B.6) from equation (B.5), we obtain the Continuum Stress Surface Force formulation (CSF) (B.7):

$$\mathbf{F}^{ST} = -\sigma \nabla \cdot \left(\frac{\nabla C}{\|\nabla C\|} \right) \nabla C = \sigma \kappa \nabla C. \quad (\text{B.7})$$

Where κ describes the interface curvature which is expressed as $\kappa = -\nabla \cdot \mathbf{n} = -\nabla \cdot \left(\frac{\nabla C}{\|\nabla C\|} \right)$, with \mathbf{n} is the unit normal vector to the interface.

Appendix C

The internal forces associated to the surface stress tensor are tangent to the interface ?

In this appendix, we show that the stress surface tension is tangential to the fluid interface. We can write the surface tension as a volumetric force as follows:

$$F^{ST} = \nabla \cdot \Pi \quad (\text{C.1})$$

Where $\Pi = \left(\sigma \|\nabla C\| I - \sigma \frac{\nabla C}{\|\nabla C\|} \otimes \nabla C \right)$ is the stress surface tensor.

This formulation allows the interpretation of the tension force as a internal body forces of the continuum medium (as viscous tensor). So, we will investigate if these efforts are carried by the tangent direction to the interface. For this reason we will applied the stress tensor Π on an arbitrary vector f see figure [C.1](#) :

$$\Pi \cdot f = \sigma \|\nabla C\| (f - (f \cdot n)n) \quad (\text{C.2})$$

$$\Pi \cdot f = \sigma \|\nabla C\| \Xi_T \cdot f \quad (\text{C.3})$$

Where Ξ_T is the projection operator on the tangent plane to the interface. Equation [\(C.3\)](#) indicates that the internal forces associated to the surface stress tensor are tangent to the interface.

240 The internal forces associated to the surface stress tensor are tangent to the interface ?

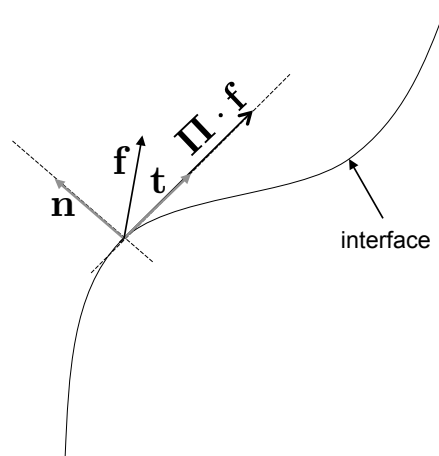


Figure C.1 – Application of stress surface tensor Π on an arbitrary vector f . Where n and t are the normal and tangential vectors on the interface, respectively.

Appendix D

Pseudo-code of SPH interfacial multiphase model.

In this appendix, we summarize the proposed SPH model via a pseudo-code.

```

/* Initialization */
The physical properties of the heavier phase must be assigned to all fluid phases;
The initial particles velocity and pressure are set to zero;
Set  $c_0, p_b, \delta t, T_D, T_{end}$ ;
while  $\delta t * i_t < T_{end}$  do
  Search for each particle  $i \in \Omega = \Omega_f \cup \Omega_s$ , its particles neighbor  $j$ . /* linked list method is employed in this
  work.  $\Omega_f$  and  $\Omega_s$  denote the fluid and solid particles, respectively. */
  /* Damping process */
  if  $\delta t * i_t < T_D$  then
    | Compute  $\xi_D$  using Eq.4.35;
  end
  if  $i_t = \lceil \frac{T_D}{\delta t} \rceil$  then
    | Assign the real physical properties to each fluid phase;
  end
  for  $i \in \Omega_s$  do
    | Compute  $p_w$  and  $\mathbf{v}_w$  using Eqs.5.50 and 5.48, respectively;
  end
  /* Prediction Step */
  for  $i \in \Omega_f$  do
    Compute  $\nabla p_i, \mathbf{F}_i^{Vis}$  and  $\mathbf{F}_i^{ST}$  using Eqs.5.51, 4.26 and 4.20, respectively;
     $\tilde{\mathbf{v}}_i^{n+1} = \mathbf{v}_i^n + \delta t \left( \frac{1}{\rho_i} (-\nabla p_i + \mathbf{F}_i^{Vis} + \mathbf{F}_i^{ST})^n + \xi_D \mathbf{g} \right)$ ;
     $\tilde{\mathbf{r}}_i^{n+1} = \mathbf{r}_i^n + \delta t \mathbf{v}_i^n$ ;
  end
  for  $i \in \Omega$  do
    /* In this loop, the predicted particle velocities and positions are used for the
    calculation of  $\Pi_i, p_w$  and  $\mathbf{v}_w$ . */
    if  $i \in \Omega_f$  and  $\delta t * i_t \geq T_D$  then
      | Compute  $\Pi_i$  using Eq.4.16;
    end
    if  $i \in \Omega_s$  then
      | Compute  $p_w, \mathbf{v}_w$  using Eqs 5.50 and 5.48, respectively;
    end
  end
end
  /* Correction Step */
  for  $i \in \Omega_f$  do
    /* In this loop, the predicted particle velocities and positions are used for the
    calculation of  $\nabla p_i, \mathbf{F}_i^{Vis}$  and  $\mathbf{F}_i^{ST}$ . */
    Compute  $\nabla p_i, \mathbf{F}_i^{Vis}$  and  $\mathbf{F}_i^{ST}$  using Eqs.5.51, 4.26 and 4.20, respectively;
     $\mathbf{v}_i^{n+1} = \frac{1}{2} \{ \mathbf{v}_i^n + \tilde{\mathbf{v}}_i^{n+1} \} + \frac{\delta t}{2} \left( \frac{1}{\rho_i} (-\nabla p_i + \mathbf{F}_i^{Vis} + \mathbf{F}_i^{ST})^n + \xi_D \mathbf{g} \right)$ ;
     $\mathbf{r}_i^{n+1} = \mathbf{r}_i^n + \delta t \mathbf{v}_i^{n+1}$ ;
  end
  for  $i \in \Omega_f$  do
    /* In this loop, the predicted particle positions are used for the calculation of  $\rho_i$  and
    thus  $p_i$ . */
    Compute  $\rho_i$  and  $p_i$  using Eqs.4.8 and 5.2, respectively;
    if  $\delta t * i_t \geq T_D$  then
      | Compute  $\Pi_i$  using Eq.4.16;
    end
  end
end
   $i_t = i_t + 1$ ;
   $n = n + 1$ ;
end

```

Algorithm 1: Pseudo-code of SPH interfacial model.

Modélisation des écoulements fluide multiphasiques avec une approche SPH

RESUME :

La méthode Smoothed Particle Hydrodynamics (SPH) est une méthode lagrangienne, sans maillage développée initialement pour des simulations de phénomènes astrophysiques. Depuis, elle a connu de nombreuses applications, notamment pour la simulation des écoulements des fluides. Contrairement aux méthodes utilisant un maillage, la méthode SPH peut gérer de manière naturelle et sans traitement spécifique les simulations des écoulements à surface libre et multiphasiques avec interface subissant de grandes déformations. Dans cette thèse, une modélisation SPH des écoulements des fluides multiphasiques a été réalisée en tenant compte de différentes complexités (écoulements à surface libre et multiphasiques interfaciaux) et de natures d'écoulement (simulation des fluides, des sols et les deux en interactions). Un modèle SPH faiblement compressible (WCSPH) a été proposé pour simuler les écoulements des fluides multiphasiques avec interface comprenant plus de deux phases de fluide. Ce modèle inclut le développement d'une nouvelle formulation de force de tension de surface en utilisant un opérateur SPH consistant de premier ordre. Une modification de condition généralisée aux parois solides a été apportée pour qu'elle soit appliquée sur les écoulements des fluides multiphasiques avec des rapports de densité et de viscosité élevés. Une nouvelle loi de comportement dépendant de la pression nommée RBMC- α_μ (Regularized Bingham Mohr Coulomb où α_μ est un paramètre libre) a également été développée. Cette loi peut simuler les fluides (Newtonien, Binghamien), les sols (cohésif, frictionnel) et les deux en interactions. La loi précédente étant sensible à la pression, une extension du terme diffusif Δ -SPH a été faite pour le cas des écoulements des fluides multiphasiques afin de réduire les oscillations de pression à haute fréquence qui sont dues à l'utilisation d'une équation d'état. La validation et l'application des modèles développés dans cette thèse sont montrées à travers plusieurs cas tests de difficulté croissante.

Mots clés : Méthode SPH, écoulements multiphasiques, interactions fluide-structure.

Modeling of multiphase fluid flows with Smoothed Particle Hydrodynamics approach

ABSTRACT :

Smoothed Particle Hydrodynamics (SPH) is a Lagrangian gridless method developed initially to simulate astrophysical phenomena, and since it has been known for a large number of applications, especially for fluid flow simulations. Contrary to the grid-based method, the SPH method can handle free surface and interfacial fluid flow simulation including large deformations naturally and without the need for any specific treatment. In this thesis a SPH modeling of multiphase fluid flows has been achieved with consideration of different complexities (free surface and interfacial fluid flows) and natures (simulation of fluids, soil and both in interactions). A consistent weakly compressible SPH model (WCSPH) has been proposed to simulate interfacial multiphase fluid flows with more than two fluid phases. This model includes a new expression of the surface tension force using a first order consistency SPH operator. A modification to the well known generalized wall boundary condition have been brought in order to be applied to multiphase fluid flow with large density and viscosity ratios. A new pressure-based constitutive law named RBMC- α_μ (Regularized Bingham Mohr Coulomb with α_μ is free parameter) has been developed in this thesis. This model can simulate fluids (Newtonian, Binghamton), soils (cohesive, frictional) and both in interactions. Because the previous model is pressure sensitive, an extension of Δ -SPH diffusive term has been proposed for multiphase fluid flows to overcome the high frequency pressure oscillations due to the determination of pressure from an equation of state. The validation and application of the developed models have been shown in this thesis through several test-cases of increasing difficulty.

Keywords : SPH method, multiphase flows, fluid-structure interactions.